**UPC**                    **CTTC**

# Suitability of Different RANS Models in the Description of Turbulent Forced Convection Flows. Application to Air Curtains

Centre Tecnològic de Transferència de Calor
Departament de Màquines i Motors Tèrmics
Universitat Politècnica de Catalunya

Julián Ernesto Jaramillo Ibarra
Doctoral Thesis

# Suitability of Different RANS Models in the Description of Turbulent Forced Convection Flows. Application to Air Curtains

Centre Tecnològic de Transferència de Calor
Departament de Màquines i Motors Tèrmics
Universitat Politècnica de Catalunya

Julián Ernesto Jaramillo Ibarra
Doctoral Thesis

# Suitability of Different RANS Models in the Description of Turbulent Forced Convection Flows. Application to Air Curtains

Julián Ernesto Jaramillo Ibarra

TESI DOCTORAL

presentada al

Departament de Màquines i Motors Tèrmics
E.T.S.E.I.A.T.
Universitat Politècnica de Catalunya

per a l'obtenció del grau de

Doctor per la Universitat Politècnica de Catalunya

Terrassa, 2008

# Suitability of Different RANS Models in the Description of Turbulent Forced Convection Flows. Application to Air Curtains

Julián Ernesto Jaramillo Ibarra

**Directors de la Tesi**

Dr. Carles David Pérez-Segarra

Dr. Assensi Oliva Llena

**Tribunal Qualificador**

A Rocío y a la memoria de mis padres.

# Acknowledgements

Esta tesis no habría sido posible sin la ayuda de varias personas a quienes quiero expresarles mis más sinceros agradecimientos.

En primer lugar, quiero agradecer la colaboración brindada por los directores de esta tesis. A Assensi Oliva por haberme dado la oportunidad de integrarme en el CTTC y por su apoyo ante las dificultades que la realización de este Doctorado ha conllevado. A David Pérez-Segarra, por su tiempo, ideas, consejos, explicaciones esclarecedoras y comentarios acertados.

De igual manera, a todos mis compañeros del CTTC, a quienes crearon y desarrollaron DPC, programa básico para el desarrollo de esta tesis. Vale la pena mencionar a algunos de ellos que me brindaron especial colaboración: Conchita Lifante por su tutoría durante mis comienzos en CFD, Kilian Claramunt por su soporte en mis primeros contactos con los modelos de turbulencia y por el tiempo que me dedicó y Jordi Cadafalch por su meticulosidad en el trabajo y dejarnos el legado de las ppt's, herramienta valiosa de verificación...

A Ivette y Carles, por de manera voluntaria leer algunos apartados de este trabajo. A Elisabet por su contribución con los subdominios multiconectados. A Manolo por su colaboración con los montajes experimentales. A Gustavo por su soporte con los conocimientos eléctricos y su ayuda con algunos temas claves de la anemometría de hilo caliente. De igual forma a los demás compañeros del CTTC con los que compartí conocimientos, experiencias y que de una manera u otra han contribuido en el desarrollo de esta tesis.

A Ramiro y Dani por el apoyo brindado con todos los temas informáticos.

A los compañeros de sala, quienes aportaron pluriculturalidad y amenas charlas enriqueciendo mi diario devenir en el laboratorio, especialmente a Sergio.

A todos los amigos, los que están lejos y los que de alguna manera me han ayudado a olvidar que estoy lejos de casa.

En un plano más personal, a mis hermanos, quienes siempre han creído en mis capacidades y han sido una fuente constante de motivación.

Finalmente, a Rocío por su amor, paciencia, ayuda y comprensión durante todos estos años.

# Contents

*Contents*

16

# Abstract

The main motivation of this thesis is the analysis of turbulent flows. Turbulence plays an important role in engineering applications due to the fact that most flows in industrial equipment and surroundings are in turbulent regime. The thesis has a double purpose and is divided in two main parts. The first one is focussed on the basic and fundamental analysis of turbulence models. In the second part the know-how acquired in the first part is applied to the study of air curtains.

Regarding to the first part, the principal difficulty of computing and modelling turbulent flows resides in the dominance of nonlinear effects and the continuous and wide spectrum of time and length scales. Therefore, the use of turbulence modelling employing statistical techniques for high Reynolds numbers or complex geometries is still necessary. In general, this modelization is based on time averaging of the Navier-Stokes equations (this approach is known as Reynolds-Averaged Navier-Stokes Simulations, RANS). As consequence of the average new unknowns, so-called Reynolds stresses, arise. Different approaches to evaluate them are: i) Differentially Reynolds Stress Models (DRSM), ii) Explicit Algebraic Reynolds Stress Models (EARSM), and iii) Eddy Viscosity Models (EVM).

Although EVM models assuming a linear relation between the turbulent stresses and the mean rate of strain tensor are extensively used, they present various limitations. In the last few years, with the even-increasing computational capacity, new proposals to overcome many of these deficiencies have started to find their way. Thus, algebraic or non-linear relations are used to determinate the Reynolds stress tensor without introducing any additional differential equation.

Therefore, the first part of this thesis is devoted to the study of several EARSM and EVM models involving linear and higher order terms in the constitutive relation to evaluate turbulent stresses. Accuracy and numerical performance of these models is tested in different flow configurations such as plane channel, backward facing step, and both plane and round impinging jets. Special attention is paid to the verification of the code and numerical solutions, and the validation of the mathematical models used. In the impinging plane configuration, improvements of models using higher order terms in the constitutive relation are limited. Whereas, in the rest of studied cases these non-linear models show a reasonably good behavior.

Moreover, taken into account models convergence, robustness and predictive realism observed in the analysis of these benchmark flows, some of them are selected for the study of air curtains and their interaction with the environment where they are placed. Air curtains are generally one or a set of vertical or horizontal plane jets used as ambient separator of adjacent areas presenting different conditions. The jet acts as a screen against energy losses/gains, moisture or mass exchanges between the areas.

As was indicated before, the main purpose of the second part of this thesis is to characterize in detail actual air curtains using both experimental and different numerical approaches. Semi-empirical models to design air curtains are presented. Then, an experimental set-up used to study air curtain discharge and jet downstream is explained. Experimental measurements of velocity and temperature are shown. As a result of the experiments carried out, an improved air curtain with a new design of the discharge nozzle is obtained. Furthermore, air curtain experiments are numerically reproduced and predictions validated against the experimental data acquired. Good agreement between numerical and experimental results is observed.

Finally, systematic parametric studies of air curtains in heating and refrigeration applications are done. Global energetic balances are specially considered together with global parameters selected in order to evaluate air curtain performance. It is found that discharge velocity, discharge angle and turbulence intensity of the jet are the most sensitive parameters. Inadequate values for these variables can produce undesirable effects and contribute to increase energy gains/losses.

# Chapter 1

# Introduction

## 1.1 Prologue

Turbulence plays an important role in engineering applications due to the fact that most flows in industrial equipment and surroundings are in turbulent regime. In nature there are many situations where turbulent flows are present: smoke from chimneys, rivers, waterfalls or buffeting of strong wind. In engineering applications turbulent flows are prevailing. For example, they are found in impelling of liquids or gases with pumps, compressors, pipe lines, etc. Flows around vehicles such as, airplanes, automobiles, and ships are also turbulent. Moreover, the mixing of fuel and air in engines and the mixing of the reactants in chemical reactors are in turbulent regime [1].

Therefore, the motivation to study turbulent flows is the combination of three factors: most of the flows are turbulent; mixing and transport of mass, momentum and heat are important and desirable in many situations; and finally, turbulence accelerates these processes.

Turbulent flows are transitory, highly diffusive, three-dimensional, irregular, seemingly random and chaotic. Turbulence is a nonlinear phenomenon with a wide range of spatial and temporal scales. Thus, the principal difficulty of computing and modelling turbulent flows resides in the dominance of nonlinear effects and the continuous and extensive spectrum of observed scales. The largest scales are generally determined by the geometry of the case studied, whereas the smallest scales are set by the flow itself. Therefore, Direct Numerical Simulation (DNS) of these flows using full three dimensional and time dependent integration of Navier-Stokes (NS) equations is generally restricted to simple geometries and low Reynolds numbers due to the large computational resources required to resolve all the scales. From simple dimensional reasoning is possible to have an idea about the size of the smallest scales. If is assumed that the Kolmogorov microscale ($\eta$) only depends on the fluid viscosity ($\nu$) and the rate of dissipation of energy ($\epsilon$), it can be defined as:

$$\eta = \left(\frac{\nu^3}{\epsilon}\right)^{1/4} \tag{1.1}$$

A connection with flow Reynolds number can be made if some further assumptions are made. Production can be taken equal to dissipation of energy for a flow in equilibrium. The production can be assumed to scale as $u^3/L$, where $u$ is a reference bulk velocity and $L$ a length scale of the problem under consideration, normally associated to the geometry studied. Both $u$ and $L$ are characteristic of the largest scales of the turbulence. Thus:

$$\frac{\eta}{L} \approx Re^{-3/4} \tag{1.2}$$

where $Re = uL/\nu$. Then, the number of grid points that is required in each direction for a given simulation is proportional to $L/\eta \approx Re^{3/4}$ ($cost \propto Re^3$). Furthermore, a corresponding Kolmogorov micro-timescale for the smallest eddies ($\tau$) is given by:

$$\tau = \left(\frac{\nu}{\epsilon}\right)^{1/2} \tag{1.3}$$

Therefore, the time step has to be selected in such a way that the smallest timescales of turbulence are accurately computed [2]. Nevertheless, DNS of the NS-equations suplies with data to study turbulence, including quantities that can not be accurately measured experimentally. Thus, in the last decades Direct Numerical Simulation of the Navier-Stokes equations has been made possible by the development of fast computers, and the improvement of parallelization techniques. Consequently, DNS has provided data that have been used for the development, calibration and validation of turbulence models.

However, for high Reynolds numbers and/or complex geometries is necessary the use of turbulence modelling using statistical techniques. This modelization can be based on volume filtering (Large Eddy Simulation, LES) or time averaging (Reynolds-Averaged Navier-Stokes Equations, RANS) of the NS-equations. Which is sufficient and practical to describe most of the main characteristics of the fluid motions [1]. LES models are still too expensive for routine calculation because, even though the smallest eddies are modelled, the large ones have to be solved in detail (3D and unsteady). In LES only the energy-containing eddies are resolved, and the effects of the unresolved modes are modelled.

To understand the basic idea of LES, suppose somebody wants to perform a DNS but the grid that would be required exceeds the capacity of the available computer; thus, a coarser grid is used. However, there is an interaction between the motions on all scales, resolved and not resolved, so that the result for the large scales would be wrong without taking into account the influence of the fine scales on the large ones. This requires a so-called subgrid-scale model. Despite widespread academic use

of LES, there are still few industrial LES calculations. After more than a decade in which LES has been viewed as the route for by-passing turbulence model limitations, it is still necessary to shown that industry is ready to invest its own resources, manpower and computing to resolve, using LES, a relevant engineering problem. It due to industry has taken advantage of increased computer power to model more realistic geometries and complex physical processes rather than resorting to advanced turbulence modelling. Therefore, the increases in computer power that make the LES of simple industrial problems possible today, are used instead to analyze more and more complex flows and geometries with RANS models [2].

RANS models solve the governing equations by modelling both large and small eddies, taking a time-averaged of variables. Although this process eliminates the need to completely resolve all scales of motion, its drawback is that unknown single-point, higher correlations appear in both mean and turbulent equations. The need to model these correlations is the well known "closure problem". However, RANS technique is a robust, friendly and relatively cost effective way to compute both mean flow and turbulent stresses. In RANS exists three different levels to evaluate the Reynolds stresses generated as consequence of the average process: i) Differentially Reynolds Stress Models (DRSM), ii) Algebraic Reynolds Stress Models (ARSM) and iii) Eddy Viscosity Models (EVM) [1].

DRSM provide the unknown second moments (turbulent stresses) by solving model transport equations for these quantities. Hence, DRSMs have a reasoned physical basis and treat some important turbulence interactions, primarily the stress generation, exactly. This allows capturing of evolution of the turbulent stress field and its anisotropy. The potential of the DRSM, although long recognized, has so far neither been fully explored nor exploited, mainly due to the persisting numerical difficulties, and uncertainties in modelling some of the processes, such as pressure-redistribution. Also, DRSMs do not always show superiority over EVM models. One reason for this is that more terms need to be modelled. While, this offers an opportunity to capture the physics of several turbulence interactions, the advantage may be lost if some of the terms are modelled wrongly [2].

Algebraic stress models convert the differential equations used in DRSM models into algebraic ones by assuming a weak equilibrium assumption. Finally, EVM models couple turbulent stresses with RANS equations through a turbulent eddy viscosity (velocity × length scale). In this last type of models, a hierarchy of closure schemes exists, ranging from zero-equations to two equations models. In zero-equation models, time and length turbulence scales are set by means of algebraic relations whereas, two-equation EVMs calculate eddy viscosity by means of two more differential transport equations: turbulent kinetic energy and some length scale determining equation.

In the context of two-equation models, both linear and non-linear eddy viscosity models appear. The word forms "linear" and "non-linear" refer to the tensor

21

representation used for the model. The linear models assume a Boussinesq relation between turbulent stresses (second moments) and mean rate strain tensor by means of an isotropic eddy viscosity. Non-linear models assume a higher-order tensor representation involving either powers of the mean velocity gradient tensor or combinations of the mean strain rate and vorticity tensors [2].

Even though Two-Equation models using a linear relation are extensively used, they present various limitations [3]. Instead, to overcome some of these deficiencies, non-linear or algebraic stress models are used without introducing any additional differential equation. This kind of models are capable of resolving Reynolds-stress anisotropy, secondary motions, swirling, strong strain and curvature of stream-traces. Also, they are thought to preserve computational economy and numerical robustness of linear models [4]. Thus, the study of NLEVMs and EARSMs is interesting due to they offer a solution between LEVMs and DRSMs, keeping some key aspects from both formulations. The first ones with several limitations but with reduced computational time. The last ones, more complex and with an increased computational cost.

For the reasons mentioned before, this thesis is mainly focussed in the numerical modelling of turbulent flows based on RANS models. It is carried out by means of a comparison of the different modelization levels, taking into account precision, level of description, application range (generality) and computational cost. Specifically, two-equation models ($k - \epsilon$ and $k - \omega$) using a linear (*linear Eddy Viscosity Model, LEVM*), non-linear (*Nonlinear Eddy Viscosity Model, NLEVM*) and algebraic (*Explicit Algebraic Reynolds Stress Model, EARSM*) relation for the calculation of the turbulent stresses, are broadly studied.

To allow the integration of the equations near solid walls the approximation known as low Reynolds number (LRN) is selected. This technique use damping functions to permit the models to be used within the viscous near-wall region [1].

Once the models have been analyzed and their advantages and shortcomings determined in benchmark flows, a selection of the models is carried out in order to apply them in the study of air curtains and its interaction with the environment where they are placed.

Air curtains are generally one or a set of vertical or horizontal plane jets used as ambient separator of adjacent areas presenting different conditions. The jets act as a screen against energy losses/gains, moisture or mass exchanges (smoke, dust, insects,...) between the areas. Air curtains are specially appropriate for configurations where solid barriers become unacceptable for practical, technical or safety reasons [5]. For instance, they are used in doorways or displays cabinets to reduce the penetration of heat or contaminants through the opening, while permitting the passage of people or vehicles.

Air curtains have been mainly studied by means of experimentation or designed with simple mathematical models and only some numerical works have been carried

out. Therefore, the present thesis takes a more comprehensive step toward under-standing and quantification of all major parameters that affect the air curtain per-formance, by the utilization of modern computational and experimental techniques adopting a systematic approach [6].

## 1.2 Literature survey

In this section a brief summary of the state of the art in both RANS modelling and air curtains is presented.

### 1.2.1 Low Reynolds number RANS models

The development of LRN models started at the beginning of 70s. Jones and Launder [7] in 1972 proposed a $k - \epsilon$ model based on the calculation of the eddy viscosity through the numerical solution of transport equations for the turbulent kinetic energy ($k$) and the turbulent kinetic energy dissipation ($\epsilon$). Their main contribution was to make a modification to the model to allow its use in regions of low turbulent Reynolds number. They stated that, to do a correct prediction of the flow within the viscosity sublayer, the model should consider, viscous diffusion in the equations of $k$ and $\epsilon$, empirical functions have to be dependent of the turbulent Reynolds number, and that it is necessary to include additional terms to take into account wall-near processes. Many versions followed this original work, which have been specially focussed in the improvement of the model performance in regions of low turbulent Reynolds number.

In 1985 Patel et al. [8] made a comprehensive revision of LRN models. They included seven variations of the basic $k - \epsilon$ model and the model by Wilcox and Rubesin [3], in which instead of solving an equation for $\epsilon$, it is solved one for the pseudo-vorticity or specific dissipation $\omega$. Patel et al. suggested the necessity of improving damping function associated with the eddy viscosity, due to no one of the models studied could reproduce adequately experimental results near solids walls.

Launder in 1988 [9], published a summary of the different methods used to cal-culate heat transfer coefficients in the numerical simulation of turbulent flows. He demonstrated that accuracy and applicability range of LRN models when a fine enough grid is used near a solid wall were better than those obtained using wall functions. He concluded that the research and advances in turbulence modelling goes hand by hand with process velocity of computers.

Turbulence models using $\omega$ as the length scale determining variable have been gaining importance since 90s, because of their robustness and numerical stability. In 1994, Wilcox [10] presented a model including transition terms, which improved the performance of the model published in 80s near solid walls. After that, Menter [11] proposed a zonal model that use a mix of Wilcox model and Jones and Launder

model. This model solves $\omega$ equation near solid walls and $\epsilon$ equation far from them. Good results were obtained with this model and it is still used in routine calculations.

Since DNS results were first obtained, a detailed knowledge of the viscous sublayer has been possible. Therefore, a lot of attention has gone to the correct asymptotic behavior of the turbulent variables in the regions near solid walls. In order to obtain a reasonable distribution of turbulent variables in confined flows, an effort to avoid dimensionless wall distance ($y^+$), expressed in terms of friction velocity ($u_\tau$), has been done. Instead, Abe et al. [12] replaced this friction velocity with Kolmogorov velocity scale, to improve results in flows with recirculation. Subsequents attempts with the purpose of getting a correct near-wall $\epsilon$ distribution have been done among others by Golberg et al. [13] and Abe et al. [14]. However, it has not been possible to achieve a model with a wide application range. Moreover, after different efforts to improve LEVM performance, such as to model the pressure diffusion term for the $k$ transport equation carried out by Nagano and Shimida [15]; or introducing a modelled gradient production term and the effect of production to dissipation into the sink term made by Rodi and Mansour [16]; several well known anomalies still remain and these factors limit the applicability of LEVMs in complex flows. Thus, the study of this kind of models continues valid at the present time.

Then, to extend the applicability of EVMs the early work of Rivlin [17] and Lumley [18] on a nonlinear relation appealed the similarities between the laminar flow of a non-Newtonian fluid and the mean turbulent flow of a Newtonian fluid. They expressed turbulent stresses as nonlinear polynomial functions of the mean velocity gradient tensors [19]. However, it was until 1987 when Speziale [20] presented a quadratic nonlinear model showing advantages of this kind of formulation. After, Thangham and Speaziale [21] tested this model in a backward facing step configuration achieving good results. Also, in 1987 Nisizima and Yoshizawa [22] obtained a quadratic non-linear relation based on the Yoshizawa's [23] direct interaction approximation model. Furthermore, Myong and Kasagi [24] and Shi et al. [25] have also proposed quadratic nonlinear $k - \epsilon$ models. Even though these models use similar expressions in the stress-strain relation, the coefficients of their nonlinear terms are very different from one to another due to each model has been optimized for different flow configurations. Craft et al. [26] also presented a nonlinear model including terms up to third order. Recently, Abe et al. [27] and Merci et al. [28] have proposed quadratic nonlinear models with additional terms which depend on wall-direction indicators, and that procure the correct behavior due to strong anisotropy in the near-wall region of the Reynolds stresses. So then, this kind of models are not consolidated yet and their benefits in different flow configurations are still under consideration [4].

As it was previously mentioned, there is another approach to build a NLEVM based on the ARSM approach to find the coefficients of the nonlinear relation. The first implicit ARSM model was developed by Rodi [29], who reduced the Reynolds

stress transport equation to a simple algebraic equation, which describes turbulent stresses as non-linear functions of the mean velocity gradients. Later, Pope [30] used Cayley-Hamilton theorem in order to obtain an explicit expression for the turbulent stresses. However, he was not able to provide the coefficients for three-dimensional flows because of the complexity of the algebra involved. This approach is generally known as *explicit algebraic Reynolds stress model, EARSM*, rather than NLEVM. It was not until 90s, when Taulbee [31] and Gatski and Speziale [32] presented detailed coefficients for the three dimensional relation form of Pope. However, these authors considered an equilibrium between production and dissipation, and flow near equilibrium condition, in their work. They also calibrated their models only for homogeneous or high Reynolds number flows. Later, in 2000 Wallin and Johansson [33] developed a model for both compressible and incompressible three-dimensional flows, where the production to dissipation ratio is obtained as a solution of a nonlinear algebraic equation.

This literature survey suggests that there is still a necessity of testing LEVM, NLEVM and EARSM models in a variety of different configurations in order to assess their real capacities and shortcomings.

### 1.2.2 Air curtains

The study of air curtains has been present in the scientific literature since 60s. Thus, the past research mostly relies on experimental work and simplified semi-analytical solutions for jets. Although this research used simplistic formulations for air curtains, its importance lies in identifying most parameters that affect air curtain performance, e.g. turbulence intensity at the jet discharge as a boundary condition is a measure of mixing enhancement; the more distance the air curtain travels provides more opportunities for the air curtain to widen; the width of air curtains provides the initial length for the flow to move laterally, which also can enhance widening of the jet; the velocity at the jet discharge specifies how much kinetic energy is available. These parameters are crucial to understand air curtains performance.

One of the first works found is that by Hetsroni and Hall [34], who studied experimentally air entrainment-spill mechanism across air curtains, and presented results in terms of dimensionless ratios. They introduced analytical expressions to quantify the heat transfer through the air curtain. Hayes and Stoecker [35, 36] presented a comprehensive explanation of the different kind of pressure differences, which must be taken into account in air curtains design. They considered in all their studies that the building was sealed except for the opening doorway where the air curtain was located, then presented analytical expressions and one example for the design of air curtains.

Studies by Howell and Shiabata [37] revealed that the ratio of the opening height (H) to the discharge width (w) and the jet velocity (V) affect the "performance" of

air curtains. They stated that there is a direct proportionality of heat transfer across an air curtain to the discharge air velocity. Howell and Shiabata [37] also showed that a higher turbulence intensity at the discharge accelerates the widening of the jet, causing a higher heat transfer across the air curtain. They found that 75% of the refrigeration load in an open vertical display case is a result of the warm air entrainment across the air curtain.

Partyka [38] carried out an analytical study of flow impact region of two jets to develop a mathematical model that yields data for the air curtain performance. The theory permitted him to establish the quantitative influence of the jet properties and duct geometry on the pressure difference and to predict flow conditions. He programmed resulting equations and presented some computed and experimental results.

Faramarzi and Kemp [39] experimentally studied display cabinets. Their object was to evaluate the performance of two models with respect to energy efficiency and product temperature maintenance. They achieved the conclusion that the most important loss is due to infiltration. Therefore, it is very important the correct design of the air curtain to prevent it in display cases. In the same year, Faramarzi [40] presented a discussion about the cooling load composition in an open display cabinet.

In the paper of Stribling et al. [41] is presented a two-dimensional computational study with a commercial code of a vertical display. They found that this model could be used in the design and optimization of such equipment but it needs further validation to be accepted as quantitatively accurate. Further application of computational fluid dynamics (CFD) codes to air curtains has been inconclusive. They stated that one should realize that CFD provides a numerical solution of the Navier-Stokes (NS) equations. That it is mathematically known that there is not an unique solution for these equations. So it is quite possible that a careless implementation of a boundary condition (from a user or programmer) could propagate and yield inconsistent results.

Solliec et al. [42] studied the possibility of using air curtains to reduce transport of contaminants and to explain how the mass transfer happens, thus showing the interest to use such systems of containment to fight against olfactive harmful effects. Pavageau et al. [5] experimented with different configurations of air curtains: air jet tightness and double flux. Flow visualization and particle image velocimetry (PIV) measurements were carried out. The main results were reported and recommendations were drawn.

By the year 2001, Ge and Tassou [43] studied numerically an air curtain in a display cabinet by means of finite differences technique, based on their results developed correlations for the heat transfer across air curtains in refrigerated display cabinets. He validated both models against experimental results. Also, in this year Kim et al. [44] carried out a CFD 3D simulation, using the standard $k - \epsilon$ model, with the purpose of analyzing indoor cooling/heating. The CFD study is coupled with

a radiative analysis. Heating, ventilating and air-conditioning (HVAC) controlling system in a room is also coupled to the CFD simulation. The loop feed backs the outputs of the HVAC system control to the input boundary conditions of the CFD. Furthermore, this method included a human model to evaluate the thermal comfort environment.

Navaz et al. [45, 46] demonstrated that a marriage between the digital PIV experimental technique and CFD simulation can be quite effective to study the flow field characteristics and performance of the air curtain of an open vertical display case. The PIV can calibrate the numerical technique after which the CFD code can be used for parametric studies. They demonstrated that the validation of a CFD model with reliable and comprehensive experimental data is a pre-requisite for generating reasonable results. Other example of the combination of CFD and experimental techniques was presented by Foster et al. [47]. They used a CFD model of air movement through a doorway, which was verified against laser Doppler anemometry (LDA) measurements.

One of the last analytical models found in the literature for the design of air curtains was developed by Sirén [48, 49], who provided valuable information for the design of vertically upwards-blowing air curtains. He presented a technical dimensioning of an air curtain considering effects of building envelope and ventilation system, then presented practical mathematical formulations for the dimensioning of air curtains. The method was based on the momentum-of-momentum principle, which enables the considerations of the jet impact point.

The effect of the Richardson and Reynolds numbers on the shape of the streamlines representing the entrained air at the discharge grill of display cabinets has been studied by Chen and Yuan [50] by means of CFD simulations. This work is valuable because it quantified the effects of the Richardson number, $Ri = \frac{Gr}{Re^2}$ (ratio of Grashof to the square of Reynolds number), on the entrainment of ambient air into the cold air jet.

In 2006 Navaz et al. [51] presented a work to address the effects of velocity profile at the discharge air grill on the amount of entrained air into an open refrigerated display case. The study was carried out using experimental (PIV and LDA) and numerically by means of CFD simulations. They found that a skewed parabolic profile with the peak shifted towards the inner section of the case generates the minimum entrainment, and demonstrates that with simple changes to the geometry of the discharge grill, a significant reduction in the entrainment rate could be achieved.

Finally, a couple of works dealing with air curtains placed in door openings to separate two different ambient have been published. Foster et al. [52, 53] studied the effectiveness of a commercially available air curtain at different jet velocities and found the optimum jet velocity to give the maximum effectiveness. Then, compared the experimental results with predictions from an analytical model and CFD simulations. Moreover, Costa et al. [54] have studied numerically the influence of the different dynamic and geometrical parameters on the sealing efficiency of a down

ward-blowing air curtain device, which is installed between two contiguous room with distinct ambient temperatures. Therefore, only stack effect was considered.

As it can be observed only few publications where air curtains are studied on a door acting as ambient separator in a building have been found. Furthermore, no one takes into account wind velocity. On the other hand, the rest of them restrict their studies to display cabinets, where external air velocity is not an important factor and the environment conditions can be easily determined, therefore, used in numerical simulations and physical domain can be simplified to a 2D computational domain. Also, it was only possible to find one paper that study the air curtain with the environment influence together by means of fully 3D simulations. Furthermore, it seems that the influence of important variables such as the turbulence model and the grid used in the computations have not been studied in detail. Then, future works should include these parameters and the combination of CFD 3D simulations with advanced experimental techniques (PIV, LDA, hot-wire anemometry, etc.) to validate the numerical results. These aspects are taken into account in this thesis.

## 1.3   Background

This thesis has been elaborated at the Heat and Mass Transfer Technological Center (CTTC) of the Technical University of Catalonia (UPC). The research at the CTTC is focussed on two main lines: i) mathematical formulation, numerical resolution and experimental validation of heat and mass transfer phenomena. ii) application of the acquired know-how from the basic studies mentioned to the thermal and fluid dynamic optimization of thermal system and equipment. Thus, a general flow modelling software, known as DPC, has been developed [55].

In the first research line, CTTC has given special attention to the study of turbulent flows. Two different research areas in this field have been specially considered, LEVM RANS models and DNS. Then, this thesis constitutes an effort to widen the spectra of turbulence RANS models available in the DPC code, by the inclusion and testing of new NLEVM and EARSM RANS models. LEVM RANS models used in this thesis to perform comparative studies, which have been previously implemented by another CTTC researchers, can be found in different publications [56, 57, 58, 59, 60, 61] and two PhD thesis [62, 63].

Furthermore, in the framework of applied research at CTTC, the second part of this thesis is focussed on the study and analysis of air curtains. Thus, chapters 5 and 6 have been developed within two research European CRAFT projects [64, 65], and one collaborative agreement between an air curtain manufacturer and CTTC.

Verification of numerical solutions using CFD has been considered as an relevant aspect in order to produce reliable results. In order to determine numerical results quality, a post-processing procedure has been implemented at the CTTC [66]. Thus,

whenever is possible, solutions obtained are submitted to this process to estimate the order of accuracy and the error band where the grid independent solution is expected to be contained.

In order to reduce computational resources and to allow complex geometries to be studied, a parallel multiblock algorithm using loosely coupled computers is used [67, 68]. CTTC facilities includes a Beowulf cluster called Joan Francesc Fernandez (JFF). Nowadays, it is formed by 125 CPUs with 100Gbytes of RAM and 7.25Tbytes of disk space. Main contributions on parallel computing and multiblock techniques are gathered in the PhD thesis of M. Soria [69] and J. Mora [70].

## 1.4 Thesis outline

This thesis has a double purpose. It is intended to test LEVM, NLEVM and EARSM models in a variety of different configurations in order to assess their real capacities and shortcomings. Then, accordingly to the results obtained, some models are selected to be applied in the study of air curtain devices. Thus, in Chapter 2 is carried out an introduction to the mathematical formulation used throughout this thesis. Special attention is devoted to the turbulence modelling selected to simulate flows in turbulence regime. Within this topic, the different possibilities to study turbulent flows are briefly summarized. Since, RANS modelling is selected in this thesis the explanation is centered on it. Furthermore, discretization of the governing equations, computational methodology details, verification tools and solvers used in this thesis are also introduced in Chapter 2.

The aim of Chapter 3 is to study the adequacy of different RANS models in terms of accuracy and numerical performance in the description of three different turbulent internal forced convection flows, i.e. plane channel, backward facing step, and confined impinging slot jet. Within RANS modelization, linear and non-linear eddy-viscosity models and explicit algebraic models are explored. A comparison of the suitability of different two-equation platforms such as $k - \epsilon$ and $k - \omega$ is also carried out.

In Chapter 4 this work is extended to studying numerical performance and accuracy of models when they are used in the simulation of both, plane and round impinging jets. With this purpose, results from numerical simulations using different models, are compared among them and with experimental data available in the literature.

Once capabilities of the models are assessed. The work is centred in the use of them to study air curtains. Therefore, the main purpose of Chapter 5 is to present an introduction to air curtains. Different approaches are explained. At the beginning, semi-empirical models developed to design air curtains are shown. After, an experimental setup used in the study of air curtain discharge and downstream jet produced is explained. Thus, measurements of different air curtian prototypes are presented

in order to characterize the air-curtain fluid-dynamic and thermal fields. Finally, air curtains are simulated using CFD and the code is validated using experimental data acquired.

After code validation and air curtains physics understanding is accomplished, in Chapter 6 a set of numerical studies to test air-curtains is carried out. Thus, systematic parametric studies are performed, providing conclusions about the influence on the air-curtain behavior of the air curtain location, discharge velocity, discharge angle, and discharge temperature. Applications to both, air conditioning and refrigeration are numerically studied.

Finally, a chapter with conclusions is included to present the main achievements and limitations of the work carried out in this thesis. Future actions in both areas turbulence modelling and air curtain research are also suggested. Moreover, a list of the main publications carried out in the context of this thesis can be found in Appendix B.

# References

[1] S.B. Pope. *Turbulent Flows*. Cambridge University Press, 2000.

[2] B. E. Launder and N. D. Sandham. *Closure Strategies for Turbulent and Transitional Flows*. Cambridge University Press, 2002.

[3] D.C. Wilcox. *Turbulence modeling for CFD*. DCW Industries, Inc. CA, 1998.

[4] Y. J. Jang, M. A. Leschziner, K. Abe, and L. Temmerman. Investigation of Anisotropy-Resolving Turbulence Models by Reference to Highly-Resolved LES data for Separated flow. *Flow, Turbulence and Combustion*, 69(2):161–203, 2002.

[5] M. Pavageau, E. M. Nieto, and C. Rey. Odor and VOC confining in Large Enclosure. *Water, Science and Technology*, 4(9):165–171, 2001.

[6] H. K. Navaz, D. Dabiri, M. Amin, and R. Faramarzi. Past, Present, and Future Research Toward Air Curtain Performance Optimization. *ASHRAE Transactions*, 111:1083–1088, 2005.

[7] W.P. Jones and B.E. Launder. The prediction of laminarization with a two-equation model of turbulence. *International Journal of Heat and Mass Transfer*, 15:301–314, 1972.

[8] V. C. Patel, W. Rodi, and G. Scheuerer. Turbulence models for near-wall and low Reynolds number flows - A review. *AIAA Journal*, 23:1308–1319, 1985.

*References*

[9] B. E. Launder. On the Computation of Convective Heat Transfer in Complex Turbulent Flows. *ASME J. Heat Transfer*, 110:1112–1128, 1988.

[10] D. C. Wilcox. Simulation of Transition with a Two-Equation Turbulence Model. *AIAA Journal*, 32:247–255, 1994.

[11] F.R. Menter. Two-Equation Eddy-Viscosity Turbulence Models for Engineering Applications. *AIAA Journal*, 32(8):1598–2005, 1994.

[12] K. Abe, T. Kondo, and Y. Nagano. A New Turbulence Model for predicting Fluid, Flow and Heat Transfer in Separating and Reattaching Flows-I. Flow field calculations. *International Journal of Heat and Mass Transfer*, 37(1):139–151, 1994.

[13] U. Goldberg, O. Peroomian, and S. Chakravarthy. A Wall-Distance-Free k-$\epsilon$ Model with Enhanced Near-Wall Treatment. *Journal of Fluids Engineering*, 120(3):457–462, 1998.

[14] K. Abe, T. Kondoh, and Y. Nagano. On Reynolds-Stress expresions and near-wall scaling parameters for predicting wall and homogeneous turbulent shear flows. *International Journal of Heat and Fluid Flow*, 18:266–282, 1997.

[15] Y. Nagano and M. Shimida. Modelling the dissipation rate equation for two equation turbulence model. In *Proceedings of the 9th Symp. Turbulent Shear Flows*, pages 2–23, 1993.

[16] W. Rodi and N. Mansour. Low Reynolds number $k - \epsilon$ modelling with the aid of direct simulation data. *Journal of Fluid Mechanics*, 250:509–529, 1993.

[17] R. S. Rivlin. The relation between the flow of non-Newtonian fluids and tubulent Newtonian fluids. *Quarterly Applied Mathematics*, 15:212–215, 1957.

[18] J. L. Lumley. Toward a turbulent constitutive relation. *Journal of Fluid Mechanics*, 41(2):413–434, 1970.

[19] K. Suga. *Development and Application of a Non-linear Eddy Viscosity Model Sensitized to Stress and Strain Invariants*. PhD thesis, University of Manchester, 1995.

[20] C. G. Speziale. On Nonlinear K-l and $k - \epsilon$ Models of Turbulence. Two-Equation Models. *Journal of Fluid Mechanics*, 178:459–475, 1987.

[21] S. Thangam and C. G. Speziale. Turbulent Flow Past a Backward-Facing Step: A Critical Evaluation of Two-Equation Models. *AIAA Journal*, 30:1314–1320, 1992.

[22] S. Nisizima and A. Yoshizawa. Turbulent channel and Couette flows using an anisotropic $k - \epsilon$ model. *AIAA Journal*, 25(3):414–420, 1987.

[23] A. Yoshizawa. Statistical analysis of the deviation of the Reynolds stress from its eddy viscosity representation. *Physics of Fluids*, 27:1377–1387, 1984.

[24] H. K. Myong and N. Kasagi. Prediction of anisotropy of the near wall turbulence with an anisotropic low-Reynolds number $k - \epsilon$ turbulence model. *Journal of Fluids Engineering*, 112:521–524, 1990.

[25] T. H. Shi, J. Zhu, and J. L. Lumley. A new Reynolds stress algebraic equation model. *Computer Methods in Applied Mechanics and Engineering*, 125(1):287–302, 1995.

[26] T.J. Craft, B.E. Launder, and K. Suga. Development and Application of Cubic Eddy-Viscosity Model of Turbulence. *International Journal of Heat and Fluid Flow*, 17(1):108–115, 1996.

[27] K. Abe, Y. J. Jang, and M. A. Leschziner. An Investigation of Wall-Anisotropy Expressions and Length-Scale Equations for Non-Linear Eddy-Viscosity Models. *International Journal of Heat and Fluid Flow*, 24(2):181–198, 2003.

[28] B. Merci, V. M. Karin, and E. Dick. Impingement heat transfer with a nonlinear first-order $k - \epsilon$ model. *Journal of Thermophysics and Heat Transfer*, 20(1):144–148, 2006.

[29] W. Rodi. *The prediction of free turbulent boundary layers by use of a two-equation model of turbulence.* PhD thesis, University of London, 1972.

[30] S. B. Pope. A more effective-viscosity hypothesis. *Journal of Fluid Mechanics*, 72:331–340, 1975.

[31] D. B. Taulbee. An improved algebraic Reynolds stress model and corresponding nonlinear stress model. *Physics of Fluids*, 4(11):2555–2561, 1992.

[32] T.B. Gatski and C.G. Speziale. On Explicit Algebraic Stress Models for Complex Turbulent Flows. *Journal of Fluid Mechanics*, 254(1):59–78, 1993.

[33] S. Wallin and A. V. Johansson. An Explicit Algebraic Reynolds Stress Model for Incompressible and Compressible Turbulent Flows. *Journal of Fluid Mechanics*, 403:89–132, 2000.

[34] G. Hetsroni, C. W. Hall, and A. M. Dhanak. Heat Transfer Properties of an Air Curtain. *ASAE Transactions*, 1:328–334, 1963.

*References*

[35] F. C. Hayes and W. F. Stoecker. Design Data for Air Curtains. *ASHRAE Transactions*, 2121:168–179, 1969.

[36] F. C. Hayes and W. F. Stoecker. Heat Transfer Characteristics of the Air Curtain. *ASHRAE Transactions*, 2120:153–167, 1969.

[37] R. H. Howell and M. Shiabata. Optimum Heat Transfer Through Turbulent Recirculated Plane Air Curtains. *ASHRAE Transactions*, 86(1):188–200, 1980.

[38] T. S. Park and H.J. Sung. A Nonlinear low-Reynolds-number $k - \epsilon$ model for Turbulent Separated and Reattaching FLows–I. Flow Field Computations. *International Journal of Heat and Mass Transfer*, 38:2657–2666, 1995.

[39] R. Faramarzi and K. Kemp. Comparing Older and Newer Refrigerated Display Cases. *ASHRAE Journal*, Aug.:45–49, 1999.

[40] R. Faramarzi. Efficient Display Case Refrigeration. *ASHRAE Journal*, Nov.:46–54, 1999.

[41] D. Stribling, S.A. Tassou, and D. Marriott. A Two Dimensional CFD Model of a Refrigerated Display Case. *ASHRAE Transactions*, 103(1):88–94, 1999.

[42] C. Solliec, S. Maurel, M. Pavageau, and P. Le Cloirec. Isolation of contaminated areas and control of fugitive emissions using air curtains. *Pollution Atmosphérique*, 169:127–137, 2001.

[43] Y.T. Ge and S.A. Tassou. Simulation of the Performance of Single Jet Air Curtains for Vertical Refrigerated Display Cabinets. *Applied Thermal Engineering*, 21:201–219, 2001.

[44] T. Kim, S. Kato, and S. Murakami. Indoor cooling/heating load analysis based on coupled simulation of convection, radiation and HVAC control. *Building and Environment*, 36:901–908, 2001.

[45] H.K. Navaz, R. Faramarzi, M. Gharib, D. Dabiri, and D. Modarress. The Application of Advanced Methods in Analyzing the Performance ot the Air Curtain in a Refrigerated Display Case. *Journal of Fluids Engineering*, 124(1):756–764, 2002.

[46] H. K. Navaz, B. S. Henderson, R. Faramarzi, A. Pourmovahed, and F. Taugwalder. Jet entrainment rate in air curtain of open refrigerated display cases. *International Journal of Refrigeration*, 28:267–275, 2005.

[47] A. M. Foster, R. Barrett, S. J. James, and M. J. Swain. Measurement and prediction of air movement through doorways in refrigerated rooms. *International Journal of Refrigeration*, 25(8):1102–1109, 2002.

[48] K. Sirén. Technical Dimensioning of a Vertically Upwards Blowing Air Curtain. Part I. *Energy and Buildings*, 35:681–695, 2003.

[49] K. Sirén. Thechnical Dimensioning of a Vertically Upwards Blowing Air Curtain-part II. *Energy and Buildings*, 35:697–705, 2003.

[50] Y. G. Chen and X. L. Yuan. Simulation of a cavity insulated by a vertical single band cold air curtain. *Energy Conversion Management*, 46:1745–1756, 2005.

[51] H. K. Navaz, M. Amin, S. C. Rasipuram, and R. Faramarzi. Jet entrainment minimization in an air curtain of open refrigerated display case. *International Journal for Numerical Methods for Heat and Fluid Flow*, 16(4):417–430, 2006.

[52] A. M. Foster, M. J. Swain, R. Barrett, P. D'Agaro, and S. J. James. Effectiveness and optimum jet velocity for a plane jet air curtain used to restrict cold room infiltration. *International Journal of Refrigeration*, 29(5):692–699, 2006.

[53] A. M. Foster, M. J. Swain, R. Barrett, P. DAgaro, L. Ketteringham, and S. J. James. Three-Dimensional Effects of an Air Curtain Used to Restrict Cold Room Infiltration. *Applied Mathematical Modelling*, 31(6):1109–1123, 2007.

[54] J. J. Costa, L. A. Oliveira, and M. C. G. Silva. Energy savings by aerodynamic sealing with a downward-blowing plane air curtain-A numerical approach. *Energy and Buildings*, 38:1182–1193, 2006.

[55] CTTC-UPC. DPC: library for the development of programs focussed on the resolution of combined heat and mass transfer problems, 2004.

[56] C.D. Pérez-Segarra, A. Oliva, and M. Costa. Benchmark of turbulent natural convection in a square cavity. Comparison between different k-$\epsilon$ turbulence models. pages 109–120, 1993.

[57] J. Cadafalch, C. D. Pérez-Segarra, M. Sòria, and A. Oliva. Fully conservative multiblock method for the resolution of turbulent incompressible flows. In *Proceedings of the Fourth European Computational Fluid Dynamics Conference (ECCOMAS CFD)*, pages 1234–1239, 1998.

[58] R. Cònsul, C. D. Pérez-Segarra, J. Cadafalch, and K. Claramunt. Numerical experiments on turbulent forced convection using low reynolds number two-equation models. In *Proceedings of the Third European Congress on Computational Methods in Applied Sciences and Engineering (ECCOMAS)*, pages 1–19, 2000.

*References*

[59] K. Claramunt, J. Jaramillo, X. Albets, and D. Piedrafita. Simulación numérica de flujos turbulentos en base a modelos de de dos ecuaciones de transporte turbulento. In *Anales de Ingeniería Mecánica (Revista de la Asociación Española de Ingeniería Mecánica, Año 14)*, pages 1840–1844, 2002.

[60] X. Albets, C. D. Pérez-Segarra, J. Cadafalch, C. Lifante, and K. Claramunt. Numerical experiments in turbulent natural convection using two-equation eddy-viscosity models. In *Proceedings of the IV International Symposium on Turbulence, Heat and Mass Transfer*, pages 853–860, 2003.

[61] X. Albets, C. D. Pérez-Segarra, and A. Oliva. Analysis of wall function approaches using two-equation turbulence models. In *Proceedings of the 9th UK National Heat Transfer Conference*, pages 1–16, 2005.

[62] J. Cadafalch. *Numerical simulation of turbulent flows. Multiblock techniques. Verification and experimental validation.* PhD thesis, Universitat Politècnica de Catalunya, 2002.

[63] X. Albets. *Numerical Studies of Natural and Forced Convective Heat Transfer Processes Using Two-Equation Turbulence Models.* PhD thesis, Universitat Politècnica de Catalunya, 2006.

[64] C.D. Pérez-Segarra, C. Oliet, S. Danov, J. Jaramillo, C. Orozco, E. Mas de les Valls, and A. Oliva. COMHEX project: Publishable Final Technical Report. Technical report, 2005.

[65] C. Oliet, C. D. Pérez-Segarra, J. jaramillo, A. Sadurni, and O. Lehmkuhl. EFROST project: PUBLISHABLE FINAL ACTIVITY. Technical report, 2007.

[66] J. Cadafalch, C. D. Pérez-Segarra, R. Cònsul, and A. Oliva. Verification of Finite Volume Computations on Steady State Fluid Flow and Heat Transfer. *Journal of Fluids Engineering*, 124(11):11–21, 2002.

[67] J. Cadafalch, J. Salom, M. Costa, and A. Oliva. Domain decomposition as a method for the parallel computing of laminar incompressible flows. In *Proceedings of the Second European Congress on Computational Methods in Applied Sciences and Engineering (ECCOMAS)*, pages 845–851, 1996.

[68] M. Soria, C.D. Pérez-Segarra, and A. Oliva. A direct schur-fourier decomposition for the solution of three-dimensional poisson equation of incompressible flow using loosely coupled parallel computers. *Numerical Heat Transfer, Part B*, 43(5):467–488, 2003.

[69] M. Soria. *Parallel multigrid algorithms for computational fluid dynamics and heat transfer.* PhD thesis, Universitat Politècnica de Catalunya, 2000.

[70] J. Mora. *Desarrollo y validación de algoritmos tridimensionales aplicados a la transferencia de calor, masa y mecánica de fluidos en coordenadas cilíndricas.* PhD thesis, Universitat Politècnica de Catalunya, 2001.

# Chapter 2

# Mathematical formulation and numerical methodology.

**Abstract.** The objective of this chapter is to carry out an introduction to the mathematical formulation used troughout this thesis. Special attention is devoted to the turbulence modelling selected to simulate flows in turbulence regime. Since, RANS modelling is used in this thesis the explanation is centered on it. Thus, a detailed explanation of the process followed to obtain averaged equations is shown. Derivation of the equations used to solve the turbulent quantities is also presented. Furthermore, a brief description of the discretization of the governing equations, computational methodology, verification tools and solvers used in this thesis is included.

## 2.1 Introduction

As it was explained in the previous Chapter, turbulence is that state of fluid motion which is characterized by apparently random and chaotic three-dimensional vorticity. When turbulence is present, it usually dominates all other flow phenomena and results in increased energy dissipation, mixing, heat transfer, and drag. Just like the solutions of non-linear dynamic systems, turbulent solutions are thought to be determined by their boundary and initial conditions. As non-linear dynamic systems, these deterministic solutions of the non-linear fluid mechanics equations exhibit behavior that appears for all intents and purposes to be random. Such solutions are called turbulent, and the phenomenon turbulence. Because of this random behavior of turbulence, statistical techniques are needed for most of the study of turbulence. All fluid motions, whether turbulent or not, are governed by the Navier-Stokes equations. Although laminar solutions to the equations often exist that are consistent with the boundary conditions, perturbations to these solutions can cause them to become turbulent. To see how this can happen, it is convenient to analyze the flow in two components, a mean (or average) part and a fluctuating part. This technique for decomposing the instantaneous motion is referred to as the Reynolds decomposition. Applying this method to the instantaneous equations, a set of new averaged equations is obtained. Moreover, as a result of this decomposition new unknowns arise (Reynolds stresses and turbulent heat flux), leaving the mathematical formulation based on averaged equations not closed (turbulence closure problem). Therefore, relations had to be introduced to relate the stresses to the mean flow itself (mean rate of strain). In this Chapter closure attempts for these relations and the mathematical models involved are explained.

Researchers dedicate their attention to two fundamental aspects in CFD: physical modeling and numerics. In physical modeling, we seek a set of equations or mathematical relations that allow us to close the governing equations. Moreover, the focus in numerics is to devise efficient, robust, and trustworthy algorithms for the solution of the partial differential equations (PDEs). PDEs are a combination of differential terms (rates of change) that describe a conservation principle. CFD process requires the discretization of the governing PDEs, i.e. the derivation of equivalent algebraic relations that should reliably represent the original PDEs. This is done by transforming each differential term into an approximate algebraic relation. Thus, three key aspects arise, i.e. discretization methodology, algorithm of resolution, and verification and validation of the obtained results.

## 2.2 Mathematical turbulence modelling

### 2.2.1 The Navier-Stokes equations

The equations expressing conservation of mass, momentum and energy, govern fluid dynamics and heat transfer for both laminar and turbulent flows, these are known as Navier-Stokes equations, which for incompressible Newtonian fluids assuming negligible heat friction, and radiative effects, may be written as follows:

$$\frac{\partial u_i}{\partial x_i} = 0 \tag{2.1}$$

$$\frac{\partial(\rho u_i)}{\partial t} + \frac{\partial(\rho u_j u_i)}{\partial x_j} = -\frac{\partial p}{\partial x_i} + \frac{\partial}{\partial x_j}(2\mu S_{ij}) + \rho g_i \tag{2.2}$$

$$\frac{\partial(\rho T)}{\partial t} + \frac{\partial(\rho u_i T)}{\partial x_i} = \frac{\partial}{\partial x_i}\left(\frac{\lambda}{c_p}\frac{\partial T}{\partial x_i}\right) \tag{2.3}$$

where $T$ is the temperature; t time; $u_i$ the velocity; $\rho$, $\mu$, $\lambda$ and $c_p$ are respectively: density, viscosity, conductivity and specific heat; and $S_{ij} = \frac{1}{2}\left(\frac{\partial u_i}{\partial x_j} + \frac{\partial u_j}{\partial x_i}\right)$ is the strain-rate tensor.

### 2.2.2 Statistical approach of turbulence: RANS modelling

As it was mentioned in the introduction, in the time averaged Navier-Stokes technique (RANS), introduced by Reynolds [1], the equations are averaged statistically before being solved. Thus, for stationary turbulence (statistically steady), the instantaneous variable under consideration (e.g. $\phi(x,t)$) can be expressed as the sum of a mean part ($\bar{\phi}(x,t)$) and a fluctuating part ($\phi'(x,t)$):

$$\phi(x,t) = \bar{\phi}(x,t) + \phi'(x,t) \tag{2.4}$$

where the variable $\bar{\phi}(x,t)$ is time-averaged and defined as

$$\bar{\phi}(x,t) = \frac{1}{\Delta T}\int_t^{t+\Delta T}\phi(x,t)dt \tag{2.5}$$

and the time-average of the fluctuating part is zero $\overline{\phi'(x,t)} = 0$.
To carry out the time-average, special care must be taken with the averaging time ($\Delta T$), because this has to be large enough compared with turbulent time-scales, but also sufficiently short compared with the characteristic time-scales of the mean flow, i.e. it should filter small fluctuations due to turbulence effects, but not the main time variations of the flow.

### 2.2.3   Reynolds-averaged Navier-Stokes equations

If the procedure explained above is applied to velocity, pressure and temperature fields, and their instantaneous values are replaced by the sum of their mean and fluctuating parts in equations 2.1, 2.2 and 2.3, time-averaged governing equations are obtained. These equations express the transport of mean quantities as follows

$$\frac{\partial \bar{u}_i}{\partial x_i} = 0 \tag{2.6}$$

$$\frac{\partial(\rho \bar{u}_i)}{\partial t} + \frac{\partial(\rho \bar{u}_j \bar{u}_i)}{\partial x_j} = -\frac{\partial \bar{p}}{\partial x_i} + \frac{\partial}{\partial x_j}\left(2\mu \bar{S}_{ij} - \rho \overline{u'_i u'_j}\right) + \rho g_i \tag{2.7}$$

$$\frac{\partial(\rho \bar{T})}{\partial t} + \frac{\partial(\rho \bar{u}_i \bar{T})}{\partial x_i} = \frac{\partial}{\partial x_i}\left(\frac{\lambda}{c_p}\frac{\partial \bar{T}}{\partial x_i} - \rho \overline{u'_i T'}\right) \tag{2.8}$$

As equations 2.7 and 2.8 show, a model for the Reynolds (turbulent) stress $-\rho \overline{u'_i u'_j}$ and turbulent heat flux $-\rho \overline{u'_i T'}$ is needed (closure problem). These additional terms appears as consequence of the non-linearity characteristics of the convective terms.

As it was previously mentioned, there are different approaches to calculate these terms depending on the degree of empiricism involved and hypothesis assumed (see [1] or [2]). In this thesis three types of RANS models are used in order to calculate Reynolds stresses: explicit algebraic Reynolds stress models (EARSM), non-linear eddy-viscosity models (NLEVM), and linear eddy-viscosity models (LEVM). Therefore, attention is now focussed in these kind of models.

### 2.2.4   Reynolds-stress transport equation

Even though differential Reynolds stress models (DRSM) are not considered in this thesis, it is worth to explained the transport equation for the turbulent stresses because it is used to obtain the equation for the turbulent kinetic energy. Therefore, in order to obtain transport equations for the turbulent stresses, equation 2.7 is multiplied by a fluctuating quantity and then time-averaged the product. If mass equation is written as $M_a(\rho) = 0$ and the momentum equation as $M_o(u_i) = 0$, then by doing $\overline{u'_i M_o(u_i) + u'_j M_o(u_i) + u'_i u'_j M_a(\rho)} = 0$ the Reynolds-stress equation can be obtained

[1]:

$$\underbrace{\frac{\partial \overline{u_i' u_j'}}{\partial t}}_{\zeta_{ij}} + \underbrace{\bar{u}_k \frac{\partial \overline{u_i' u_j'}}{\partial x_k}}_{C_{ij}} = \underbrace{-\overline{u_i' u_k'} \frac{\partial \bar{u}_j}{\partial x_k} - \overline{u_j' u_k'} \frac{\partial \bar{u}_i}{\partial x_k}}_{P_{ij}} - \underbrace{2\nu \overline{\frac{\partial u_i'}{\partial x_k} \frac{\partial u_j'}{\partial x_k}}}_{\epsilon_{ij}}$$

$$+ \underbrace{\overline{\frac{p'}{\rho} \left( \frac{\partial u_i'}{\partial x_j} + \frac{\partial u_j'}{\partial x_i} \right)}}_{\Pi_{ij}} + \underbrace{\frac{\partial}{\partial x_k} \left[ \underbrace{\nu \frac{\partial \overline{u_i' u_j'}}{\partial x_k}}_{D_{ij}^v} - \underbrace{\overline{u_i' u_j' u_k'}}_{D_{ij}^t} - \underbrace{\frac{\overline{p' u_i'}}{\rho} \delta_{jk} - \frac{\overline{p' u_j'}}{\rho} \delta_{ik}}_{D_{ij}^p} \right]}_{D_{ij}} \qquad (2.9)$$

where $\zeta_{ij}$ represents the local change in time; $C_{ij}$ the convective transport; $P_{ij}$ the production by mean-flow deformation; $\epsilon_{ij}$ the viscous destruction through the smaller eddies; $\Pi_{ij}$ the stress redistribution due to fluctuating pressure, i.e. the tendency to return to isotropicity by the redistribution of Reynolds stresses; and $D_{ij}$ the diffusive transport. The las term consists of three parts, the first term $(D_{ij}^v)$ is the molecular diffusion term, the second $(D_{ij}^t)$ is the turbulent diffusion term (transport through velocity fluctuations), and the remaining term $(D_{ij}^p)$ correspond to the pressure transport.

Terms $\Pi_{ij}$, $\epsilon_{ij}$ and the last two parts of $D_{ij}$ $(D_{ij}^t$ and $D_{ij}^p)$ must be modelled. This means that the exact equation (eq. 2.9) is not used any more, but a model which approximates this equation need to be introduced.

### 2.2.5   Turbulent kinetic energy equation

An important measure of any turbulent flow is how intense the turbulent fluctuations are. This can be quantified in terms of each one of the normal turbulent stress components, $\overline{u'^2}$, $\overline{v'^2}$ and $\overline{w'^2}$. These stresses may also be understood as the kinetic energy per mass unit of the fluctuating velocity field in each direction, which are different because of anisotropy properties of the turbulent flows. Then, if the sum of these stresses is divided by two the variable known as turbulence kinetic energy $(k)$ is obtained:

$$k \equiv \frac{1}{2}(\overline{u'^2} + \overline{v'^2} + \overline{w'^2}) = \frac{1}{2}\overline{u_i' u_i'} \qquad (2.10)$$

This quantity is helpful to model and predict turbulent flow in the different approaches studied in this thesis. However, due to transport equations for the Reynolds stresses are not solved in any of the approaches under consideration, it is necessary to find a new transport equation for the turbulent kinetic energy. Thus, using the Reynolds-stress equation (eq. 2.9) is possible to obtain the $k$-equation by applying eq. 2.10,

and noting that the trace of the tensor $\Pi_{ij}$ disappears for incompressible flows. So then, the next scalar transport equation for the turbulent kinetic energy is obtained

$$\underbrace{\frac{\partial(\rho k)}{\partial t}}_{(\Upsilon)} + \underbrace{\frac{\partial(\rho \bar{u}_k k)}{\partial x_k}}_{(C)} = \underbrace{-\rho \overline{u_i' u_k'} \frac{\partial \bar{u}_i}{\partial x_k}}_{(P_k)} - \underbrace{\rho\epsilon}_{(E)} + \underbrace{\frac{\partial}{\partial x_k}\left[\mu\frac{\partial k}{\partial x_k} - \frac{\rho}{2}\overline{u_i' u_i' u_k'} - \overline{p' u_k'}\right]}_{(D)} \quad (2.11)$$

where

$$\rho\epsilon = \nu\overline{\frac{\partial u_i'}{\partial x_k}\frac{\partial u_i'}{\partial x_k}} \quad (2.12)$$

The terms in eq. 2.11 represent: $(\Upsilon)$ unsteady term; $(C)$ convective transport; $(P_k)$ production (transfer of energy from the mean flow to the turbulent fluctuations); $(E)$ dissipation due to viscous effects (rate at which $k$ is converted into thermal energy); $(D)$ is composed of three parts: molecular diffusion, turbulent transport and pressure diffusion.

As equation for Reynolds stresses (eq. 2.9), $k$-equation (eq. 2.11) also requires modelling, in this case of turbulent transport and pressure diffusion terms, dissipation ($\epsilon$) and Reynolds stresses. In the context of two-equation models an additional transport equation is used for $\epsilon$ or a similar quantity in order to calculate the turbulent length scale. This point will be studied in detail later due to it is one of the most difficult items related to turbulence modelling.

The standard approximation used to evaluate turbulent transport of scalar variables in a turbulent flow is to make an analogy with the molecular transport process, which is known as simple gradient-diffusion hypothesis. Furthermore, pressure diffusion is generally grouped with turbulent transport term [1]. Thus, they may be written as follows

$$\frac{\rho}{2}\overline{u_i' u_i' u_k'} + \overline{p' u_k'} \approx -\frac{\mu_t}{\sigma_k}\frac{\partial k}{\partial x_k} \quad (2.13)$$

with $\sigma_k$ being a turbulence model constant. After these considerations the exact equation for the turbulent kinetic energy (eq. 2.11) becomes eq. 2.14, which is also the usual form adopted in two-equation turbulence models:

$$\frac{\partial(\rho k)}{\partial t} + \frac{\partial(\rho \bar{u}_k k)}{\partial x_k} = -\rho\overline{u_i' u_k'}\frac{\partial \bar{u}_i}{\partial x_k} - \rho\epsilon + \frac{\partial}{\partial x_k}\left[\left(\mu + \frac{\mu_t}{\sigma_k}\right)\frac{\partial k}{\partial x_k}\right] \quad (2.14)$$

At this point, it can be seen that in order to obtain a closed formulation, the Reynolds stresses remain to be modelled. In the next sections the different approaches used in this thesis will be explained in detail.

### 2.2.6   Explicit algebraic Reynolds stress models (EARSM)

A considerable simplification respect to DRSM can be obtained if instead of writing six transport equations for the turbulent stresses, they are converted into algebraic ones. The algebraic stress modelling (ASM) consists in removing the Reynolds-stress advection and diffusion terms in the Reynolds-stress equation [3]. This step can be done by taking as starting point the modeled equation for the Reynolds stress anisotropy tensor ($b_{ij}$) [4] given by:

$$
\begin{aligned}
\frac{Db_{ij}}{Dt} &= \frac{1}{2k}\left(\frac{D\tau_{ij}}{Dt} - \frac{\tau_{ij}}{k}\frac{Dk}{Dt}\right) \\
&= -b_{ij}\left(\frac{P_k}{k} - \epsilon\right) - \frac{2}{3}\bar{S}_{ij} - \left(b_{ik}\bar{S}_{kj} + \bar{S}_{ik}b_{kj} - \frac{2}{3}b_{mn}\bar{S}_{mn}\delta_{ij}\right) \\
&\quad + (b_{ik}\bar{W}_{ij} - \bar{W}_{ik}b_{kj}) + \frac{\Pi_{ij}}{2k} + \frac{1}{2k}\left(D_{ij} - \frac{\tau_{ij}}{k}D\right)
\end{aligned}
\tag{2.15}
$$

where $b_{ij} = \frac{\overline{u_i'u_j'}}{2k} - \frac{1}{3}\delta_{ij}$; $\tau_{ij} = \overline{u_i'u_j'}$; $\Pi_{ij}$ is the pressure-strain rate correlation; and $D_{ij}$ is the combined effect of turbulent transport and viscous diffusion ($D = D_{ii}/2$). Furthermore, it is necessary for the development of the algebraic stress model to define a form for the pressure-strain rate model. In this thesis the SSG (Speziale, Sarkar and Gatski [5]) model will be used, which can be written in the form

$$
\begin{aligned}
\Pi_{ij} = -&\left(C_1^0 + C_1^1\frac{P_k}{\epsilon}\right)\epsilon b_{ij} + C_2 k\bar{S}_{ij} \\
&+ C_3 k\left(b_{ik}\bar{S}_{jk} + b_{jk}\bar{S}_{ik} - \frac{2}{3}b_{mn}\bar{S}_{mn}\delta_{ij}\right) - C_4 k(b_{ik}\bar{W}_{kj} - \bar{W}_{ik}b_{kj})
\end{aligned}
\tag{2.16}
$$

where the closure coefficients ($Cs$) are generally functions of the invariants of the stress anisotropy. It should be noted that the form given in eq. 2.16 is representative of any pressure-strain rate model which could be used as well, e.g. Launder, Reece and Rodi model [6]. It is also possible to use a non-linear relation for this term such as that presented by Wallin and Johansson [7]. Replacing eq. 2.16 into eq. 2.15 next form is obtained

$$
\begin{aligned}
\frac{Db_{ij}}{Dt} - \frac{1}{2k}\left(D_{ij} - \frac{\tau_{ij}}{k}D\right) = -\bigg[&\frac{b_{ij}}{a_4} + a_3\left(b_{ik}\bar{S}_{kj} + \bar{S}_{ik}b_{kj} - \frac{2}{3}b_{mn}\bar{S}_{mn}\delta_{ij}\right) \\
&- a_2(b_{ik}\bar{W}_{kj} - \bar{W}_{ik}b_{kj}) + a_1\bar{S}_{ij}\bigg]
\end{aligned}
\tag{2.17}
$$

The coefficients $a_i$ are related to the pressure-strain correlation model by

$$
\begin{aligned}
a_1 &= \frac{1}{2}\left(\frac{4}{3} - C_2\right), \quad a_2 = \frac{1}{2}(2 - C_4) \\
a_3 &= \frac{1}{2}(2 - C_3), \qquad a_4 = g\tau
\end{aligned}
\tag{2.18}
$$

whit

$$g = \left[ \left( \frac{C_1^1}{2} + 1 \right) \frac{P_k}{\epsilon} + \frac{C_1^0}{2} - 1 \right]^{-1} = \left[ \gamma_0 \frac{P_k}{\epsilon} + \gamma_1 \right]^{-1} \qquad (2.19)$$

and $\tau$ is the turbulent time scale ($k/\epsilon$, $1/\omega$); $C_1^0 = 3.4$, $C_1^1 = 1.8$, $C_2 = 0.36$, $C_3 = 1.25$, and $C_4 = 0.4$. An *implicit* algebraic stress relation is obtained from the modelled transport equation for the Reynolds stress anisotropy equation (eq. 2.15) when the next hypothesis [8] are made:

$$\frac{Db_{ij}}{Dt} = 0, \qquad \text{or} \qquad \frac{D\tau_{ij}}{Dt} = \frac{\tau_{ij}}{k} \frac{Dk}{Dt} \qquad (2.20)$$

and

$$D_{ij} = \frac{\tau_{ij}}{k} D \qquad (2.21)$$

Eq. 2.20 means that the turbulence has reached and equilibrium state (convective and transport terms can be neglected), and eq. 2.21 take into account the assumption that any anisotropy of the turbulent transport and viscous diffusion is proportional to the anisotropy of the Reynolds stresses [8]. As shown, both hypothesis impose limitations on the range of applicability of the algebraic stress model.

With these assumptions, the left hand side of eq. 2.17 disappears and the equation becomes algebraic:

$$0 = \frac{b_{ij}}{a_4} + a_3 \left( b_{ik}\bar{S}_{kj} + \bar{S}_{ik}b_{kj} - \frac{2}{3}b_{mn}\bar{S}_{mn}\delta_{ij} \right)$$
$$- a_2(b_{ik}\bar{W}_{kj} - \bar{W}_{ik}b_{kj}) + a_1\bar{S}_{ij} \qquad (2.22)$$

which also can be written using matrix notation as

$$-\frac{1}{a_4}\mathbf{b} - a_3 \left( \mathbf{bS} + \mathbf{Sb} - \frac{2}{3}\{\mathbf{bS}\}\mathbf{I} \right) + a_2(\mathbf{bW} - \mathbf{Wb}) = \mathbf{R} \qquad (2.23)$$

If a linear pressure-strain rate model is used and an isotropic dissipation rate is assumed, it follows that $\mathbf{R} = a_1\mathbf{S}$. However, $\mathbf{R}$ can contain any known symmetric, traceless tensor [7]. This equation (eq. 2.23) is clearly implicit and has to be solved for $\mathbf{b}$. Such equation can be solved numerically in an iterative form. However, one feature of implicit algebraic relations is the lack of damping or diffusion, what for general complex situations often can be numerically stiff [8]. Therefore, the computational effort sometimes becomes even larger than that for a full DRSM. Thus, it is desirable to obtain an explicit solution to this equation which still retains its algebraic character.

The first attempt in order to generate an explicit algebraic Reynolds stress model (EARSM) from an implicit ASM begins from the observation that the solution of the

implicit equation (eq. 2.23) is of the general form [4, 9]

$$\mathbf{b} = \sum_{n=1}^{N} \alpha_n \mathbf{T}^{(n)} \tag{2.24}$$

where $\mathbf{T}^{(n)}$ is the integrity basis for functions of a symmetric and antisymmetric tensor, and $\alpha_n$ are scalar functions of the irreducible invariants of these tensors. Moreover, $N = 3$ for two-dimensional flows or $N = 10$ for general three-dimensional flows, then the discussion here is limited to $N = 3$ following methodology found in [8]. For the case under consideration, the integrity basis consists of terms as $\mathbf{T}^{(1)} = \mathbf{S}$, $\mathbf{T}^{(2)} = \mathbf{SW} - \mathbf{WS}$, and $\mathbf{T}^{(3)} = \mathbf{S}^2 - \frac{1}{3}[\mathbf{S}^2]$, while $\alpha_1 = [\mathbf{S}^2]$ is an example of an invariant (see Pope [9]).

The implicit equation, eq. 2.23, can be solved by projecting this algebraic relation onto the tensor basis $\mathbf{T}^{(m)}$ itself. For this solution, the scalar product of eq. 2.23 is formed with each of the tensors $\mathbf{T}^{(m)}$, $(m = 1, 2, ..., N)$. This procedure leads to the following system of equations:

$$\sum_{n=1}^{N} \alpha_n \Big[ -\frac{1}{a_4}(\mathbf{T}^{(n)}, \mathbf{T}^{(m)}) - 2a_3(\mathbf{T}^{(n)}\mathbf{S}, \mathbf{T}^{(m)}) + 2a_2(\mathbf{T}^{(n)}\mathbf{W}, \mathbf{T}^{(m)}) \Big] = (\mathbf{R}, \mathbf{T}^{(m)})$$

$$\tag{2.25}$$

where the scalar product is defined as $(\mathbf{T}^n, \mathbf{T}^m) = [\mathbf{T}^{(n)}\mathbf{T}^{(m)}]$ and $[\mathbf{M}]$ means trace of matrix $\mathbf{M}$. Or in a more compact form,

$$\sum_{n=1}^{N} \alpha_n A_{nm} = (\mathbf{R}, \mathbf{T}^{(m)}) \tag{2.26}$$

where matrix $\mathbf{A}$ is:

$$A_{nm} \equiv -\frac{1}{a_4}(\mathbf{T}^{(n)}, \mathbf{T}^{(m)}) - 2a_3(\mathbf{T}^{(n)}\mathbf{S}, \mathbf{T}^{(m)}) + 2a_2(\mathbf{T}^{(n)}\mathbf{W}, \mathbf{T}^{(m)}) \tag{2.27}$$

For a two dimensional mean flow field, the matrix $\mathbf{A}$ can be written as (see [10]):

$$A_{nm} = \begin{bmatrix} -\frac{1}{a_4}\eta^2 & -2a_2\eta^4 R^2 & -\frac{1}{3}a_3\eta^4 \\[2mm] 2a_a\eta^4 R^2 & -\frac{2}{a_4}\eta^4 R^2 & 0 \\[2mm] -\frac{1}{3}a_3\eta^4 & 0 & -\frac{1}{6a_4}\eta^4 \end{bmatrix} \tag{2.28}$$

where $\eta = \sqrt{S_{ik}S_{ki}}$ is a scalar invariant and $R^2 = -[\mathbf{W}^2]/[\mathbf{S}^2]$ is a flow parameter, which is useful for characterizing the flow [10]; for example, $R^2 = 0$ for a plain strain

flow, while $R^2 = 1$ for a pure shear flow. This matrix, when inverted, results in the next expressions for the representation coefficients

$$\alpha_1 = -\frac{a_4}{\alpha_0 \eta^2} \left( [\mathbf{RS}] + 2a_2 a_4 [\mathbf{RWS}] - 2a_3 a_4 [\mathbf{RS}^2] \right) \tag{2.29}$$

$$\alpha_2 = a_4 \left[ a_2 \alpha_1 + \frac{[\mathbf{RWS}]}{\eta^4 R^2} \right] \tag{2.30}$$

$$\alpha_3 = -a_4 \left[ 2a_3 \alpha_1 + \frac{6[\mathbf{RS}^2]}{\eta^4} \right] \tag{2.31}$$

whit $\alpha_0 = \left( 1 - \frac{2}{3} a_3^2 a_4^2 \eta^2 + 2 a_2^2 a_4^2 \eta^2 R^2 \right)$. This group of equations is the general solution valid for two-dimensional mean flow and for any arbitrary (symmetric traceless) tensor $\mathbf{R}$ [8]. If $\mathbf{R} = a_1 \mathbf{S}$, the right-hand side of eq. 2.26 will be

$$(\mathbf{R}, \mathbf{T}^{(m)}) = \begin{bmatrix} [\mathbf{RS}] \\ -2[\mathbf{RWS}] \\ [\mathbf{RS}^2] \end{bmatrix} = \begin{bmatrix} a_1 \eta^2 \\ 0 \\ 0 \end{bmatrix} \tag{2.32}$$

Replacing eq. 2.32 in eq. 2.29-2.31 and substituting into eq. 2.24 leads to the general explicit relation for the Reynolds stress tensor ($\tau_{ij}$)

$$\tau_{ij} = \frac{2}{3} k \mathbf{I} + 2k\alpha_a \left[ \mathbf{S} + a_2 a_4 (\mathbf{SW} - \mathbf{WS}) - 2a_3 a_4 \left( \mathbf{S}^2 - \frac{1}{3} [\mathbf{S}^2] \mathbf{I} \right) \right] \tag{2.33}$$

As shown, in the "explicit" equation (eq. 2.33) $a_4$ is a function of $P_k/\epsilon$, what actually makes eq. 2.33 implicit. Gatski and Speziale [4] simplified this expression by assuming the coefficient $g$ in eq. 2.19 to be constant, that is, $g \equiv \frac{a_4}{\tau} = 0.233$ based on the equilibrium value of the ratio $P_k/\epsilon = 1.88$ for homogeneous flows. However, there is another possibility, which accounts for the variation of the production-to-dissipation ratio in the formulation [7, 10, 11]. Thus, it can be shown that the production-to-dissipation ratio is given by:

$$\frac{P_k}{\epsilon} = -2[\mathbf{bS}]\tau \tag{2.34}$$

and that the invariant $[\mathbf{bS}]$ is directly related to the coefficient $\alpha_1$ through $[\mathbf{bS}] = \alpha_1 \eta^2$ [10]. Then, from eq. 2.18 and eq. 2.19, it is possible to write the coefficient $a_4$ as:

$$a_4 = \left[ \gamma_1 - 2\gamma_0 \alpha_1 \eta^2 \tau \right]^{-1} \tau \tag{2.35}$$

Therefore, it is possible to have a cubic equation for $\alpha_1$ and therefore find a correct value for $a_4$, which can be written as:

$$\gamma_0^2 \alpha_1^3 - \frac{\gamma_0 \gamma_1}{\eta^2 \tau} \alpha_1^2 \frac{1}{4\eta^4 \tau^2} \left[ \gamma_1^2 - 2\tau^2 \gamma_0 [\mathbf{RS}] - 2\eta^2 \tau^2 \left( \frac{a_3^2}{3} - R^2 a_2^2 \right) \right] \alpha_1$$
$$+ \frac{1}{a\eta^6 \tau} \left[ \gamma_1 [\mathbf{RS}] + 2\tau \left( a_2 [\mathbf{RWS}] - a_3 [\mathbf{RS}^2] \right) \right] = 0 \tag{2.36}$$

46

The expansion coefficients of the non-linear terms, $\alpha_2$ and $\alpha_3$, retain the same functional dependency on $\alpha_1$ as before. Furthermore, if eq. 2.36 is solved together with $\mathbf{R} = a_1\mathbf{S}$ produce equivalent results to the previous ones. The correct choice of the root of eq. 2.36 has been proposed by different authors [7, 10, 11].

Within this kind of formulation several models are implemented in this thesis. A summary of the models with the corresponding equations used, closure coefficients and damping functions is presented at the end of this section. Moreover, their abilities to correctly predict different flows are tested in Chapters 3 and 4.

### 2.2.7 Non-linear eddy-viscosity models (NLEVM)

When a non-linear eddy-viscosity model is being developed, a relation of the same form of eq. 2.24 is used, but instead of introducing this relation into an ASM, as in the EARSM approach, efforts are made to use a form for the scalar coefficients $\alpha_n$ which allow good Reynolds stresses predictions in different flow configurations.

The complexity of the non-linear terms depends on both the number and form of the terms chosen for the tensor representation. The selection of the adequate tensor basis is based on the functional dependencies associated with the Reynolds stress ($\tau_{ij}$) or anisotropy tensor ($b_{ij}$). As observed from eq. 2.9, the only dependency of the Reynolds stresses on the mean flow is through the mean velocity gradient. Therefore, it is assumed in developing non-linear models for the Reynolds stresses, that in addition to the functional dependency, due to dimensional grounds, on the turbulent velocity and length scales, also the dependence on the mean velocity gradient has to be included [8]. The turbulent velocity scale is usually based on the turbulent kinetic energy ($k$) and the turbulent length scale on the variable used in the corresponding transport equation, which for the purposes of this section will be the isotropic turbulent dissipation rate $\epsilon$. Then, by applying dimensional analysis, imposing invariance under co-ordinate transformations and exploiting the tensor properties of $\frac{\partial u_i}{\partial x_j}$ and $\overline{u'_i u'_j}$, the form of the general stress-strain relation can be deduced.

The number of independent invariants considered is based on the number of independent tensors which can be formed. Shih and Lumley [12] showed a procedure in order to determine the seventeen independent second rank tensors which can be formed using Caley-Hamilton theorem. Thus, assuming the Reynolds stresses to be a function of mean velocity gradient, $k$ and $\epsilon$:

$$\overline{u'_i u'_j} = F_{ij}\left(\frac{\partial u_i}{\partial x_j}, k, \epsilon\right) \tag{2.37}$$

Non-dimensionalization results in regrouping arguments as $A_{ij} = \tau\frac{\partial u_i}{\partial x_j}$ and $\frac{\overline{u'_i u'_j}}{2k} = F_{ij}(A_{ij})$. Since $\mathbf{A}$ is a general tensor, its transpose $\mathbf{B} \neq \mathbf{A} \Rightarrow B_{ij} = A_{ij}^T = \tau\frac{\partial u_j}{\partial x_i}$. In

order to obtain a general relationship, a tensorial form of $F_{ij}(A_{ij}, B_{ij})$ is first sought. After, $B_{ij}$ is replaced by $A_{ij}^T$. Shih and Lumley [12] have shown that the independent tensors formed by $\mathbf{A}$ and $\mathbf{B}$ are the following seventeen tensors:

$$\mathbf{A}, \mathbf{A}^2, \mathbf{B}, \mathbf{B}^2, \mathbf{AB}, \mathbf{BA}, \mathbf{AB}^2, \mathbf{A}^2\mathbf{B}, \mathbf{BA}^2, \mathbf{B}^2\mathbf{A}, \mathbf{A}^2\mathbf{B}^2, \mathbf{B}^2\mathbf{A}^2,$$
$$\mathbf{ABA}^2, \mathbf{B}^2\mathbf{AB}, \mathbf{AB}^2\mathbf{A}^2, \mathbf{B}^2\mathbf{A}^2\mathbf{B}, \mathbf{ABA}^2\mathbf{B}^2$$

To find the form of the tensor function $F_{ij}$, an invariant basis is first formed using two arbitrary non-dimensional vectors $\alpha_i$ and $\beta_i$ as follows:

$$\delta_{ij}\alpha_i\beta_j, A_{ij}\alpha_i\beta_j, ..., B_{ij}^2\alpha_i\beta_j, ..., (AB)_{ij}\alpha_i\beta_j, ..., (AB^2)_{ij}\alpha_i\beta_j, ...,$$
$$(A^2B^2)_{ij}\alpha_i\beta_j, ..., (ABA^2)_{ij}\alpha_i\beta_j, ..., (AB^2A^2)_{ij}\alpha_i\beta_j, ..., (ABA^2B^2)_{ij}\alpha_i\beta_j$$

Therefore $\frac{\overline{u_i'u_j'}\alpha_i\beta_j}{2k}$ is required to be a linear function of the above invariants. This is due to $\alpha_i$ and $\beta_j$ are arbitrary vectors, and $\frac{\overline{u_i'u_j'}\alpha_i\beta_j}{2k}$ is bilinear in $\alpha_i\beta_j$, thus, the form of the function should also be bilinear in $\alpha_i$ and $\beta_j$ [13]. Thus, the next expression is obtained:

$$\begin{aligned}
\frac{\overline{u_i'u_j'}}{2k} =& a_1\delta_{ij} + a_2\mathbf{A} + a_3\mathbf{B} + a_4\mathbf{A}^2 + a_5\mathbf{B}^2 + a_6\mathbf{AB} + a_7\mathbf{BA} \\
&+ a_8\mathbf{AB}^2 + a_9\mathbf{A}^2\mathbf{B} + a_{10}\mathbf{BA}^2 + a_{11}\mathbf{B}^2\mathbf{A} + a_{12}\mathbf{A}^2\mathbf{B}^2 \\
&+ a_{13}\mathbf{B}^2\mathbf{A}^2 + a_{14}\mathbf{ABA}^2 + a_{15}\mathbf{B}^2\mathbf{AB} + a_{16}\mathbf{AB}^2\mathbf{A}^2 \\
&+ a_{17}\mathbf{B}^2\mathbf{A}^2\mathbf{B} + a_{18}(\mathbf{ABA}^2\mathbf{B}^2 + \mathbf{A}^2\mathbf{B}^2\mathbf{AB})
\end{aligned}$$

where, $a_1 - a_{18}$ associated with this representation can, in general, be functions of the invariants of the flow. Furthermore, making use of conditions: $\overline{u_i'u_j'} = \overline{u_j'u_i'}$, $\overline{u_i'u_i'} = 2k$ and $B_{ij} = A_{ij}^T = A_{ji}$; the next relations between the coefficients can be obtained: $a_2 = a_3$, $a_4 = a_5$, $a_8 = a_9$, $a_{10} = a_{11}$, $a_{14} = a_{15}$, $a_{16} = a_{17}$, and

$$\begin{aligned}
a_1 =& \frac{1}{3}\Big[ 1 - 2a_2A_{ii} - 2a_4A_{ik}A_{ki} - (a_6 + a_7)A_{ik}B_{ki} - 2(a_8 + a_{10})A_{ik}B_{ki}^2 \\
&- (a_12 + a_13)A_{ik}^2B_{ki}^2 - 2a_{14}A_{ik}B_{kl}A_{li}^2 - 2a_{16}A_{ik}B_{kl}^2A_{li}^2 \\
&- 2a_{18}A_{ik}B_{kl}A_{lm}^2B_{mi}^2 \Big]
\end{aligned} \qquad (2.38)$$

where $A_{ij}^2 = A_{ik}A_{kj}$ or $u_{i,j}^2 = u_{i,k}u_{k,j}$, being $u_{i,j} = \frac{\partial u_i}{\partial x_j}$. Therefore it is obtained:

$$
\begin{aligned}
\frac{\overline{u_i' u_j'}}{k} &= \frac{2}{3}\delta_{ij} + 2a_2\tau(u_{i,j} + u_{j,i} - \frac{2}{3}u_{k,k}\delta_{ij}) \\
&+ 2a_4\tau^2(u_{i,j}^2 + u_{j,i}^2 - \frac{2}{3}\Pi_1\delta_{ij}) + 2a_6\tau^2(u_{i,k}u_{j,k} - \frac{1}{3}\Pi_2\delta_{ij}) \\
&+ 2a_7\tau^2(u_{k,i}u_{k,j} - \frac{1}{3}\Pi_2\delta_{ij}) + 2a_8\tau^3(u_{i,k}u_{j,k}^2 + u_{i,k}^2 u_{j,k} - \frac{2}{3}\Pi_3\delta_{ij}) \\
&+ 2a_{10}\tau^3(u_{k,i}u_{k,j}^2 + u_{k,j}u_{k,i}^2 - \frac{2}{3}\Pi_3\delta_{ij}) \\
&+ 2a_{12}\tau^4(u_{i,k}^2 u_{j,k}^2 - \frac{1}{3}\Pi_4\delta_{ij}) + 2a_{13}\tau^4(u_{k,i}^2 u_{k,j}^2 - \frac{1}{3}\Pi_4\delta_{ij}) \\
&+ 2a_{14}\tau^4(u_{i,k}u_{l,k}u_{l,j}^2 + u_{j,k}u_{l,k}u_{l,i}^2 - \frac{2}{3}\Pi_5\delta_{ij}) \\
&+ 2a_{16}\tau^5(u_{i,k}u_{l,k}^2 u_{l,j}^2 + u_{j,k}u_{l,k}^2 u_{l,i}^2 - \frac{2}{3}\Pi_6\delta_{ij}) \\
&+ 2a_{18}\tau^6(u_{i,k}u_{l,k}u_{l,m}^2 u_{j,m}^2 + u_{j,k}u_{l,k}u_{l,m}^2 u_{i,m}^2 - \frac{2}{3}\Pi_7\delta_{ij})
\end{aligned}
\tag{2.39}
$$

where,

$$
\begin{aligned}
\Pi_1 &= u_{i,k}u_{k,i}, \ \Pi_2 = u_{i,k}u_{i,k}, \ \Pi_3 = u_{i,k}u_{i,k}^2, \ \Pi_4 = u_{i,k}^2 u_{i,k}^2 \\
\Pi_5 &= u_{i,k}u_{l,k}u_{l,i}^2, \ \Pi_6 = u_{i,k}u_{l,k}^2 u_{l,i}^2, \ \Pi_7 = u_{i,k}u_{l,k}u_{l,m}^2 u_{i,m}^2
\end{aligned}
\tag{2.40}
$$

As it can be observed eq. 2.39 is the most general model for obtaining Reynolds stresses under non-linear formulation. It contains eleven undetermined coefficients which must be found by other model constraints such as, rapid distortion theory, experimental data or data from DNS, and realizability constrains:

$$
\tau_{\beta\beta} \geq 0, \qquad \text{subscript no sum} \tag{2.41}
$$

$$
\tau_{\beta\gamma}^2 \leq \tau_{\beta\beta}\tau_{\gamma\gamma}, \qquad \text{Schwarz inequaltity} \tag{2.42}
$$

However, in this thesis the non-linear models analysed only include up to third order terms from the twelve terms that eq. 2.39 contains, which can be written using shear

and rotational tensors instead of strains:

$$
\begin{aligned}
2b_{ij} =& \frac{\overline{u_i' u_j'}}{k} - \frac{2}{3}\delta_{ij} \\
=& -2C_\mu (S_{ij} - \frac{1}{3}S_{ll}\delta_{ij}) \\
& + c_1(S_{ik}S_{kj} - \frac{1}{3}S_{lk}S_{kl}\delta_{ij}) + c_2(W_{ik}S_{kj} - S_{ik}W_{kj}) \\
& + c_3(W_{ik}W_{kj} - \frac{1}{3}W_{lk}W_{kl}\delta_{ij}) + c_4(W_{ik}S_{kl}S_{lj} - S_{ik}S_{kl}W_{lj}) \\
& + c_5(W_{ik}W_{kl}S_{lj} + S_{ik}W_{kl}W_{lj} - W_{lk}W_{kl}S_{ij} - \frac{2}{3}W_{kl}S_{lm}W_{mk}\delta_{ij}) \\
& + c_6(S_{lk}S_{kl}S_{ij}) + c_7(W_{lk}W_{kl}S_{ij})
\end{aligned}
\tag{2.43}
$$

Finally, is possible to write last equation in matrix notation differencing between coefficients of second ($\beta_i$) and third ($\gamma_i$) order terms as:

$$
\begin{aligned}
\frac{\overline{u_i' u_j'}}{k} =& \frac{2}{3}\delta_{ij} - 2C_\mu^* f_\mu^* \mathbf{S} + \beta_1(\mathbf{S}^2 - \frac{1}{3}[\mathbf{S}^2]I) + \beta_2(\mathbf{WS} - \mathbf{SW}) \\
& + \beta_3(\mathbf{W}^2 - \frac{1}{3}[\mathbf{W}^2]I) - \gamma_1[\mathbf{S}^2]\mathbf{S} - \gamma_2[\mathbf{W}^2]\mathbf{S} \\
& -\gamma_3(\mathbf{W}^2\mathbf{S} + \mathbf{SW}^2 - [\mathbf{W}^2]\mathbf{S} - \frac{2}{3}[\mathbf{WSW}]I) - \gamma_4(\mathbf{WS}^2 - \mathbf{S}^2\mathbf{W})
\end{aligned}
\tag{2.44}
$$

where, $\bar{W}_{ij} = \frac{1}{2}\left(\frac{\partial \bar{u}_i}{\partial x_j} - \frac{\partial \bar{u}_j}{\partial x_i}\right)$; $\mathbf{W} = \tau(\bar{W}_{ij})$; $\tau$ is $k/\epsilon$ or $1/\omega$; $I = \delta_{ij}$ and $[\mathbf{M}]$ represents the trace of matrix $\mathbf{M}$.

Details of implemented models used in this thesis under this category are given at the end of this section, and in Appendix A.

### 2.2.8 Linear eddy viscosity models (LEVM)

In this type of models, a turbulent or apparent viscosity depending of flow features, relates Reynolds stresses to the mean strain rate tensor in the same way as the molecular viscosity, which is a property of the fluid. The turbulent eddy viscosity ($\mu_t$) can be viewed as a diffusivity determined by the macroscopic velocity and length scales of the large energy containing eddies. On the other hand, the molecular viscosity is determined by the smallest scales on the molecular level. Thus, for LEVMs eq. 2.7 is closed by assuming Boussinesq hypothesis [2], where the Reynolds stress tensor is linearly related to the mean rate of strain as follows:

$$
\rho\overline{u_i' u_j'} = \frac{2}{3}\rho k\delta_{ij} - 2\mu_t \bar{S}_{ij}
\tag{2.45}
$$

A closer look at this relation shows that it is of the same form as the first term in the non-linear relation (eq. 2.44). In terms of the Reynolds stress anisotropy tensor, the following relation is obtained:

$$b_{ij} = -\rho \frac{\mu_t}{k} S_{ij} \tag{2.46}$$

Which shows that at this level of closure an anisotropy of the Reynolds stresses can only be supported by a mean strain because of the insensitivity of the relation to the vorticity tensor. The exclusive dependence on the strain rate tensor, together with the form of the turbulent kinetic energy equation (eq. 2.14) shows that this level of closure is frame indifferent. However, such behavior is opposite to DNS results for even the simplest turbulent flows, e.g. decaying isotropic turbulence. DNS simulations have shown that turbulence decay depends on the frame rotation which is prevented using equation 2.45. Moreover, two of the more relevant deficiencies are, the above mentioned, material-frame indifference of the models and the isotropy of the eddy viscosity. These deficiencies prevent, for example, the prediction of turbulent secondary motions in ducts and the insensitivity of the turbulence to noninertial effects such as imposed rotation, as well as those mentioned in the introduction of this thesis. Nevertheless, LEVMs have proven to be a valuable tool in turbulent flow-field predictions, since the turbulent viscosity is larger than the molecular viscosity, this approach is numerically robust, specially compared to DRSMs [10]. Therefore, this kind of models remains as an engineering tool in routine calculations.

From dimensional analysis can be seen that the eddy viscosity is given by the product of a turbulent velocity scale and a turbulent length scale. As noted early, the velocity scale used in practically all existing RANS models is the square root of the turbulent kinetic energy ($k^{1/2}$). Thus, the eddy viscosity can be expressed as:

$$\mu_t = \rho C_\mu k^{1/2} l = \rho C_\mu k^n Z^m \tag{2.47}$$

where $l$ is a characteristic measure of the length scale of the energetic eddies. Or as an alternative to it, some other related variable $Z$ can be used as a measure of a characteristic "scale" of the turbulence. So then, exponents $m$ and $n$ are chosen to guarantee correct dimensionality of the eddy viscosity. Usual choices of $Z$ are the dissipation rate ($\epsilon \sim k^{3/2}/l)[m^2/s^3]$, previously introduced as the isotropic turbulent dissipation rate; a specific dissipation rate ($\omega \sim \epsilon/k \sim k^{1/2}/l)[1/s]$; or a turbulent time scale ($\tau \sim k/\epsilon \sim l/k^{1/2})[s]$ [1].

In this thesis two scalar transport equations are included in the model for both the turbulent velocity and length scales, thus **two-equation eddy viscosity models** are the framework where all models studied (EARSMs, NLEVMs and LEVMs) are supported. Furthermore, due to the length scale equation is the most difficult and controversial piece of the formulation presented it is studied in detail in the next section.

### 2.2.9   Turbulent length scale determining equation

In this thesis two-equation platforms, i.e. $k - \epsilon$ and $k - \omega$, are analyzed. Therefore, here a deeper study of the dissipation rate ($\epsilon$) equation and the specific dissipation ($\omega$) equation is carried out. The length scale, characterizing the size of the large energy containing eddies, is subject to transport processes in a similar way to the turbulent kinetic energy. Therefore, this length scale is determined by introducing an additional differential transport equation. The $Z$-equation ($\epsilon$ or $\omega$) can be result of two possible approaches. The first one consists of constructing a $Z$-equation in an ad-hoc manner, trying to simulate some of the physics believed to be essential. The second approach tries to derive the exact transport equation for $Z$, and after an effort is done in order to model the specific unknown terms. Both approaches usually leads to similar results.

**The $k - \epsilon$ model**

The selection of $Z = \epsilon$ has been the most common choice for the length scale determining variable in last decades. However, the exact equation is not of much help as a basis for modelling, except to give some indication of the meaning and importance of some terms. Nevertheless, it is instructive to look at the exact transport equation for $\epsilon$, which following the second approach before mentioned, is obtained by taking the next moment of the Navier-Stokes equations (eq. 2.7),

$$2\nu \overline{\frac{\partial u_i'}{\partial x_j} \frac{\partial}{\partial x_j}[M_o(u_i)]} = 0 \tag{2.48}$$

which after algebra application, leads to the form:

$$\frac{\partial \epsilon}{\partial t} + \bar{u}_i \frac{\partial \epsilon}{\partial x_k} = P_{\epsilon 1} + P_{\epsilon 2} + P_{\epsilon 3} + P_{\epsilon 4} + Y + D_\epsilon^v + D_\epsilon^t + D_\epsilon^p \tag{2.49}$$

being,

$$P_{\epsilon 1} + P_{\epsilon 2} = -2\nu \left( \overline{\frac{\partial u_i'}{\partial x_l} \frac{\partial u_k'}{\partial x_l}} + \overline{\frac{\partial u_i'}{\partial x_i} \frac{\partial u_l'}{\partial x_k}} \right) \frac{\partial \bar{u}_i}{\partial x_k}$$

$$P_{\epsilon 3} = -2\nu \overline{u_k' \frac{\partial u_i'}{\partial x_l}} \frac{\partial^2 \bar{u}_i}{\partial x_k \partial x_l}, \qquad P_{\epsilon 4} = -2\nu \overline{\frac{\partial u_i'}{\partial x_k} \frac{\partial u_i'}{\partial x_l} \frac{\partial u_k'}{\partial x_l}}$$

$$Y = -2 \left( \nu \overline{\frac{\partial^2 u_i'}{\partial x_k \partial x_l}} \right)^2, \qquad D_\epsilon^v = \nu \frac{\partial^2 \epsilon}{\partial x_k \partial x_k}$$

$$D_\epsilon^t = -\frac{\partial}{\partial x_k}(\overline{u_k' \epsilon}), \qquad D_\epsilon^p = -\frac{2\nu}{\rho} \overline{\frac{\partial p}{\partial x_i} \frac{\partial u_k}{\partial x_i}}$$

As can be seen this equation is much more complicated than eq. 2.11 and involves various unknown double and triple correlations of fluctuating velocity, pressure and

velocity gradients, which need closure approximations. $P_{\epsilon 1} + P_{\epsilon 2}$ are the mixed and mean production respectively; $P_{\epsilon 3}$ is the gradient production; $P_{\epsilon 4}$ is the turbulent production; $D_\epsilon^v$ is the viscous diffusion; $D_\epsilon^t$ is the turbulent diffusion; $D_\epsilon^p$ is the pressure diffusion; and $Y$ is the destruction of dissipation. Therefore, it is necessary further simplifications, which try to build a dimensionally correct approach. Thus, the following assumptions are required:

- At high Reynolds numbers the source terms, $P_{\epsilon 4}$ and $Y$ are dominant, whereas $P_{\epsilon 3}$ can be neglected as smaller [14]. Thus, $P_{\epsilon 4}$ and $Y$ are modeled together as:

$$-2\nu \overline{\frac{\partial u_i'}{\partial x_k}\frac{\partial u_i'}{\partial x_l}\frac{\partial u_k'}{\partial x_l}} - 2\overline{\left(\nu\frac{\partial^2 u_i'}{\partial x_k \partial x_l}\right)^2} = -C_{\epsilon 2}\frac{\epsilon^2}{k} \qquad (2.50)$$

on the basis of the reasoning that at high turbulent Reynolds number, these two terms may be taken as being controlled by the dynamics of the energy cascade process transporting energy from the lower to the higher wave numbers [14].

Furthermore, $P_{\epsilon 1} + P_{\epsilon 2}$ are modeled by contracting the indices as:

$$
\begin{aligned}
-2\nu \left( \overline{\frac{\partial u_i'}{\partial x_l}\frac{\partial u_k'}{\partial x_l}} + \overline{\frac{\partial u_l'}{\partial x_i}\frac{\partial u_l'}{\partial x_k}} \right) \frac{\partial \bar{u}_i}{\partial x_k} &= \left( C_{\epsilon 1}\frac{\epsilon}{k}\overline{u_i'u_j'} + C_{\epsilon 1}'\delta_{ij}\epsilon \right) \frac{\partial \bar{u}_i}{\partial x_k} \\
&= C_{\epsilon 1}\frac{\epsilon}{k}\overline{u_i'u_j'}\frac{\partial \bar{u}_i}{\partial x_k} \qquad (2.51)
\end{aligned}
$$

For incompressible flows, the term containing $C_{\epsilon 1}'$ vanishes when it is multiplied by $\partial \bar{u}_i/\partial x_k$.

- The simple gradient diffusion hypothesis is used to model turbulent diffusion, in a similar way that it was done in eq. 2.13.

Hence, the following modelled form of the $\epsilon$ equation can be derived:

$$\frac{\partial(\rho\epsilon)}{\partial t} + \frac{\partial(\rho\bar{u}_i\epsilon)}{\partial x_i} = \frac{\partial}{\partial x_i}\left[\left(\mu + \frac{\mu_t}{\sigma_\epsilon}\right)\frac{\partial\epsilon}{\partial x_i}\right] + C_{\epsilon 1}\frac{\epsilon}{k}P_k - C_{\epsilon 2}\rho\frac{\epsilon^2}{k} \qquad (2.52)$$

where, $P_k = -\rho\overline{u_i'u_j'}(\partial\bar{u}_i/\partial x_j)$ ; $C_{\epsilon 1}$, $C_{\epsilon 2}$ and $\sigma_\epsilon$ are model constants.

If the first possible approach, above mentioned, is followed a similar equation is obtained.
Then, in the $k - \epsilon$ model, Reynolds averaged Navier-Stokes equations are solved together with eq. 2.14 and eq. 2.52. Moreover, at this point it should be put forward that this model is a high Reynolds model: near-wall treatment (low Reynolds formulation), origin of model constants and damping functions will be discussed later. Moreover, specific functions and models constants will be defined in section 2.2.11 and appendix A.

**Origin of the constants in $k - \epsilon$ equations**

In what follows a brief summary of a way to obtain model constants in a high-Reynolds $k - \epsilon$ model is carried out. The constant $C_{\epsilon2}$ is determined by taking into account decaying homogeneous turbulence, where the $k - \epsilon$ equations reduce to:

$$\frac{Dk}{Dt} = -\epsilon \tag{2.53}$$

$$\frac{D\epsilon}{Dt} = -C_{\epsilon2}\frac{\epsilon^2}{k} \tag{2.54}$$

which leads to:

$$\frac{D^2k}{Dt^2} - \frac{C_{\epsilon2}}{k}\left(\frac{Dk}{Dt}\right)^2 \tag{2.55}$$

When last equation is solved, it defines a decay law for the turbulent kinetic energy given by $k \approx t^{-n}$ with $n = 1/(C_{\epsilon2} - 1)$. In the standard $k - \epsilon$ model, $n = 1.09$ produces $C_{\epsilon2} = 1.92$.

For the determination of $C_{\epsilon1}$ homogeneous shear flows are used. They seem to reach an equilibrium state when $k$ and $\epsilon$ grown in such a way that the turbulent time scale ($\tau = k/\epsilon$) is approximately constant. Transport equations (eq. 2.14 and 2.52) can be written for these flows as:

$$\frac{Dk}{Dt} = P_k - \epsilon \tag{2.56}$$

$$\frac{D\epsilon}{Dt} = \frac{C_{\epsilon1}P_k - C_{\epsilon2}\epsilon}{\frac{k}{\epsilon}} \tag{2.57}$$

what combined with the before assumption yields:

$$\begin{aligned}
\frac{D(k/\epsilon)}{Dt} &= \frac{Dk}{Dt}\frac{1}{\epsilon} + k(-\frac{1}{\epsilon^2})\frac{D\epsilon}{Dt} \\
&= \frac{P_k}{\epsilon} - 1 - \frac{k}{\epsilon^2}\left(\frac{C_{\epsilon1}P_k\epsilon}{k} - \frac{C_{\epsilon2}\epsilon^2}{k}\right) \\
&= C_{\epsilon2} - 1 - (C_{\epsilon1} - 1)\frac{P_k}{\epsilon} \\
&= 0
\end{aligned} \tag{2.58}$$

Which leads to

$$C_{\epsilon1} = \frac{C_{\epsilon2} - 1}{P_k/\epsilon} + 1 \tag{2.59}$$

If a value of $C_{\epsilon2} = 1.83$ is used in a shear flow, where $P_k/\epsilon \approx 1.8$ and $\tau \approx cte$, a value of $C_{\epsilon1} = 1.46$ results. However, the common value given to $C_{\epsilon1}$ is 1.44.

The value for $\sigma_\epsilon$ is sometimes chosen from computer optimization. Otherwise, a value for $C_{\epsilon 1}$ is imposed and subsequently $\sigma_\epsilon$ is determined, which is done by means of the use of a relation expressing the compatibility of the $k-\epsilon$ model with the inertial sublayer near a wall [13] as:

$$\sigma_\epsilon = \frac{\kappa^2}{(C_{\epsilon 2} - C_{\epsilon 1})\sqrt{C_\mu}} \tag{2.60}$$

where $C_\mu$ can be a constant or a function of strain tensor, $\kappa = \frac{u_\tau^2}{\sqrt{C_\mu}}$ and $u_\tau$ is friction velocity.

**Improvements to $\epsilon$ equation**

Even though different terms have been used in order to improve accuracy and generality of $k - \epsilon$ models, the most commonly accepted are: $E$ and $YAP$. $E$ term was included by Jones and Launder [15] to increase the destruction of dissipation in viscous and transitional regions. Thus, to produce a correct profile of $k$ with distance from solid walls. Despite, they can not provide a physical argument for its adoption, its inclusion is due to the fact that without $E$-term the maximum of $k$ at $y^+ \approx 20$ did not match experiments [15].

The $YAP$ correction was proposed by Yap [16] in order to increase $\epsilon$ therefore, reducing $k$ in non-equilibrium flows, e.g. flows with separating, reattaching and stagnation regions. It was designed by Yap after study heat transfer rates downstream from an abrupt pipe expansion. He found heat transfer rates as high as five times experimental results in the vecinity of the reattachment point. Therefore, Yap added a source term $(YAP)$ to the right side of the $\epsilon$ transport equation:

$$YAP = 0.83\Big(\frac{k^{3/2}}{\epsilon c_l y} - 1\Big)\Big(\frac{k^{3/2}}{\epsilon c_l y}\Big)^2 \frac{\epsilon^2}{k} \tag{2.61}$$

where, $y$ is the distance from the wall and $c_l = 2.5$ is the slope of the turbulent length scale $(k^{3/2}/\epsilon)$ in the near wall region of a constant shear stress flow. Therefore, the term is zero in a wall flow in local equilibrium and is uninfluential at the outer region. In a near wall separated or recirculated region, $YAP$ term drives the length scale level toward its local equilibrium value [17].

This term has been transformed for different authors in the last years due to numerical problems occasioned by the inclusion of the distance to the wall in complex geometries. Thus, Iacovides and Raise [18] proposed a form independent of the wall distance, making use of the length-scale gradient:

$$YAP = c_w \frac{\epsilon^2}{k} max[F(F+1)^2, 0] \tag{2.62}$$

where $F = [((\partial l/\partial x_j)(\partial l/\partial x_j))^{1/2} - dl_e dy]/c_l$ represents the difference between the predicted length-scale gradient, with $l = k^{3/2}/\epsilon$, and the "equilibrium length-scale gradient", $dl_e dy$, defined by $dl_e dy = c_l[1 - exp(-B_\epsilon R_t)] + B_\epsilon c_l R_t exp(-B_\epsilon R_t)$. This is obtained by differentiating the length-scale employed in a one-equation model [19]. The coefficients $(c_l, B_\epsilon, c_w)$ are given in section 2.2.11. Also, details of model containing both functions $E$ and $YAP$, will be specified in section 2.2.11 and appendix A.

**The $k - \omega$ model**

The choice of $Z = \omega$ is mainly due to the work done by Wilcox and coworkers [1]. They state that the main advantage of this formulation compared to the $k - \epsilon$ one, lies in a more natural treatment of the near wall region. The quantity $\omega$ can be seen as an inverse time-scale of the large eddies or as the rate of dissipation of energy in unit volume and time. Furthermore, contrary to the dissipation rate ($\epsilon$), there exists no exact equation for $\omega$. Thus, in order to obtain this variable, the transport equation need to be constructed. This can be done by means of a multiplication of the $k$ equation by $\omega/k$ to yield a new secondary transport equation.

Hence, starting with eq. 2.14, reemplacing dissipation ($\epsilon \equiv \beta^* \omega k$) and rearranging terms, lead to the next equation:

$$\frac{\partial(\rho\omega)}{\partial t} + \frac{\partial(\rho\bar{u}_i\omega)}{\partial x_i} = \frac{\partial}{\partial x_i}\left[\left(\mu + \frac{\mu_t}{\sigma_\omega}\right)\frac{\partial\omega}{\partial x_i}\right] + \alpha\frac{\omega}{k}P_k - \beta\rho\omega^2 \qquad (2.63)$$

where, $\alpha$, $\beta$ and $\sigma_\omega$ are specific model constants, which will be studied in detailed in section 2.2.11 and that can be obtained in a similar way to that of $k - \epsilon$ models.

In these kind of models, RANS equations are solved jointly with the $k$ equation and $\omega$ equation. The turbulent viscosity is also redefined as $\mu_t = \alpha^*\frac{\rho k}{\omega}$.

**Improvements to $\omega$ equation**

A different way to construct $\omega$ equation consists in transform the modelled $k$ and $\epsilon$ equations, by substitutin $\omega$ with $\epsilon/k$. Following this choice a number of new terms appear in the equation thus obtained. Using, this tecnique the constructed model will be identical to the original $k - \epsilon$ model, however expressed in a new secondary variable with a different, and improved, near-wall behaviour. Depending on the complexity of the equations for $k$ and $\epsilon$ used as starting point, there will be different versions of the resulting $\omega$-equation. So then, using the standard $k - \epsilon$ model as a basis (eqs. 2.14

and 2.52), the resulting transport equation for $\omega$ can be written as:

$$\frac{\partial(\rho\omega)}{\partial t} + \frac{\partial(\rho\bar{u}_i\omega)}{\partial x_i} = \frac{\partial}{\partial x_i}\left[\left(\mu + \frac{\mu_t}{\sigma_\epsilon}\right)\frac{\partial\omega}{\partial x_i}\right] + (C_{\epsilon 1} - 1)\frac{\omega}{k}P_k - (C_{\epsilon 2} - 1)\rho\omega^2$$
$$+ \frac{2\rho}{k}\left(\mu + \frac{\mu_t}{\sigma_\epsilon}\right)\frac{\partial k}{\partial x_i}\frac{\partial\omega}{\partial x_i} + \frac{\rho\omega}{k}\left(\frac{\mu_t}{\sigma_\epsilon} - \frac{\mu_t}{\sigma_k}\right)\frac{\partial^2 k}{\partial x_i^2} \tag{2.64}$$

As it can be seen, this equation contains two new terms in relation to the previously $\omega$ equation presented. These are shown in the second line of eq. 2.64. The last term (including second derivative of $k$) can be neglected because of the similar values of $\sigma_k$ and $\sigma_\epsilon$. However, the first term in the second line of eq. 2.64, known as cross diffusion ($E_w$), has been retained in $k - \omega$ models that have appeared in the last years, in an effort to improve model performance in flows with a freestream boundary. Thus, in free shear flows the cross diffusion term increases the production of $\omega$, thereby, enhances dissipation of $k$ [1]. Although this term reduces problems of $k - \omega$ models in the kind of flows above mentioned, the efficiency of this term is not proved yet, therefore, model details as well as a study about the suitability of this term in different flow configurations will be addressed later in this thesis.

**Near-wall treatment: low Reynolds modelling**

The models above presented have been developed for regions with sufficiently high Reynolds number. However, most of the flows in engineering applications are confined or related to walls and complex geometries, what imply the presence of different turbulent regimes, low and high Reynolds numbers. Therefore, the high Reynolds form of the equations is not valid in the vicinity of a wall, where viscous effects become important, e.g. turbulent boundary layer flows at low Reynolds numbers, unsteady flows and flows with separation and recirculation regions. Although, in the case of the $k - \omega$ model, which is capable of providing acceptable results for wall bounded flows, a deeper study of low-Reynolds-number (LRN) effects is needed in order to improve industrial and engineering usefulness of the turbulence models.

The LRN approach consists of changing the equations in such a way that they are valid up to the wall. This can be done by taking into account the limiting behavior of the variables under consideration approaching a solid boundary i.e., asymptotic consistency. In order to achieve this, damping functions and another modifications are introduced in the $k$, $\epsilon$ or $\omega$ equations to model viscous interaction. In the case of $k - \epsilon$ models Jones and Launder work [15] can be taken as example. They modified the standard high Reynolds number model by including three damping functions. Making in this way model constants ($C_{\epsilon 1}$, $C_{\epsilon 2}$ and $C_\mu$), appearing in eqs. 2.14 and 2.52, dependent upon the turbulence Reynolds number ($R_t = \rho k^2/\mu\epsilon$). Moreover, they added further terms to account for the fact that the dissipation processes are

not isotropic and to facilitate computational calculations by letting $\epsilon$ go to zero at the wall. Thus, they solved $\tilde{\epsilon}$-equation, which may be interpreted as the isotropic part of the energy dissipation. Therefore, now $\epsilon = \tilde{\epsilon} + D$, where $D$ is the value of dissipation at wall and is specific for each model (see appendix A).

A similar procedure is also used in $k - \omega$ models. Wilcox [1] uses perturbation methods to analyze the viscous sublayer. It is done to determine a set of functional forms dependent upon the turbulence Reynolds number ($Re_t = \rho k / \mu \omega$), in order to achieve the desired asymptotic behavior near solid walls. Furthermore, to make $k - \omega$ model capable of predicting transition in boundary layers. Therefore, coefficients appearing in eqs. 2.14 and 2.63 are modified. Details of these coefficients are given in appendix A.

There is a second possibility that allows the use of high Reynolds number equations. They are used only in fully developed turbulent regions, while using empirical wall functions to bridge the distance to the wall. However, these called wall-functions have been designed based on the law of the wall and they are, in general, not suitable for flows with separation, recirculation and adverse pressure regions. Considering that this work is focussed in flows exhibiting all these characteristics, this option is not contemplate in this thesis.

### 2.2.10   Turbulent heat flux

As result of the Reynolds averaging process carried out on the energy equation (eq. 2.3), a new unknown appears in the energy averaged equation (eq. 2.8) (see section 2.2.3 for details). This new term is known as turbulent heat flux ($-\rho \overline{u_i' T'}$), which can be modelled similarly to the Reynolds stress. Thus, a new differential transport equation can be derived. Furthermore, it can be simplified to obtain an algebraic relation in order to evaluate turbulent heat flux or, at the end, a more simplified linear approach based on the eddy viscosity can be used to calculate it.

Although the use of a differential transport equation to obtain the turbulent heat flux improves heat transfer predictions, its numerical complexity is higher and the numerical robustness is limited. Therefore, in this work the last option based on the use of an eddy or turbulent viscosity is applied. Thus, the simple gradient diffusion hypothesis is assumed. In this, the turbulent scalar flux is expected to be aligned with the mean scalar gradient. The turbulent diffusion coefficient is usually considered proportional to the eddy viscosity by means of a turbulent Prandtl number, which is a specific constant of the turbulence model. This approach is due to Reynolds, who based on the similarities between the momentum and energy transfer, proposed this analogy: as Boussinesq hypothesis associates turbulent stresses with mean strains,

58

turbulent heat flux is proportional to mean temperature gradient. So that,

$$-\rho \overline{u_i' T'} = -\frac{\mu_t}{\sigma_T} \frac{\partial \bar{T}}{\partial x_i} \tag{2.65}$$

where $\sigma_T$ is the turbulent Prandtl number. A constant value for this quantity is often used and this is usually satisfactory, provided the heat transfer rate is not too high. The most common values assumed for $\sigma_T$ are 0.89 or 0.90, in the case of a boundary layer. Heat transfer predictions could be improved somewhat by letting $\sigma_T$ vary through the boundary layer [1].

### 2.2.11 Summary of implemented two-equation turbulence models

Two-equation turbulence models used in this thesis consist of: the time-averaged governing equations (RANS), some relation for the Reynolds stress tensor and turbulent heat flux and extra transport equations for the determination of turbulence time and lenght scales, e.g. turbulent kinetic energy ($k$) and dissipation ($\epsilon$) or specific dissipation ($\omega$).

The time-averaged governing equations with the assumptions already noted are:

$$\frac{\partial \bar{u}_i}{\partial x_i} = 0 \tag{2.66}$$

$$\frac{\partial(\rho \bar{u}_i)}{\partial t} + \frac{\partial(\rho \bar{u}_j \bar{u}_i)}{\partial x_j} = -\frac{\partial \bar{p}}{\partial x_i} + \frac{\partial}{\partial x_j}\left(2\mu \bar{S}_{ij} - \rho \overline{u_i' u_j'}\right) + \rho g_i \tag{2.67}$$

$$\frac{\partial(\rho \bar{T})}{\partial t} + \frac{\partial(\rho \bar{u}_i \bar{T})}{\partial x_i} = \frac{\partial}{\partial x_i}\left(\frac{\lambda}{c_p}\frac{\partial \bar{T}}{\partial x_i} - \rho \overline{u_i' T'}\right) \tag{2.68}$$

Moreover, as mentioned before, two transport differential equations are added in two-equation models, one for $k$ and another for $\epsilon$ or $\omega$; which in their low Reynolds version can be written as follows:

$$\frac{\partial(\rho k)}{\partial t} + \frac{\partial(\rho \bar{u}_i k)}{\partial x_i} = \frac{\partial}{\partial x_i}\left[\left(\mu + \frac{\mu_t}{\sigma_k}\right)\frac{\partial k}{\partial x_i}\right] + P_k - \rho Dis \tag{2.69}$$

$$\frac{\partial(\rho \tilde{\epsilon})}{\partial t} + \frac{\partial(\rho \bar{u}_i \tilde{\epsilon})}{\partial x_i} = \frac{\partial}{\partial x_i}\left[\left(\mu + \frac{\mu_t}{\sigma_\epsilon}\right)\frac{\partial \tilde{\epsilon}}{\partial x_i}\right] + f_1 C_{\epsilon 1}\frac{\tilde{\epsilon}}{k}P_k - f_2 C_{\epsilon 2}\rho\frac{\tilde{\epsilon}^2}{k} + E + Y_c \tag{2.70}$$

$$\frac{\partial(\rho \omega)}{\partial t} + \frac{\partial(\rho \bar{u}_i \omega)}{\partial x_i} = \frac{\partial}{\partial x_i}\left[\left(\mu + \frac{\mu_t}{\sigma_\omega}\right)\frac{\partial \omega}{\partial x_i}\right] + \alpha\frac{\omega}{k}P_k - \beta\rho\omega^2 + E_\omega \tag{2.71}$$

$$\mu_t = C_\mu f_\mu \frac{\rho k^2}{\epsilon} = \alpha^* \frac{\rho k}{\omega} \tag{2.72}$$

where, $P_k = -\rho\overline{u_i'u_j'}(\partial\bar{u}_i/\partial x_j)$ ; $Dis = \epsilon$ for $k - \epsilon$ models; $Dis = \beta^*\omega k$ for $k - \omega$ models; and $\tilde{\epsilon} = \epsilon - D/\rho$; $\sigma_k, \sigma_\epsilon, \sigma_\omega, C_{\epsilon 1}, C_{\epsilon 2}, \beta, \beta^*$ are model constants; $D$, $E$, $E_w$ and $Y_c$ are extra terms and $f_1, f_2$ , $C_\mu, f_\mu$ and $\alpha^*$ are damping functions depending on the specific model used.

For details about damping functions and closure coefficients of each model see appendix A.

The general expression used in this thesis in order to evaluate turbulent stresses is:

$$\frac{\overline{u_i'u_j'}}{k} = \frac{2}{3}\delta_{ij} - 2C_\mu^* f_\mu^* \mathbf{S} + \beta_1(\mathbf{S}^2 - \frac{1}{3}[\mathbf{S}^2]I) + \beta_2(\mathbf{WS} - \mathbf{SW}) + \beta_3(\mathbf{W}^2 - \frac{1}{3}[\mathbf{W}^2]I)$$
$$-\gamma_1[\mathbf{S}^2]\mathbf{S} - \gamma_2[\mathbf{W}^2]\mathbf{S} - \gamma_3(\mathbf{W}^2\mathbf{S} + \mathbf{SW}^2 - [\mathbf{W}^2]\mathbf{S} - \frac{2}{3}[\mathbf{WSW}]I) - \gamma_4(\mathbf{WS}^2 - \mathbf{S}^2\mathbf{W})$$
$$(2.73)$$

This expression has the advantage that terms associated with coefficients $\gamma_3$ and $\gamma_4$ dissapear in 2D incompressible flows. It is also evident that setting $\beta$'s and $\gamma$'s coefficients to zero in eq. 2.73 the linear relation (eq. 2.45) is obtained.

The coefficients of the general expression (eq. 2.73) can be found in appendix A. Finally, for the calculation of the turbulent heat flux the next relation:

$$-\rho\overline{u_i'T'} = -\frac{\mu_t}{\sigma_T}\frac{\partial\bar{T}}{\partial x_i} \tag{2.74}$$

which is applied for all models in this work assuming a constant Prandtl number ($\sigma_T = 0.9$).

Models considered in this work, based on $k - \epsilon$ platform:

- **Ince and Launder model (IL k$\epsilon$-LEVM)** [17]: low-Reynolds linear model including Yap correction [16]. It also includes additional source terms in the dissipation equation to improve its behaviour near solid walls.

- **Goldberg, Peroomian and Chakravarthy model (GPC k$\epsilon$-LEVM)** [20]: wall-distance-free low-Reynolds linear model. It includes an extra source term in the dissipation equation to increase the dissipation level in nonequilibrium regions.

- **Abid, Morrison, Gatski and Speziale model (AMGS k$\epsilon$-EARSM)** [21]: high-Reynolds model derived under weak-equilibrium condition and converted into an explicit algebraic model by assuming that the ratio $P_k/\epsilon$ is constant and known.

- **Craft, Launder and Suga model (CLS k$\epsilon$-NLEVM)** [22]: low-Reynolds cubic non-linear model. It was calibrated by reference to direct numerical simulation data for homogeneously strained flow. Furthermore, it was proposed paying attention to the representation of viscous near-wall processes. Also, it includes Yap correction [16].
  In this work, the original $C_\mu$ function proposed in [22] is replaced by that recommended later by Craft et al. [19].

Those models studied which use $\omega$ as turbulent dissipation variable are:

- **Wilcox standard model (WX $k\omega$-LEVM)** [23]: standard $k-\omega$ linear model proposed to account the effects of streamwise pressure gradients, and to overcome deficiencies of $\epsilon$-based models in the regions near solid walls.

- **Wilcox transition model (WXT $k\omega$-LEVM)** [24]: similar to standard linear model, but coefficients are now based on turbulence Reynolds number to achieve asymptotic consistency with the exact behaviour of the turbulent variables when approaching a solid boundary, i.e. transition zones.

- **Wilcox cross-diffusion model (WXCD $k\omega$-LEVM)** [1]: linear model that includes cross-difussion term in order to improve predictive accuracy for free shear flows. Coefficients are calibrated to provide correct spreading rates in plane, round and axial jets.

- **Larsson model (LAR $k\omega$-NLEVM)** [25]: non-linear quadratic model based on the standard WX ($k\omega$-LEVM) model, and derived using dimensional analysis, rapid distortion theory and realisability constraints.

- **Wallin and Johansson model (WJO $k\omega$-EARSM)** [7]: quadratic model derived formally from an algebraic form of a DRSM, subject to the weak-equilibrium assumption. It is complemented by a non-linear scalar equation for $P_k/\epsilon$.

- **Abid, Rumsey and Gatski model (ARG $k\omega$-EARSM)** [26]: $k-\omega$ version of the AMGS (k$\epsilon$-EARSM) model.

- **Abe, Jang and Leschziner model (AJL $k\omega$-NLEVM)** [27]: quadratic low-Reynolds model. This model introduces two new terms in the basic constitutive relation (Eq. 2.44), to account for high normal straining and strong near-wall anisotropy.

Table 2.1 indicates which terms of eq. 2.73 are taken into account in the models used in this work.

| Model | $\beta_1$ | $\beta_2$ | $\beta_3$ | $\gamma_1$ | $\gamma_2$ |
|---|---|---|---|---|---|
| LEVM | N | N | N | N | N |
| AMGS-EARSM [21] | Y | Y | N | N | N |
| CLS-NLEVM [22] | Y | Y | Y | Y | Y |
| LAR-LEVM [25] | N | Y | N | N | N |
| ARG-EARSM [26] | Y | Y | N | N | N |
| WJO-EARSM [7] | Y | Y | N | N | N |
| AJL-NLEVM [27] | Y | Y | N | N | N |

**Table 2.1:** Terms appearing in the general stress-strain relationship ($Y = yes$, $N = no$).

## 2.3   Numerical methodolgy

### 2.3.1   Introduction

By definition, Computational fluid dynamics (CFD) is one of the branches of fluid mechanics that uses numerical methods and algorithms to solve and analyze problems that involve fluid flows. Computers are used to perform calculations required to simulate the interaction of fluids with the complex surfaces used in engineering. However, even with simplified equations and fast computers, only approximate solutions can be obtained in many situations.

Historically, this method was first developed to solve the Linearized Potential equations. Two-dimensional methods, using conformal transformations of the flow about a cylinder to the flow about an airfoil were developed in the 1930s. But, it was until 1960s that the first paper on a practical three-dimensional method to solve the linearized potential equations was presented.

The most fundamental consideration in CFD is how a continuous fluid is simulated in a discretized manner on a computer. In this thesis, the standard approach known as finite volume method (FVM) is used. The first step in the FVM is to divide the domain into a number of control volumes, where the variable of interest is located at the centroid of the control volume. The next step is to integrate the differential form of the governing equations over each control volume. Interpolation profiles are then assumed in order to describe the variation of the concerned variable between cell centroids. The resulting equation is called the discretized equation. This integral approach yields a method that is inherently conservative. This is satisfied for any control volume as well as for the whole computational domain and for any number of control volumes.

Once FVM is applied to all control volumes in a given mesh, we obtain a full linear system of equations that needs to be solved. The basic solution of the system of equations arising after discretization is accomplished by many of the familiar algorithms of

numerical linear algebra. Any stationary iterative method such as, symmetric Gauss-Seidel, successive overrelaxation (SOR), or a Krylov subspace method, can be used to solve this linear system [28].

### 2.3.2 Discretization of general transport equations

RANS equations (eqs. 2.66, 2.67 and 2.68) and turbulence transport equations (eqs. 2.69 and 2.70 or 2.71) all can be written in a general *convection-diffusion* form:

$$\underbrace{\frac{\partial(\rho\phi)}{\partial t}}_{transient} + \underbrace{\nabla \cdot (\rho\mathbf{u}\phi)}_{convection} - \underbrace{\nabla \cdot (\Gamma\nabla\phi)}_{diffusion} = \underbrace{S_\phi}_{source} \tag{2.75}$$

where $\phi$ is the dependent variable and the source term varies for each equation to be solved and $\Gamma$ represents the diffusion coefficient for scalar variables and the effective viscosity for vector variables. For the discretization of eq. 2.75 the finite volume method is applied using a structured and staggered grid. The explanation in this section is restricted to two dimensions, although the extrapolation to three dimensions is straightforward.

As can be observed in Figure 2.1, three different control volumes (CVs) are defined, in all of them nodal points are located in the center of the corresponding CV. The first one (dashed) is centered for the evaluation of scalar quantities (pressure, temperature, $k$ and $\epsilon$ or $\omega$). The grid staggered half control volume to the right is used to evaluate $x$-direction velocity (dashed line in Fig. 2.1) and the one staggered to the top is defined to calculate $y$-direction velocity (dotted line in Fig. 2.1).

If in eq. 2.75 a new total flux ($\mathbf{J}$) is used to group convective flux ($\rho\mathbf{u}\phi$) and diffusive flux ($\Gamma\nabla\phi$) as, $\mathbf{J} = \rho\mathbf{u}\phi - \Gamma\nabla\phi$. It is possible to write eq. 2.75 in a more compact form,
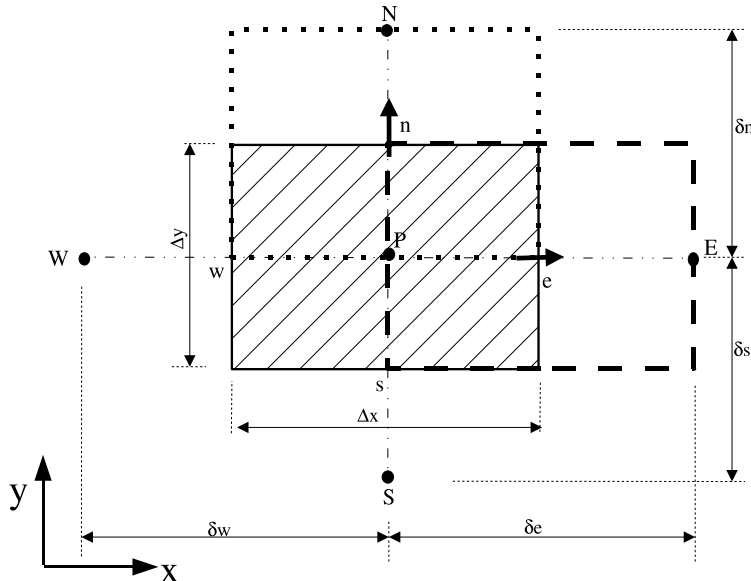
$$\frac{\partial(\rho\phi)}{\partial t} + \nabla \cdot \mathbf{J} = S_\phi \tag{2.76}$$

which can be integrated over a given CV. An integral form of eq. 2.76 can be written using the divergence theorem to convert the divergence term to a surface integral in the following form:

$$\int_\Omega \frac{\partial(\rho\phi)}{\partial t} d\Omega + \oint_{\partial\Omega} \mathbf{J} \cdot \vec{n} \, dS = \overline{S_\phi}\Omega \tag{2.77}$$

where, $\Omega$ is the volume of the CV and $d\Omega$ its exterior surface.

Now each term of this equation is studied separately. First, to proceed with the integration of the second term of the previous equation the total flux ($\mathbf{J}$) is again splitted into the diffusive flux ($J^D$) and convective flux ($J^C$). Thus, taking only the $e$-face (see Fig. 2.1) as example, the integration of the diffusive flux over that face

**Figure 2.1:** General control volumes distribution and nodal points location. Staggered dashed CV used to evaluate x-direction velocity and dotted CV to calculate y-direction velocity.

yields:

$$
\begin{aligned}
J_e^D &= \int_e -\Gamma \nabla \phi \cdot dS = \int_e -\Gamma \frac{\partial \phi}{\partial x} dS \\
&\approx -\Gamma_e \left( \frac{\partial \phi}{\partial x} \right)_e \Delta y \approx -\Gamma_e \left( \frac{\phi_E - \phi_P}{\delta e} \right) \Delta y = -D_e(\phi_E - \phi_P)
\end{aligned}
\tag{2.78}
$$

where, a second order central difference scheme has been applied to evaluate derivative and $\Gamma_e$ is assumed to be a suitable face average between nodes $E$ and $P$ (see Fig. 2.1), and it is considered constant in the whole face.

The integration of the convective flux in the same face of the CV is as follows:

$$
J_e^C = \int_e \rho \mathbf{u} \phi \cdot \vec{n} \, dS = \int_e \rho u_e \phi dS \approx \rho u_e \phi_e \Delta y = F_e \phi_e
\tag{2.79}
$$

A key aspect in this integration is the approximation applied to obtain the dependent variable at the face of the CV ($\phi_e$). Different numerical schemes to evaluate it have

been published in the last decades, which are generally classified according to the number of nodes taking into account in the approximation of the variable at the face. The numerical schemes used in this thesis are: upwind, power law [29], second order accurate upwind [30] and SMART [31] schemes. The deferred correction approach has been utilized for the application of high order schemes in the evaluation of convective terms, so then:

$$Fe\phi_e = Fe\phi_e^U - Fe(\phi_e^U - \phi_e^H) \tag{2.80}$$

where, $\phi_e^U$ is the value of the variable evaluated using upwind scheme and $\phi_e^H$ calculated with a high order scheme. The second right hand side term is now introduced in the source term as $b_{de}$ (for details see [31]).

The temporal discretization is slightly easier to deal with than that for the spatial effects. Since the general transport equation is hyperbolic/parabolic in time, the solution at time $t$ depends upon its history and not on its future. Applying fully implicit integration, the transient term is evaluated as,

$$\int_\Omega \int_{t-\Delta}^t \frac{\partial(\rho\phi)}{\partial t} d\Omega \approx \frac{(\rho\phi_P)^t - (\rho\phi_P)^{t-\Delta t}}{\Delta t}\Omega_P \tag{2.81}$$

so then an iterative solution method has to be applied.

Source term deserves a special attention in the case of turbulent flows computations because of the linearization required. In the $k$ and $\epsilon$ or $\omega$ equations the source term is linearized as follows, $S_\phi = S_c + S_p\phi_p$, in order to prevent numerical instabilities and avoid negative values of turbulence quantities. For instance, in the $k$-equation (eq. 2.69) the source terms have been included in the form: $S_c = max(P_k + G_k, 0)$ (giving a positive value) and $S_p = -[\rho\tilde{\epsilon} + D - min(P_k + G_k, 0)]/k$ (giving a negative value). Thus production terms have been included in the $S_c$ term and all the destruction terms in the $S_p$ term [32]. This procedure is relevant to improve numerical convergence. Moreover, the use of NLEVM or EARSM has further implications in convergence. Therefore, in later sections some tricks that have been applied to increase stability in the calculation process are explained.

Finally, an algebraic equation relating nodal value ($\phi_P$) with their neighbours ($\phi_W$, $\phi_E$, $\phi_S$, $\phi_N$) can be written in the following manner:

$$a_P\phi_P = \sum_{nb} a_{nb}\phi_{nb} + b \tag{2.82}$$

with the subscript $_{nb}$ indicating neighbours nodes.

Because of the non-linearity of the transport equations, an iterative method to solve the discretized equations to obtain a converged solution is applied in this thesis.

At this point it is worth to note that there is no equation for pressure, but its gradient appear in the momentum equation. Thus, it is possible to take advantage of this link to construct an iterative solution (segregated).

### 2.3.3 SIMPLEC (Semi-Implicit Method for Pressure-Linked Equations Consistent)

If the discretized form of the Navier-Stokes system is considered, the form of the equations shows linear dependence of velocity on pressure and vice-versa. This inter-equation coupling is called velocity pressure coupling. In this thesis a pressure based method of the SIMPLE family, specifically SIMPLEC, is applied to provide an useful means to couple pressure and velocity fields for segregated solvers [29].

The SIMPLEC algorithm may be summarized as follows:

- An approximation of the velocity field is obtained by solving the momentum equation. The pressure gradient term is calculated using the pressure distribution from the previous iteration or an initial guess.

- The pressure-correction equation is formulated, taking as starting point conitnuity equation, and solved in order to obtain the new pressure distribution.

- Velocities are corrected and a new set of conservative fluxes is calculated.

Further details are not explained here for briefness, an interested reader is remitted to [29].

### 2.3.4 General algorithm for the solution of a general two-equation turbulence model

Once the set of algebraic equations is obtained, a key element in the calculation of turbulent flows is constituted by the general algorithm used in the global solution of the system, in order to achieve numerical convergence. It due to the strong couplings present in RANS models, e.g. pressure-velocity, energy-momentum and turbulent stresses-mean strains.

In this thesis the next steps are followed during the solution of a given problem:

- During preprocessing

  - The geometry (physical domain) of the problem is defined.
  - The volume to be studied is divided into discrete cells, i.e., control volumes of the mesh.

– The physical model is defined, e.g., the equations of motions + energy + turbulence quantities.

– Boundary conditions are specified. This involves the definition of the fluid behavior and properties at the boundaries of the problem. In transient computations, initial conditions are also defined.

- The simulation is started and the equations are solved iteratively:

  1. Apply a SIMPLE-like method to solve pressure-velocity coupling.

  2. Calculate mean strains, mass fluxes, turbulent heat fluxes and source terms (e.g. $P_k$, $D$, $E$, $YAP$, $E_w$).

  3. Solve the discretization equations for scalar variables ($T$, $k$, $\epsilon$ or $\omega$).

  4. Evaluate turbulent viscosity and turbulent stresses.

  5. Repeat the process until a converged solution is obtained.

- Numerical results are adequately verified.

- Finally a post-process is used for the analysis of the numerical solution obtained.

In step 4 verification is mentioned. Thus, verification and validation aspects are considered later due to the crucial role they exert in the credibility of the final results.

## 2.3.5  Some ideas about Multigrid methods

In this thesis this methodology is applied in order to accelerate the convergence rate in the solution of the algebraic system of equations. The convergence rate of standard iterative solvers (Gauss-Seidel, Jacobi, SOR) has a tendency to fail in effectively reducing errors after a few number of iterations. The problem is more prominent when the meshes are refined. In fact, standard solver behave much better on coarse grids. A close inspection of this behavior reveals that the convergence rate is a function of the error field frequency, i.e. the gradient of the error from node to node. If the error is distributed in a high frequency mode, the convergence rate is fast. However, after the first few iterations, the error field is smoothed out and the convergence rate deteriorates.

For many iterative methods, the number of iterations required to reach a converged solution is linearly proportional to number of nodes in one direction. This behavior could be rooted out to the fact that during the iteration process, the information travels only one grid size per iteration. While for proper convergence, the information has to travel back and forth several times [8].

To take advantage of this fact, Multigrid methods are based on the idea of defining coarser grids on which a low frequency error will be seen as a high frequency one.

Multigrid methods effectively reduce the distribution of low frequency errors which makes them a good choice to be used with standard solvers. In recent years, Multigrid algorithms have become very popular, because of their efficiency for larger systems of equations. However, it has to be noted that multigrid method is NOT a solver, it is a technique used in conjunction with a linear solver to yield a better convergence rate (for more details about Multigrid technique see [28]).

## 2.4    Verification and validation

The verification and validation process is required to obtain confidence that a science and engineering simulation code is producing accurate numerical results. Verification refers to the process of determining that a model implementation accurately represents the developer's conceptual description of the model and the solution to the model. Validation is the process of determining the degree to which a model is an accurate representation of the real world from the perspective of the intended uses of the model. These processes are applied throughout this thesis to ensure that credible results are obtained.

When a study about errors present in a numerical simulation is carried out, it is necessary to follow three types of analysis:

- **Code verification.** This step is intended to detect possible bugs incurred in the coding stage. It is concerned with establishing that a code is accurately solving the governing equations that are being used to simulate a physical problem, and therefore the coding has been performed correctly. The objective is to guarantee that results obtained correspond to the solution of the posed equations. This study can be done by means of global or local balances verification, comparison with analytical solution, if they exist, or the application of the *Manufactured Solutions (MMS)* method [33].

- **Verification of the numerical results.** It is used to determine the discretization error or solution accuracy, obtained with a verified code, to ensure that the solution has the desired exactitude. The discretization is the main source of error in the generation of a numerical solution using CFD. Thus, if double precision variables are being used and the convergence criterion is strict enough, the solution error depends mainly on the numerical schemes applied and the grid used. In order to verify the solutions exist two possibilities. The basic and simplest one consist of running different grids increasing the number of control volumes used and observe that some characteristic global parameter (e.g. Nusselt number, re-attachment point or skin-friction coefficient) tends to an asymptotic value when the grid is refined. The solution is considered grid

68

independent when the differences between two consecutive meshes are less than a prescribed value.

Another procedure applied in this thesis involves a process more reliable, detailed and that provides much more information about uncertainties. This post-processing procedure, implemented by Cadafalch et al.[34], is based on the generalized Richardson extrapolation for *h-refinement* studies and on the Grid Convergence Index (GCI) proposed by Roache [35]. It has been used in order to establish a criteria about the sensitivity of the simulation to the computational model parameters that account for the discretization: the mesh spacing and the order of accuracy of the numerical schemes used (observed order of accuracy $p$) and the error band where the independent grid solution is expected to be contained (uncertainty due to discretization GCI), thus giving criteria about the credibility of these estimations (see [34] for more details).

The procedure uses a group of numerical results ($\phi_1(x)$, $\phi_2(x)$ and $\phi_3(x)$) corresponding to three consecutive meshes: $h_1 = fine$, $h_2 = middle$ and $h_3 = coarse$, of the *h-refinement* study, which are interpolated to the coarsest grid (post-processing grid). The nodes where a monotonic solution is observed, i.e. $[(\phi_2(x) - \phi_3(x))/(\phi_1(x) - \phi_2(x))] > 0$, and therefore this post-processing procedure can be applied, are known as *Richardson nodes* (Rn). In these nodes local estimators of the *GCI* and $p$ are calculated as follows:

$$p(x) = \frac{ln[(\phi_2(x) - \phi_3(x))/(\phi_1(x) - \phi_2(x))]}{ln(r)} \qquad (2.83)$$

$$GCI_1(x) = F_s \left| \frac{\phi_1(x) - \phi_2(x)}{1 - r^{p(x)}} \right| \qquad (2.84)$$

where, $r$ is the refinement ratio and $F_s$ is a safety factor, here considered as 1.25 according to Cadafalch et al. [34]. These estimations are obtained for each of the dependent variables solved in the problem. Furthermore, a volumetric averaged global value of $p$ as well as a global *GCI* are evaluated at all the *Richardson nodes.*

It is considered that the *GCI* is credible, when the global observed order of accuracy $p$ approaches the theoretical value, and when the number of *Richardson nodes* is high enough. See [34] for details. This method has been applied with success in several works. For instance, it can be found in publications by Cònsul et al. [36], Celik et al. [37] and Claramunt et al. [38]. However, as it will be illustrated later, it is not always possible to apply this procedure. Therefore, the first procedure is used.

- **Validation of the mathematical formulation.** It is needed to demonstrate that a well-posed mathematical problem has been formulated, and a unique

solution exists. Moreover, this is required to establish the accuracy of the model used to simulate the physical problem being investigated. Verified solutions from a verified code are required for the evaluation of the models used in the code. So then, verification must precede validation. The validation issue is done by means of: comparison with experimental, DNS or other numerical simulation results, which can be considered reliable by the scientific community.

## 2.5   Conclusions

An introduction to the mathematical formulation used troughout this thesis has been presented. Since, RANS modelling is used in this research the explanation has been centered on it. Thus, a detailed explanation of the process followed to obtain averaged equations has been shown. Derivation of the equations used to solve the turbulent quantities has also been presented. Moreover, the models used in this thesis to relate turbulent stresses with the mean rate of strain are explained. Furthermore, a brief description of the discretization of the governing equations, computational methodology and verification tools used in this thesis has been included.

## References

[1] D.C. Wilcox. *Turbulence modeling for CFD.* DCW Industries, Inc. CA, 1998.

[2] S.B. Pope. *Turbulent Flows.* Cambridge University Press, 2000.

[3] W. Rodi. *The prediction of free turbulent boundary layers by use of a two-equation model of turbulence.* PhD thesis, University of London, 1972.

[4] T.B. Gatski and C.G. Speziale. On Explicit Algebraic Stress Models for Complex Turbulent Flows. *Journal of Fluid Mechanics*, 254(1):59–78, 1993.

[5] C.G. Speziale, S. Sarkar, and T.B. Gatski. Modelling the Pressure-Strain Correlation of Turbulence: an Invariant Dynamical systems Approach. *Journal of Fluid Mechanics*, 227:245–272, 1991.

[6] B. E. Launder, G. J. Reece, and W. Rodi. Progress in the development of a Reynolds-stress turbulence closure. *Journal of Fluid Mechanics*, 68:537–566, 1975.

[7] S. Wallin and A. V. Johansson. An Explicit Algebraic Reynolds Stress Model for Incompressible and Compressible Turbulent Flows. *Journal of Fluid Mechanics*, 403:89–132, 2000.

*References*

[8] B. E. Launder and N. D. Sandham. *Closure Strategies for Turbulent and Transitional Flows.* Cambridge University Press, 2002.

[9] S. B. Pope. A more effective-viscosity hypothesis. *Journal of Fluid Mechanics*, 72:331–340, 1975.

[10] T. Gatski and T. Jongen. Nonlinear eddy viscosity and algebraic stress models for solving complex turbulent flows. *Progress in Aerospace Sciences*, 36:655–682, 2000.

[11] S. Girimaji. Fully explicit and self-consistent algebraic Reynolds stress model. *Theoretical and Computational Fluid Dynamics*, 8:387–402, 1996.

[12] T. H. Shih and J. L. Lumley. Remarks on turbulent constitutive relations. *Mathematical and Computer Modelling*, 18(2):9–16, 1993.

[13] Pattijn Saskia. *Nonlinear, low Reynolds, two-equations turbulence models.* PhD thesis, Ghent University, 1998.

[14] C. J. Chen and S. Y. Jaw. *Fundamentals of Turbulence Modeling.* Taylor and Francis, 1998.

[15] W.P. Jones and B.E. Launder. The prediction of laminarization with a two-equation model of turbulence. *International Journal of Heat and Mass Transfer*, 15:301–314, 1972.

[16] C. J. Yap. *Turbulent Heat and Momentum Transfer in Recirculating and Impinging Flows.* PhD thesis, University of Manchester, 1987.

[17] N.Z. Ince and B.E. Launder. Computation of Buoyancy-Driven Turbulent Flows in Rectangular Enclosures. *International Journal of Heat and Fluid Flow*, 10(1):110–117, 1989.

[18] H. Iacovides and M. Raisee. Recent progress in the computation of flow and heat transfer in internal cooling passages of turbine blades. *International Journal of Heat and Fluid Flow*, 20(3):320–328, 1994.

[19] T. J. Craft, H. Iacovides, and J. H. Yoon. Progress in the Use of Non-linear Two-Equation Models in the Computation of Convective Heat-Transfer in Impinging and Separated Flows. *Flow, Turbulence and Combustion*, 63(1):59–81, 1999.

[20] U. Goldberg, O. Peroomian, and S. Chakravarthy. A Wall-Distance-Free k-$\epsilon$ Model with Enhanced Near-Wall Treatment. *Journal of Fluids Engineering*, 120(3):457–462, 1998.

[21] R. Abid, J.H. Morrison, T.B. Gatski, and C.G. Speziale. Prediction of Aerodynamic FLows with a New Explicit Algebraic Stress Model. *AIAA Journal*, 34(12):2632–2635, 1996.

[22] T.J. Craft, B.E. Launder, and K. Suga. Development and Application of Cubic Eddy-Viscosity Model of Turbulence. *International Journal of Heat and Fluid Flow*, 17(1):108–115, 1996.

[23] D. C. Wilcox. Reassessment of the Scale-Determining Equation for Advanced Turbulence Models. *AIAA Journal*, 26:1299–1310, 1988.

[24] D. C. Wilcox. Simulation of Transition with a Two-Equation Turbulence Model. *AIAA Journal*, 32:247–255, 1994.

[25] J. Larsson. Two-Equation Turbulence Models for Turbine Blade Heat Transfer Simulations. In *Proceedings 13th ISABE Conference*, pages 1214–1222, 1997.

[26] R. Abid, C. Rumsey, and T.B. Gatski. Prediction of Nonequilibrium Turbulent FLows with Explicit Algebraic Stress Models. *AIAA Journal*, 33(11):2026–2031, 1995.

[27] K. Abe, Y. J. Jang, and M. A. Leschziner. An Investigation of Wall-Anisotropy Expressions and Length-Scale Equations for Non-Linear Eddy-Viscosity Models. *International Journal of Heat and Fluid Flow*, 24(2):181–198, 2003.

[28] M. Soria. *Parallel multigrid algorithms for computational fluid dynamics and heat transfer*. PhD thesis, Universitat Politècnica de Catalunya, 2000.

[29] S. V. Patankar. *Numerical Heat Transfer and Fluid Flow*. Hemisphere Publishing Corporation, 1980.

[30] W. Shyy. A study of finite difference approximations to steady state convection dominated flow problems. *Journal of Computational Physics*, 57:415–438, 1985.

[31] M. S. Darwish and F. Moukalled. An Efficient Very-High Resolution Scheme Based on an Adaptive-Scheme Strategy. *Numerical Heat Transfer, Part B*, 34(2):191–213, 1998.

[32] C.D. Pérez-Segarra, A. Oliva, M. Costa, and F. Escanes. Numerical experiments in turbulent natural and mixed convection in internal flows. *International Journal for Numerical Methods for Heat and Fluid Flow*, 5(1):13–33, 1995.

[33] P. J. Roache. Code Verification by the Method of Manufactured Solutions. *Journal of Fluids Engineering*, 124(1):4–10, 2002.

*References*

[34] J. Cadafalch, C. D. Pérez-Segarra, R. Cònsul, and A. Oliva. Verification of Finite Volume Computations on Steady State Fluid Flow and Heat Transfer. *Journal of Fluids Engineering*, 124(11):11–21, 2002.

[35] P. J. Roache. Perspective: a method for uniform reporting of grid refinement studies. *Journal of Fluids Engineering*, 116(3):405–413, 1994.

[36] R. Cònsul, C.D. Pérez-Segarra, K. Claramunt, J. Cadafalch, and A. Oliva. Detailed numerical simulation of laminar flames by a parallel multiblock algorithm using loosely coupled computers. *Combustion Theory and Modelling*, 7(3):525–544, 2003.

[37] I. Celik and Vei-Ming Zhang. Calculation of numerical uncertainty using Richardson extrapolation: application to some simple turbulent flow calculations. *Journal of Fluids Engineering*, 117:439–445, 1995.

[38] K. Claramunt, R. Cònsul, C.D. Pérez-Segarra, and A. Oliva. Multidimensional mathematical modeling and numerical investigation of co-flow partially premixed methane/air laminar flames. *Combustion and Flame*, 137:444–457, 2004.

*References*

# Chapter 3

# Verification, validation and numerical studies on three benchmark flow configurations.

**Abstract.** The aim of this work is to study the adequacy of different RANS models in terms of accuracy and numerical performance in the description of turbulent internal forced convection flows. Within RANS modelizations, linear and non-linear eddy-viscosity models and explicit algebraic models are explored. A comparison of the suitability of different two-equation platforms such as $k - \epsilon$ and $k - \omega$ is also carried out. Three different internal forced convection flows are studied: turbulent plane channel, backward facing step, and confined impinging slot jet. The results are compared with DNS or experimental data available in the literature, reviewing mean and fluctuating velocities, turbulent stresses and global parameters like Nusselt number, skin friction coefficient or reattachment point. Governing partial differential equations are transformed to algebraic ones by a general fully implicit finite-volume method over structured and staggered grids. A segregated SIMPLE-like algorithm is used to solve pressure-velocity fields coupling. A verification procedure based on the generalized Richardson extrapolation is applied to ensure the credibility of the numerical solutions.

## 3.1 Introduction

Turbulence plays an important role in engineering applications since most flows in industrial equipment and surroundings are in turbulent regime. Direct Numerical Simulation (DNS) of these flows using full 3D and time dependent Navier-Stokes (NS) equations is generally restricted to simple geometries and low Reynolds number flows due to the large, if not prohibitive, computational resources required to resolve all the scales of motion. Therefore, the use of turbulence modelling employing statistical techniques for high Reynolds numbers or complex geometries is still necessary. In general, this modelization can be based on volume filtering (Large Eddy Simulation, LES) or time averaging (Reynolds-Averaged Navier-Stokes Simulations, RANS) of the NS-equations. LES models are still too expensive for routine calculation because, even though the smallest eddies are modelled, the larger ones have to be solved in detail (3D and unsteady). Otherwise, RANS models can be appropriate to describe most of the main characteristics of the fluid motions [1].

In the past decades RANS-technique has received great interest because of its wide range of applicability and reasonable computational cost. This technique solves the governing equations by modelling both the large and the small eddies, taking a time-average of variables. As consequence of the average new unknowns, so-called Reynolds stresses arise. Different approaches to evaluate them are: i) Differentially Reynolds Stress Models (DRSM), ii) Algebraic Reynolds Stress Models (ARSM), and iii) Eddy Viscosity Models (EVM) [1].

Although EVM models assuming a linear relation between the turbulent stresses and the mean rate of strain tensor ($S$) are extensively used, they present limitations such as isotropy, no-prediction of secondary motions in non-circular ducts, boundary-layer separation, erroneous predictions of the production of turbulence in strong strain fields, etc. In the last few years, with the even-increasing computational capacity, new proposals to overcome many of these deficiencies have started to find their way. Thus, algebraic or non-linear relations can be used to determinate the Reynolds (turbulent) stress tensor without introducing any additional differential equation. Most of these models are or will be incorporated into computational tools and there is no sufficient clarity about which model behaves better even in basic situations with different flow structure. Therefore, systematic studies to establish their properties, numerical performance and spatial requirement in basics and widely studied flows are required.

The main goal of this work is to contribute in an effort to provide conclusions about accuracy, convergence, predictive realism, advantages and shortcomings in the use of explicit algebraic Reynolds stress and linear/non-linear eddy-viscosity models. Furthermore, the effect of using $\epsilon$ or $\omega$ as length scale variable in the simulated configurations is also studied.

Three basic and intensively investigated configurations, which present different flow structure, are numerically studied. The first case tested is one of the best studied

situations: a fully developed turbulent flow in a plane channel [2]. The second case is the flow in a backward facing step, that has a more complex flow structure due to separation and recirculation phenomena [3]. The third case is the flow in an impinging slot jet, which presents a very complex structure despite its relatively simple geometry, involving stagnation, recirculation and adverse pressure zones [4]. The first case serves as a baseline test, and the second and third cases are representative of situations where non-linear and explicit algebraic relations should improve results of LEVM due to their characteristics.

Conclusions are extracted after the application of two processes to the studied flows. Firstly, a verification procedure based both on the generalized Richardson extrapolation and the Grid Convergence Index (GCI) is applied to the numerical solutions obtained[5]. Once credibility of the numerical results is assured, the mathematical models are validated by comparison with experimental data and/or DNS results from the literature.

## 3.2 Mathematical formulation

The turbulent flows studied in this chapter are considered to be described by the time-averaged governing equations (continuity, momentum and energy) for incompressible Newtonian fluids, assuming negligible body forces, heat friction, and radiative effects (equations explained in section 2.2).

Three types of RANS models are used in this study in order to calculate Reynolds stresses: explicit algebraic Reynolds stress models (EARSM), non-linear eddy-viscosity models (NLEVM), and linear eddy-viscosity models (LEVM). In the context of two-equation turbulence models, the solution of a set of equations to account for the transport of some turbulent quantities, specifically the turbulent kinetic energy rate per unit mass ($k$) (eq. 2.69), and some length-scale determining equation, such as the dissipation rate ($\epsilon$) (eq. 2.70) or the specific dissipation rate ($\omega$)(eq. 2.71), amongst others [6], is required.

In the present Chapter five linear models are taken into account: IL(Ince-Launder [7]), GPC(Goldberg-Peroomian-Chakravarthy [8]), WX (Wilcox [9]), WXT (Wilcox [10]) and WXCD (Wilcox [6]). The IL and GPC models use $\epsilon$ as dissipation variable, while WX, WXT and WXCD models use $\omega$.

In Non-linear and explicit algebraic models, the Reynolds stress tensor is calculated using algebraic expressions based on the weak-equilibrium assumption and including terms up to third order in the constitutive relation in function of mean velocity gradients [11].
While both the EARSM and the NLEVM models have similar functional forms, their development follow different paths. In NLEVM the coefficients in the relation of Reynolds stresses are calibrated for some representative flows and they are based on

some physical constraints [11]. On the other hand, in EARSM the coefficients appearing in the tensorial expansion are consistent with the differential Reynolds stress model (DRSM) which it is derived [12]. The aim of these models is to calculate the Reynolds Stress tensor with one approximation different from the Boussinesq approximation. They use algebraic expressions based on the weak-equilibrium assumption and include terms up to third order in the $\overline{u_i' u_j'}$ equation [11] (see section 2.2 for details).

The general expression for $\overline{u_i' u_j'}$ in both EARSM and NLEVM can be found in section 2.2. The coefficients in this relation (eq. 2.73) can be found in appendix A.

In this type of formulation, six representative models are implemented: CLS-NLEVM (Craft et al. [11]), AMGS-EARSM (Abid et al. [13]), LAR-NLEVM (Larsson [14]), AJL-NLEVM (Abe et al. [15]), ARG-EARSM (Abid et al. [16]) and WJO-EARSM (Wallin-Johansson [17]). CLS and AMGS models use $k - \epsilon$, whereas LAR, AJL, WJO and ARG models use $k - \omega$ platform.

For details about damping functions and closure coefficients of each model see appendix A.

In the present study the simple linear eddy diffusivity approach is used for the computation of the turbulent heat flux (see section 2.2 for details).

## 3.3 Numerical procedure

The governing partial differential equations are converted into algebraic ones by means of fully implicit finite volume techniques. They are solved on a structured and staggered grid intensified using a tanh-like function where necessary [18]. The set of equations is solved in a segregated manner using a pressure based method, of the SIMPLE family, to couple the velocity and pressure fields [19]. Central differences are employed for the evaluation of diffusion terms while convective terms are discretized using upwind, power law [19] or high order SMART [20] schemes. The latter scheme has not been applied to the turbulence variables $(k, \epsilon, \omega)$ due to instability problems. A multi-grid iterative solver is used to solve the algebraic linear system of equations [21] (for details see section 2.3).

The addition of higher order terms in the constitutive relation for turbulent stresses has further implications in convergence. Then, an artificial eddy viscosity is used to introduce as many terms as possible in the diffusive terms of the momentum equations [22]. Thus, only the remaining terms of the constitutive relation are maintained explicitly in the source term.

In the $k$, $\epsilon$ or $\omega$ equations the source term is linearized in order to avoid negative values. All production terms are included in the source term (right side), while dissipation terms are transferred to the left hand side of the discretized equation [18].

In order to verify the numerical solutions obtained, a post-processing procedure

based on the generalized Richardson extrapolation for *h-refinement* studies and on the Grid Convergence Index (GCI), has been used in order to establish a criterion about the sensitivity of the simulation to the computational model parameters that account for the discretization: the mesh spacing and the order of accuracy of the numerical solution. Local estimators of the error band, where the independent grid solution is expected to be contained (uncertainty due to discretization, *GCI*), and the observed order of accuracy (*p*) are calculated at the grid nodes where their evaluation has been possible. These grid nodes are named *Richardson nodes*. Global values of *GCI* and *p* are calculated by means of a volumetric averaging. An estimation is considered to be credible when the global observed order of accuracy *p* approaches the theoretical value, and when the number of *Richardson nodes* is high enough. See section 2.4 and [5] for details.
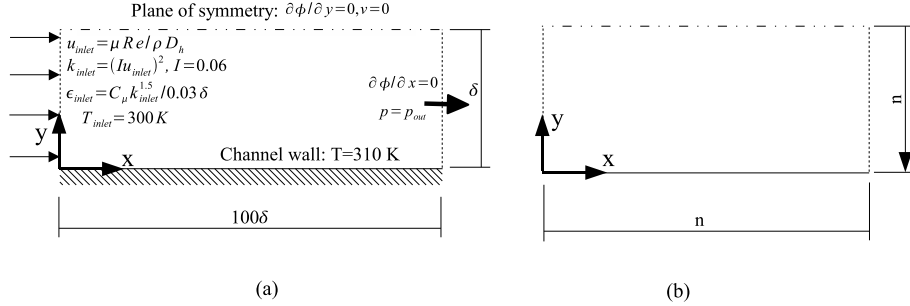
## 3.4 Plane channel flow

### 3.4.1 Problem definition

This flow constitutes one of the most basic confined cases due to its simplicity and parabolic flow structure, where the shear stress is the most important characteristic. Some examples of works found in literature studying channel flow are herewith summarized. Heyerichs [23] studied several turbulence models in a channel at high Reynolds and presented results for Nusselt number, skin-friction coefficient and log-law for dimensionless stream velocity. Craft et al. [11] applied their model to a channel with two Reynolds numbers, and compared it with results from DNS. Apsley et al. [24] first used the NLEVM model in a channel, and Moser [2] studied the channel by means of DNS for the same Reynolds numbers considered in this study.

In general, this flow is used as a basic case to check the correct implementation or to fit the constants of turbulence models. Three different friction Reynolds numbers based on half channel height and friction velocity $(u_\tau)$, are herewith selected: $Re_\tau = 180$, $Re_\tau = 395$ and $Re_\tau = 590$. The fluid is air $(Pr = 0.71)$.

In Figure 3.1(a), the physical domain and boundary conditions are shown. The Reynolds number $(Re_{Dh})$ based on hydraulic diameter $(D_h)$ and inlet mean velocity $(u_{in})$ is calculated using $Re_\tau \approx 0.09 Re_{Dh}^{0.88}$ [1]. The specific turbulent kinetic energy dissipation $(\omega_{in})$ is evaluated from $\epsilon_{in}$ with the relation $\omega_{in} = \epsilon_{in}/\beta^* k_{in}$ (where $\beta^*$ is a model constant). At the exit, a pressure outflow boundary condition is imposed, and a null gradient in $x$-direction of scalar variables $(T, k, \epsilon$ or $\omega)$ is assumed.

**Figure 3.1:** Channel flow test case. (a) Geometry and boundary conditions. (b) Computational domain, number of control volumes ($n$), and mesh distribution in $x$ and $y$ directions. Solid triangle indicates direction of mesh concentration.

| | **Channel flow** | | | | | | | | |
| --- | --- | --- | --- | --- | --- | --- | --- | --- | --- |
| | $u^* = u/u_{in}$ | | | $k^* = k/k_{in}$ | | | $T^* = T/T_{in}$ | | |
| grids | $Rn$ | $p$ | $GCI^*$ | $Rn$ | $p$ | $GCI^*$ | $Rn$ | $p$ | $GCI^*$ |
| $n$ | [%] | | [%] | [%] | | [%] | [%] | | [%] |
| 20/40/80 | 98 | 1.5 | 1.5e-01 | 96 | 1.6 | 3.3e+00 | 98 | 1.4 | 2.2e+00 |
| 40/80/160 | 97 | 1.7 | 4.8e-02 | 96 | 1.8 | 9.2e-01 | 97 | 1.6 | 6.0e-01 |
| 80/160/320 | 89 | 1.7 | 2.7e-02 | 93 | 1.9 | 2.5e-01 | 93 | 1.6 | 3.1e-01 |

**Table 3.1:** Grid refinement study. $Re_\tau = 590$ and IL model. Richardson nodes ($R_n$), global order of accuracy ($p$) and global uncertainty ($GCI^*$). The global uncertainty is normalized using all of the inlet values.

### 3.4.2 Verification

Although the $h-refinement$ study has been carried out for all models and Reynolds numbers, only results for the IL ($k\epsilon$-LEVM) model at $Re_\tau = 590$ using upwind scheme for convective terms are presented in Table 3.1. The grid distribution is shown in Figure 3.1(b). The number of control volumes is represented by the parameter $n$, e.g. when $n = 40$ it expresses the problem is solved on 40x40 control volumes (cv's). The mesh is intensified near solid wall, which is indicated in the figure with a solid triangle. The grids employed for verification correspond to $n = 20$, 40, 80, 160 and 320. Taking advantage of symmetry, only half of the channel is simulated.

As can be observed in Table 3.1, the Richardson nodes are sufficiently large for the three estimations shown (more than 88%). The observed order of accuracy $p$ also

| Channel flow. | | | | | | |
|---|---|---|---|---|---|---|
| | $Re_\tau = 180$ | | $Re_\tau = 395$ | | $Re_\tau = 590$ | |
| Model | $Nu$ | % | $Nu$ | % | $Nu$ | % |
| Correlation | 35.00 | - | 71.40 | - | 102.97 | - |
| IL | 30.54 | -12.74 | 64.55 | -9.59 | 93.48 | -10.14 |
| GPC | 38.87 | 11.06 | 76.19 | 6.71 | 107.82 | 5.18 |
| CLS | 30.66 | -12.40 | 66.28 | -7.17 | 96.05 | -7.39 |
| AMGS | 35.42 | 1.20 | 70.42 | -1.37 | 101.06 | -2.04 |
| WX | 40.42 | 15.48 | 72.26 | 1.20 | 108.84 | 5.7 |
| WXT | 42.11 | 20.31 | 78.23 | 9.56 | 108.66 | 5.52 |
| WXCD | 39.27 | 12.20 | 75.33 | 5.50 | 105.26 | 2.22 |
| LAR | 36.18 | 3.37 | 68.90 | -3.5 | 97.16 | -5.64 |
| ARG | 39.82 | 13.77 | 73.42 | 2.83 | 106.22 | 3.15 |
| WJO | 42.43 | 21.22 | 79.46 | 11.28 | 110.06 | 6.88 |
| AJL | 41.47 | 18.48 | 81.39 | 13.99 | 115.27 | 11.94 |

**Table 3.2:** Validation. Nusselt number and relative discrepancy with empirical correlation [25].

agrees with its theoretical value, from 1 to 2, considering the upwind scheme and the almost parallel flow structure. The reduction from mesh to mesh of GCI values shows a tendency to an asymptotic value (i.e. a grid independent solution). Similar results are observed for the other models and Reynolds number. Therefore, they are not presented. The SMART scheme has also been used obtaining a similar accuracy. According to this study, the fourth grid is used in the comparative study.

### 3.4.3 Validation and comparative study

For a detailed comparison of both the mean velocity and the turbulent stresses, the turbulence models tested are validated with DNS results obtained by Moser et al. [2]. The mean Nusselt number $Nu$ is compared versus Dittus-Bolter correlation ($Nu = 0.023Re_{Dh}^{0.8}Pr^{0.4}$) (cited in [25]). Moreover, the skin-friction factor $C_f$ is compared in the fully developed region and is obtained from: $1 = 2\sqrt{C_f}[2log(2Re_{Dh}\sqrt{C_f}) - 0.8]$ (cited in [25]).

Results for $Nu$ and $C_f$ are presented in Table 3.2 and Table 3.3 respectively. In

| Channel flow. | | | | | | |
|---|---|---|---|---|---|---|
| | $Re_\tau = 180$ | | $Re_\tau = 395$ | | $Re_\tau = 590$ | |
| Model | $C_f x 10^3$ | % | $C_f x 10^3$ | % | $C_f x 10^3$ | % |
| Correlation | 7.484 | - | 5.994 | - | 5.390 | - |
| IL | 7.210 | -3.66 | 5.774 | -3.67 | 5.283 | -1.98 |
| GPC | 8.629 | 15.29 | 6.820 | 13.78 | 6.034 | 11.94 |
| CLS | 7.478 | -0.08 | 5.953 | -0.68 | 5.379 | -0.20 |
| AMGS | 7.950 | 6.22 | 6.331 | 5.62 | 5.695 | 5.65 |
| WX | 8.967 | 19.81 | 6.867 | 14.56 | 6.075 | 12.71 |
| WXT | 9.311 | 24.41 | 6.974 | 16.34 | 6.126 | 13.65 |
| WXCD | 8.783 | 17.36 | 6.771 | 12.96 | 5.943 | 10.26 |
| LAR | 8.083 | 8.00 | 6.156 | 2.70 | 5.434 | 0.82 |
| ARG | 8.839 | 18.10 | 6.541 | 9.12 | 5.948 | 10.35 |
| WJO | 9.294 | 24.18 | 7.056 | 17.72 | 6.134 | 13.80 |
| AJL | 8.717 | 16.47 | 6.672 | 11.31 | 5.892 | 9.31 |

**Table 3.3:** Channel flow. Validation. Skin-friction coefficient and relative discrepancy with empirical correlation [25].
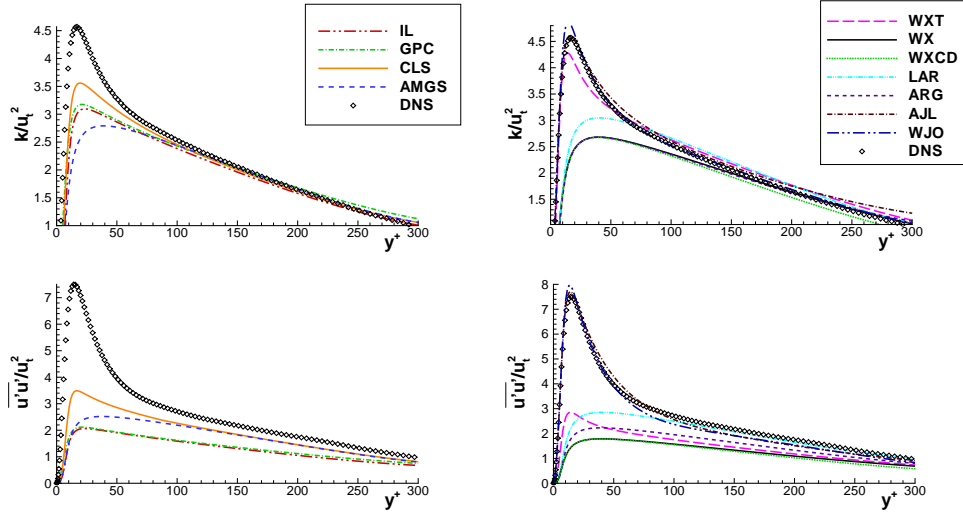
general, LEVM, NLEVM and EARSM exhibit a proper performance compared to the empirical correlations. Only GPC ($k\epsilon$-LEVM), WX ($k\omega$-LEVM), WXT ($k\omega$-LEVM) and WJO ($k\omega$-EARSM) models show poor solutions for $C_f$. The best results for $C_f$ are obtained with CLS ($k\epsilon$-NLEVM) model.

The Nusselt number is better predicted by AMGS ($k\epsilon$-EARSM) model followed by LAR ($k\omega$-NLEVM) model. Thus, comparing these parameters in this configuration, NLEVM and EARSM perform better than LEVM. Nevertheless, the model that most accurately predicts the $C_f$ is not the same as the one which better predicts the $Nu$.

Dimensionless turbulent kinetic energy ($k$) and turbulent normal stream-wise stress maps ($\overline{u'u'}$) for $Re_\tau = 395$ are plotted in Figure 3.2. Results are compared to DNS data [2]. The AJL ($k\omega$-NLEVM) model gives the most accurate prediction of $k$ peak. WJO ($k\epsilon$-NLEVM) and WXT ($k\omega$-LEVM) model also show reasonable results for this variable, while the rest of models under-predict it. This deficiency is more evident in the region near the wall ($y^+ < 70$) for all Reynolds numbers, in the case of WX ($k\omega$-LEVM), WXCD ($k\omega$-LEVM) ARG ($k\omega$-EARSM) and AMGS ($k\epsilon$-EARSM) models.

However, as can be seen in Figures 3.2 and 3.3, proper results for $k$ not always mean
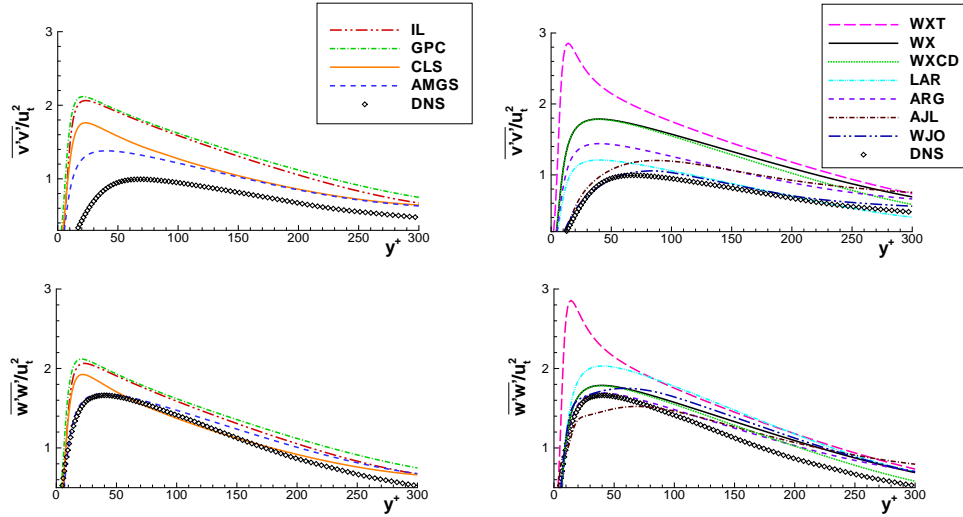
**Figure 3.2:** Channel flow. Turbulent kinetic energy and normal Reynolds stress in $x$ direction $Re_\tau = 395$.

an adequate prediction of normal turbulent stresses. This is more notable in the case of LEVM models. As consequence of the isotropy assumption, they incorrectly predict similar profiles for all of them. Such situation is clearly illustrated in the WXT ($k\omega$-LEVM) model. It gives an adequate level for the turbulent kinetic energy and tends to reproduce the $\overline{u'u'}$ peak. Nevertheless, it poorly predicts $\overline{v'v'}$ and $\overline{w'w'}$. A superior accomplishment of the WXT ($k\omega$-LEVM) model for $k$ and $\overline{u'u'}$ is darkened with its poor performance in the estimation of the other normal stresses. On the other hand, models using a higher order constitutive relation, such as AJL ($k\omega$-NLEVM) or WJO ($k\omega$-EARSM), predict correctly these stresses. This, as result of the predicted anisotropy level. Therefore, taking these results into account, the use of NLEVM and EARSM is beneficial.

When NLEVM are compared with EARSM, it is important to keep in mind that the first ones are tuned for this kind of flows. Thus it is expected that they perform adequately. Nevertheless, neither CLS ($k\epsilon$-NLEVM) nor LAR ($k\omega$-NLEVM) model properly reproduce any turbulent normal stress. Therefore, empirical coefficients in the constitutive relation should be adjusted to predict higher anisotropy levels in these models.

In addition, it is remarkable that EARSM lead to acceptable results with only one damping function, whereas the other models require up to four ($f_\mu$, $f_2$, E and D)

83

**Figure 3.3:** Channel flow. Normal Reynolds stresses in $y$ and $z$ directions $Re_\tau = 395$.

when $k - \epsilon$ platform is used.
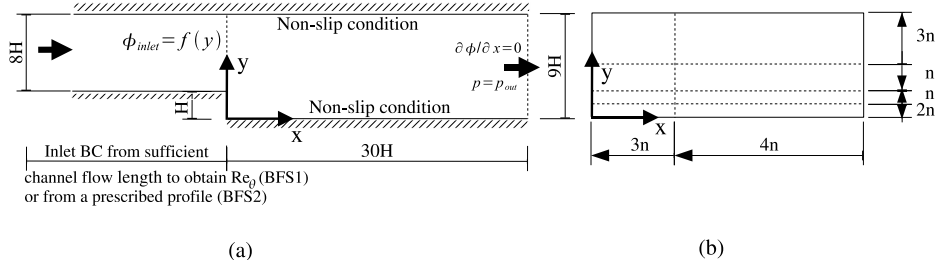
## 3.5 Backward facing step flow (BFS)

### 3.5.1 Problem definition

This configuration is usually used to compare the performance of turbulence models for recirculating, re-attaching and separated turbulent boundary-layer flows. Moreover, it includes shear-layer mixing process and a region with adverse pressure gradient.

Several experimental studies have been reported in the last decades. For example, those carried out by Eaton and Johnston [26], Vogel and Eaton [27], Kim et al. [28] and Driver and Seegmiller [3]. Most of them have then been numerically simulated. For example, Heyerichs and Pollard [23] studied the configuration of Vogel and Eaton [27], and presented results for global parameters i.e. Nusselt and Stanton number for several LEVM. Park et al. [29] applied a new model to this case and compared mean velocity, normal turbulent stresses at two positions and skin friction coefficient along step wall. Thangam et al. [30] used the experimental data by Kim et al. [28] to evaluate standard k-$\epsilon$ and NLEVM models with different approaches near solid walls.

(a)

(b)

**Figure 3.4:** Backward facing step flow (BFS). (a) Geometry and boundary conditions. (b) Computational domain, number of cv's $(n)$, and mesh distribution in $x$ and $y$ directions. Solid triangles indicate direction of mesh concentration.

They presented results for mean velocity, shear stress and global variables.

The experimental configuration by Driver and Seegmiller [3], hereafter referred as BFS1, is studied in this work. The expansion ratio (outlet/inlet height) is 1.125. The inlet boundary conditions $(u_{in}(y), v_{in}(y), k_{in}(y), \epsilon_{in}(y)$ or $\omega_{in}(y))$ correspond to the numerical solution of a channel flow at the section where $Re_\theta = 5000$ (where $Re_\theta$ is the Reynolds number based on momentum thickness). The turbulence model used to generate the above mentioned inlet boundary condition was the IL-LEVM for $k - \epsilon$ models and WXT-LEVM for $k - \omega$ based models. At the exit a pressure outflow boundary condition is imposed (see Figure 3.4(a) for details). The free stream velocity in the channel, $u_{ref} = 44.2m/s$, is used for non-dimensionalization purposes.

In this flow, inlet boundary condition is crucial for the development of the recirculation zone and, as a consequence, for a critical evaluation and comparison of turbulence models. Therefore, in [31] a study has been carried out to compare different options to obtain it.

Furthermore, the experimental setup used by Vogel and Eaton [27] is analysed here for a Reynolds number based on step height of $Re_H = 28000$ (hereafter referred as BFS2). Geometry and boundary conditions are imposed according to [23]. The inlet boundary condition corresponds to a boundary layer with $\delta/H = 1.1$, $u_{in} = u_{ref}(y/\delta)^{1/7.05}, v_{in} = 0, k_{in} = C_\mu^{-0.5}l^2(\partial u_{in}/\partial y)^2, l = min[\kappa y, 0.09\delta], \epsilon_{in} = C_\mu k^2(l^2\partial u_{in}/\partial y)^{-1}$ and $T_{in} = 300K$. For values of $y > \delta$, $u_{in} = u_{ref} = f(Re_H), v_{in} = 0, k_{in} = 1.5(Iu_{ref})^2, \epsilon_{in} = C_\mu k_{in}^{1.5}/(0.09\delta)$ and $T_{in} = 300K$ are imposed. With $H$ being the step height, subscript $_{in}$ inlet value, $\kappa$ the von Karman's constant $= 0.41$, Non-slip condition and $q_w = 270W/m^2$ are used at the bottom wall, and at the top boundary main stream values are fixed.

85

### 3.5.2   Verification

Results of the *h-refinement* study for $u$, $v$ and $k$ are presented in Table 3.4 for BFS1. Convective terms of eq. 2.7 and 2.8 are discretized with SMART scheme while in eq. 2.69, 2.70 and 2.71 power law scheme is used.

For this case the grid is represented by the parameter $n$ (number of cv's) in Figure 3.4(b). The mesh has been intensified near the solid walls and the step, as it is indicated with solid triangles in the figure. Five grids have been used $n = 3$, 6, 12, 24 and 48 (i.e. meshes of 21x21, 42x42, 88x88, 176x176 and 352x352 cv's respectively). For these meshes, the first node nearest to the wall is located at $y^+ = 12$, 6.5, 3.8, 1.2 and 0.6 respectively (with $y^+$ being dimensionless distance to the nearest wall). Also, for completeness, some models are applied using a sixth mesh of $n = 96$ (704x704 cv's). All models exhibit similar trends and only three of them are herewith presented.

The number of Richardson nodes (Rn) in the last two set of grids is over 80%. The order of accuracy (p) is also within the expected theoretical range when the mentioned schemes are used in reattaching flows. However, some exceptions have been found for the set of grids with $n = 6/12/24$, and are explained below. Furthermore, the first set of meshes ($n = 3/6/12$) has displayed neither an adequate *Rn* nor a *p*.

The results from the second set of grids reflect the importance of $y^+$ parameter (dimensionless distance to the nearest wall) in the correct performance of the models, specially of LEVM using $k - \omega$ platform. Due to the boundary condition used for these models, $y^+$ corresponding to the first inner node from the wall should be lower than 2.5 [6]. The grids with $n = 3$, 6 and 12 are above this limit, while the fourth mesh ($n = 24$) presents a $y^+$ below it. Thus, there is an oscillation between results of these grids and the asymptotic behavior is broken. A similar trend is observed in $k - \epsilon$ models, although their boundary condition for solid walls shows less sensitivity to this distance.

Summarizing, it is found that the uncertainty due to discretization ($GCI$) for the last grid ($n = 48$) is small enough as to consider its results as credible. Thus, the fifth mesh is used for comparative purposes.

| Backward facing step flow (BFS1). | | | | | | | | | |
|---|---|---|---|---|---|---|---|---|---|
| CLS model | | | | | | | | | |
| | u*=u/$u_{in}$ | | | v*=v/$u_{in}$ | | | k*=k/$k_{in}$ | | |
| grids | $Rn$ | $p$ | $GCI^*$ | $Rn$ | $p$ | $GCI^*$ | $Rn$ | $p$ | $GCI^*$ |
| $n$ | [%] | | [%] | [%] | | [%] | [%] | | [%] |
| 3/6/12 | 45 | 0.1 | 7.2e+00 | 49 | 0.6 | 2.5e-01 | 74 | 1.2 | 2.3e+01 |
| 6/12/24 | 90 | 0.5 | 5.2e-01 | 87 | 0.6 | 1.0e-01 | 87 | 1.1 | 1.2e+01 |
| 12/24/48 | 96 | 1.2 | 7.7e-02 | 93 | 1.2 | 2.0e-02 | 94 | 1.4 | 3.3e+00 |
| WX model | | | | | | | | | |
| | u*=u/$u_{in}$ | | | v*=v/$u_{in}$ | | | k*=k/$k_{in}$ | | |
| grids | $Rn$ | $p$ | $GCI^*$ | $Rn$ | $p$ | $GCI^*$ | $Rn$ | $p$ | $GCI^*$ |
| $n$ | [%] | | [%] | [%] | | [%] | [%] | | [%] |
| 3/6/12 | 54 | 0.7 | 1.8e+00 | 52 | 1.0 | 1.4e-01 | 88 | 2.9 | 1.8e+01 |
| 6/12/24 | 87 | 0.9 | 6.1e-01 | 82 | 0.6 | 1.7e-01 | 90 | 1.7 | 1.8e+01 |
| 12/24/48 | 93 | 1.5 | 9.9e-02 | 91 | 1.3 | 2.9e-02 | 93 | 1.8 | 4.9e+00 |
| 24/48/96 | 92 | 2.3 | 1.1e-02 | 93 | 2.3 | 2.7e-03 | 92 | 2.4 | 4.3e-01 |
| LAR model | | | | | | | | | |
| | u*=u/$u_{in}$ | | | v*=v/$u_{in}$ | | | k*=k/$k_{in}$ | | |
| grids | $Rn$ | $p$ | $GCI^*$ | $Rn$ | $p$ | $GCI^*$ | $Rn$ | $p$ | $GCI^*$ |
| $n$ | [%] | | [%] | [%] | | [%] | [%] | | [%] |
| 3/6/12 | 57 | 0.4 | 2.9e+00 | 56 | 0.8 | 3.2e-01 | 89 | 3.0 | 1.0e+01 |
| 6/12/24 | 89 | 1.5 | 2.0e-01 | 84 | 1.0 | 7.7e-02 | 91 | 1.9 | 6.9e+00 |
| 12/24/48 | 91 | 1.8 | 4.5e-02 | 92 | 1.6 | 1.6e-02 | 88 | 1.9 | 2.1e+00 |

**Table 3.4:** Results from grid refinement study. Richardson nodes ($R_n$), global order of accuracy ($p$) and global uncertainty ($GCI^*$). The global uncertainty is normalized using inlet values.

For BFS2 a similar grid to that of BFS1 is used, but instead of the mesh concentration applied in BFS1 near the top wall, a uniform distribution is occupied in BFS2. For this case an analogous $h-refinement$ procedure is also applied. Results of the the study are correct and comparable to those of BFS1. For example, for the set of meshes with $n = 6$, 12 and 24 using WXT ($k\omega$-LEVM) a number of $R_n > 75\%$ is achieved for all variables. Furthermore, $GCI's$ values of 1.5%, 0.48% and 0.84% are obtained for velocity, temperature and turbulent kinetic energy respectively. Therefore, extensive results of the $h-refinement$ study for BFS2 are not included in this work.

### 3.5.3   Validation and comparative study

**Reattachment point**

One of the common quantities used to evaluate the performance of a turbulence model in the backward-facing step configuration, is the reattachment length of the flow separation $(X_r/H)$.

For BFS1, Table 3.5 shows that LEVM under-predicts the reattachment point, with

| BFS1. | | | | |
|---|---|---|---|---|
| Models | $X_r/H$ | % | $C_f$min.x$10^3$ | % |
| Driver [3] | 6.26±0.1 | - | 1.02 | - |
| IL | 5.85 | -6.55 | 1.612 | 58.04 |
| GPC | 6.13 | -2.08 | 1.405 | 37.74 |
| CLS | 6.54 | 4.47 | 1.275 | 25.00 |
| AMGS | 6.89 | 10.06 | 1.603 | 57.16 |
| WX | 5.87 | -6.23 | 1.244 | 21.96 |
| WXT | 6.28 | 0.319 | 1.151 | 12.84 |
| WXCD | 6.19 | -1.12 | 1.248 | 22.35 |
| LAR | 6.46 | 3.19 | 0.862 | -15.49 |
| ARG | 6.32 | 0.895 | 1.081 | 5.98 |
| WJO | 6.55 | 4.63 | 0.978 | -4.12 |
| AJL | 6.05 | -3.35 | 0.967 | -5.19 |

**Table 3.5:** Validation. Reattachment point $(X_r/H)$ and minimum skin-friction $(C_f$min) coefficient. Relative discrepancy (%) with experimental data.

the exception of WXT ($k\omega$-LEVM) model. The shortest length is exhibited by the IL ($k\epsilon$-LEVM) model. Otherwise, the $X_r/H$ calculated with NLEVM and EARSM is a bit longer than experimental data. Due to the under-prediction of turbulence levels in the separated shear layer, AMGS ($k\epsilon$-EARSM) model presents the largest value. Thus, the generation term in equation 2.70 should be increased for a better behavior of this model in flows with adverse pressure gradients. This conclusion has also been found by other authors [22, 24].

For BFS2, results of $X_r/H$ are presented in Table 3.6. Observing this quantity is seen that higher order models do not improve linear models results. NLEVM and EARSM predict an excessively long recirculation region [27]. Furthermore, this overestimation is more evident in $k - \epsilon$ based models, giving an idea about the low level of turbulent mixing predicted by these models in this case.
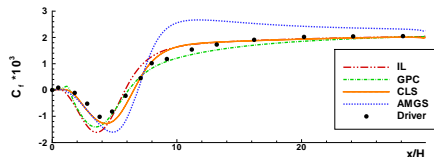
| BFS2 | | | | |
|------|------|------|------|------|
| Models | $X_r/H$ | % | $C_f$min.x$10^3$ | % |
| Vogel [27] | 6.67 | - | 1.14 | - |
| IL | 7.42 | 11.2 | 1.77 | 55.3 |
| GPC | 7.46 | 11.8 | 1.55 | 36.0 |
| CLS | 8.68 | 30.1 | 1.38 | 21.1 |
| AMGS | 8.34 | 25.1 | 1.67 | 46.5 |
| WX | 6.73 | 0.90 | 1.43 | 25.4 |
| WXT | 7.71 | 15.6 | 1.25 | 9.6 |
| WXCD | 7.47 | 12.0 | 1.37 | 20.2 |
| LAR | 7.87 | 18.0 | 0.98 | -14.0 |
| ARG | 7.31 | 9.6 | 1.19 | 4.38 |
| WJO | 8.26 | 23.8 | 1.06 | -7.0 |
| AJL | 7.69 | 15.3 | 1.02 | -10.5 |
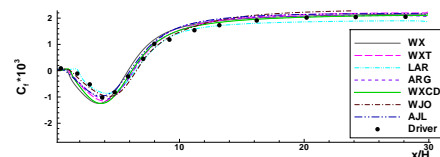
**Table 3.6:** Validation. Reattachment point $(X_r/H)$ and minimum skin-friction $(C_f$min) coefficient. Relative discrepancy (%) with experimental data.

**Minimum skin-friction coefficient**

Reviewing the differences of the minimum skin-friction coefficient $(C_{fmin})$ obtained respect to the experimental data, the superiority and advantages of using higher order terms in the constitutive relation is clear (see Table 3.5 for BFS1 and Table 3.6 for BFS2). For example, and considering $k - \epsilon$ platform, CLS ($k\epsilon$-NLEVM) model gives better results than IL ($k\epsilon$-LEVM) model in both configurations. Moreover, in the case of $k - \omega$ platform, all models using a high order relation predict the minimum more accurately than WX ($k\omega$-LEVM) model, which is their linear counterpart.
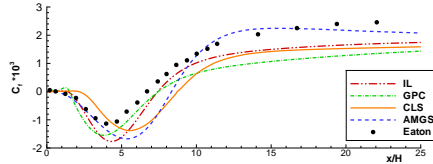


**Figure 3.5:** BFS1. Skin-friction coefficient for $k - \epsilon$ models.
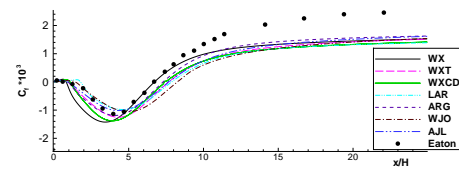


**Figure 3.6:** BFS1. Skin-friction coefficient for $k - \omega$ models.

**Skin friction coefficient at the bottom wall**

Figures 3.5 and 3.6 present the comparison of skin-friction coefficient ($C_f$) at the bottom wall with the experimental data [3] for BFS1. Moreover, for BFS2 it is plotted in Figures 3.7 and 3.8. $C_f$ is usually related with the near-wall characteristics of the turbulence model used. In general, the influence of using higher order terms are more notorious in $k - \epsilon$ than in $k - \omega$ models (see Figures 3.5 and 3.7). Furthermore, $k - \omega$ models have outperformed $k - \epsilon$ ones, which is expected due to the better performance of the $\omega$-based models near solid walls. However, the last ones underestimate $C_f$ downstream the redeveloping region in BFS2. Good accordance with the results for the LEVM presented in [23] is shown here for this configuration, i.e. WXT ($k\omega$-LEVM) and IL ($k\epsilon$-LEVM) models.



**Figure 3.7:** BFS2. Skin-friction coefficient for $k - \epsilon$ models.



**Figure 3.8:** BFS2. Skin-friction coefficient for $k - \omega$ models.

**Stanton number bottom wall**
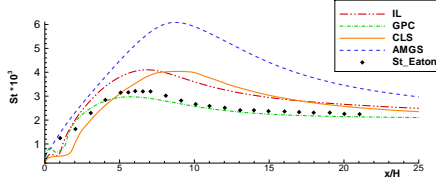
Stanton number (St) is chosen to evaluate turbulence models performance for the estimation of the heat transfer in BFS2. St profiles together with the corresponding experimental data [27] are presented in Figures 3.9 and 3.10. All $k - \omega$ models show good agreement with measurements. Otherwise, $k - \epsilon$ models predict dispersed results, being GPC ($k\epsilon$-LEVM) the only model capable of reproducing the experiment [27]. Thus, based on the view of Figures 3.9 and 3.10, benefits of using NLEVM or EARSM are rather limited for this case.

**Mean velocity BFS1**
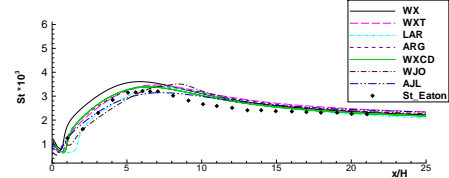
The predicted mean stream-wise velocity profiles at different cross-sections are shown in Figure 3.11 along with experimental results [3]. The numerical profiles estimated by all models seem to be in agreement with the data, except at the bottom wall near the reattachment point.

The $k - \omega$ linear models somewhat depart from experimental data away the wall.
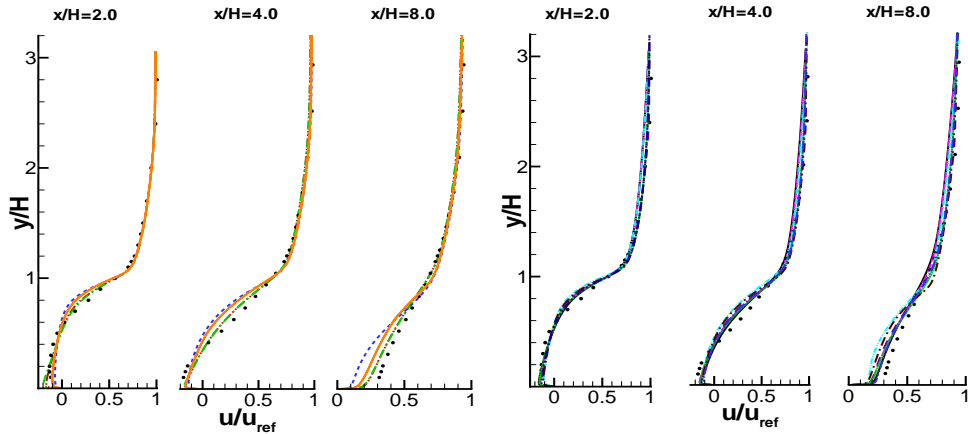
**Figure 3.9:** BFS2. Stanton number for $k - \epsilon$ models.
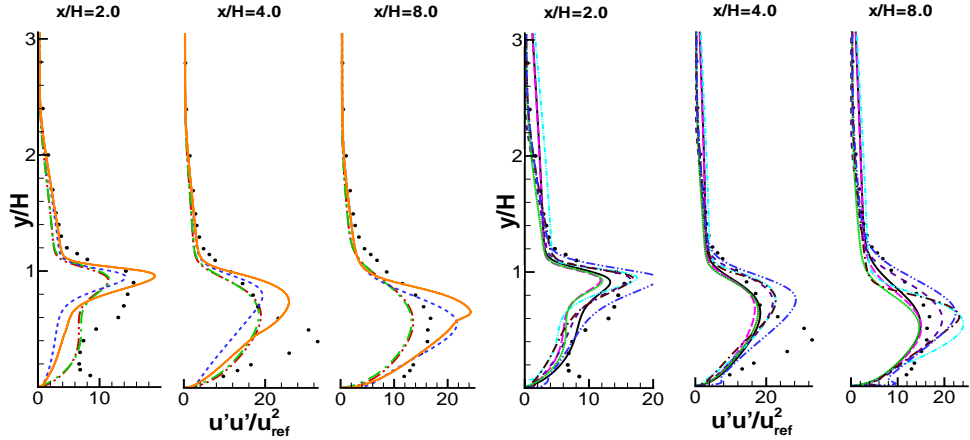


**Figure 3.10:** BFS2. Stanton number for $k - \omega$ models.

This departure is larger in the recovery region. Only ARG ($k\omega$-EARSM) reproduces experimental results correctly.

In the redeveloping zone AMGS ($k\epsilon$-EARSM) and LAR ($k\omega$-NLEVM) models present some deviations. These differences remain downstream. Therefore, reviewing this quantity, it can be said there is an inappreciable improvement with the use of higher order terms.



**Figure 3.11:** BFS1. Dimensionless streamwise velocity profiles, left $k - \epsilon$ models - ·· - IL, - · - GPC, — CLS, - - - AMGS, right $k - \omega$ models — WX,– – – WXT, · · · WXCD, - ·· - LAR(cyan), - - - ARG, - · - WJO, - ·· - AJL (blue) and symbols experiments [3].

91

**Figure 3.12:** BFS1. Dimensionless streamwise turbulent stress profiles, left $k - \epsilon$ models - ·· - IL, - · - GPC, —-CLS, - - - AMGS, right $k - \omega$ models —- WX,– – – WXT, · · · WXCD, - ·· - LAR, - - - ARG, - · - WJO, - ·· - AJL (blue) and symbols experiments [3].

**Turbulent stresses BFS1**
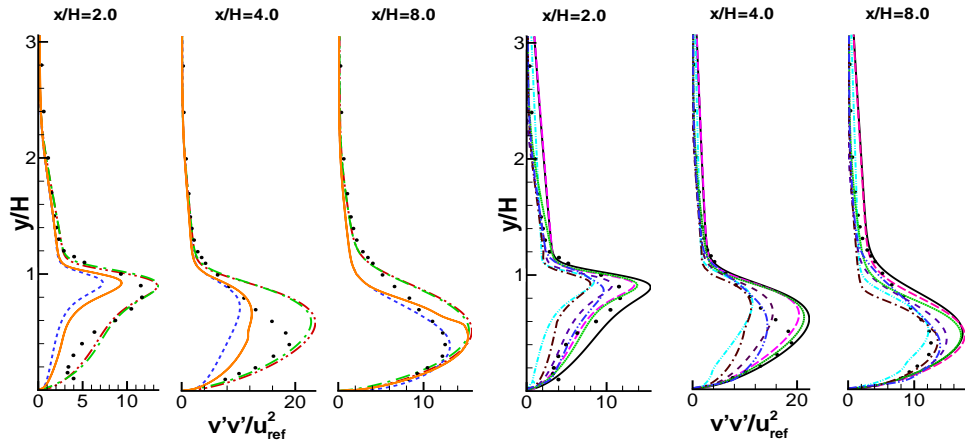
When normal Reynolds stresses are analyzed, remarkable differences between models and experimental results are found (see Figures 3.12 and 3.13). LEVM models erroneously predict a value for $\overline{v'v'}$ larger than for $\overline{u'u'}$. This trend is corrected by NLEVM and EARSM models, presenting at least qualitatively correct results due to the addition of higher order terms. Furthermore, Reynolds stresses predictions show that the addition of these terms in the constitutive relation tends to increase $\overline{u'u'}$, but have less effect on the shear stress. Thus, analyzing these variables the use of NLEVM or EARSM is important. Also, it is worth to note that the inclusion of cross-diffusion term (see Appendix A) in WXCD ($k\omega$-LEVM) model improves Reynolds stresses predictions far from the bottom wall.

## 3.6 Impinging slot jet flow

### 3.6.1 Problem definition

In spite of its simple geometry, the impinging slot jet presents a complex flow structure with stagnation, recirculation and adverse pressure regions. This case has been chosen
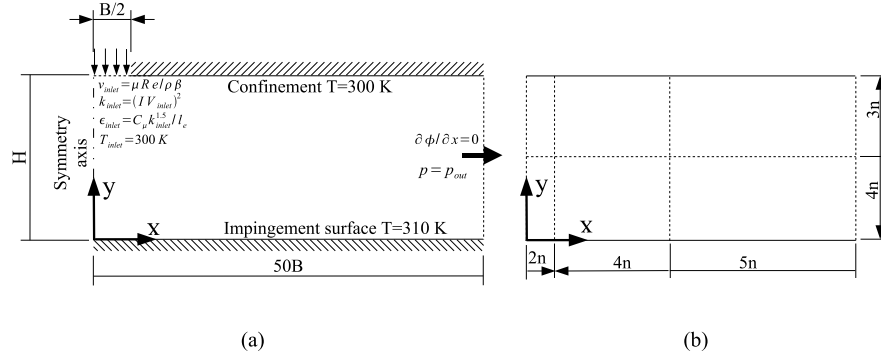
**Figure 3.13:** BFS1. Dimensionless $y$-direction turbulent stress profiles, left $k - \epsilon$ models - ·· - IL, - · - GPC, —- CLS, - - - AMGS, right $k - \omega$ models —- WX,– – – WXT, · · · WXCD, - ·· - LAR, - - - ARG - · - WJO, - ·· - AJL (blue) and symbols experiments [3].

to investigate the performance of the models in the presence of normal straining (the flow in the stagnation region is nearly irrotational and a large strain along streamlines is produced) [11, 24].

Experimental studies for thermal field have been carried out by Gardon and Akfirat [32] and Van Heiningen [4], among others, for several Reynolds numbers.

Numerical studies were published by Heyerichs et al. [23] and Wang et al. [33], who examined an impinging slot jet at a Reynolds number of 10000 based on nozzle width and bulk velocity. Seyedin et al. [34] performed other work for various Reynolds numbers and nozzle-to-impingement surface spacing (H/B) ratios. More recently, Shi et al. [35] studied the effect of inlet conditions over the heat transfer.

In this work a single turbulent confined impinging air slot jet is numerically studied at $Re_B = 10200$ and $H/B = 2.6$ ($B$ is the nozzle width and $H$ is the height of jet discharge above plate)[4]. Inlet vertical velocity ($V_{in}$) is obtained from the Reynolds number value. Turbulent kinetic energy ($k_{in}$) is calculated with an intensity of $I = 0.02$, and the characteristic length used to determine the turbulent kinetic energy dissipation rate ($\epsilon_{in}$) at inlet is $l_e = 0.015 * B$. No-slip condition is imposed at solid walls. At the exit, a pressure boundary condition is used (see Figure 3.14(a) for details). These boundary conditions are the same as the ones used by Heyerichs et al. [23].

93

**Figure 3.14:** Impinging jet. (a) Geometry and boundary conditions. (b) Computational domain, number of cv's ($n$), and mesh distribution in $x$ and $y$ directions. Solid triangles indicate direction of mesh concentration.

### 3.6.2  Verification

Results obtained using the verification procedure based on the Richardson extrapolation are shown in Table 3.7. Details of the number of grid nodes (represented by the parameter $n$) and mesh concentration are given in Figure 3.14(b). The verification study is performed with five levels (grids) of refinement: $n = 3$, 6, 12, 24, 48 (i.e. meshes of 33x21, 66x42, 132x84, 264x168 and 528x336 control volumes respectively). For these meshes, the first node nearest to the wall is located at $y^+ = 8.5$, 3.8, 1.7, 0.85 and 0.42, respectively. Due to symmetry, only half of the flow domain has been considered. For all variables central difference scheme has been used for diffusive terms and power law scheme for convective ones. Higher order schemes have not been used due to convergence difficulties in the finest grids.

For the third set of grids, $n = 12/24/48$, an asymptotic behavior with a number of Richardson nodes ($Rn$) over 70% are obtained for most of the models. The observed order of accuracy ($p$) is around the unity, which is expected when a combination of central difference and power law schemes are applied. However, for the first two sets ($n = 3/6/12$ and $n = 6/12/24$), the $p$ obtained does not fit its theoretical value. Thus, the results for these two sets can not be considered credible.

It is important to highlight that the *h-refinement* procedure is applicable as long as a smoothness and asymptotic behavior is presented, a converged solution has been reached and the variable studied is not almost zero. Two exceptions of these requirements have been found in this study:

- WX ($k\omega$-LEVM), WXT ($k\omega$-LEVM) and ARG ($k\omega$-EARSM) models: The same

| Impinging plane jet flow. | | | | | | | | | | | |
|---|---|---|---|---|---|---|---|---|---|---|---|
| IL model | | | | | | | | | | | |
| | u | | | v | | | T | | | k | |
| grid | $Rn$ | $p$ | $GCI$ | $Rn$ | $p$ | $GCI$ | $Rn$ | $p$ | $GCI$ | $Rn$ | $p$ | $GCI$ |
| $n$ | [%] | | [%] | [%] | | [%] | [%] | | [%] | [%] | | [%] |
| 12 | 75 | 0.1 | 3.0e+02 | 69 | -0.3 | 1.2e+01 | 68 | 1.2 | 6.8e+00 | 73 | 0.4 | 1.1e+01 |
| 24 | 83 | -0.8 | 1.8e+02 | 85 | 0.1 | 2.9e+01 | 77 | 0.9 | 8.7e+00 | 78 | 0.1 | 1.6e+02 |
| 48 | 85 | 0.7 | 1.3e+01 | 84 | 0.6 | 2.1e+00 | 76 | 1.1 | 5.4e+00 | 81 | 0.7 | 6.5e+00 |
| AMGS model | | | | | | | | | | | |
| | u | | | v | | | T | | | k | |
| grid | $Rn$ | $p$ | $GCI$ | $Rn$ | $p$ | $GCI$ | $Rn$ | $p$ | $GCI$ | $Rn$ | $p$ | $GCI$ |
| $n$ | [%] | | [%] | [%] | | [%] | [%] | | [%] | [%] | | [%] |
| 12 | 72 | 1.2 | 6.5e+00 | 76 | 1.0 | 9.2e-01 | 72 | 1.2 | 7.5e+00 | 70 | 1.3 | 2.0e+00 |
| 24 | 85 | 1.1 | 2.4e+00 | 68 | 1.2 | 5.1e-01 | 64 | 2.8 | 4.0e-01 | 80 | 1.6 | 4.2e-01 |
| 48 | 89 | 1.1 | 1.0e+00 | 82 | 1.1 | 2.1e-01 | 76 | 1.5 | 5.3e-01 | 83 | 1.4 | 2.4e-01 |
| ARG model | | | | | | | | | | | |
| | u | | | v | | | T | | | k | |
| grid | $Rn$ | $p$ | $GCI$ | $Rn$ | $p$ | $GCI$ | $Rn$ | $p$ | $GCI$ | $Rn$ | $p$ | $GCI$ |
| $n$ | [%] | | [%] | [%] | | [%] | [%] | | [%] | [%] | | [%] |
| 12 | 49 | 1.6 | 1.1e+00 | 43 | 1.5 | 3.4e-01 | 57 | 1.4 | 3.9e+00 | 44 | 2.6 | 2.0e-01 |
| 24 | 85 | 0.4 | 1.1e+01 | 83 | 0.3 | 3.2e+00 | 76 | 0.8 | 5.0e+00 | 86 | 0.4 | 4.8e+00 |
| 48 | 78 | 1.2 | 9.7e-01 | 74 | 1.2 | 2.8e-01 | 78 | 1.2 | 1.5e+00 | 76 | 1.2 | 5.0e-01 |

**Table 3.7:** Results from grid refinement study. Richardson nodes ($R_n$), global order of accuracy ($p$) and global uncertainty ($GCI$).
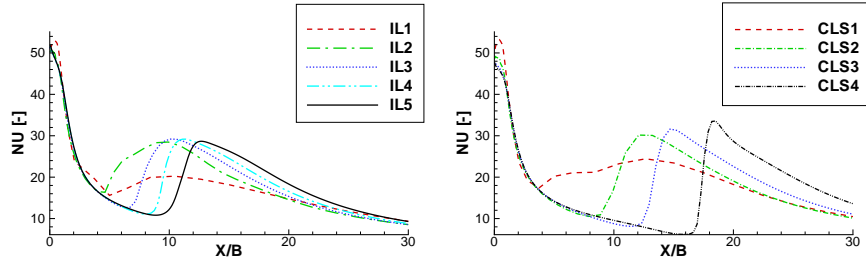
oscillatory behavior observed in BFS case is presented here in function of the $y^+$ parameter. However, as it has been pointed out, the last set ($n = 12/24/48$) presents an asymptotic behavior, making our numerical results credible and ensuring that the mathematical model is adequately solved. As the $y^+$ corresponding to the nearest grid point to the wall is also lower than 2.5, the restriction for the boundary condition imposed for $\omega$-based models is fulfilled.

- IL ($k\epsilon$-LEVM) and CLS ($k\epsilon$-NLEVM) models: Even though fine grids have been used in the simulation, IL ($k\epsilon$-LEVM) and CLS ($k\epsilon$-NLEVM) models have not shown an asymptotic behavior in this case. This is demonstrated in the results obtained when the verification procedure is applied (see Table 3.7). Moreover, results for Nusselt number are presented in Figure 3.15. It seems that the results

for the finest mesh are still far from the grid independent solution. Therefore, the finest converged grid for each model is used in the comparative study, even though asymptotic behavior has not been completely reached.

In the case of LAR ($k\omega$-NLEVM) and AJL ($k\omega$-NLEVM) models, it has not been possible to achieve a sufficiently converged solution for the finest mesh. Thus, the obtained results have not been adequately verified. For this reason, the results presented must be taken with caution for these models.

Apart from the situations explained above, Table 3.7 shows that at least the fourth mesh is necessary to ensure grid independent solution, and that the first three grids are not adequate to simulate the current case.



**Figure 3.15:** Impinging jet. Verification. Nusselt number impingement plate for different grids. Left IL model and right CLS model. - - - coarse grid; $- \cdot - \cdot -$ second grid; $\cdots$ third grid; $- \cdot \cdot - \cdot \cdot -$ fourth grid, ——— finest grid.

### 3.6.3  Validation and comparative study

In this section numerical results are compared with experimental data from Van Heiningen [4]. As mentioned previously, the same boundary conditions, as those applied by Heyerichs et al. [23] and Wang et al. [33], have been used. However, as was pointed out by Shi et al. [35] inlet conditions are critical in impinging plane jets evaluation. Thus, a study of the influence of turbulence level and different velocity profiles at the nozzle exit on Nusselt number is also carried out.
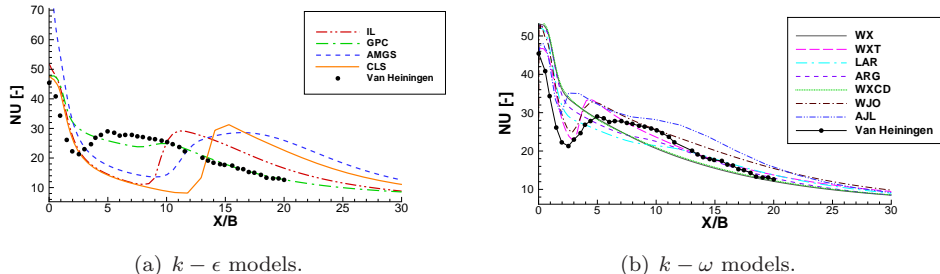
For the studied case, velocity and turbulent stresses are not reported in the experimental study; thus the analysis is restricted to the thermal field. The parameter compared is the Nusselt number at the impingement plate. The Nusselt number has been determined as: $Nu = \frac{[\partial T/\partial y]_w}{(T_w - T_{in})/B}$, where $T_w$ is the impingement plate temperature and $T_{in}$ the inlet jet temperature.

The calculated Nusselt number is presented together with experimental results in Figure 3.16(a) for $k - \epsilon$ based models and in Figure 3.16(b) for $k - \omega$ models.

**Stagnation region**

Models using $\omega$ like dissipation variable perform better than models using $\epsilon$ variable (see Figure 3.16). The model that most correctly predicts local Nusselt at stagnation point is the WXT ($k\omega$-LEVM) model (see Figure 3.16(b)), followed for the CLS ($k\epsilon$-NLEVM) model, which shows better behavior than IL ($k\epsilon$-LEVM) model and similar to GPC ($k\epsilon$-LEVM) and AJL ($k\omega$-NLEVM) models in this region (see Figures 3.16(a) and 3.16(b)). LAR ($k\omega$-NLEVM) and WJO ($k\omega$-EARSM) models come next. They predict a local Nusselt at the stagnation point closer to experiments than WX ($k\omega$-LEVM) model, which is its linear counterpart (see Figure 3.16(b)). Furthermore, results of WXCD ($k\omega$-LEVM) are nearly identical to WX ($k\omega$-LEVM) model in this zone. The worst result is exhibited by AMGS ($k\epsilon$-EARSM) model, because it is a high-Reynolds model. The same trend has been observed by Abdon [36] for LAR ($k\omega$-NLEVM) and AMGS ($k\epsilon$-EARSM) models.



(a) $k - \epsilon$ models.  (b) $k - \omega$ models.
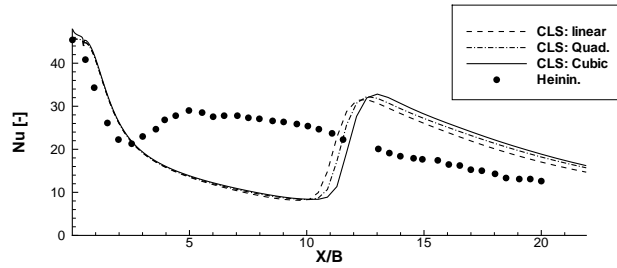
**Figure 3.16:** Impinging jet. Validation. Local Nusselt impingement plate. Lines numerical results and symbols experiments by Van Heiningen. [4].

In the stagnation region, it seems to be more important the use of extra-terms in the length scale determining equation, such as YAP correction together with adequate damping functions, rather than the relation used to evaluate the turbulent stress tensor [24, 36]. For example, Figure 3.17 shows CLS model prediction using linear, quadratic and the complete set of terms in the constitutive relation. It reveals that second and third order terms have a small influence in this region. Thus, it is shown that the results in the stagnation zone mostly depend on the coefficient ($C_\mu$, $C_\mu^*$) used in the linear term of the constitutive relation.

**Secondary maximum**

The secondary maximum is attributed to a transition phenomena [37] due to an important increment of turbulence [38, 36], three-dimensional effects or impingement of secondary eddies [37].

In this work it has been found that the second $Nu$ maximum coincides with a steep positive gradient in the turbulence level near the bottom wall for IL ($k\epsilon$-LEVM), CLS ($k\epsilon$-NLEVM) and WXT ($k\omega$-LEVM), AJL ($k\omega$-NLEVM) and WJO ($k\omega$-EARSM) models. It is also observed that GPC ($k\epsilon$-LEVM), WX ($k\omega$-LEVM), WXCD ($k\omega$-LEVM), ARG ($k\omega$-EARSM) and LAR ($k\omega$-NLEVM) models do not exhibit an enhancement of turbulence. Consequently, they do not present a secondary peak in the local Nusselt profile.



**Figure 3.17:** Impinging jet. Nusselt number for different truncation levels of non-linear constitutive relation for CLS model. - - - linear terms; $-\cdot-\cdot-$ including quadratic terms; —— complete model.

CLS ($k\epsilon$-NLEVM) and AMGS ($k\epsilon$-EARSM) models predict with delay the secondary peak of $Nu$. On the other hand AJL ($k\omega$-NLEVM) shows this peak too early. Moreover, ARG ($k\omega$-EARSM) and LAR ($k\omega$-NLEVM) models do not predict it. Only WJO ($k\omega$-EARSM) present a correct location of the peak. So, there is limited benefit in the use of higher order terms in the constitutive relation for the turbulent stresses in this zone.

Figure 3.17 shows the influence of second and third order terms in the non-linear relation using CLS ($k\epsilon$-NLEVM) model. The main difference is observed in the step gradient of the curve. Furthermore, as it is pointed out by Wilcox [9], IL ($k\epsilon$-LEVM) and CLS ($k\epsilon$-NLEVM) models employ a damping function, that can prevent, or at least delay, transition. In fact, it is observed that the critical Reynolds for $\epsilon$ may be smaller than that for $k$ for these models, which is opposed to the desired effect.

Finally, it is important to highlight that the CLS ($k\epsilon$-NLEVM) model has been applied by other authors (and lately in this thesis) [11, 22] to round impinging jets,
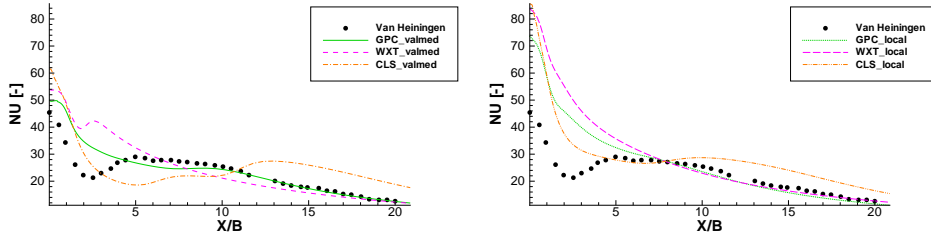
exhibiting better results that the observed in plane jets. This is probably due to three-dimensional effects, inclusion of some different parameters in $C_\mu$ and the use of an alternative formulation for YAP correction applied by Craft et al. [22]. AMGS ($k\epsilon$-EARSM) and LAR ($k\omega$-NLEVM) models have also been applied to round jets by Abdon et al. [36], and a similar behavior to that observed in slot jets is shown.

**Influence of inlet boundary conditions on Nusselt number**

For all situations studied in this part the same impinging air jet configuration has been maintained at $Re_B = 10200$ and $H/B = 2.6$. All boundary conditions have also been preserved as in figure 3.14a, but inlet boundary condition is modified in order to analyze its effect on Nusselt number. Three models are selected to carry out this study: GPC ($k\epsilon$-LEVM), WXT ($k\omega$-LEVM) and CLS ($k\epsilon$-NLEVM).

**Influence of inlet profiles**

A previous simulation of a plane channel, long enough to obtain a fully developed flow, is made. The results of this preliminary calculation are used to investigate the effect of two different profiles at the jet discharge on the local $Nu$ number. In the first study, local values of the fully developed region are interpolated to obtain the nozzle exit profiles. Whereas, in the second test a mean value of all variables in the same region is calculated. This constant value obtained is used in the current calculation for the impinging jet.



**Figure 3.18:** Impinging jet. Comparison of the Nusselt number predicted by selected models when mean (constant)(left) and local (right) values from fully developed flow are imposed at the nozzle exit. Together with experimental data by Van Heiningen [4].

Although in both situations integral values of momentum and turbulence are maintained at the same level at the nozzle exit, it is clear from Figure 3.18 that, when local

value distributions are taken into account, they change local Nusselt number profile, specially increasing it near the stagnation region. It may be due to the concentration of the jet momentum to the symmetry axis.

**Influence of length scale at the nozzle exit**
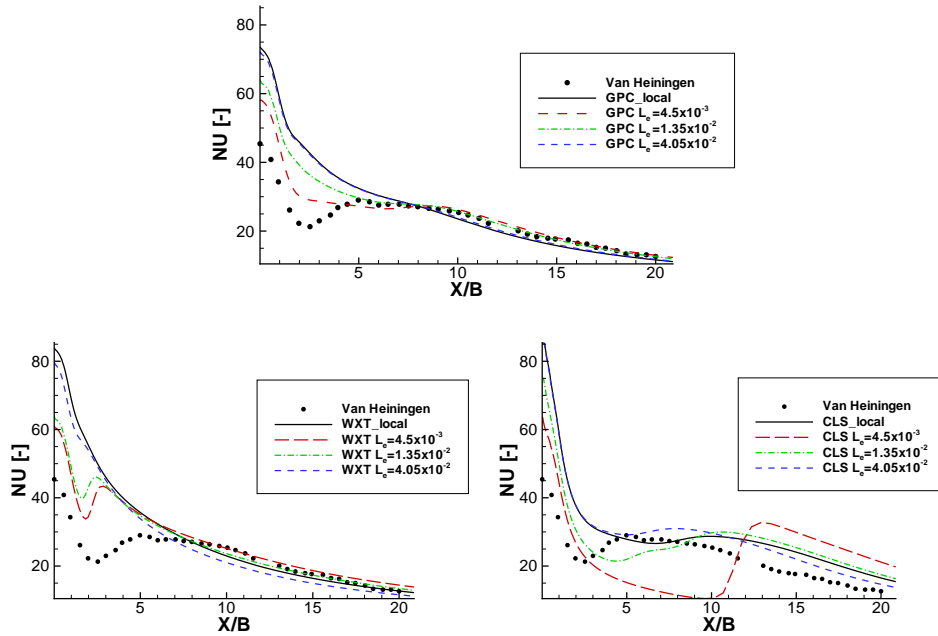
Due to the difficulty in measuring the length scale in experiments, two studies of its effect on local Nusselt number are carried out. First, local values for variables (velocities, temperature and turbulent kinetic energy) are taken from the fully developed channel region (in the same way as the previous study), but different local values for the turbulent dissipation variable are calculated like a function of the local value of $k_{in}$, and a given length scale ($l_e$), $\epsilon_{in} = C_\mu k_{in}^{1.5}/l_e$ in $k - \epsilon$ models and $\omega_{in} = k_{in}^{0.5}/l_e$ in $k - \omega$ models. The following values of $l_e = 4.5 \cdot 10^{-3}B, l_e = 1.35 \cdot 10^{-2}B$ and $l_e = 4.05 \cdot 10^{-2}B$ are considered. Results from this study are presented in Figure 3.19. It is shown that the local Nusselt increases proportionally to the length scale used to evaluate dissipation variable in the impinging region for the LEVM, and for values of $x/B \leq 10$ for the NLEVM tested.

Moreover, when a constant value for velocity and turbulent quantities is considered at the nozzle exit, i.e. $v_{in} = f(Re)$ and $k_{in} = f(v_{in}, I = 0.04)$ (see Figure 3.14a), the effect of varying the length scale on the local Nusselt number has been found to be the same as the previous one. As $l_e$ increases, the Nusselt number increases appreciably near stagnation region and downstream for $x/B < 10$. Similar results are presented by Wang et al. [33].

**Influence of turbulence intensity**

If instead of varying the length scale, it is now maintained constant at $l_e = 1.5 \cdot 10^{-2}B$, the turbulence intensity is changed from 0.01 to 0.08, and a mean value for inlet velocities is assumed, $v_{in} = f(Re)$, according to figure 3.14a. All models are sensitive to this parameter. The effect on the local Nusselt number distribution can be seen in Figure 3.20. It is observed that NLEVM and LEVM using $k - \epsilon$ or $k - \omega$ platforms present a similar behavior. Local Nusselt is increased near stagnation region and the secondary peak tends to disappear. However, some models are more sensitive to the inlet condition imposed, for example, CLS ($k\epsilon$-NLEVM) model presents a major variation near the stagnation region. The $Nu$ number in this region (and downstream) is strongly influenced by the turbulence level near the bottom wall, and in this work is observed that an important factor in the turbulence level predicted in the stagnation zone is the $y$-direction turbulent normal stress. Finally, it must be kept in mind that unlike the length scale, the turbulent intensity can be easily determined in experimental measurements.

**Figure 3.19:** Impinging jet. Effect of length scale on Nusselt number distribution with local values of variables in the inlet boundary condition. Left: WXT model. Right: CLS model.
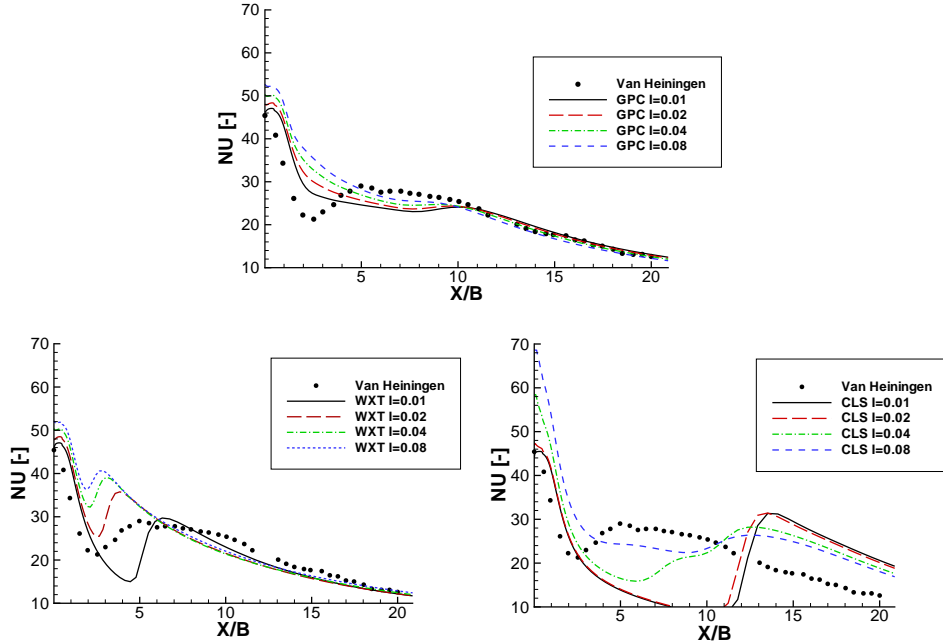
## 3.7  Conclusions

Three basic test cases have been studied using linear and non-linear eddy viscosity models (LEVM, NLEVM) and explicit algebraic Reynolds stress models (EARSM), based on $k - \epsilon$ as well as $k - \omega$ platforms.

A verification procedure has been applied in order to ensure the credibility of numerical results. In general, reasonable values for the uncertainty and the order of accuracy of the numerical solution have been obtained. Some exceptions found were analyzed in detail.

Reviewing the plane channel, which is the simplest case studied, non-linear or explicit algebraic models show reasonably good behavior. These kind of models improve results of linear models, and they do not demand a major computational effort in this configuration.

**Figure 3.20:** Impinging jet. Effect of turbulence intensity on Nusselt number distribution, all variables are considered constant at the nozzle exit. Top: GPC model. Left: WXT model. Right: CLS model.

In the case of backward facing step flow, NLEVM improve the accuracy in the predictions of skin friction coefficient and reattachment point, while the improvements in Stanton number, Reynolds stress tensor and mean velocity fields are limited. For these kind of flows, models such as CLS ($k\epsilon$-NLEVM) or ARG ($k\omega$-EARSM) should be used if a good prediction of global parameters, mean variables and qualitative turbulent stresses is desired.

Terms of higher order in the relation between turbulent stresses and mean strain rates do not improve considerably results in the impinging jet case for the models studied. Whereas the use of better tuned dumping functions and/or additional terms, such as YAP correction, in the length-scale determining equation seems to play a more important role. However, NLEVM slightly improve the predicted local Nusselt number compared with LEVM at the stagnation point.

When different turbulence intensities and velocity profiles are imposed at the inlet,

all models studied exhibit different local Nusselt distribution until a critical value of $X/B$ is achieved. Moreover, the effect of turbulence length scale at the nozzle exit produces significant changes in the Nusselt number distribution, but only near impinging region.

Throughout this work it has been found that the use of $\omega$ like length-scale quantity produces better results near solid walls. These models have presented better convergence and stability properties than $k-\epsilon$ models. Moreover, robustness of NLEVM and EARSM reduces when the complexity of the flow pattern increases (e.g. impinging jet) and the grid is densified.

# Acknowledgements

# References

[1] S.B. Pope. *Turbulent Flows*. Cambridge University Press, 2000.

[2] R. Moser, J. Kim, and N.N. Mansour. Direct Numerical Simulation of Turbulent Channel Flow up to $Re_\tau = 590$. *Physics of Fluids*, 11:943–945, 1999.

[3] D.M. Driver and H.L. Seegmiller. Features of a Reattaching Turbulent Shear Layer in Divergent Channel Flow. *AIAA Journal*, 23:163–171, 1985.

[4] A.R.P. Van Heiningen. *Heat transfer under impinging slot jet*. PhD thesis, McGill University, 1982.

[5] J. Cadafalch, C. D. Pérez-Segarra, R. Cònsul, and A. Oliva. Verification of Finite Volume Computations on Steady State Fluid Flow and Heat Transfer. *Journal of Fluids Engineering*, 124(11):11–21, 2002.

[6] D.C. Wilcox. *Turbulence modeling for CFD*. DCW Industries, Inc. CA, 1998.

[7] N.Z. Ince and B.E. Launder. Computation of Buoyancy-Driven Turbulent Flows in Rectangular Enclosures. *International Journal of Heat and Fluid Flow*, 10(1):110–117, 1989.

[8] U. Goldberg, O. Peroomian, and S. Chakravarthy. A Wall-Distance-Free k-$\epsilon$ Model with Enhanced Near-Wall Treatment. *Journal of Fluids Engineering*, 120(3):457–462, 1998.

[9]  D. C. Wilcox.  Reassessment of the Scale-Determining Equation for Advanced Turbulence Models. *AIAA Journal*, 26:1299–1310, 1988.

[10] D. C. Wilcox. Simulation of Transition with a Two-Equation Turbulence Model. *AIAA Journal*, 32:247–255, 1994.

[11] T.J. Craft, B.E. Launder, and K. Suga. Development and Application of Cubic Eddy-Viscosity Model of Turbulence. *International Journal of Heat and Fluid Flow*, 17(1):108–115, 1996.

[12] T.B. Gatski and C.G. Speziale. On Explicit Algebraic Stress Models for Complex Turbulent Flows. *Journal of Fluid Mechanics*, 254(1):59–78, 1993.

[13] R. Abid, J.H. Morrison, T.B. Gatski, and C.G. Speziale.  Prediction of Aerodynamic FLows with a New Explicit Algebraic Stress Model.  *AIAA Journal*, 34(12):2632–2635, 1996.

[14] J. Larsson. Two-Equation Turbulence Models for Turbine Blade Heat Transfer Simulations. In *Proceedings 13th ISABE Conference*, pages 1214–1222, 1997.

[15] K. Abe, Y. J. Jang, and M. A. Leschziner. An Investigation of Wall-Anisotropy Expressions and Length-Scale Equations for Non-Linear Eddy-Viscosity Models. *International Journal of Heat and Fluid Flow*, 24(2):181–198, 2003.

[16] R. Abid, C. Rumsey, and T.B. Gatski. Prediction of Nonequilibrium Turbulent FLows with Explicit Algebraic Stress Models. *AIAA Journal*, 33(11):2026–2031, 1995.

[17] S. Wallin and A. V. Johansson. An Explicit Algebraic Reynolds Stress Model for Incompressible and Compressible Turbulent Flows. *Journal of Fluid Mechanics*, 403:89–132, 2000.

[18] C.D. Pérez-Segarra, A. Oliva, M. Costa, and F. Escanes. Numerical experiments in turbulent natural and mixed convection in internal flows. *International Journal for Numerical Methods for Heat and Fluid Flow*, 5(1):13–33, 1995.

[19] S. V. Patankar. *Numerical Heat Transfer and Fluid Flow*. Hemisphere Publishing Corporation, 1980.

[20] M. S. Darwish and F. Moukalled.  An Efficient Very-High Resolution Scheme Based on an Adaptive-Scheme Strategy.  *Numerical Heat Transfer, Part B*, 34(2):191–213, 1998.

[21] B.R. Hutchinson and G.D.Raithby.  A multigrid method based on the additive correction strategy. *Numerical Heat Transfer, Part B*, 9(5):511–537, 1986.

*References*

[22] T. J. Craft, H. Iacovides, and J. H. Yoon. Progress in the Use of Non-linear Two-Equation Models in the Computation of Convective Heat-Transfer in Impinging and Separated Flows. *Flow, Turbulence and Combustion*, 63(1):59–81, 1999.

[23] K. Heyerichs and A. Pollard. Heat transfer in separated and impinging turbulent flows. *International Journal of Heat and Mass Transfer*, 39(12):2385–2400, 1996.

[24] D.D. Apsley and M.A. Leschziner. Advanced Turbulence Modelling of Separated Flow in a Diffuser. *Flow, Turbulence and Combustion*, 63(1):81–112, 1999.

[25] M.N. Ozisik. *Heat transfer. A basic approach.* McGraw-Hill, 1985.

[26] J.K. Eaton and J. P. Johnston. A review of Research on Subsonic Turbulent Flow Reattachment. *AIAA Journal*, 19:1093–1100, 1981.

[27] J.C. Vogel and J.K. Eaton. Combined Heat Tranfer and Fluid Dynamic Measurements. *Journal of Heat Transfer - Transactions of Asme*, 107:922–929, 1985.

[28] J. Kim, S. J. Kline, and J. P. Johnston. Investigation of a Reattaching Turbulent Shear Layer: Flow Over a Backward-Facing Step. *Journal of Fluids Engineering*, 102:302–308, 1980.

[29] T. S. Park and H.J. Sung. A Nonlinear low-Reynolds-number $k - \epsilon$ model for Turbulent Separated and Reattaching FLows–I. Flow Field Computations. *International Journal of Heat and Mass Transfer*, 38:2657–2666, 1995.

[30] S. Thangam and C. G. Speziale. Turbulent Flow Past a Backward-Facing Step: A Critical Evaluation of Two-Equation Models. *AIAA Journal*, 30:1314–1320, 1992.

[31] J. E. Jaramillo, K. Claramunt, C. D. Pérez-Segarra, R. Cònsul, and J. Cadafalch. Numerical study of different RANS models applied to turbulent forced convection. In *Proceedings of the IV International Symposium on Turbulence, Heat and Mass Transfer*, pages 671–680, 2003.

[32] R. Gardon and J. C. Akfirat. Heat Transfer Characteristics of Impinging Two-Dimensional Air Jets. *Journal of Heat Transfer - Transactions of Asme*, 88(1):101–108, 1966.

[33] S.J. Wang and A.S. Mujumdar. A comparative study of five low Reynolds number $k - \epsilon$ models for impingement heat transfer. *Flow, Turbulence and Combustion*, 25(1):31–44, 2005.

[34] S. H. Seyedin, M. Hasan, and A. S. Mujumdar. Modelling of a Single Confined Turbulent Slot Jet Impinging Using Various k-$\epsilon$ Turbulence Models. *Applied Mathematical Modelling*, 18:526–537, 1994.

[35] Y. Shi, M.B. Ray, and A.S. Mujumdar. Computational Study of Impingement Heat Transfer under a Turbulent Slot Jet. *Industrial and Engineering Chemistry Research*, 41:4643–4651, 2002.

[36] A. Abdon and B. Sundén. Numerical Investigation of Impingement Heat Transfer using Linear and Non-Linear Two-equation Turbulence Models. *Numerical Heat Transfer, Part A*, 40(6):563–578, 2001.

[37] T. H. Park, H.G. Choi, J.Y. Yoo, and S.J. Kim. Streamline Upwind Numerical Simulation of Two-Dimensional Confined Impinging Slot Jets. *International Journal of Heat and Mass Transfer*, 46(2):251–262, 2003.

[38] M. Behnia, S. Parneix, Y. Shabany, and P.A. Durbin. Numerical Study of Turbulent Heat Transfer in Confined and Uncofined Impinging Jets. *International Journal of Heat and Fluid Flow*, 20(1):1–9, 1999.

# Chapter 4

# Further studies of RANS models in complex flows: impinging plane and round jets.

**Abstract.** In this chapter different impinging jet configurations are studied by means of time averaged Navier-Stokes simulations. Within this technique, explicit algebraic Reynolds stress models and both non-linear and linear eddy viscosity models are explored jointly with $k - \epsilon$ and $k - \omega$ platforms. The main object of this chapter is to study numerical performance and accuracy of models when they are used in the simulation of both plane and round impinging jets. With this purpose, results from numerical simulations, using different models, are compared among them and with experimental data available in the literature. Comparisons are performed in terms of mean and fluctuating velocities and global parameters, i.e. the local Nusselt number. A verification procedure is applied in order to ensure the credibility of the numerical solutions.

**Nomenclature**

$B$ nozzle width

$C_{\epsilon 1}, C_{\epsilon 2}$ turbulent model constant

$c_p$ specific heat at constant pressure

$D$ nozzle diameter, turbulent model extra term

$E, E_\omega$ turbulent model extra terms

$f_1, f_2, C_\mu, f_\mu$ damping functions

$H$ height of jet discharge above impingement plate

$I$ turbulent intensity

$k$ turbulent kinetic energy

$l_c$ characteristic length scale

$Nu$ Nusselt number

$P_k$ production of $k$ due to shear stress

$Pr$ Prandtl number

$Re$ Reynolds number based on pipe diametes

$Re_B$ Reynolds number based on nozzle width

$\bar{S}_{ij}$ mean rate of strain tensor

$\bar{T}$ mean temperature

$t$ time

$\bar{u}_i$ mean velocity

$\overline{u_i' u_j'}, \overline{u'u'}, \overline{v'v'}, \overline{w'w'}, \overline{u'v'}$ Reynolds stresses

$\overline{u_i' T'}$ turbulent heat flux

$\bar{p}$ mean pressure

$\bar{v}_{in}$ bulk inlet velocity

$\bar{W}_{ij}$ mean vorticity tensor

$Y_c$ Yap correction

$y^+ = \frac{\rho x_n u_\tau}{\mu_t}, \quad u_\tau = \sqrt{\tau_w/\rho}$ is friction velocity and $x_n$ is the distance to the nearest wall

Greek symbols

$\alpha^*, \beta, \beta^*, \beta_k, \gamma_k$ turbulent model constants

$\delta_{ij}$ Kronecker delta

$\epsilon$ dissipation rate of $k$

$\tilde{\epsilon}$ isotropic dissipation rate of $k$

$\lambda$ thermal conductivity

$\mu$ dynamic viscosity

$\mu_t$ eddy or turbulent viscosity

$\rho$ density

$\sigma_k, \sigma_\epsilon, \sigma_\omega$ turbulent model constant

$\tau$ time scale

$\omega$ specific dissipation rate of $k$
$x_i$ Cartesian coordinate in the $i$-direction

Subscripts
*ext* exterior
*in* inlet
*out* outlet

## 4.1 Introduction

Because of the highly localised mass, momentum and heat transfer, impinging jets are used in heating, cooling or drying processes for the production of paper, textiles, glass, annealing of metal sheets, cooling of turbine blades and electronic components, air curtains, etc. Thus, a correct prediction of flow structure and heat transfer in this kind of flows is of great importance in many industrial applications.

Predictive inaccuracies of linear eddy-viscosity models have motivated that a great deal of effort has gone into the elaboration of constitutive expressions that, assuming a higher-order tensor representation, relate Reynolds-stress tensor non-linearly to the strain-rate and vorticity tensors. This kind of models are capable of solving Reynolds-stress anisotropy and streamlines curvature. They are also thought to preserve computational economy and numerical robustness of linear models [1].

The main goal of this chapter is to study the suitability, in terms of accuracy and numerical performance, of different RANS models in the description of plane and round impinging jets. Furthermore, Reynolds number and nozzle-to-impingement surface distance are changed in both configurations to test their influence on turbulence models behaviour. Thus, this work is not intended to improve the models, but to present a detailed evaluation of them according to their capability to predict imping-ing jet flows. The analysis of the models in this complex flow is attractive because of the presence of strong curvature of streamlines, stagnation, recirculation and adverse pressure regions. A brief overview of different works found in the literature studying plane and round impinging jets is presented in section 4.2.

Within RANS technique, two-equation linear eddy-viscosity models (LEVM) [2], non-linear eddy viscosity models (NLEVM) [3] and explicit algebraic Reynolds stress models (EARSM) [4], are taken into account in this chapter. Moreover, a comparison in the use of different dissipation variables, such as $\epsilon$ or $\omega$ for the turbulence length scale calculation, is carried out. In summary, four $k - \epsilon$ and seven $k - \omega$ models are analysed in order to increase the number of turbulence models tested in both plane and round impinging jets.

The set of equations (continuity, momentum, energy and turbulent quantities) are transformed to algebraic equations using a general fully implicit finite-volume
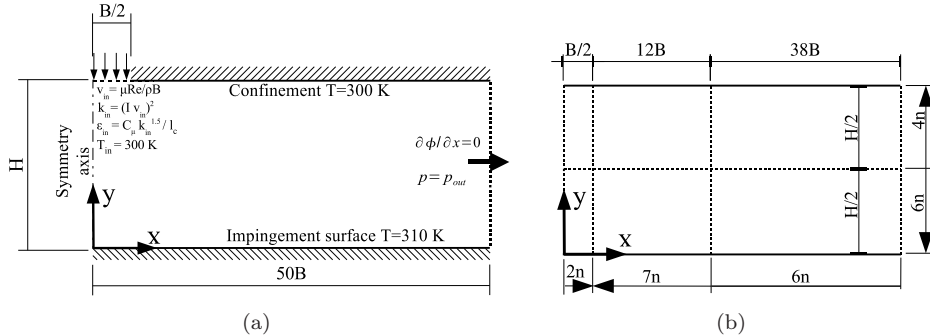
technique over structured and staggered grids. The SIMPLEC algorithm [5] is used for solving, in a segregated manner, the velocity-pressure fields coupling. First and higher order schemes are used to approximate convective terms.

Results obtained with the models under consideration are carefully verified applying a post-processing procedure based on the generalised Richardson extrapolation [6], and validated with experimental data from literature [7, 8]. Furthermore, a detailed analysis of mean velocities, turbulent stresses and global parameters such as Nusselt number is presented.

## 4.2    Description of studied cases

Two chosen configurations of single turbulent impinging jets are numerically studied in this chapter. They involve plane and round nozzle geometries at different Reynolds numbers and nozzle-to-impingement surface distances (aspect ratios: $H/D$ round jet or $H/B$ plane jet).

### 4.2.1    Plane impinging jets



**Figure 4.1:** Plane impinging jet. (a) Geometry and boundary conditions. (b) Grid distribution: number of control volumes ($n$ is a parameter) and size of zones; solid triangles indicate grid refinement direction.

Turbulent plane impinging jets have received extensive attention in the last decades considering different geometries, flow and thermal conditions. Experimental studies for thermal field have been carried out, among others, by Gardon and Akfirat [9] and Van Heiningen [10] for various Reynolds numbers. For the fluid-dynamic field, Ashforth-Frost et al. [11] reported measurements of velocity and turbulence characteristics for a slot jet with a Reynolds number of 20000 and two aspect ratios of 4 and

110

9.2. Zhe and Modi [7] also examined the velocity field for several Reynolds numbers and aspect ratios. Numerical studies were published by Heyerichs and Pollard [12], who examined an impinging slot jet at Reynolds number of 10000. Hosseinalipour and Mujumdar [13] also realized a similar study at a lower Reynolds number. Seyedein et al. [14] performed another work for various Reynolds numbers and aspect ratios. More recently Shi et al. [15] studied the effect of inlet conditions over the heat transfer.

Single turbulent confined impinging air slot jets are studied in this work (see Figure 4.1). Two Reynolds numbers based on inlet mean velocity and nozzle width B, of 20000 and 30000, and two aspect ratios of 4 and 9.2 [7, 11] have been tested.

Inlet turbulent kinetic energy ($k_{in}$) is calculated with an intensity of $I = 0.02$ and the characteristic length used to determine the turbulent kinetic energy dissipation rate ($\epsilon_{in}$) is $l_c = 0.015B$. The specific turbulent kinetic energy dissipation rate ($\omega_{in}$) is evaluated with the relation $\omega = \frac{\epsilon}{\beta^* k}$ (where $\beta^*$ is a model constant). The walls are considered isothermal: impingement plate at 310 K and confinement plate at 300 K. No-slip condition is imposed at solid walls and the value of turbulent quantities depend on the specific turbulence model used (see section 4.3). At the exit, a pressure outflow boundary condition is imposed [16], and a null gradient in $x$-direction of temperature and turbulence quantities ($k, \epsilon$ or $\omega$) is assumed. Due to symmetry, only half domain is simulated. See Figure 4.1(a) for details.

## 4.2.2 Round impinging jets



**Figure 4.2:** Round impinging jet. (a) Geometry and boundary conditions. (b) Grid distribution: number of control volumes ($n$ is a parameter) and size of zones; solid triangles indicate grid refinement direction.

This configuration has been extensively studied as well. Some examples of the experimental works carried out considering heat transfer are Martin [17], Baughn and Shimizu [18], Baughn et al. [19], Viskanta [20], and Lytle and Webb [21]. Flow

measurements have been presented by Cooper et al. [8], Fairweather and Hargrave [22], and recently by Geers et al. [23]. This configuration has been considered as a test case by ERCOFTAC. Data of mean velocity, turbulent stresses, and heat transfer at two Reynolds numbers (Re = 23000 and 70000), and two aspect ratios (H/D = 2 and 6), are reported in this database [8, 18, 19]. These experimental data have been used by researchers to review turbulence models. For example, Craft et al. [24] studied the performance of a $k - \epsilon$ LEVM and three differential Reynolds stress models (DRSM). Dianat et al. [25] used a $k - \epsilon$ LEVM and a modified DRSM to analyse velocity field. Behnia et al. [26] compared the V2F model with the standard $k - \epsilon$ model for two aspect ratios and three Reynolds numbers. Abdon and Sunden [27] also studied the performance of various LEVM and NLEVM in this flow configuration.

In this work, unconfined round impinging jets are studied (see Figure 4.2). For this configuration two aspect ratios are also considered, $H/D = 2$ and $H/D = 6$ [8]. A Reynolds number based on pipe diameter ($D$) and inlet bulk velocity ($\bar{v}_{in}$) of 23000, similar to that used in the plane impinging jet case, and another higher of 70000 have been selected. The problem can be studied as a two-dimensional axisymmetric one. At the inlet, fully developed profiles ($v_{in}$, $k_{in}$, $\epsilon_{in}$) are obtained from a separate computation in an adiabatic pipe flow with the same inlet diameter and a length of $80D$. A constant inlet temperature ($T_{in}$) of $298K$ is imposed. At the upper boundary, a coflow is prescribed in order to avoid instabilities and ensure a supply of fluid for jet entrainment. Thus, a exterior velocity ($v_{ext}$) expressed as a fraction of $\bar{v}_{in}$ is imposed. The temperature ($T_{ext}$) is also set equal to that of the main inlet jet ($T_{in}$). This flow is considered non-turbulent and therefore turbulent kinetic energy is set to zero. At the outer boundary a pressure outlet condition is defined [16]. At the wall, isothermal surface at $318K$ and no-slip boundary conditions are considered. See details in Figure 4.2(a).

## 4.3   Mathematical model

Turbulence models considered in this work are based on the time-averaged Navier-Stokes equations. Therefore, some relation for the Reynolds stress ($\overline{\rho u_i' u_j'}$) and turbulent heat flux ($\overline{\rho u_i' T'}$) must be specified. Furthermore, extra transport equations for the turbulent kinetic energy ($k$) and some length-scale determining equation ($\epsilon$ or $\omega$) to close the system are needed [28]. A detailed description is given in section 2.2.

In order to evaluate the Reynolds stresses three approaches are considered: explicit algebraic Reynolds stress models (EARSM), non-linear eddy-viscosity models (NLEVM), and linear eddy-viscosity models (LEVM).

Linear eddy viscosity models assume the Boussinesq hypothesis and, by analogy with Stokes's law for viscous stresses, it introduces a mixing coefficient to evaluate Reynolds stresses in turbulent flows. This mixing coefficient is frequently called ap-

parent, virtual or eddy viscosity ($\mu_t$) [2]. Therefore, the Reynolds stress is linearly related to the mean rate of strain.

Non-linear and explicit algebraic models use algebraic expressions based on the weak-equilibrium assumption and include terms up to third order in the $\overline{u_i' u_j'}$ relation [29]. NLEVM are based on physical constraints and their coefficients are calibrated for some representative flows [29]. Whereas, EARSM are formally derived from differential Reynolds stress models (DRSM) and, therefore, coefficients appearing in the tensorial expansion are consistent with the DRSM used [4].

A general expression for $a_{ij} \equiv \frac{\overline{u_i' u_j'}}{k} - \frac{2}{3}\delta_{ij}$ in the models considered can be written, identifying Cartesian tensor of rank 2 by bold symbols (e.g. $a_{ij} \to \mathbf{a}$), and contracted products as for matrix multiplication (e.g. $\mathbf{ab} = a_{ik}b_{kj}$, $\mathbf{abc} = a_{ik}b_{kl}c_{lj}$, etc.), according to the relation given in eq. 2.73[30]. Obviously, setting $\beta$'s and $\gamma$'s coefficients to zero in Eq. 2.44 the linear relation used in LEVM is obtained (for details see section 2.2).

For the turbulent heat flux ($\rho\overline{u_i' T'}$) the models use the simple eddy diffusivity approach (see section 2.2).

All models studied in this chapter require the solution of two extra transport equations to close the mathematical formulation. One is for the turbulent kinetic energy, $k$, and the other for its dissipation rate, $\epsilon$ or $\omega$ [2], which are explained in section 2.2. The models considered in this chapter using $\epsilon$ as turbulent dissipation variable are: IL ($k\epsilon$-LEVM) [31], GPC ($k\epsilon$-LEVM) [32], CLS ($k\epsilon$-NLEVM) [29], and AMGS ($k\epsilon$-EARSM) [4]. Those studied which use $\omega$ are: WX ($k\omega$-LEVM) [33], WXT ($k\omega$-LEVM) [34], WXCD ($k\omega$-LEVM) [28], LAR ($k\omega$-NLEVM) [35], ARG ($k\omega$-EARSM) [36], AJL ($k\omega$-NLEVM) [30] and WJO ($k\omega$-EARSM) [37].

For details about coefficients in the constitutive relation (eq. 2.73), damping functions and closure coefficients appearing in each model see appendix A.

## 4.4 Solution procedure

The governing partial differential equations are converted into algebraic ones by means of the finite volume technique. They are solved, in a segregated manner, using an orthogonal, structured and staggered grid, applying fully implicit time integration. SIMPLEC method is applied to couple the velocity and pressure fields [38]. Central differences are used for the evaluation of diffusive terms, while convective terms are discretized using power law [38] or higher order (second order upwind or SMART) schemes [39]. A multigrid iterative solver is used to solve the algebraic linear system of equations [40].

The grid used is described in Figures 4.1(b) and 4.2(b) for the plane and round impinging jets respectively. The number of control volumes per zone is represented by the $n$-parameter and the concentration direction is indicated by solid triangles.

Refinement is accomplished by means of a tanh-like function [41]. Thus, concerning the $x$ or $r$ directions, the number of grids nodes is increased when approaching the impingement region from the outlet towards the stagnation zone. The grid is also concentrated near solid walls. The specific meshes used in both cases (plane and round jets) are fully described in next section.

## 4.5 Verification of numerical results

| $Re_B = 20000$, $H/B = 4$ , GPC ($k\epsilon$-LEVM) model | | | | | | | | | | | | | | | |
|---|---|---|---|---|---|---|---|---|---|---|---|---|---|---|---|
| | | u | | | v | | | T | | | k | | | | |
| mesh | $Rn$ | $p$ | $GCI^*$ | $Rn$ | $p$ | $GCI^*$ | $Rn$ | $p$ | $GCI^*$ | $Rn$ | $p$ | $GCI^*$ | | | |
| m | [%] | | [%] | [%] | | [%] | [%] | | [%] | [%] | | [%] | | | |
| 3 | 94 | 1.0 | 1.5e-00 | 93 | 0.7 | 5.7e-01 | 79 | 1.2 | 7.5e-01 | 92 | 1.2 | 5.8e-01 | | | |
| 4 | 92 | 1.1 | 8.0e-01 | 93 | 0.9 | 2.8e-01 | 82 | 2.1 | 1.6e-01 | 93 | 1.1 | 3.8e-01 | | | |
| $Re_B = 30000$, $H/B = 9.2$, WXCD ($k\omega$-LEVM) model | | | | | | | | | | | | | | | |
| | | u | | | v | | | T | | | k | | | | |
| mesh | $Rn$ | $p$ | $GCI^*$ | $Rn$ | $p$ | $GCI^*$ | $Rn$ | $p$ | $GCI^*$ | $Rn$ | $p$ | $GCI^*$ | | | |
| m | [%] | | [%] | [%] | | [%] | [%] | | [%] | [%] | | [%] | | | |
| 3 | 96 | 1.4 | 8.0e-00 | 92 | 1.5 | 2.5e-00 | 92 | 1.4 | 4.7e-00 | 95 | 1.5 | 5.1e-00 | | | |
| 4 | 97 | 1.3 | 5.4e-00 | 95 | 1.3 | 1.6e-00 | 91 | 1.5 | 2.1e-00 | 98 | 1.3 | 3.8e-00 | | | |

**Table 4.1:** Plane jet. Results from mesh refinement study: Richardson nodes ($R_n$), global order of accuracy ($p$) and non-dimensional global uncertainty ($GCI^*$).

In order to verify the obtained numerical solutions a detailed and reliable process is applied to determine the numerical uncertainties. The post-processing procedure, previously explained in section 2.4, is based on the generalised Richardson extrapolation for *h-refinement* studies and on the Grid Convergence Index (GCI). It is used in order to establish a criteria about the sensitivity of the simulation to the computational model parameters that account for the computational domain discretization. See section 2.4 and [6] for details.

Because of the difficulties found in the previous chapter, when the verification procedure was applied in coarse grids. Furthermore, due to turbulence models here used are of the turbulence low-Reynolds number type, care has to be taken to assure enough grid nodes in the viscous near-wall region [42]. As a criterion, the nearest grid node to the wall is located at a distance $y^+ < 2.5$. Therefore, a fine enough grid has to be used as the coarsest mesh in the *h-refinement* study, what obligates to reduce

the refinement ratio of two consecutive meshes to 1.5, and the number of grids to be considered in the refinement process to 4 [6].

| mesh | $Rn$ | $p$ | $GCI^*$ | $Rn$ | $p$ | $GCI^*$ | $Rn$ | $p$ | $GCI^*$ | $Rn$ | $p$ | $GCI^*$ |
|------|------|-----|---------|------|-----|---------|------|-----|---------|------|-----|---------|
| $Re = 23000$, $H/D = 2$, WX ($k\omega$-LEVM) model | | | | | | | | | | | | |
| | \multicolumn{3}{c}{u} | | \multicolumn{3}{c}{v} | | \multicolumn{3}{c}{T} | | \multicolumn{3}{c}{k} | |
| m | [%] | | [%] | [%] | | [%] | [%] | | [%] | [%] | | [%] |
| 3 | 93 | 1.1 | 2.7e-01 | 88 | 1.4 | 5.2e-02 | 48 | 2.2 | 5.3e-01 | 89 | 0.8 | 7.2e-02 |
| 4 | 93 | 1.8 | 6.0e-02 | 87 | 1.2 | 5.0e-02 | 40 | 2.5 | 2.1e-01 | 86 | 1.7 | 1.1e-02 |
| $Re = 70000$, $H/D = 6$, GPC ($k\epsilon$-LEVM) model | | | | | | | | | | | | |
| | \multicolumn{3}{c}{u} | | \multicolumn{3}{c}{v} | | \multicolumn{3}{c}{T} | | \multicolumn{3}{c}{k} | |
| m | [%] | | [%] | [%] | | [%] | [%] | | [%] | [%] | | [%] |
| 3 | 96 | 1.6 | 4.0e-01 | 94 | 1.7 | 3.3e-01 | 57 | 1.3 | 2.6e-01 | 92 | 1.6 | 1.4e-01 |
| 4 | 94 | 1.4 | 1.9e-01 | 93 | 1.5 | 1.6e-01 | 48 | 2.4 | 2.1e-02 | 93 | 1.3 | 1.0e-01 |

**Table 4.2:** Round jet. Results from mesh refinement study: Richardson nodes ($R_n$), global order of accuracy ($p$) and non-dimensional global uncertainty ($GCI^*$).

Control volumes distribution is shown in Figures 4.1(b) and 4.2(b). In the plane impinging jet case (see Figure 4.1(b)) four meshes are defined according to the parameter $n$: 8, 12, 18 and 27 (i.e. m1: 120x80, m2: 180x120, m3: 270x180, and m4: 405x270 CVs respectively). For the round impinging jet (see Figure 4.2(b)) the meshes used are obtained with a $n = 4$, 6, 9 and 14 (i.e. m1: 80x80, m2: 120x120, m3: 180x180 and m4: 270x270 CVs). Moreover, the concentration near the walls and towards the jet has been adjusted depending on the aspect ratio and Reynolds number in each case. Thus, a maximum $y^+ < 2$ for the first inner node from the wall in the coarsest grid is assured in all the cases.

Tables 4.1 and 4.2 show results of a grid refinement study in plane and round jets respectively, using three different LEVM turbulence models: GPC ($k\epsilon$-LEVM), WX ($k\omega$-LEVM) and WXCD ($k\omega$-LEVM), and three meshes for each case (m3/m2/m1 and m4/m3/m2). The Tables show the number of Richardson nodes ($R_n$) (i.e. the number of nodes with monotone error convergence), the order of accuracy ($p$), and the non-dimensional grid convergence index ($GCI^*$) (details in [6]). As can be seen, numerical results have an asymptotic behaviour. The number of Richardson nodes ($R_n$) of the numerical solutions are found to be large enough. In general, over 85% with the exception of $R_n$ for temperature ($T$) in the round impinging jet configuration, where certain part of the domain presents a constant value because of the imposed boundary conditions. The observed order of accuracy ($p$) for each variable

115

also agrees with its theoretical value in impinging flows. Furthermore, the uncertainty due to discretization ($GCI$) presents good accuracy for all the variables and diminishes when the grid is refined. Therefore, results obtained using m3 or m4 meshes can be considered credible.

| | | | | | | | | | | | | |
|---|---|---|---|---|---|---|---|---|---|---|---|---|
| $Re = 23000$, $H/D = 2$, CLS ($k\epsilon$-NLEVM) model | | | | | | | | | | | | |
| | u | | | v | | | T | | | k | | |
| mesh | $Rn$ | $p$ | $GCI^*$ | $Rn$ | $p$ | $GCI^*$ | $Rn$ | $p$ | $GCI^*$ | $Rn$ | $p$ | $GCI^*$ |
| m | [%] | | [%] | [%] | | [%] | [%] | | [%] | [%] | | [%] |
| 3 | 78 | 1.1 | 1.1e-00 | 75 | 1.6 | 6.8e-02 | 44 | 3.2 | 3.2e-00 | 87 | 1.3 | 1.3e-01 |
| $Re = 23000$, $H/D = 2$, AJL ($k\omega$-NLEVM) model | | | | | | | | | | | | |
| | u | | | v | | | T | | | k | | |
| mesh | $Rn$ | $p$ | $GCI^*$ | $Rn$ | $p$ | $GCI^*$ | $Rn$ | $p$ | $GCI^*$ | $Rn$ | $p$ | $GCI^*$ |
| m | [%] | | [%] | [%] | | [%] | [%] | | [%] | [%] | | [%] |
| 3 | 91 | 1.4 | 7.1e-01 | 86 | 1.4 | 1.2e-01 | 60 | 2.7 | 1.9e-00 | 91 | 1.1 | 2.6e-01 |

**Table 4.3:** Round jet. Results from mesh refinement study using NLEVM: Richardson nodes ($R_n$), global order of accuracy ($p$) and non-dimensional global uncertainty ($GCI^*$).

Table 4.3 shows results of a grid refinement study in round jets for the first three meshes (m1, m2, m3) using two of the more complex turbulence models tested in this work: CLS ($k\epsilon$-NLEVM) and AJL ($k\omega$-NLEVM). As can be seen, similar results to those presented in Tables 4.1 and 4.2 are obtained.

Finally, taking into account results presented in Tables 4.1, 4.2 and 4.3, results from the third mesh can be considered grid independent. Therefore, this mesh is used for comparative purposes for all the turbulence models tested.

## 4.6   Results and discusion

In this section, verified numerical results are compared with experimental data. For both cases under study (plane and round impinging jets), four different aspects are studied: thermal field, fluid flow field, influence of the aspect ratio, and Reynolds number. For clarity, the results obtained are grouped depending on the dissipation variable used ($\epsilon$ or $\omega$).
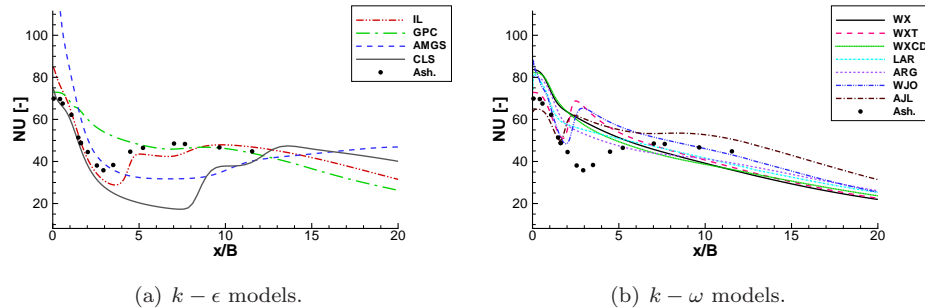
### 4.6.1 Thermal field: Nusselt number

One of the most representative parameters of the thermal field found in this configuration is the local Nusselt number along the impingement plate. This is defined as: $Nu = \left[\frac{\partial T}{\partial y}\right]_w / \left[\frac{T_w - \bar{T}_{in}}{l}\right]$, where $l = B$ in plane jets and $l = D$ in round jets (see Figures 4.1(a) and 4.2(a) respectively), $T_w$ is the impingement plate temperature, and $\bar{T}_{in}$ the inlet jet temperature.

**Plane impinging jet, $Re_B = 20000$ and $H/B = 4$**

Results for the Nusselt number are presented together with experimental data in Figure 4.3. Despite poor results presented by AMGS ($k\epsilon$-EARSM) model, the rest of the tested models predict acceptable local $Nu$ near stagnation point. In general, NLEVM models improve predictions of LEVM models in this region, i.e. CLS ($k\epsilon$-NLEVM) vs. IL ($k\epsilon$-LEVM), and LAR ($k\omega$-NLEVM) and ARG ($k\omega$-EARSM) vs. WX ($k\omega$-LEVM). Moreover, only AJL ($k\omega$-EARSM) slightly underpredicts Nu at the stagnation point. The same trend has been observed by Abdon et al. [27] for LAR ($k\omega$-NLEVM) and AMGS ($k\epsilon$-EARSM) models. Furthermore, comparing $k - \epsilon$ with $k - \omega$ based models, the last ones present less dispersed values in the stagnation zone.



(a) $k - \epsilon$ models.      (b) $k - \omega$ models.
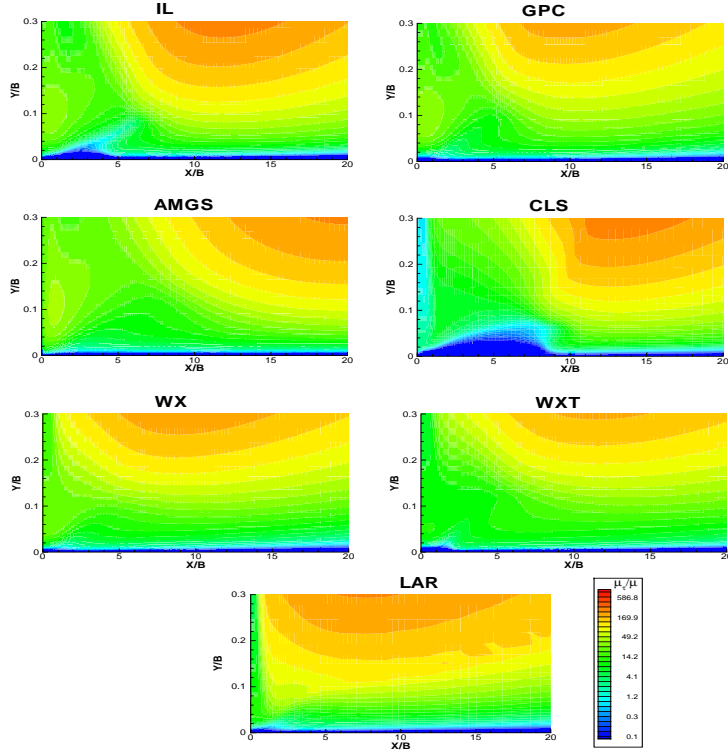
**Figure 4.3:** Plane jet, $Re_B = 20000$ and $H/B = 4$. Local Nusselt at the impingement plate. Lines: numerical results; symbols: experiments by Ashforth-Frost et al. [11].

Downstream, IL ($k\epsilon$-LEVM) reproduces correctly experimental data for the Nusselt number [11]. Nevertheless, CLS ($k\epsilon$-NLEVM) predicts with delay Nusselt secondary maximum, whereas WXT ($k\epsilon$-LEVM), AJL ($k\epsilon$-NLEVM) and WJO ($k\omega$-EARSM) predict the maximum earlier than experimental data. On the other hand, GPC ($k\epsilon$-LEVM), WX ($k\omega$-LEVM), WXCD ($k\omega$-LEVM), LAR ($k\omega$-NLEVM) and

ARG ($k\omega$-EARSM) do not exhibit the secondary $Nu$ peak. Thus, observing this quantity in redeveloping region, there is not appreciable benefit in using higher order relations. For this configuration, it seems more important the use of extra-terms and adequate damping functions rather than more elaborate constitutive equations to evaluate turbulent stresses.



**Figure 4.4:** Plane jet, $Re_B = 20000$ and $H/B = 4$. Non-dimensional Eddy Viscosity of selected models.
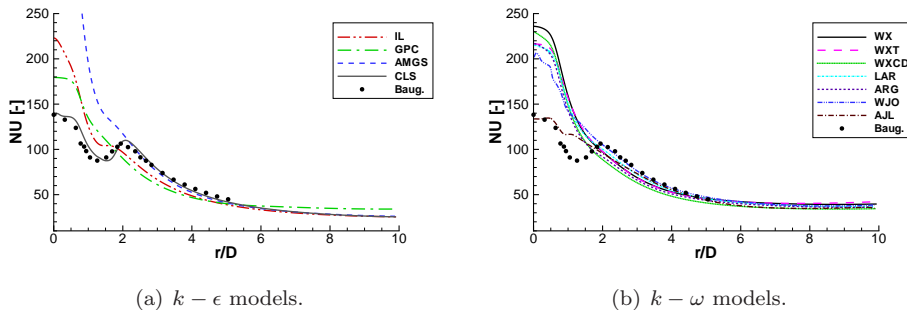
In order to illustrate the connection between the turbulence level and the Nusselt number secondary peak, Figure 4.4 shows results for the eddy viscosity ($\mu_t$) normalised by molecular viscosity ($\mu$). The second Nusselt maximum in Figure 4.3 coincides with a steep positive gradient in the turbulence level (represented by $\mu_t/\mu$) near the bottom wall. It is also observed that models which do not exhibit an enhancement of turbulence downstream stagnation region do not present a secondary peak in Nusselt

number.

**Round impinging jet,** $Re = 23000$ **and** $H/D = 2$

Figure 4.5 shows the local Nusselt results along the impingement plate for the round impinging jet with an aspect ratio of 2. The most accurate prediction for this quantity is obtained with the CLS ($k\epsilon$-NLEVM). For this configuration, it is clear the necessity of using this model if a correct prediction of the local $Nu$ number is desired (see Figure 4.5). The AJL ($k\omega$-NLEVM) model also tends to follow experimental data, but fails in the prediction of the secondary maximum.



(a) $k - \epsilon$ models.　　　　　(b) $k - \omega$ models.

**Figure 4.5:** Round jet, $Re = 23000$ and $H/D = 2$. Local Nusselt at the impingement plate. Lines: numerical results; symbols: experiments by Baughn and Shimizu [18].

In spite of the results shown in the plane jet configuration, $k - \omega$ models do not improve $k - \epsilon$ results in the round case. Furthermore, none of the $k - \omega$ models, with exception of AJL ($k\omega$-NLEVM), reproduce correctly experimental data near stagnation region, nor the secondary $Nu$ maximum. As it is noted above, the secondary peak of the local Nusselt number profile is attributed to a turbulence increase away the stagnation point, which is produced by high shear in the region of streamline convergence, where the turbulent shear layer is impinging on the plate [26]. Similar results for this configuration have been presented by other researchers [3, 27].
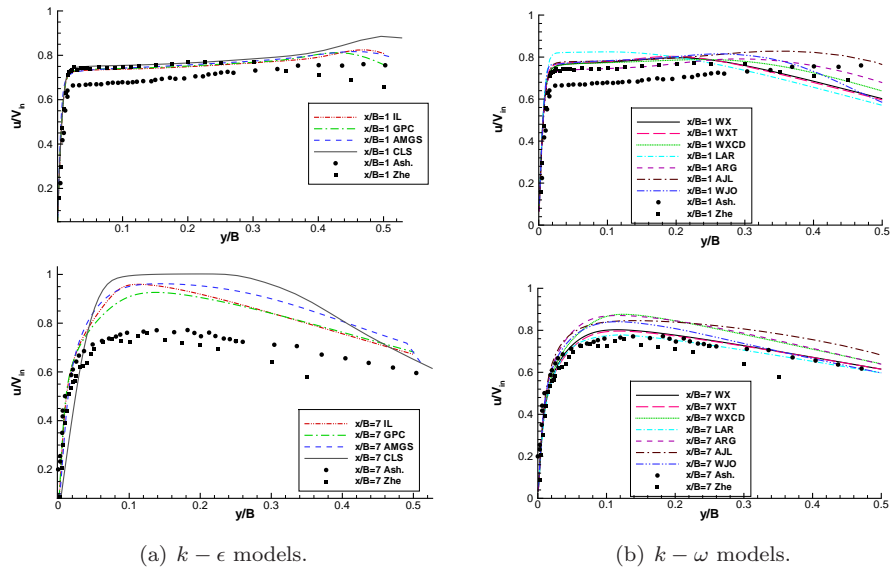
## 4.6.2 Fluid-flow field

In this section fluid-flow field predicted by the models is analysed in terms of mean and fluctuating velocities at different positions for both plane and round impinging jet configurations under consideration.

**Plane impinging jet, $Re_B = 20000$ and $H/B = 4$**

In two experimental works, carried out by Ashforth-Frost et al. [11] and by Zhe and Modi [7], the fluid-flow field for this case is studied with similar boundary conditions and geometric characteristics. Here, both works are taken into account to study model performance.



(a) $k - \epsilon$ models.  (b) $k - \omega$ models.
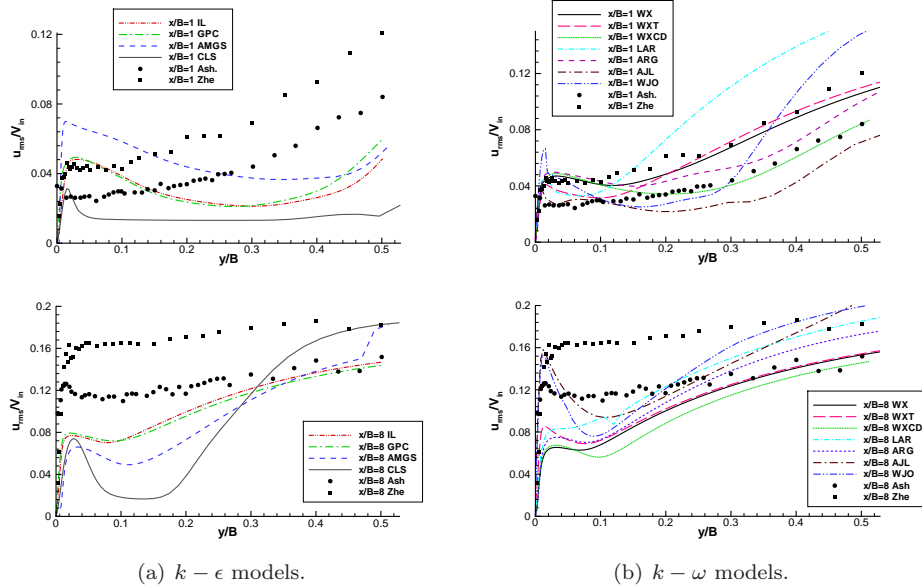
**Figure 4.6:** Plane jet, $Re_B = 20000$ and $H/B = 4$. Comparison of calculated $x$-direction component of mean velocity with experimental results, at x/B=1 and x/B=7. Lines: numerical solutions; symbols: experiments by Zhe and Modi [7] and Ashforth-Frost et al. [11].

Figure 4.6 shows non-dimensional mean velocity distribution in $x$-direction ($u/v_{in}$) at two axial positions. Numerical results are compared with the mentioned experimental data [7, 11]. This Figure illustrates an appropriate behaviour of all models near the stagnation region at $x/B = 1$, if they are compared with experiments by Zhe and Modi [7]. However, LAR ($k\omega$-NLEVM) model over-predicts velocity at $x/B = 1$.

Downstream deceleration of the velocity near the wall (shown in Figure 4.6 at $x/B = 7$ location) appears when the jet is dispersed causing the development of a vortex in the upper part [43]. At that point all $k - \epsilon$ models have difficulties to correctly reproduce experimental results. Nevertheless, WX ($k\omega$-LEVM) and LAR ($k\omega$-NLEVM) models produce closer solutions to experiments at this point, whereas

WXCD ($k\omega$-LEVM), ARG ($k\omega$-EARSM) and AJL ($k\omega$-NLEVM) models overpredict mean velocity profile (see figure 4.6(b)).



(a) $k - \epsilon$ models.　　　　　　(b) $k - \omega$ models.

**Figure 4.7:** Plane jet, $Re_B = 20000$ and $H/B = 4$. Comparison of calculated $x$-direction component of fluctuating velocity with experimental results at x/B=1 and x/B=8. Lines: numerical solutions; symbols: experiments by Zhe and Modi [7] and Ashforth-Frost et al. [11].
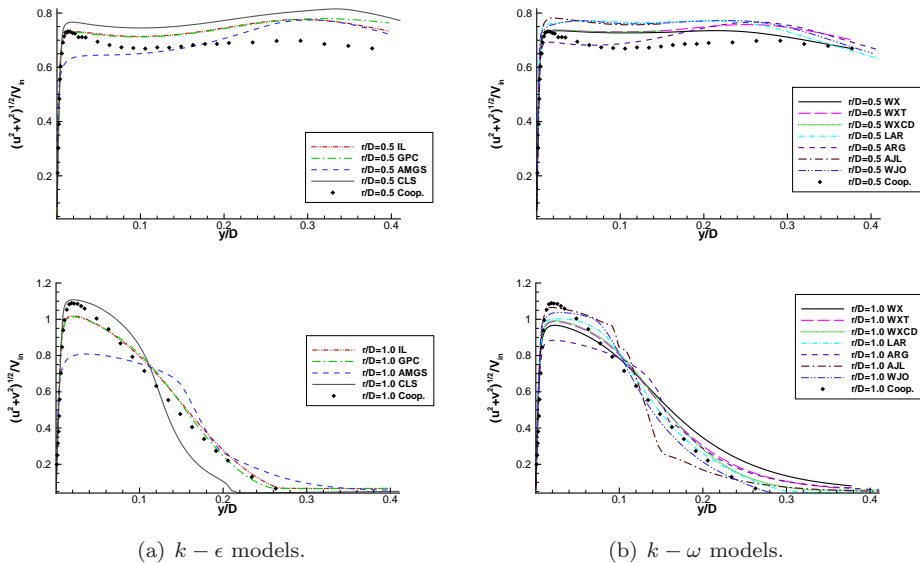
In order to gain a better understanding of the performance of each model is necessary to compare also the fluctuating part or root mean square value (rms) of the velocity in $x$-direction ($u'/v_{in}$). Comparative results are presented in Figure 4.7, where most of the models differ from experimental data. At this stage, it is clear the more accurate behaviour of $k - \omega$ models near the impingement plate, reinforcing results presented for the mean velocity field. The $k - \epsilon$ LEVM and NLEVM models fail in predicting the fluctuating velocity profile near $x/B = 7$. Furthermore, among $k - \omega$ based models, only AJL ($k\omega$-NLEVM) and WJO ($k\omega$-EARSM) models tend to reproduce experimental data near the wall at this position, but this improvement is not reflected in the mean velocity profile.

Reviewing $u'/v_{in}$ profile, it can be seen that the influence of higher order terms in the relation for Reynolds stresses is more relevant in models using $k - \omega$ platform. Thus, in the stagnation region, LAR ($k\omega$-NLEVM) model over-predicts $u'/v_{in}$ far

from the bottom wall. For $k - \epsilon$ based models, differences between using linear or non-linear relations are smaller [27, 44], e.g. CLS ($k\epsilon$-NLEVM) model only reproduces appropriately experimental data near the bottom wall at $x/B = 1$ and under-predicts experimental profile in the other positions. Moreover, AMGS ($k\epsilon$-EARSM) model over-predicts $u'/v_{in}$ velocity near stagnation region, but it performs in a similar way as IL ($k\epsilon$-LEVM) and GPC ($k\epsilon$-LEVM) models in the other regions analysed. Therefore, in the case of $k - \epsilon$ models, the constitutive relation to evaluate turbulent stresses and the correct behaviour of the turbulent dissipation equation near the impingement plate also, play an important role.

**Round impinging jet,** $Re = 23000$ **and** $H/D = 2$



(a) $k - \epsilon$ models.　　　　(b) $k - \omega$ models.
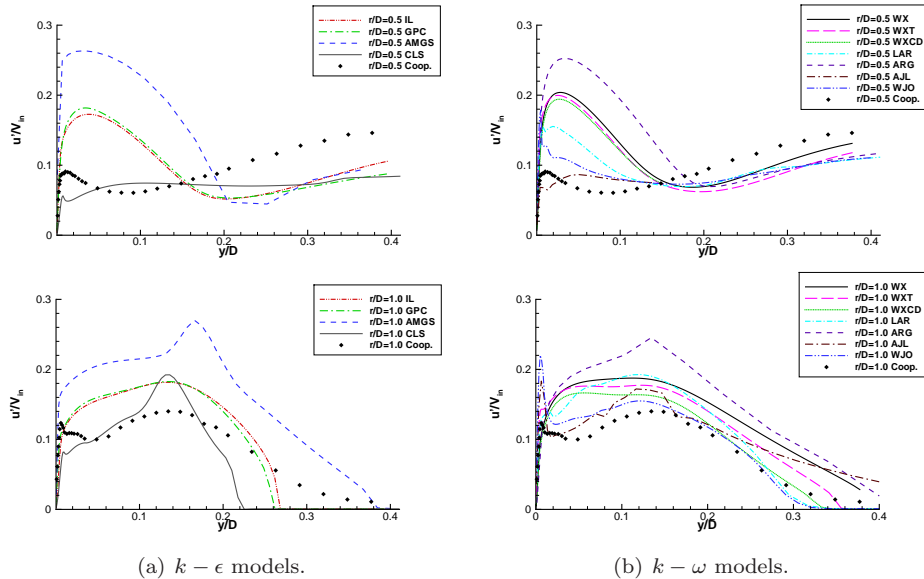
**Figure 4.8:** Round jet, $Re = 230000$ and $H/D = 2$. Comparison of mean velocity at $r/D = 0.5$, $r/D = 1$. Lines: numerical results; symbols: experiments by Cooper et al. [8].

In Figure 4.8, mean velocities in radial direction are presented for the round impinging jet case with $H/D = 2$. At $r/D = 0.5$, a change of the mean flow velocities from axial to radial direction is observed. At that stage, the comparison with experiments shows different quality fittings for the turbulence models used. However, in this position, the mean velocity is dominated by pressure and is only slightly affected by

Reynolds stresses. For this reason, predictions derived from the different turbulence models are similar. Downstream, at $r/D = 1$ position, only CLS ($k\epsilon$-NLEVM) and AJL ($k\omega$-NLEVM) fit the velocity peak. Furthermore, the rest of models give too much spreading of the jet because of the high levels of turbulence predicted in the stagnation zone [3].



(a) $k - \epsilon$ models.  (b) $k - \omega$ models.

**Figure 4.9:** Round jet, $Re = 230000$ and $H/D = 2$. Comparison of rms velocity at $r/D = 0.5$, $r/D = 1$. Lines: numerical results; symbols: experiments by Cooper et al. [8].

Fluctuating velocities are shown in Figure 4.9. As can be seen, LEVM overpredict fluctuating velocity values near stagnation point. Furthermore, at $r/D = 1.0$, it is illustrated that an adequate prediction of turbulent stresses contributes to capture more accurately mean velocity peak. Moreover, improvements of CLS ($k\epsilon$-NLEVM) in predicting fluctuating values (consequently turbulence energy), and AJL ($k\omega$-NLEVM), particularly in the impingement region ($x/B = 0.5$), result in a better prediction of $Nu$ number in this zone (see Figure 4.5). Thus, the analysis of rms values confirms that the model that overpredicts fluctuating velocity levels also produces an excessively rapid mixing. Moreover, it is found that the anisotropy of the Reynolds stresses predicted by NLEVM plays an important role in the production of turbulence kinetic energy at the jet centre line. As a result of the differences predicted for each

123
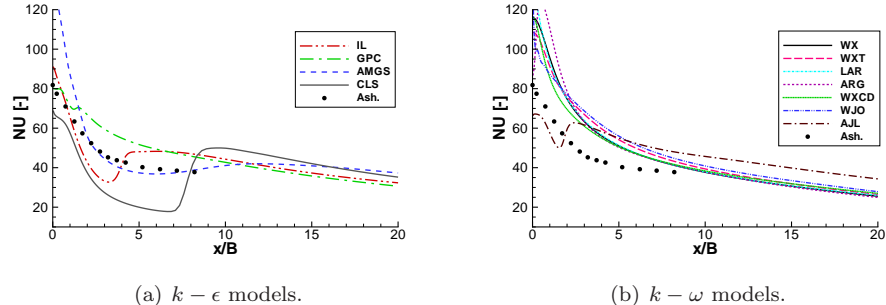
one of the normal stresses (anisotropy), $P_k$ becomes negative in the stagnation region, which is in accordance with experimental results presented by Geers et al. [23].

### 4.6.3 Influence of the aspect ratio

In this subsection the Reynolds number is maintained, but the aspect ratio is changed to test its influence on turbulence models performance. Thus, for the plane jet the new aspect ratio of $H/B = 9.2$ is studied, whereas for round jet the new aspect ratio is set to $H/D = 6$.

**Plane impinging jet, $Re_B = 20000$ and $H/B = 9.2$**

In Figure 4.10 local $Nu$ number results for the plane impinging jet case with $H/B = 9.2$ are shown. Similarly to the previous results presented in Figure 4.3 for the small aspect ratio of $H/B = 4$, results of $k - \epsilon$ models present a large scattering, and none of them reproduce adequately the experimental $Nu$ profile. Moreover, IL ($k\epsilon$-LEVM) and CLS ($k\epsilon$-NLEVM) incorrectly predict a secondary maximum for this quantity. As to $k - \omega$ models, all except AJL ($k\epsilon$-NLEVM) predict similar profiles overpredicting experimental data near stagnation region. Furthermore, AJL ($k\epsilon$-NLEVM) incorrectly presents a secondary maximum. Therefore, there are no advantages in using this platform (see Figure 4.10(b)), nor in the use of higher order terms in the constitutive relation used to calculate Reynolds stresses.



(a) $k - \epsilon$ models.  (b) $k - \omega$ models.

**Figure 4.10:** Plane jet, $Re_B = 20000$ and $H/B = 9.2$. Local Nusselt at the impingement plate. Lines: numerical results; symbols: experiments by Ashforth-Frost et al. [11].
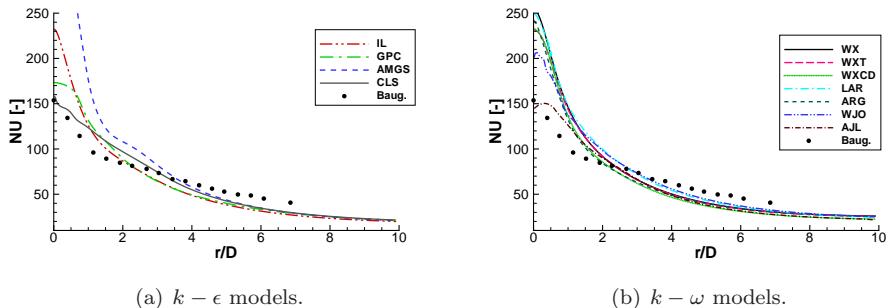
For this case, fluctuating (rms) velocities have also been studied. Profiles obtained are comparable to those shown in Figure 4.7 for $H/B = 4$. Thus, $k - \epsilon$ models present deficient results near bottom wall. On the other hand, LEVM $k - \omega$ models predict

streamwise rms velocity adequately at $x/B = 1$. However, downstream (at $x/B = 5$) $k - \omega$ models also under-predict it near the impingement plate, with exception of WJO ($k\omega$-EARSM) and AJL ($k\omega$-NLEVM) models that reproduce experimental rms data in this zone [45].

**Round impinging jet, $Re = 23000$ and $H/D = 6$**
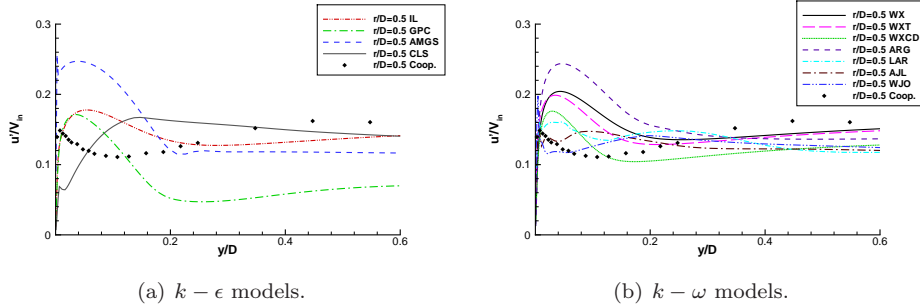
In Figure 4.11 local $Nu$ results for the round impinging jet configuration with $Re = 23000$ and $H/D = 6$ are shown. In general, the same trend observed for $H/D = 2$ (see Figure 4.5), is found for this aspect ratio. Thus, $k - \omega$ based models present poor predictions of the $Nu$ number at the stagnation region. However, AJL ($k\omega$-NLEVM) reproduces experimental data and WJO ($k\omega$-EARSM) slightly improves LEVM results (see Figure 4.11(b)). Whereas, among $k - \epsilon$ models, CLS ($k\epsilon$-NLEVM) correctly reproduces experimental data, followed by GPC ($k\epsilon$-LEVM). Once again, the use of CLS ($k\epsilon$-NLEVM) is necessary, or in this case AJL ($k\omega$-NLEVM), to obtain adequate results for the $Nu$ number near stagnation region (see Figures 4.5 and 4.11).



(a) $k - \epsilon$ models.　　　　(b) $k - \omega$ models.

**Figure 4.11:** Round jet, $Re = 23000$ and $H/D = 6$. Local Nusselt at the impingement plate. Lines: numerical results; symbols: experiments by Baughn and Shimizu [18].

Fluctuating velocities are considered in Figure 4.12. In line with the results of Figure 4.9, LEVM continue overestimating rms velocity near the stagnation region ($r/D = 0.5$). This difference can be attributed to the fact that models based on linear relations between turbulent stresses and the rate of strain do not account adequately for the sensitivity of the wall jet to streamline curvature effects [25].

Moreover, as can be seen in Figures 4.5 and 4.9 for $H/D = 2$, and also in Figures 4.11 and 4.12 for $H/D = 6$, the wall normal Reynolds stress plays an important role. An inaccurate evaluation of this component at impingement and reattachment

(a) $k - \epsilon$ models.

(b) $k - \omega$ models.

**Figure 4.12:** Round jet, $Re = 23000$ and $H/D = 6$. Streamwise fluctuating velocity component. Lines: numerical results; symbols: experiments by Cooper et al. [8].

points can give rise to important errors in the $Nu$ number [30]. However, this trend does not prevail downstream because of the inadequacy of LEVM it becomes less important as shear stress dominates turbulence energy production. Furthermore, far from stagnation regions the heat transfer rate is more influenced by shear stress and there is no clear connection with the normal Reynolds stresses.

### 4.6.4 Influence of Reynolds number
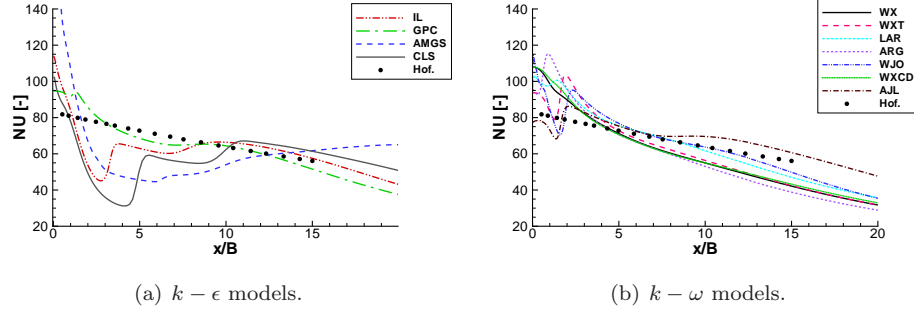
In order to check the generality of the models, a higher Reynolds number is imposed and its effects are analysed in both plane and round impinging jet configurations, keeping the same aspect ratios considered before.

**Plane impinging jet** $Re_B = 30000$, $H/B = 4$ **and** $H/B = 9.2$

For the plane impinging jet configuration a Reynolds number of $Re_B = 30000$ is studied. Analysis is centred in the lower aspect ratio of $H/B = 4$ due to the fact that there is no experimental information of the fluid-dynamic field for the larger aspect ratio of $H/B = 9.2$. However, illustrative results are also presented for the larger aspect ratio.
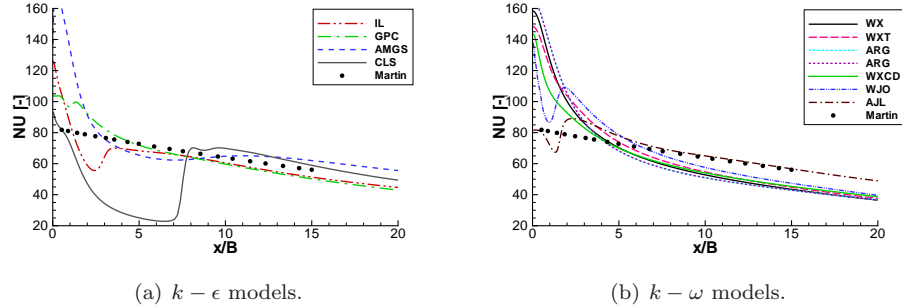
In Figure 4.13, the obtained local Nusselt number for $H/B = 4$ is compared with the empirical correlation presented by Hofmann et al. [46]: $Nu = 0.042Pr^{0.42}(Re_B^3 + 10Re_B^2)^{0.25}exp^{-0.052x/2B}$. This correlation presents an almost linear profile without the minimum and subsequent secondary peak which should exist. Furthermore, the aspect ratio is not taken into account in this expression. In general, behaviour of all models is similar to that shown for the plane jet at $Re_B = 20000$ already studied (see

(a) $k - \epsilon$ models.

(b) $k - \omega$ models.

**Figure 4.13:** Plane jet, $Re_B = 30000$ and $H/B = 4$. Local Nusselt at the impingement plate. Lines: numerical results; symbols: empirical correlation by Hofmann et al. [46].

Figure 4.3). Thus, it seems that CLS ($k\epsilon$-NLEVM) presents a delay in the transition. Conversely, WXT ($k\omega$-LEVM), WJO ($k\omega$-EARSM) and AJL ($k\omega$-NLEVM) present the secondary $Nu$ maximum too soon.



(a) $k - \epsilon$ models.

(b) $k - \omega$ models.

**Figure 4.14:** Plane jet $Re_B = 30000$ and $H/B = 9.2$. Local Nusselt for impingement plate. Lines numerical results and symbols empirical expression by Hofmann et al. [46].
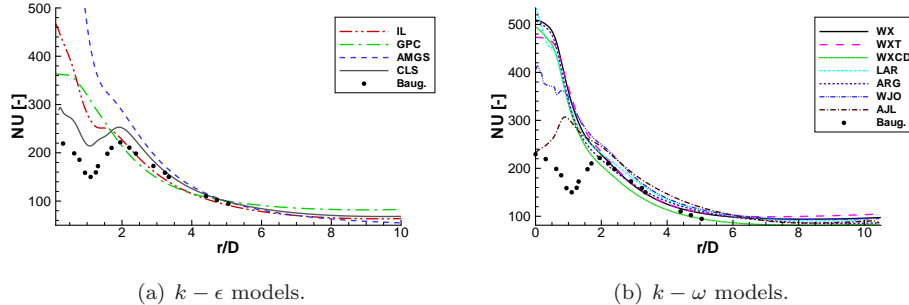
In Figure 4.14 local Nusselt number for $H/B = 9.2$ is also compared with the empirical correlation given by Hofmann et al. [46]. As shown, AJL ($k\omega$-NLEVM) and CLS ($k\epsilon$-NLEVM) predict adequately Nusselt at the stagnation region, and downstream in the redeveloping region ($x/B > 7$). However, the secondary maximum presented, incorrectly follows the same trend observed in Figures 4.3 and 4.10 for the plane jet at $Re_B = 20000$.

Concerning fluctuating velocity parallel to the wall, deficiencies observed for a Reynolds number of 20000 continue for this Reynolds number (see Figure 4.7). These results confirm the idea that a constitutive stress algebraic equation containing only velocity gradients, as a combination of strain and vorticity terms, is not enough to achieve a good representation of near-wall anisotropy in the presence of weak shear and strong normal straining associated with impingement and reattachment [30].

**Round impinging jet, $Re = 70000$, $H/D = 2$ and $H/D = 6$**

In this subsection, a higher Reynolds number of 70000 considering two aspects ratios of 2 and 6 is here studied for the round impinging jet case.

Firstly, the configuration with an aspect ratio of 2 is analysed. In Figure 4.15, a comparison of the local Nusselt number at the impingement plate with experimental data for $Re = 70000$ is presented. The performance exhibited by the models is similar to the one shown at the lower Reynolds number for this aspect ratio. However, two circumstances are highlighted: i) AJL ($k\omega$-NLEVM) incorrectly predicts Nusselt maximum far from stagnation region; ii) although CLS ($k\epsilon$-NLEVM) model overpredicts the $Nu$ in the stagnation region, it still predicts heat transfer in broadly satisfactory agreement with experiments.



(a) $k - \epsilon$ models.      (b) $k - \omega$ models.
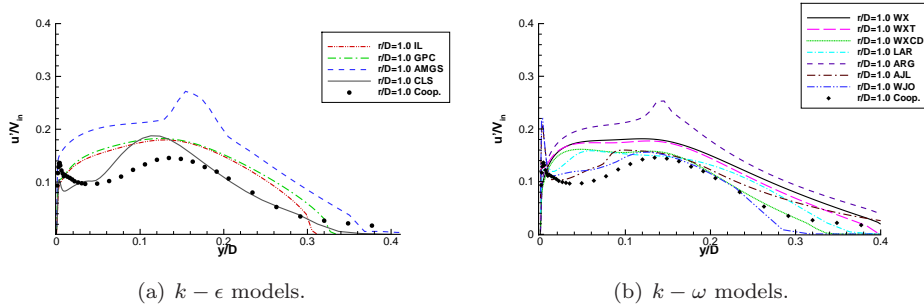
**Figure 4.15:** Round jet, $Re = 70000$ and $H/D = 2$. Local Nusselt at the impingement plate. Lines: numerical results; symbols: experiments by Baughn and Shimizu [18].

Analogous results for the streamwise fluctuating velocity to those shown in Figure 4.9 for a $Re = 23000$ are now observed for a higher Reynolds of 70000 and $H/D = 2$. Thus, the reason for the overprediction of $Nu$ around the stagnation zone can be understood from the predicted fluctuating velocity. For example, at $r/D \approx 0$ it is possible to observe that the models which overpredict fluctuating velocity, also overpredict $Nu$ near the stagnation point, e.g. IL ($k\epsilon$-LEVM), GPC ($k\epsilon$-LEVM),

WX ($k\omega$-LEVM), WXT ($k\omega$-LEVM), etc. On the other hand, CLS ($k\epsilon$-NLEVM) and AJL ($k\omega$-NLEVM) models return near-wall values closer to the experimental data allowing a more accurate prediction of $Nu$ in the stagantion region.



(a) $k - \epsilon$ models.

(b) $k - \omega$ models.
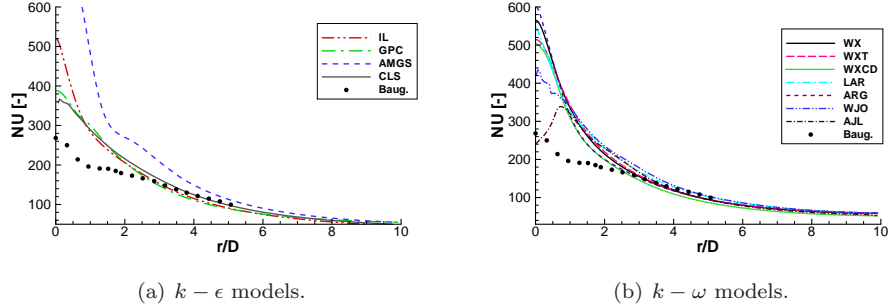
**Figure 4.16:** Round jet, $Re = 70000$ and $H/D = 2$. Streamwise fluctuating velocity component at $r/D = 0.0$ and $r/D = 1$. Lines: numerical results; symbols: experiments by Cooper et al. [8].

Furthermore, plotted rms values at $r/D = 1$ are shown in Figure 4.16, where the minimum $Nu$ according to experiments is located. From this Figure it is possible to relate the rms velocity with the erroneous maximum presented by AJL ($k\omega$-NLEVM) for the local $Nu$ far from the stagnation region. As shown, the AJL ($k\omega$-NLEVM) exhibits a pronounced peak near the wall, which generates a significant increment in the turbulence level and, therefore, a positive step gradient in the $Nu$ profile. Thus, this model improves results near stagnation region, but still presents problems downstream in strongly accelerating zones for $Re = 70000$. However, the connection between fluctuating velocity and local $Nu$ downstream is not evident for the lower Reynolds number of 23000 (see Figures 4.5(b) and 4.9).

The analysis is now focussed on the case with $H/D = 6$. Figure 4.17 shows Nu number distribution for $Re = 70000$. Even though AJL ($k\omega$-NLEVM) improves Nusselt number predictions of LEVM at the stagnation point, it also incorrectly predicts a maximum far downstream again. Furthermore, local $Nu$ profile predicted using CLS ($k\epsilon$-NLEVM) is not as good as the results obtained with $H/D = 2$, specially near stagnation region. Thus, comparing Figures 4.5 and 4.11 with Figures 4.15 and 4.17 respectively, it is observed that the performance of the models is degraded when the Reynolds number increases.

In Table 4.4 non-dimensional turbulent viscosity near the bottom wall for two radial positions (jet centreline and $r/D = 1$) is presented. It is used to illustrate once again the relation between turbulence level and impingement plate heat transfer in the situation under consideration. As shown, there is a connection between local

(a) $k - \epsilon$ models.



(b) $k - \omega$ models.

**Figure 4.17:** Round jet, $Re = 70000$ and $H/D = 6$. Local Nusselt at the impingement plate. Lines: numerical results; symbols: experiments by Baughn and Shimizu [18].

| | Turbulence model | | | | | | | | | | |
|---|---|---|---|---|---|---|---|---|---|---|---|
| Posit. | IL | GPC | AMGS | CLS | WX | WXT | WXCD | LAR | ARG | AJL | WJO |
| $\frac{r}{D} \approx 0$ | 21.2 | 16.9 | 108.9 | 8.5 | 41.5 | 42.3 | 34.0 | 32.9 | 48.3 | 1.1 | 11.3 |
| $\frac{r}{D} = 1$ | 8.2 | 6.4 | 21.7 | 7.6 | 10.0 | 10.5 | 6.7 | 8.9 | 11.2 | 6.7 | 9.2 |

**Table 4.4:** Round jet, $Re = 70000$ and $H/D = 6$. Non-dimensional turbulent viscosity ($\mu_t/\mu$) at the jet centreline and at $r/D = 1$ for $y/D = 0.005$.

$Nu$ and turbulent viscosity at both positions. At the stagnation region, where heat transfer predicted agrees with experimental data, AJL ($k\omega$-NLEVM) presents a turbulent viscosity similar to the molecular one. Downstream a marked increase of the turbulence level near the bottom wall at $r/D = 1$ seems to be the reason for the local Nusselt number peak predicted by the AJL ($k\omega$-NLEVM). On the other hand, the rest of the models present a high eddy viscosity value at the stagnation region that decreases downstream.

## 4.7   Conclusions

Both plane and round turbulent impinging jets have been simulated using LEVM, NLEVM and EARSM, based on $k - \epsilon$ as well as $k - \omega$ platforms, and using representative models of each formulation. A verification procedure has been applied in order to ensure credibility of numerical results obtained.

The correct prediction of the second peak in Nusselt number is related with the

increase of turbulence levels near the bottom wall. In some models, such as IL ($k\epsilon$-LEVM), CLS ($k\epsilon$-NLEVM), WXT ($k\omega$-LEVM) and AJL ($k\omega$-NLEVM), an increase of turbulence near the place where the second maximum of Nusselt appears is detected. Thus, a connection between Reynolds stresses, turbulence level and heat transfer is observed.

Reviewing the wall heat-transfer coefficient, local Nusselt number, in both plane and round impinging jet configurations, it is possible to observe the lack of generality of the models. In fact, models with good performance in the round jet case show poor results in the plane jet configuration.

Part of the reason for the poor performance of AMGS ($k\epsilon$-EARSM) model may be the fact the $k - \epsilon$ formulation in general does not handle very well wall-bounded adverse pressure gradients without wall damping functions and additional terms to improve its performance near solid walls.

The limitations of LEVM are more relevant at low aspect ratios, specially for the round impinging jet configuration. Furthermore, the cases studied show that the behaviour of NLEVM is better for the round impinging jet, whereas, as it was said before, their improvements are limited in the plane jet configuration.

Finally, for the kind of flows under consideration, the effect of including the cross-diffusion term in the WXCD ($k\omega$-LEVM) is only remarkable in the evaluation of fluctuating velocities. Furthermore, throughout this work it has been found that models based on the $k - \omega$ platform produce less scattered results.

## Acknowledgements

## References

[1] Y. J. Jang, M. A. Leschziner, K. Abe, and L. Temmerman. Investigation of Anisotropy-Resolving Turbulence Models by Reference to Highly-Resolved LES data for Separated flow. *Flow, Turbulence and Combustion*, 69(2):161–203, 2002.

[2] S.B. Pope. *Turbulent Flows*. Cambridge University Press, 2000.

[3] T. J. Craft, H. Iacovides, and J. H. Yoon. Progress in the Use of Non-linear Two-Equation Models in the Computation of Convective Heat-Transfer in Impinging and Separated Flows. *Flow, Turbulence and Combustion*, 63(1):59–81, 1999.

[4] R. Abid, J.H. Morrison, T.B. Gatski, and C.G. Speziale. Prediction of Aerodynamic FLows with a New Explicit Algebraic Stress Model. *AIAA Journal*, 34(12):2632–2635, 1996.

[5] J. P. Van Doormal and G. D. Raithby. Enhancements of the Simple Method for Predicting Incompressible Fluid Flows. *Numerical Heat Transfer*, 7:147–163, 1984.

[6] J. Cadafalch, C. D. Pérez-Segarra, R. Cònsul, and A. Oliva. Verification of Finite Volume Computations on Steady State Fluid Flow and Heat Transfer. *Journal of Fluids Engineering*, 124(11):11–21, 2002.

[7] J. Zhe and V. Modi. Near Wall Measurements for a Turbulent Impinging Slot Jet. *Journal of Fluids Engineering*, 123(1):112–120, 2001.

[8] D. Cooper, D.C. Jackson, B.E. Launder, and G.X. Liao. Impingement Jet Studies for Turbulence Model Assessment–I. Flow-field Experiments. *International Journal of Heat and Mass Transfer*, 36(10):2675–2684, 1993.

[9] R. Gardon and J. C. Akfirat. Heat Transfer Characteristics of Impinging Two-Dimensional Air Jets. *Journal of Heat Transfer - Transactions of Asme*, 88(1):101–108, 1966.

[10] A.R.P. Van Heiningen. *Heat transfer under impinging slot jet*. PhD thesis, McGill University, 1982.

[11] S. Ashforth-Frost, K. Jambunathan, and C. F. Whitney. Velocity and Turbulence Characteristics of a Semiconfined Orthogonally Impinging Slot Jet. *Exp. Thermal and Fluid Science*, 14(1):60–67, 1997.

[12] K. Heyerichs and A. Pollard. Heat transfer in separated and impinging turbulent flows. *International Journal of Heat and Mass Transfer*, 39(12):2385–2400, 1996.

[13] S.M. Hosseinalipour and A. S. Mujumdar. Comparative Evaluation of Different Turbulence Models For Confined Impinging and Opposing jet Flows. *Numerical Heat Transfer, Part A*, 28:647–666, 1995.

[14] S. H. Seyedin, M. Hasan, and A. S. Mujumdar. Modelling of a Single Confined Turbulent Slot Jet Impinging Using Various k-$\epsilon$ Turbulence Models. *Applied Mathematical Modelling*, 18:526–537, 1994.

[15] Y. Shi, M.B. Ray, and A.S. Mujumdar. Computational Study of Impingement Heat Transfer under a Turbulent Slot Jet. *Industrial and Engineering Chemistry Research*, 41:4643–4651, 2002.

*References*

[16] S. R. Marthur and J. Y. Murthy. Pressure Boundary Conditions for Incompressible Flow Using Unstructured Meshes. *Numerical Heat Transfer, Part B*, 32:283–298, 1997.

[17] K. Martin. Heat and Mass Transfer Between Impinging Gas Jets and Solid Surfaces. *Advances in Heat Transfer*, 13:1–60, 1977.

[18] J. W. Baughn and S. Shimizu. Heat Transfer Measurements From a Surface with Uniform Heat Flux and an Impinging Jet. *ASME J. Heat Transfer*, 111:1096–1098, 1989.

[19] J. Baughn, A. Hechanova, and X. Yan. An experimental Study of Entrainment Effects on the Heat Transfer from a Flat Surface to a Heated Circular Impinging Jet. *Journal of Heat Transfer - Transactions of Asme*, 113:1023–1025, 1991.

[20] R. Viskanta. Heat Transfer to Impinging Isothermal Gas and Flame Jets. *Exp. Thermal and Fluid Science*, 6:111–134, 1993.

[21] D. Lytle and B. Webb. Air Jet Impingement Heat Transfer at Low Nozzle-Plate Spacings. *International Journal of Heat and Mass Transfer*, 37:1687–1697, 1994.

[22] M. Fairweather and G. K. Hargrave. Experimental Investigation of an Axisymmetric, Impinging Turbulent Jet. 1. Velocity Field. *Experiments in Fluids*, 33(3):464–471, 2002.

[23] F. G. Geers, M. J. Tummers, and K. Hanjalic. Experimental Investigation of Impinging Jet Arrays. *Experiments in Fluids*, 36(6):946–958, 2004.

[24] T. Craft, L. Graham, and B. Launder. Impinging Jet Studies for Turbulence Model Assessment-II. An Examination of the Performance of Four Turbulence Models. *International Journal of Heat and Fluid Flow*, 36(10):2685–2697, 1993.

[25] M. Dianat, M. Fairweather, and W. P. Jones. Predictions of Axisymmetric and Two-Dimensional Impinging Turbulent Jets. *International Journal of Heat and Fluid Flow*, 17(6):530–538, 1996.

[26] M. Behnia, S. Parneix, and P. A. Durbin. Prediction of Heat Transfer in an Axisymmetric Turbulent Jet Impinging on a Flat Plate. *International Journal of Heat and Mass Transfer*, 41(12):1845–1855, 1998.

[27] A. Abdon and B. Sundén. Numerical Investigation of Impingement Heat Transfer using Linear and Non-Linear Two-equation Turbulence Models. *Numerical Heat Transfer, Part A*, 40(6):563–578, 2001.

[28] D.C. Wilcox. *Turbulence modeling for CFD*. DCW Industries, Inc. CA, 1998.

133

[29] T.J. Craft, B.E. Launder, and K. Suga. Development and Application of Cubic Eddy-Viscosity Model of Turbulence. *International Journal of Heat and Fluid Flow*, 17(1):108–115, 1996.

[30] K. Abe, Y. J. Jang, and M. A. Leschziner. An Investigation of Wall-Anisotropy Expressions and Length-Scale Equations for Non-Linear Eddy-Viscosity Models. *International Journal of Heat and Fluid Flow*, 24(2):181–198, 2003.

[31] N.Z. Ince and B.E. Launder. Computation of Buoyancy-Driven Turbulent Flows in Rectangular Enclosures. *International Journal of Heat and Fluid Flow*, 10(1):110–117, 1989.

[32] U. Goldberg, O. Peroomian, and S. Chakravarthy. A Wall-Distance-Free k-$\epsilon$ Model with Enhanced Near-Wall Treatment. *Journal of Fluids Engineering*, 120(3):457–462, 1998.

[33] D. C. Wilcox. Reassessment of the Scale-Determining Equation for Advanced Turbulence Models. *AIAA Journal*, 26:1299–1310, 1988.

[34] D. C. Wilcox. Simulation of Transition with a Two-Equation Turbulence Model. *AIAA Journal*, 32:247–255, 1994.

[35] J. Larsson. Two-Equation Turbulence Models for Turbine Blade Heat Transfer Simulations. In *Proceedings 13th ISABE Conference*, pages 1214–1222, 1997.

[36] R. Abid, C. Rumsey, and T.B. Gatski. Prediction of Nonequilibrium Turbulent FLows with Explicit Algebraic Stress Models. *AIAA Journal*, 33(11):2026–2031, 1995.

[37] S. Wallin and A. V. Johansson. An Explicit Algebraic Reynolds Stress Model for Incompressible and Compressible Turbulent Flows. *Journal of Fluid Mechanics*, 403:89–132, 2000.

[38] S. V. Patankar. *Numerical Heat Transfer and Fluid Flow*. Hemisphere Publishing Corporation, 1980.

[39] M. S. Darwish and F. Moukalled. An Efficient Very-High Resolution Scheme Based on an Adaptive-Scheme Strategy. *Numerical Heat Transfer, Part B*, 34(2):191–213, 1998.

[40] M. Soria. *Parallel multigrid algorithms for computational fluid dynamics and heat transfer*. PhD thesis, Universitat Politècnica de Catalunya, 2000.

[41] C.D. Pérez-Segarra, A. Oliva, M. Costa, and F. Escanes. Numerical experiments in turbulent natural and mixed convection in internal flows. *International Journal for Numerical Methods for Heat and Fluid Flow*, 5(1):13–33, 1995.

*References*

[42] J. E. Jaramillo, C. D. Pérez-Segarra, A. Oliva, and K. Claramunt. Analysis of Different RANS Models Applied to Turbulent Forced Convection. *International Journal of Heat and Mass Transfer*, 50(19-20):3749–3766, 2007.

[43] T. H. Park, H.G. Choi, J.Y. Yoo, and S.J. Kim. Streamline Upwind Numerical Simulation of Two-Dimensional Confined Impinging Slot Jets. *International Journal of Heat and Mass Transfer*, 46(2):251–262, 2003.

[44] B. Merci, C. De Langhe, K. Lodefier, and E. Dick. Heat Transfer Predictions with a Cubic $k-\epsilon$ Model for Axisymmetric Turbulent Jets Impinging Onto a Flat Plate. *International Journal of Heat and Mass Transfer*, 46(3):469–480, 2003.

[45] J. E. Jaramillo, C. D. Pérez Segarra, and A. Oliva. Simulation of Flow and Heat Transfer in Impinging Jets Using RANS models. In *Proceedings of the V International Symposium on Turbulence, Heat and Mass Transfer*, pages 445–448, 2006.

[46] H. Hofmann, M. Kind, and H. Martin. Measurements on Steady State Heat Transfer and Flow Structure and New Correlations for Heat and Mass Transfer in Submerged Impinging Jets. *International Journal of Heat and Mass Transfer*, 50(19):3957–3965, 2007.

*References*

136
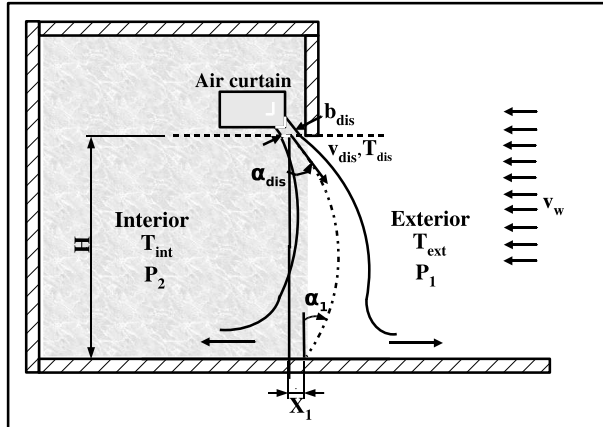
# Chapter 5

# Air curtains. Experiments and code validation.

**Abstract.** The main purpose of this chapter is to characterize in detail actual air curtains using both experimental and different types of numerical approaches. At the beginning semi-empirical models to design air curtains are shown. After that, multidimensional mathematical models based on the numerical solution of the Navier-Stokes equations using CFD are briefly summarized. Then, an experimental setup used in the study of air curtain discharge and jet downstream is explained. Measurements of different air curtian prototypes are presented in order to characterize the air-curtain fluid-dynamic and thermal fields. The technique used in velocity measurement, which is hot wire constant temperature anemometry, is introduced. Furthermore, thermal field is assessed with thermocouples type K located in several planes within adapted chamber, as well as at air inlet and outlet sections. Finally, air curtains are simulated using CFD and the mathematical formulation is validated with experimental data acquired.

## 5.1 Introduction

The principle of an air curtain mounted in buildings doorway, is to supply a jet over the whole opening with sufficient momentum to counter the pressure force across it due to wind, buoyancy and the pressure difference due to ventilation system across the opening. The design of air curtains depends on the installation site and on the size of the opening. In supermarkets, or public buildings, the velocity must be low. For industrial applications like furnace, refrigeration storage or fire security in tunnels, the velocity may be higher and the jet thicker. The air blown across the doorway can be drawn from outside the building or it can be indoor air. The air curtain can be designed as a recirculating system, where the jet is directed to the exhaust opening and a portion of the air is allowed to recirculate in the system. However, in most of the systems, the air blows partly into interior space and partly out of the building. The jet can be heated to improve comfort conditions (people through the opening). According to the jet temperature, the system can be said to be warm air curtain or cold air curtain.



**Figure 5.1:** Schematic representation of an air curtain.

The temperature difference between the spaces creates a pressure difference that drives air through the doorway, while the wind creates a second fluctuating pressure component. Additional factors to be taken into account in the design of air curtains are the space height, the building leakage characteristics and the influence of the ventilation system (the effect of imbalanced ventilation can be strong and deflect the jet inwards or outwards) [1]. Therefore, in the technical dimensioning of an air curtain both a fluid mechanical approach and a thermal approach is needed. In the first case,

it is necessary to determine the pressure differences across the opening for some given weather conditions, so fixing the required nozzle width, jet velocity exit and discharge angle. In the thermal dimensioning, it is important to establish energy losses. The heat loss through opening with the air curtain system is due to jet turbulence level and net mass flow across it. Because air is entrained into the jet from both sides, in part because of mixing process and part when the jet hits the floor, the air curtain can not totally prevent heat and/or mass transport across the doorway, but remarkably reduce them.

In this Chapter, different possibilities to study air curtains are introduced. Firstly, semi-analytical mathematical models used as a fast tool to design air curtains are presented. Afterwards, multidimensional mathematical models involving the solution of the Navier-Stokes equations using CFD are shown. Then, an experimental setup adapted in order to study air curtains is explained and measurements carried out are presented. Finally, the experimental setup is numerically reproduced using CFD and predictions compared with experimental data in order to validate mathematical formulation used in the CFD approach.

## 5.2 Semi-analytical mathematical models

The best option for analyzing and optimizing air curtains is for sure the simulation of the flow by the use of computational fluid mechanics (CFD). But three dimensional CFD simulations of the fluid flow induced by an air curtain device is time consuming and needs large computational resources. Skilled personal familiar with CFD is also required. As these requisites are not always given in industrial environments, companies often have to use more simple techniques. This simplified model only considers main boundary conditions, as the outside and inside temperature, building characteristics and wind induced forces, and gives an estimation for the major variables needed for a technical dimensioning of the air curtain. The results obtained with this model are immediate. However, it only delivers the values needed for the dimensioning and the heat exchange through the curtain. It does not give any further information needed for an optimization in terms of energy-saving.

Air curtains direct the air toward the incoming at an angle ranging from 12 to 45 grades according to user necessities [2]. They can supply heated air, air at room temperature, or air at the outdoor temperature. Air curtains with heated air are recommended for doors smaller than 3.6 by 3.6 m and for more than five aperture times or for longer than 40 minutes during 8 hours shift. Also those which are designed for regions with low winter temperatures. Air curtains that supply unheat indoor air have application in spaces: with a heat excess, with temperature stratification over the room height and in regions with a mild climate [2].

As it was said, air curtain must have the moment necessary to counter pressure

forces. Thus, the momentum of the air curtain discharge jet can be expressed as:

$$M_{dis} = \rho v_{dis}^2 W b_{dis} \tag{5.1}$$

where,

- $v_{dis}$ =discharge velocity.

- $W$ =length of supply slot (depth).

- $b_{dis}$ =effective width of supply slot (see figure 5.1).

- $\rho$ =density air supply.

If the jet is set a discharge angle $\alpha_{dis}$, by assuming conservation of the jet momentum and that the discharge angle is equal to the negative impact angle ($\alpha_{dis} = \alpha_1$), its change in a direction normal to the plane of the opening is (see Figure 5.1) [2]:

$$F_M = 2\rho v_{dis}^2 W b_{dis} sin\alpha_{dis} \tag{5.2}$$

Applying momentum balance for a control volume in the doorway, $F_M$ must be at least equal to the force due to pressure difference ($F_P$), to prevent air flow across the jet, $F_P = WH\Delta p_t$, where $H$ is the opening height and $\Delta p_t = p_2 - p_1$ is the total pressure difference (see figure 5.1).

With $F_M = F_P$ or $\sum F_P = \int_{cs} \rho v_x \bar{v} \cdot d\bar{A}$, the supply velocity $v_{dis}$ will be:

$$2\rho v_{dis}^2 W b_{dis} sin\alpha_{dis} = WH\Delta p_t$$

$$v_{dis} = \sqrt{\frac{H}{b_{dis}} \frac{\Delta p_t}{2\rho sin\alpha_{dis}}} \tag{5.3}$$

From equation 5.3 it can be seen that $v_{dis}$ depend on $b_{dis}$ and $\alpha_{dis}$ for a given value of $H, \Delta p_t$ and $\rho$.

The pressure difference ($\Delta p_t$) is calculated in an analytical way, and expressed as the sum $\Delta p_t = p_w + p_s + \Delta p_m$, being

- Wind pressure ($p_w$): Wind impacting on the building.

- Stack pressure ($p_s$): Difference in temperature (densities) between air inside and outside the building.

- Mechanical pressure ($\Delta p_m$): Pressure between the air supply and extract terminals, due to ventilation system.

A different approach is proposed by Sirén [1], who has taken moment-of-momentum balance in the doorway, assuming conservation of angular momentum. The results are slightly different but the model includes the same empirical limitations. The general moment-of-momentum is the cross product of the forces $F$ acting on a control volume and the vectors of position $r$ from a given point of rotation.

$$\sum \bar{r} \times \bar{F}_P = \int_{cs} \rho \bar{r} \times \bar{v} \bar{v} \cdot d\bar{A} \tag{5.4}$$

Which in a two-dimensional case yields [1]:

$$\sum r_n F_P = \int_{cs} \rho r_n v^2 dA \tag{5.5}$$

Where $r_n$ is the normal distance from the point of rotation to the corresponding force or velocity vector. If the impact point is chose as the point of rotation the right part of equation 5.5 gives:

$$\sum r_n F_P = \rho W b_{dis} v_{dis}^2 sin\alpha_{dis} H - \rho W b_{dis} v_{dis}^2 cos\alpha_{dis} X_1 \tag{5.6}$$

Where $X_1$ is the distance of the point of impact from the doorway. Comparing equation 5.6 with equation 5.3 the difference is that no assumption about impact angle is necessary, instead the impact point is included now ($X_1 = \pm 0.208\sqrt{b_{dis}H}$).

## 5.2.1 Wind pressure ($p_w$)

It is the force due to the impact of air against the building. It can be obtained from:

$$p_w = C_p \frac{\rho_{ext} v_w^2}{2} \tag{5.7}$$

where: $v_w$ is the wind speed at datum level (height of building or opening), $\rho_{ext}$ is the exterior ambient density and $C_p$ is static pressure coefficient. This coefficient is determined by: building geometry, wind velocity (speed and direction) relative to the building and location of the building respect to other buildings, the topography and roughness of the terrain in wind direction. $C_p$ is obtained from tables or correlations extracted from wind tunnel experimental data in scaled prototypes. Swami and Chandra [3] proposed the following empirical relation:

$$C_p = 0.6 * ln(1.248 - 0.703 sin\frac{\beta}{2} - 1.175 sin^2\beta + 0.131 sin^3(2\beta G) + \tag{5.8}$$

$$0.769 cos\frac{\beta}{2} + 0.07 G^2 sin^2\frac{\beta}{2} + 0.717 cos^2\frac{\beta}{2})$$

Where, $\beta$ is wind incidence angle. $G = ln(S) = ln(L_1/L_2)$. Where $S$ is side ratio of the lengths of adjacent walls $L_1$ and $L_2$ of the building. The determination of this coefficient is one of the most complicated tasks in designing air curtains.

Natural wind has a highly turbulent character and if a time-mean speed is defined this is found to vary with height from the ground depending on the roughness of the terrain over which the wind passes [2]. Mean velocity $v_w$ can be obtained from [2]:

$$\frac{v_w}{v_r} = cH^a \tag{5.9}$$

where: $v_r$ is mean wind speed measured at a weather station (usually 10 meters above ground), and $c$ and $a$ are terrain dependent constants (see table 5.1) and $H$ is the building height where $v_w$ is needed.

| Terrain | $c$ | a |
|---|---|---|
| Open flat country | 0.68 | 0.17 |
| Country with scattered wind breaks | 0.52 | 0.20 |
| Urban | 0.35 | 0.25 |
| City | 0.21 | 0.33 |

**Table 5.1:** Terrain factors for equation 5.9 from [4]

## 5.2.2 Stack pressure ($p_s$)

The pressure due to buoyancy effect is an additional component, which controls the air leakage through the contour of building. Neglecting the effect of the vertical distribution in the indoor temperature, the pressure difference across the facade ($p_s$) becomes a linear function of the vertical coordinate ($z$). This pressure difference can be expressed as:

$$p_s = p_i(z) - p_o(z) = (\rho_o - \rho_i)gz + (p_{ig} - p_{og}) \tag{5.10}$$

where $\rho_o$ and $\rho_i$ are the exterior and interior air densities, $g$ is the acceleration due to gravity, $z$ is the height from the ground level $p_{og}$ the exterior pressure and $p_{ig}$ is interior pressure on the ground level. The neutral pressure level ($z_{ns}$), which is the height where the pressure difference over the building facade equals zero, is

$$z_{ns} = \frac{(p_{ig} - p_{og})}{(\rho_o - \rho_i)g} \tag{5.11}$$

Once $z_{ns}$ is known the stack pressure becomes

$$p_s = (\rho_o - \rho_i)g(z - z_{ns}) \tag{5.12}$$

The neutral pressure level can be evaluated as a function of the leakage characteristics of the building:
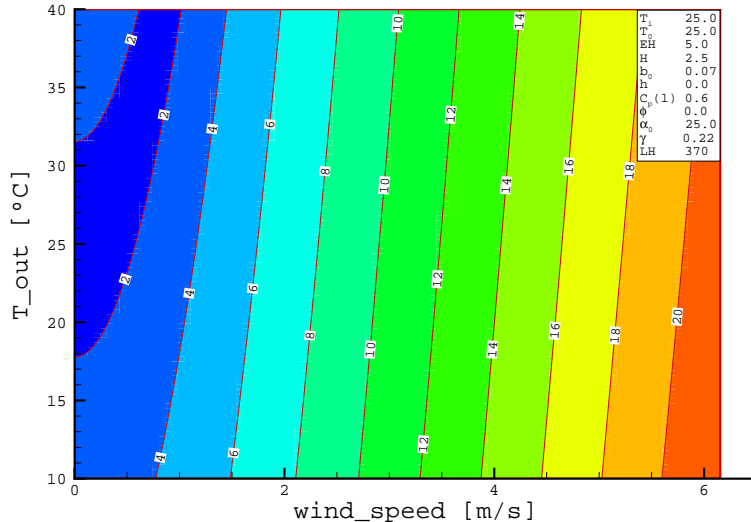
$$z_{ns} = \frac{(A_u/A_1)^m H_u + H_1}{(A_u/A_1)^m + 1} \tag{5.13}$$

where $A_u$ and $A_1$ are the total leakage areas of the upper zone and lower zone, $H_u$ and $H_1$ corresponding area-weighed vertical distances from the ground level and $m$ is the inverse of the flow exponent, characteristic of the flow type, $m = 2$ for turbulent flows and $m = 1$ for laminar flows.

### 5.2.3 Mechanical pressure ($\Delta p_m$)
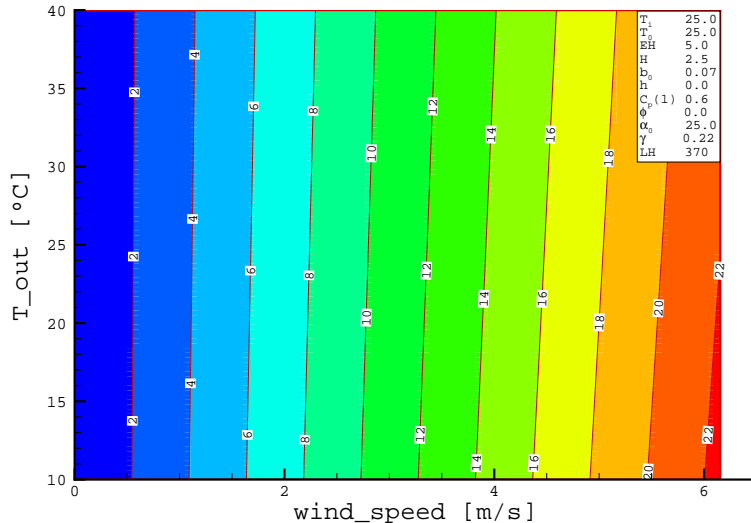
The mechanical pressure can be determined from the difference in pressure between the air supply and extract terminals of the ventilation system. The air infiltration or exfiltration rate created by a mechanical extract or supply fan on a building can be determined by matching the characteristic curve of the fan with th air leakage curve of the building [2].

### 5.2.4 Illustrative results



**Figure 5.2:** Discharge velocity contours obtained assuming conservation of angular momentum. $H = 2.5m$ , $b_0 = b_{dis}$=7cm , $\alpha_0 = \alpha_{dis} = \pm 25°$

143

Figure 5.2 shows the discharge velocity predicted using conservation of angular momentum proposed by Sirén (eq. 5.6) [1], for a discharge angle of $25°$, an indoor temperature of $25°C$, and a variable outdoor temperature varying, plotted on the y-axis. On the x-axis the wind velocity lies between no wind at all and approximative $6m/s$, which corresponds to a wind velocity of $10m/s$ measured at a meteorological station. The air for the jet is taken from the inside, its temperature is not changed. The door height is $2.5m$ and the nozzle width $7cm$. The building is assumed to be non-leaky or to have an even vertical leakage distribution.



**Figure 5.3:** Discharge velocity contours obtained assuming conservation of linear momentum. $H = 2.5m$ , $b_0 = b_{dis} = 7$cm , $\alpha_0 = \alpha_{dis} = \pm 25°$

Figure 5.3 shows the different discharge velocities for the same input parameters as for the anterior case but obtained with the more simple assumption of conservation of linear momentum (Eq. 5.3).

As shown, taking the air for the jet from the inside, the simpler Equation 5.3 predicts lower discharge velocities than Equation 5.6. This is because discharge velocities predicted by Equation 5.3 are independent of the temperature difference for an airtight building.

Although, results are not presented, some shortcomings of the simplified models are observed, e.g. the necessary discharge velocity gets lower as the discharge angle increases. It is true that the initial momentum in x-direction increases with a higher

144
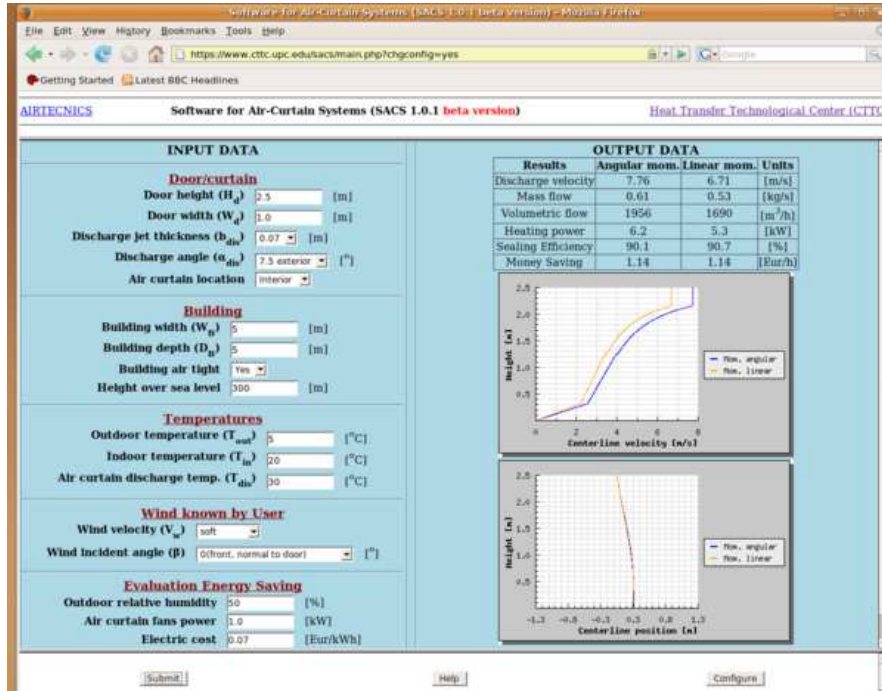
**Figure 5.4:** Interface designed to use semi-analytical model.

discharge angle, in that case also the track of the jet gets longer. The model does not take this into account and therefore does not take into account the optimization problem that actually lies behind the selection of the right angle.

### 5.2.5 Web interface designed

An interface has been created in order to allow the use of developed semi-analytic model through Internet. The software is called Software for Air-Curtains Systems (SACS). In Figure 5.4 is shown the interface as it appears in the Web Browser. The page is composed of two main blocks, the left side is used to introduce required input data to run the program. Whereas, in the right side output data are presented. At current stage, the interface is not designed for the final customer, but to the partner company. The program is designed to give the discharge velocity of the air curtain when the environment and geometry of the air curtain are known (calculated using both procedures explained). Furthermore, a graphic representation of the air curtain

145

jet centerline velocity decay and centerline position is included. Moreover, sealing efficiency of the air curtain evaluated using empirical correlations and costs savings in terms of energy are given as output data.

## 5.3   Advanced multidimensional mathematical model

In this section a brief summary of the mathematical formulation used to carry out CFD computations of air curtains is presented. Multidimensional mathematical models are introduced together with turbulence models applied for the solution of turbulence (for more details see Chapter 2).

$$\frac{\partial \bar{u}_i}{\partial x_i} = 0 \tag{5.14}$$

$$\frac{\partial \bar{u}_i}{\partial t} + \bar{u}_j \frac{\partial \bar{u}_i}{\partial x_j} = -\frac{1}{\rho}\frac{\partial \bar{p}_i}{\partial x_i} + \frac{1}{\rho}\frac{\partial}{\partial x_j}\left(2\mu \bar{S}_{ij} - \rho\overline{u_i' u_j'}\right) - \beta(T - T_o)g_i \tag{5.15}$$

$$\frac{\partial \bar{T}}{\partial t} + \bar{u}_i \frac{\partial \bar{T}}{\partial x_i} = \frac{1}{\rho c_p}\frac{\partial}{\partial x_i}\left(\lambda\frac{\partial \bar{T}}{\partial x_i} - c_p\rho\overline{u_i' T'}\right) \tag{5.16}$$

$$\frac{\partial(\rho k)}{\partial t} + \frac{\partial(\rho\bar{u}_i k)}{\partial x_i} = \frac{\partial}{\partial x_i}\left[\left(\mu + \frac{\mu_t}{\sigma_k}\right)\frac{\partial k}{\partial x_i}\right] + P_k - \rho Dis \tag{5.17}$$

$$\frac{\partial(\rho\tilde{\epsilon})}{\partial t} + \frac{\partial(\rho\bar{u}_i\tilde{\epsilon})}{\partial x_i} = \frac{\partial}{\partial x_i}\left[\left(\mu + \frac{\mu_t}{\sigma_\epsilon}\right)\frac{\partial \tilde{\epsilon}}{\partial x_i}\right] + f_1 C_{\epsilon 1}\frac{\tilde{\epsilon}}{k}P_k - f_2 C_{\epsilon 2}\rho\frac{\tilde{\epsilon}^2}{k} + E + Y_c \tag{5.18}$$

$$\frac{\partial(\rho\omega)}{\partial t} + \frac{\partial(\rho\bar{u}_i\omega)}{\partial x_i} = \frac{\partial}{\partial x_i}\left[\left(\mu + \frac{\mu_t}{\sigma_\omega}\right)\frac{\partial \omega}{\partial x_i}\right] + \alpha\frac{\omega}{k}P_k - \beta\rho\omega^2 + E_\omega \tag{5.19}$$

$$\mu_t = C_\mu f_\mu \frac{\rho k^2}{\epsilon} = \alpha^*\frac{\rho k}{\omega} \tag{5.20}$$

In these models the set of equations (continuity (5.14), momentum (5.15), energy (5.16) and turbulent quantities (5.17, 5.18 or 5.19)) are transformed to algebraic equations using a general fully implicit finite-volume technique. They are solved using a structured and staggered grid, applying fully implicit time integration. A structured grid of NxM control volumes for the scalar variables ($T, k, \epsilon$ or $\omega$) has been used and a staggered grid in the $x$ and $y$ directions has been employed to compute the $u$ and $v$ velocities respectively. Due to the presence of internal solids obstacles and/or inlet and outlet ports, the domain is divided into zones where the CV-lines are concentrated symmetrically or partially over its right or left side using a tanh-like function [5]. A pressure based method of the SIMPLE (Semi-implicit Method for Pressure-Linked Equations)[6] family is applied to couple the velocity and pressure fields central differences are employed for the evaluation of diffusion

terms and convective terms are discretized using upwind or power law [6] scheme. A multi-grid iterative solver is used to solve the algebraic linear system of equations in a segregated manner (for further details see Chapter 2).

In the $k$ and $\epsilon$ or $\omega$ equations the source terms are linearised: $S_\phi = S_c + S_p\phi_p$, where $S_\phi$ is the source term associated with the dependent variable $\phi$, in order to prevent numerical instabilities and avoid negative values in turbulence quantities. For instance in the k-equation (eq. 5.17) the source terms have been included in the form: $S_c = P_k + max(Gk, 0)$ and $S_p = -[\rho\tilde{\epsilon} + D - min(Gk, 0)]/k$. Where production terms have been included in the $S_c$ term and all the destruction terms in the $S_p$ term [5].

Global convergence is achieved when the mass balance is verified in all control volumes within a prescribed value $(10^{-8})$ and when the residual values of the different equations are sufficient low $(10^{-7})$.

## 5.3.1 Boundary conditions

### Inlet flow

When a flow is imposed entering the domain (inflow conditions), the values for velocity, temperature and turbulence quantities are given $(V_{in}, T_{in})$, the inflow turbulent kinetic energy is estimated assuming a given percentage value of the kinetic energy at the inlet $(k_{in} = (Iv_{in})^2$, where $I = 0.03)$, while its dissipation rate is estimated from $\epsilon_{in} = \frac{c_\mu^{0.75}k_{in}^{1.5}}{l_c}$ where $l_c = \alpha_\epsilon b$ and $\alpha_\epsilon = 0.03$.

### Outlet flow

Outflow conditions are evaluated specifying zero normal gradients $(\frac{\partial\phi}{\partial x} = 0$ where $\phi = v_t, T, k, \epsilon, \omega)$, except for the velocity normal to exit which is specified from a mass balance.

### Inlet/outlet flow

The boundary condition assumed in opened walls (inlet/outlet flow) are more complicated because they must permit that the fluid come in or goes out the computational domain. Where incoming external fluid must be at fixed temperature and pressure, it was necessary to implement a new condition where the code assign a value for temperature, pressure and turbulence quantities (if turbulence modelling is applied) at the boundary when the fluid flows into the computational domain or it takes the internal conditions when the fluid runs out.

One of the next set of boundary conditions is applied depending on the direction of the mass flow in the boundary studied.

The air is assumed to enter the computational domain from the surroundings at a temperature and a turbulence level which correspond to the ambient and with an adiabatic and reversible process, so that pressure energy in the surrounding air is converted to kinetic energy and pressure at the inlet:

$$T = T_\infty \qquad p_b + \frac{1}{2}\rho u^2 = p_\infty \qquad k_{in} = k_\infty = (IV_{in})^2 \qquad \epsilon_{in} = \frac{c_\mu^{0.75}k_{in}^{1.5}}{l_c} \qquad (5.21)$$

Where $I$ and $l_c$ are specified in the same way as inlet flow boundary condition (see Chapter 3).

If the air goes out the domain, the temperature is considered to remain constant and all the kinetic energy of the air is assumed to be converted to heat, resulting in an outlet pressure equal to the surrounding air pressure.

$$\frac{\partial T}{\partial x} = 0 \qquad p_b = p_\infty \qquad \frac{\partial k}{\partial x} = 0 \qquad \frac{\partial \epsilon}{\partial x} = 0 \qquad (5.22)$$

where $b$ means boundary and $\infty$ ambient.

**Solid walls**

Non-slip boundary condition is applied in the solid walls. If the wall is considered isotherm a temperature is imposed, and if the wall is adiabatic it has to satisfy $(\frac{\partial T}{\partial x})_{wall} = 0$. Turbulence quantities are imposed in walls too, for turbulent kinetic energy $k = 0.0$ is imposed and for the turbulent length scale, the value depends on the model that is used:

- $k - \epsilon$ models, if $D = 0 \Rightarrow \epsilon_{wall} = 2\nu \left(\frac{\partial \sqrt{k}}{\partial x_n}\right)^2$ else $\epsilon_{wall} = 0$.

- $k - \omega$ models, $\Rightarrow \omega_{wall} = \frac{6\nu}{\beta(x_n)^2}$
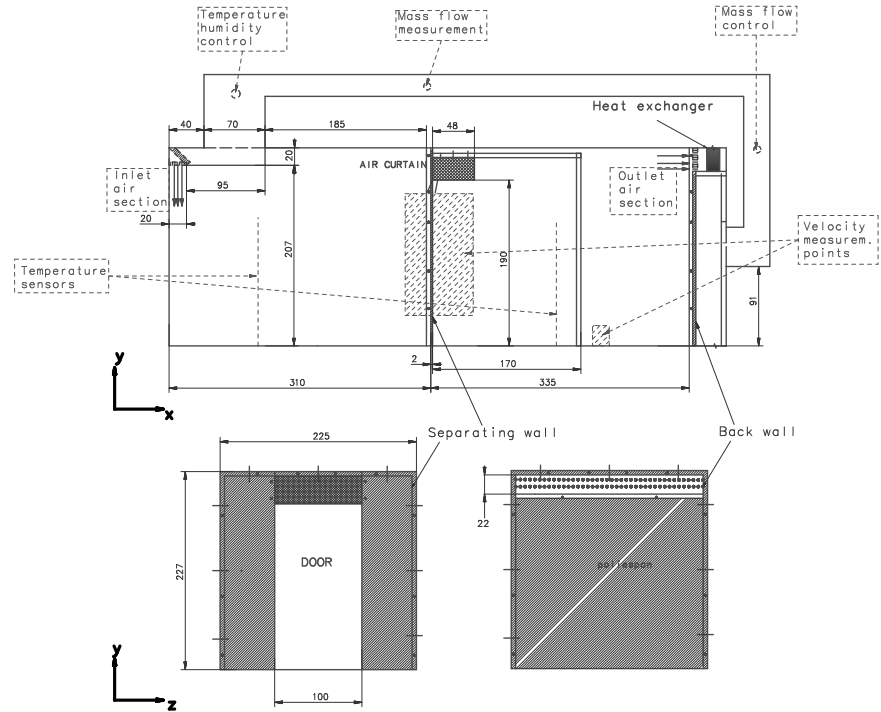
## 5.4   Air curtains: experimental setup

In this section a summary of the work carried out in order to design and construct an experimental setup to test air curtain is presented. These experiments are performed in order to characterise the air-curtain fluid-dynamic and thermal fields. Moreover, experimental data are used to validate numerical results in situations involving air curtains.

### 5.4.1   Climatic chamber

A new experimental set-up has been designed to perform experiments on air curtains. The air curtain is placed within an already existing climatic chamber adapted to
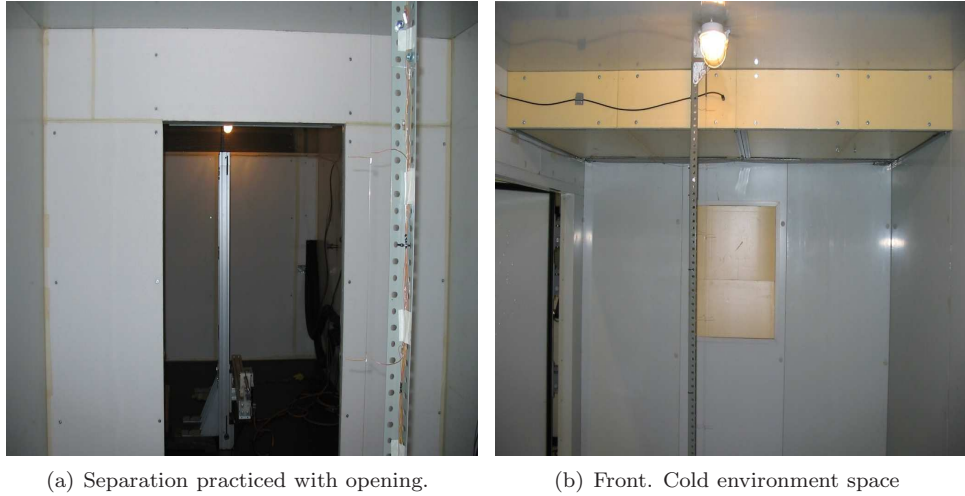
**Figure 5.5:** Draft of adapted climatic chamber.

achieve a set of desired conditions [7]. The climatic chamber has the next dimensions: 6.60 m length, 2.25 m width and 2.27 m height. A crossflow air supply of as much as approximately $1.5 kg/s$ can be imposed in the chamber. A division is practised to place the curtain, leaving an opening that acts as door of 1.90 m height and 1.0 m width (see Figures 5.5 and 5.6). The expected temperature difference between spaces is of aproximately $10^{o}C$.

The main room is divided in two spaces to obtain two areas at different conditions, with the sectioning controlled by the tested air-curtain. Local values of velocity, turbulence characteristics and temperature are measured. They are supported by positioning instrumentation and adequate data processing units. Experiments are focussed on two different zones: i) air curtain discharge; ii) downstream jet characterization. Moreover, the study is carried out with or without imposed air crossflow.

149

(a) Separation practiced with opening.  (b) Front. Cold environment space

**Figure 5.6:** Adapted climatic chamber distribution.

The technique used in velocity measurement is the hot wire constant temperature anemometry. Thermal field is assessed with K type thermocouples located at different planes in the conditioned spaces, as well as at air inlet and outlet sections. A special heat exchanger has been designed, constructed and mounted in the chamber to cool the air in the space used to simulate environmental conditions.
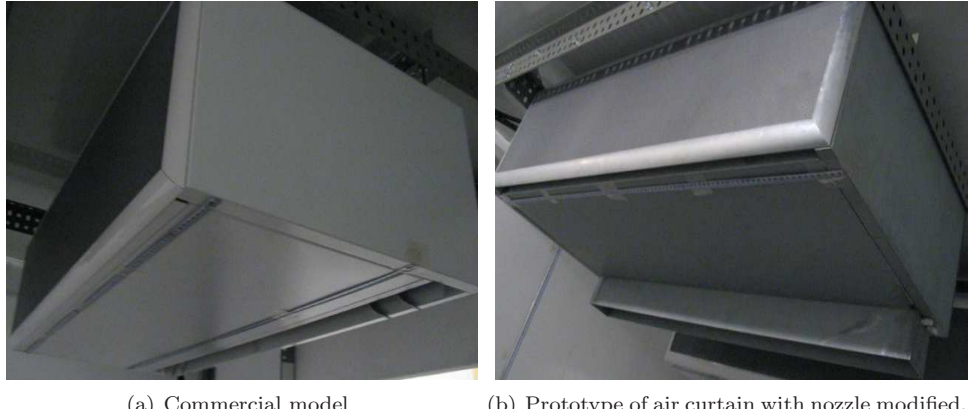
### 5.4.2   Air curtains studied

Considering the range of possible environmental conditions and the place where the air curtain is tested, a commercial type produced by one of the COMHEX project partners is selected (see Figure 5.7(a)). Furthermore, keeping the same power and air flow rate another prototype with an improved blow out nozzle is studied. In the new prototype the element used to orient discharge jet flow is removed and the nozzle is enlarged from air curtain border (see Figure 5.7(b)). Finally, within the new nozzle it is placed a flow straightener to homogenize the flow.

### 5.4.3   Positioning device

Air curtain discharge is studied in a horizontal plane ($xz$ plane) parallel to the air curtain discharge nozzle. Furthermore, an area of 1300 mm of height (y-direction) and 1000 mm of length (x-direction) is considered in order to characterize discharge jet by

(a) Commercial model          (b) Prototype of air curtain with nozzle modified.

**Figure 5.7:** Air curtains studied.

| Technical data | | | | | | | |
|---|---|---|---|---|---|---|---|
| Depth (m) | Nozzle width $b_{dis}$(m) | Air rate $(m^3/h)$ | Heating power (kW) | Fan (Volts) | Fan (kW) | Fan (A) | Weight (kg) |
| 1.0 | 0.07 | 1200-1800 | 3/6/9 | 230 | 0.555 | 2.49 | 47 |

**Table 5.2:** Air curtain prototype characteristics

means of vertical planes. Thus, horizontal and vertical movements are required. The horizontal movement is accomplished by using an automatic system type cantilever with stationary steeping motors and mobile axis body (see Figure 5.8(a)). The vertical positioning is done by means of a portal axis toothed belt driven linear system (see Figure 5.8(b)). Each movement is controlled remotely by means of a RS-232 port. Technical characteristics of horizontal (LM-A608R-AT5) and vertical (LM-P/H608R-AT5) positioning devices are shown in Table 5.3.

### 5.4.4   Hot wire anemometry

The hot wire anemometry is a well known technique, due to it has been used in the last years with considerable success and it has become a standard tool for researchers examining the nature of turbulence. The hot-wire anemometry is a device used to convert fluid velocity and its variation into an electrical output signal, which can be properly analysed. Compared with other fluid velocity techniques (PIV, PTV, LDA and so on), it is a relatively cheap and effective method to measure fast velocity

(a) Horizontal LM-A608R-AT5.          (b) Vertical LM-P/H608R-AT5.

**Figure 5.8:** Positioning system.

fluctuations. Thermal anemometry measures fluid velocity by sensing the changes in heat transfer from a small, electrically heated element exposed to the fluid. In constant temperature anemometry method, the cooling effect produced by the flow passing over the element is balanced by the electrical current to the element, then the element is maintained at a constant temperature [8]. The change in current due to a change in flow velocity shows up as a voltage at the anemometer output. The anemometer is linked to a personal computer, where the data are postprocessed. In figure 5.9(a) is shown a draft of hot wire anemometry technique.

A set of experiments using hot wire constant temperature anemometry involves three main steps. Firstly, before getting results, a function correspondence between the electrical output and the instantaneous velocities must be obtained (calibration), the probe must be calibrated in the measurement environment over the velocity range of interest. A second stage is the acquisition or measurement and store of the data. Finally, a post analysis is used to calculate mean velocity, normal stress, standard deviation (root mean square), turbulence intensity, skewness and flatness coefficients for all probes. Then, it is possible to display time history and histograms of stored data, store time history information in an ASCII file, and calculate and show power spectral density, auto-correlation and cross-correlation.

|  | | | | |
|---|---|---|---|---|
| **Technical data positioning devices** | | | | |
| | Max. load | Stroke | Max. drive torque | Idle torque |
| LM-A608R-AT5 | 18 kg | 600 mm | 15 Nm | 0.54 Nm |
| LM-P/H608R-AT5 | 30 kg | 1250 mm | 15 Nm | 0.67 Nm |
| | Max. speed | Repeatability | Stroke per revolution | Mass |
| LM-A608R-AT5 | 5 $m/s$ | ±0.05 mm | 100 mm | 10.7 kg |
| LM-P/H608R-AT5 | 5 $m/s$ | ±0.05 mm | 100 mm | 15.6 kg |
| | Drive element | Guide | Max. $F_x$ | Max. $F_y$ |
| LM-A608R-AT5. | Toothed belt | Roller guide | 300 N | 300 N |
| LM-P/H608R-AT5 | Toothed belt | Roller guide | 942 N | 300 N |
| | Max. $F_z$ | Max. $M_x$ | Max. $M_y$ | Max. $M_z$ |
| LM-A608R-AT5 | 942 N | 205 Nm | 125 Nm | 35 Nm |
| LM-P/H608R-AT5 | 300 N | 35 Nm | 100 Nm | 160 Nm |

**Table 5.3:** Horizontal and vertical positioning device characteristics (Data from BERGER-LAHR catalogue).

## Probe Calibration
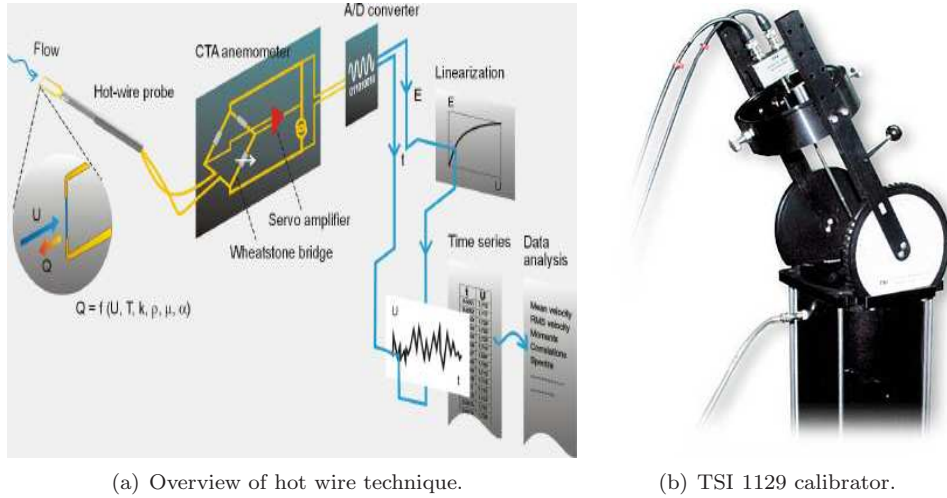
As it was mentioned above, calibration plays an important role in the anemometry technique. In this work it is carried out by means of an automated calibrator model TSI-1129, such as that shown in figure 5.9(b). The velocity in the calibrator is calculated using differential and absolute pressure, temperature and specific air properties as follows:

$$a_o = [\gamma R(T + 273.15)]^{1/2} \tag{5.23}$$

$$M = \left[ 2\frac{\left(\frac{p+\Delta p}{p}\right)^{\frac{\gamma-1}{\gamma}} - 1}{\gamma - 1} \right]^{1/2} \tag{5.24}$$

$$a = \left[ \frac{a_o^2}{1 + \left(\frac{\gamma-1}{2}M^2\right)} \right]^{1/2} \tag{5.25}$$

$$v = M \cdot a \tag{5.26}$$

(a) Overview of hot wire technique.  (b) TSI 1129 calibrator.

**Figure 5.9:** Hot wire anemometer and probe automated calibrator (Figures from TSI catalogue).

where: p is absolute pressure, $\Delta p$ differential pressure, $T$ temperature, $\gamma = 1.399$ for air, $R = R_o/MW$ with $R_o = 8314 J/kmolK$ and $MW = 28994 kg/kmol$, $a$ is speed of sound and $v$ velocity.
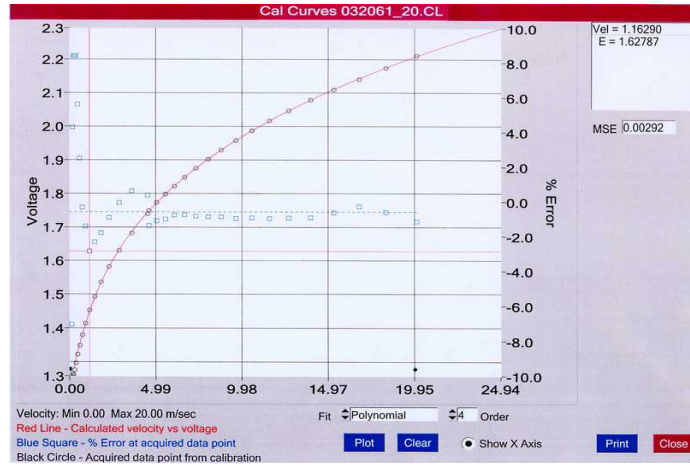
The curve presented in figure 5.10 is an example of results obtained after a calibration of a probe employing the automated calibrator. The calibration consists in obtaining a relation between the voltage at the output of the anemometer and the velocity imposed in the automated calibrator. In the calibration process a velocity is imposed and the voltage is the dependent variable.

### Data acquisition

The CTA signal is a continuous analogue voltage. In order to process it digitally it has to be sampled as a time series consisting of discrete values digitised by an analogue-to-digital converter (A/D board).

The parameters defining the data acquisition are the *sampling rate (SR)* and the *number of samples (N)*. They determine the *sampling time* as $ST = N/SR$. The values for SR and N depend primarily on the specific experiment, the required data analysis, the available computer memory and the acceptable level of uncertainty. Time-averaged analysis, such as mean velocity, requires non-correlated samples, which can be achieved when the time between samples is at least two times larger than the integral time scale of the velocity fluctuations. The number of samples depends on

**Figure 5.10:** Calibration curve.

the required uncertainty and confidence level of the results. They can be evaluated as follows:

Sampling rate:

$$SR \leq \frac{1}{2T_I} \tag{5.27}$$

Number of Samples:

$$N = \left( \frac{1}{u} \left( \frac{z_a}{2} \right) Tu \right)^2 \tag{5.28}$$

where $T_I$ integral time scale of the velocity fluctuations, $u$ uncertainty (%U), $Tu$ turbulence intensity. $\frac{z_a}{2}$ is a variable related to confidence level (1-a) of the Gaussian probability density function according to table 5.4.

| $z_a/2$ | **(1-a)**% |
|---------|------------|
| 1.65 | 90 |
| 1.96 | 95 |
| 2.33 | 98 |

**Table 5.4:** Confidence level.

The integral time-scale can be calculated from the auto-correlation. It is the time

155

that takes the auto-correlation coefficient to drop from the unity starting value to zero.

Other important factors are the skewness, which indicates the lack of statistical symmetry in the flow, and the flatness factor, which is a measure of the amplitude of the distribution.

Available acquisition parameters in the hot wire anemometer used, using the IFA300 software, are:

- Sample rate: from 1Hz to 500kHz.

- Number of channels: 3

- Frequency response: 260 kHz.

- Maximum probe current: 0.8 A

- Maximum bridge voltage: 12 VDC.

- Analog output impedance: 50 $\Omega$.

- Temperature measurement: Built-in thermocouple circuit in each cabinet.

In the adquisition process is made the assumption that the velocity is normal to the sensor axis and it has the same orientation relative to the support during both calibration and measurement.

The temperature is obtained by means of an additional channel. However, in this work it is acquired by means of an additional J-type thermocouple positioned near the sensor film.
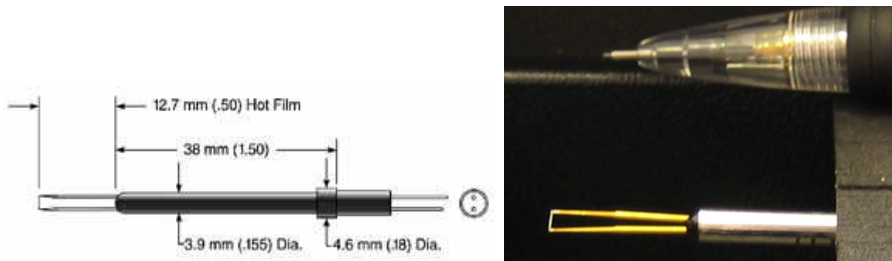
**Data obtained for each one of the velocity components:**

- Mean velocity: $U_{mean} = \frac{1}{N} \sum\limits_{i}^{N} U_i$ .

- Standard deviation of velocity: $U_{rms} = \left( \frac{1}{N-1} \sum\limits_{1}^{N} (U_i - U_{mean})^2 \right)^{0.5}$ .

- Turbulent stress: $\overline{u'u'} = (U_{rms})^2$.

- Turbulence intensity: $T_u = I = U_{rms}/U_{mean}$ .

**Hot wire versus hot film**

The traditional sensor has been a fine wire. It gives better frequency response and lower noise but is more fragile and cannot be used in conductive liquids. On the other hand, cylindrical film sensor is more rigid, stable and strong than wire sensors, making them the preferred choice. Rigidity is specially important for multi-sensor measurements. Also, film sensors are less susceptible to damage by particles in the flow than are wire sensors. Film sensors are constructed of platinum film on a fused-quartz substrate. As a result the film sensor has the same spatial resolution and conduction than wire sensor. Therefore, in this work two types of cylindrical film sensors are used: i) TSI1210-20 which is a single sensor, with a diameter of $50.8\mu m$, a sensing length of $1.02mm$, distance between supports of $1.65mm$ and maximum ambient temperature of $150^oC$ (see figure 5.11); ii) sensor model TSI1241-20 is a X-probe (measurements of two component velocity) with the same characteristics that the TSI1210-20 probe, but with the films placed at $45^o$.



**Figure 5.11:** Sensor probe TSI 1210-20 (Figure from TSI catalogue).

**Disturbing effects**

**Temperature:**  Temperature variations are normally the most important error source, as the heat transfer is directly proportional to the temperature difference between the sensor and the fluid. For a film probe operated under normal conditions, the error in measured velocity is approximately 2% per $1^oC$ change in temperature respect to the used in the calibration process [8]. In this work, the output voltage in the case of the anemometer employed is automatically corrected inside it with a temperature measured by means of a J-type thermocouple placed near velocity sensor. Therefore, this effect is not considerable.

**Pressure:**  Since pressure variations from calibration to experiment, and during an experiment are normally small, the pressure influence in the CTA can be normally

neglected. The lower limit for pressures, at which a probe can be used, are determined by the slip-flow conditions defined by the Knudsen number (ratio between molecular mean free path and sensor diameter should be smaller than 0.01 [8]).

**Contamination:** Film probes with $50\mu m$ can be used without problems in normal laboratory air, if they are re-calibrated at regular intervals. Contamination is a much bigger problem in liquid fluids than in gas fluids.

**Sensor orientation:** The only problem in our experimental setup is the sensor orientation. Although in most part of experiments the jet flows vertically (near nozzle discharge), when a cross-flow is imposed the jet is displaced and curved. Therefore, perhaps some errors can be present if this topic is not taken into account. In the case of discharge and jet characterisation without cross-flow this source of error can be neglected.

**Uncertainty in constant temperature anemometer measurements**

Following ISO uncertainty model, which combines uncertainty contributions $U(y_i)$ from each individual input variables $x_i$ into a total uncertainty at a given confidence level, it is possible to obtain the relative standard uncertainty $u(y_i)$ as a function of the standard deviation of the input variance:

$$u(y_i) = \frac{1}{y_i} \cdot S \cdot \left( \frac{\Delta x_i}{k_i} \right) \tag{5.29}$$

being $S = \frac{\partial y_i}{\partial x_i}$ the sensitivity factor and $k_i$ the coverage factor related to the distribution of the variance.

If a Gaussian error distribution is assumed with a 95% confidence level then $k = 2$. The total relative uncertainty becomes:

$$u_{tot} = 2\sqrt{\sum u^2(y_i)} \tag{5.30}$$

Therefore, the uncertainty of the results of a CTA anemometer is a combination of individual uncertainties.

**Individual uncertainties of a velocity sample**

**Anemometer:** Common anemometers have low drift, low noise and good repeatability, then $u(y_i) \approx 0$

**Calibration equipment:** It constitutes a major source of uncertainty. The error is stochastic with a normal distribution and the relative standard uncertainty is:

$$u_{cal} = \frac{1}{100} * \pm(a_{cal} + b_{cal}) \tag{5.31}$$

In the case of a good dedicated calibrator, $a_{cal} = 1$ and $b_{cal} = 0.02$.

**Linearization (conversion):** The linearization uncertainty is related to the curve fitting errors. It is stochastic:

$$u_{lin} = \frac{1}{100} * (\Delta u_{lin}) \tag{5.32}$$

where $\Delta u_{lin}$ is the standard deviation of the curve fitting errors in the calibration points in %.

**A/D board resolution:** The resolution uncertainty is stochastic with a square distribution and its relative standard uncertainty can be expressed as:

$$u_{res} = \frac{1}{\sqrt{3}} \cdot \frac{1}{u} \cdot \frac{E_{AD}}{2^n} \cdot \frac{\partial u}{\partial E} \tag{5.33}$$

being $E_{AD}$ the A/D board input range, n its resolution in bits, $u$ the velocity and $\frac{\partial u}{\partial E}$ is the sensitivity factor of the inverse calibration curve.

**Probe positioning:** The positioning uncertainty relates to the alignment of the probe in the experimental set-up after calibration. It can be expressed as:

$$u_{pos} = \frac{1}{\sqrt{3}} \cdot (1 - cos\theta) \tag{5.34}$$

Generally a probe can be positioned with an uncertainty of $\theta = \pm 1^o$.

**Temperature variations:** Temperature variations from calibration to experiment or during an experiment, if not corrected, introduce systematic errors as follows:

$$u_{temp} = \frac{1}{\sqrt{3}} \cdot \frac{1}{u} \cdot \frac{1}{T_w - T_0} \cdot \left(\frac{A}{B} \cdot u_{-0.5} + 1\right)^{0.5} \approx \frac{1}{\sqrt{3}} \cdot \frac{\Delta T}{273} \tag{5.35}$$

where $T_w$ is the sensor temperature, $T_0$ the ambient reference temperature, $\Delta T$ is the difference between the ambient reference temperature and the temperature during measurement, $A = 1.396$ and $B = 0.895$.

**Ambient pressure variations:** Ambient pressure changes influences the density and therefore the calculated velocity.

$$u_{\rho,p} = \frac{1}{\sqrt{3}} \cdot \left( \frac{p_0}{p_0 + \Delta p} \right) \tag{5.36}$$

**Gas composition, humidity:** Under normal conditions changes in gas composition are mainly caused by changes in humidity. Then it introduces a contribution of:

$$u_{hum} = \frac{1}{\sqrt{3}} \cdot \frac{1}{u} \cdot \frac{\partial u}{\partial p_{wv}} \cdot \Delta p_{wv} \tag{5.37}$$

The influence on the heat transfer is very small, $\partial u / \partial p_{wv} \approx 0.01$ per 1 kPa change in water vapour pressure $p_{wv}$.

### Velocity sample uncertainty

The relative uncertainties of a single velocity sample obtained with a single-sensor probe in air, can be summarised in Table 5.5, with the following input data: $T_w - T_0 = 200^oC$, $u = 4.5m/s$ and $\partial u / \partial E = 4 m/s\, v$. Furthermore, it is taken into account that the sample velocity is corrected during measurement and the sensor calibration is done in a good dedicated calibrator (model TSI 1129).

| Source of uncertainty | Input variants | Typical value | Typical value | Coverage factor | Relative standard uncertainty |
|---|---|---|---|---|---|
| | $\Delta x_i$ | $\Delta x_i$ | $\frac{1}{u} \cdot \Delta y_i$ | k | $\frac{1}{k} \cdot \frac{1}{u} \cdot \Delta y_i$ |
| Calibration | $\Delta u_{cal}$ | 1% | 0.01 | 2 | 0.005 |
| Linearization | $\Delta u_{lin}$ | 5% | 0.05 | 2 | 0.025 |
| A/D resolution | $E_{AD}, n$ | 10 V, 12 bit | 0.0008 | $\sqrt{3}$ | 0.0013 |
| Positioning | $\theta$ | $2^o$ | 0.0006 | $\sqrt{3}$ | 0.0004 |
| Temperature | $\Delta T$ | $2^oC$ | 0.007 | $\sqrt{3}$ | 0.004 |
| Pressure | $\Delta p$ | 10 kPa | 0.01 | $\sqrt{3}$ | 0.006 |
| Humidity | $\Delta p_{wv}$ | 1 kPa | 0.0006 | $\sqrt{3}$ | 0.0003 |

Relative uncertainty: $u_{sample} = 2 \cdot \sqrt{\sum \left( \frac{1}{k} \cdot \frac{1}{u} \cdot \Delta y_i \right)^2} = 0.053 = 5.3\%$

**Table 5.5:** Relative expanded uncertainty for one velocity sample [8].

Results presented in Table 5.5 are an example of the uncertainty of a CTA measurement. However, the uncertainty of the reduced data (mean velocity, turbulence intensity or root mean square velocity, turbulent stresses, etc.) depends on the uncertainty of the individual samples as previously described and on how true the data represents the flow. Due to the nature of turbulent flows and the random character of the data adquisition, the choice of the appropiate sampling rate and number of samples is more determinant in the uncertainty level accomplished in the sampling process.

### 5.4.5   Heat exchanger used

With the purpose of cooling air entering in the cold space to simulate environmental conditions a special heat exchanger is used (see figure 5.12), which is designed taking into account different expected air conditions, assuming the temperature is around $20^oC$ in the warm room, and that three air mass flow rates of 1000, 2000 and $4000m^3/h$ are handled.



(a) Back side exchanger.                    (b) Front and setup.

**Figure 5.12:** Heat exchanger used to refrigerate crossflow air.

Heat exchanger is designed with quickCHESS program [9]. Behind the exchanger a drops separator is mounted to eliminate water carryover, in the bottom part a recipient is placed to collect condensed fluid (see figure 5.12(a)). As it is shown in Figure 5.5, the heat exchanger is mounted in the upper part of the wall at the warm room air outflow ($x = 6500mm$, $y = 2000mm$).

## 5.5   Air curtains: experimental results

In this section acquired results of the experimental data are presented. Firstly, results of two current commercial prototypes, with discharge nozzle of $1.0m$ depth and $0.07m$ width, are shown with and without blade for flow orientation. Then, results of the different alternative nozzle configurations designed are presented. Finally, comparisons among them are shown to better illustrate improvements achieved with the new nozzle prototypes.
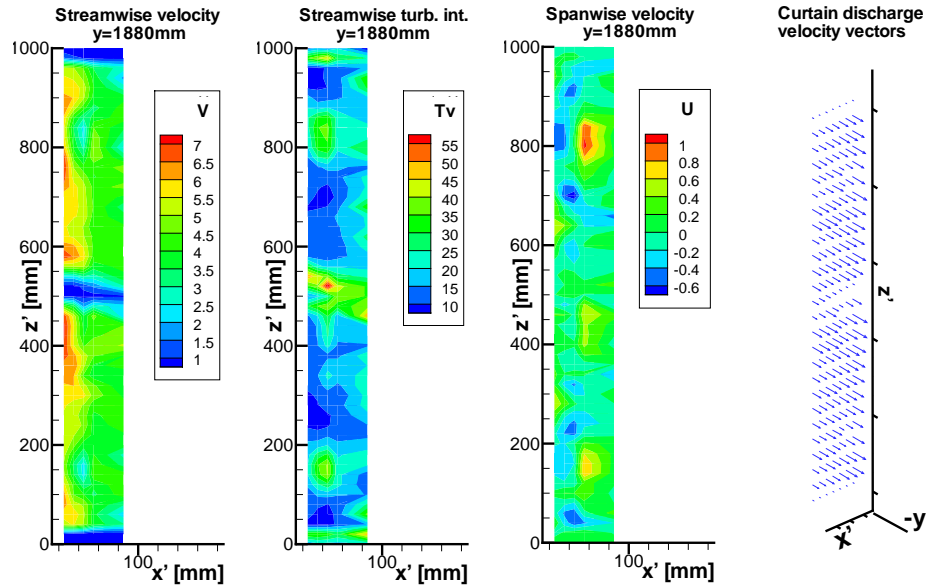


**Figure 5.13:** Local coordinates location.

As it was noted before, the attention is focused both on air curtain discharge and jet characterisation. Thus, for the depiction of the discharge, five sets of points are acquired in z-direction, at $z = 670$, $897$, $1125$, $1352$ and $1580mm$. An interval of $5mm$ in x-direction is used for these measurements. Furthermore, another set of data is acquired longitudinally at the central line of the nozzle in x-direction at $x = 3075mm$ and at intervals of $20mm$ in z-direction. For comparison purposes the air curtain discharge nozzle edge of all prototypes studied is located at the same height, $y = 1890mm$ (see Figure 5.5).

Furthermore, as is shown in Figure 5.13 a local origin of coordinates is placed in the external right edge of the air-curtain to facilitate understanding of air curtain discharge measurements.

In order to characterise the jet produced downstream discharge, data are acquired each $200mm$ in y-direction and with intervals of $20mm$ in x-direction, in the central plane of the doorway. Thus, jet centerline velocity decay and spreading of the jet can be observed. Furthermore, fluid-flow profiles near the floor of the warm room and near the front and rear walls are studied when an air crossflow is imposed. All these measurements are carried out at center plane $z = 1125mm$, $z' = 500mm$.
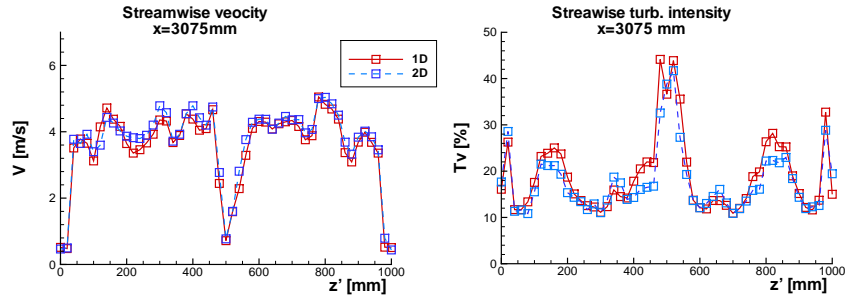
**Figure 5.14:** Prototype A. Air curtain discharge velocities, turbulence intensity and velocity vectors. $x'$ and $z'$ according to Figure 5.13 (measured from the external border of the air curtian).

The sampling rate used is changed according to the turbulent integral time obtained in each experiment. At the discharge it is set to $1000Hz$ (measurements per sample), whereas in the jet a sampling rate of $500Hz$ is selected. 12 samples were taken in every point during $1s$ or $2s$ at the discharge and jet respectively, with time intervals of $5s$ between each sample. Obtained data are postprocessed using statistical tools to obtain mean value and deviation of each variable.

### 5.5.1 Actual commercial air curtain prototype

**Discharge with blade for flow orientation**

A first group of experiments is carried out in two current commercial air curtain models of different manufacturers. They are denoted by prototype A and B respectively. The size, geometry and fan power is similar in both prototypes. However, the blade for flow orientation in prototype B is slightly different. It has a couple of small wings to orientate the flow towards the lateral walls of the doorway near each edge of the

163

**Figure 5.15:** Prototype A. Streamwise $V$ mean velocity and turbulence intensity at $x = 3075mm$, $x' = 55mm$. Comparison of measurements using TSI1210-20 and TSI1241-20 probes. $z'$ according to local coordinates (mesuared from the external border of the air curtain).

blade for flow orientation (see figure 5.7(a)).
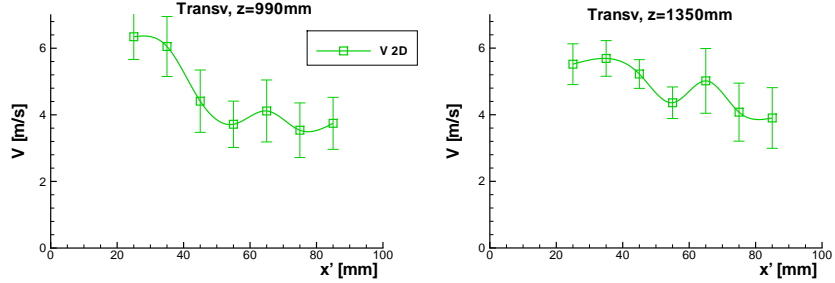
**Prototype A:** For the study of this prototype firstly some measurements are carried out with a two dimensional probe, after a one dimensional probe is used and the results are compared to establish if the flow can be considered one or two dimensional. Thus, first results of the experiments carried out with the TSI1241-20 two-dimensional probe are analyzed and plotted in Figure 5.14. In this figure is observable the irregularity of the discharge velocity profile. This, roughness contributes to increase eddies formation and therefore turbulence increasing through shear production.

Reviewing $V$-velocity component (left plot Figure 5.14), is possible to distinguish three regions with lower velocity: near the bottom, central and top regions ($z' = 0$, $z' = 0.5m$ and $z' = 1m$). Top and bottom minimums are due to the presence of the wall edges of the air curtain. Whereas, the minimum in the center corresponds with the device used to mount the blade for flow orientation. Furthermore, it can be seen that regions with the highest $V$-velocity values are near the external border of the curtain ($x' = 30mm$). In the second plot from left to right in Figure 5.14, turbulence intensity for the streamwise velocity is shown. As it can be seen, high values of between 10% and 50% are found. Moreover, the maximum values are located in the regions where velocity is low.

Turning to $U$-velocity component, it can be seen that it presents values up to $1m/s$, which are lower than the ones measured for the $V$-velocity component. Therefore, air curtain discharge velocity can be considered one-dimensional, flowing in $y$-direction.

If the centre line ($x = 3075mm$, $x' = 55mm$) along $z$-direction is plotted a

164
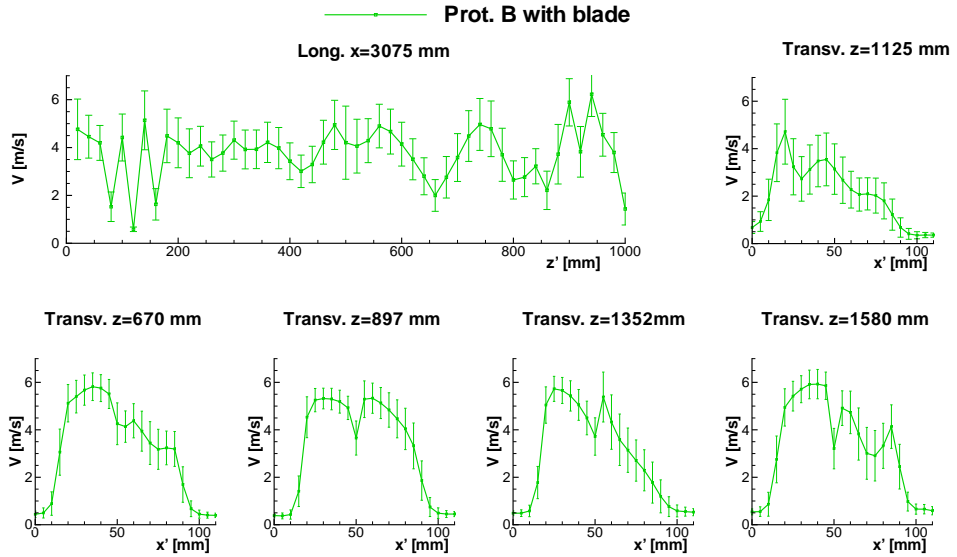
**Figure 5.16:** Prototype A. Air curtain transverse profiles of $V$ mean velocity at two different $z$, $z'$ locations. Error bars $V_{rms}$ root mean square velocity. Probe TSI1241-20. Local $x'$ coordinate (measured from the front wall of the air curtain).

more detailed information can be extracted. Thus, the $V$-velocity component and its turbulence intensity are presented in Figure 5.15. In this Figure, uneven profiles for both the mean streamwise velocity and turbulence intensity in that direction are observed.

Furthermore, a comparison of the experimental data measured with the TSI1210-20 one dimensional probe and TSI1241-20 two dimensional probe is shown in Figure 5.15. Similar results have been obtained for both probes and the differences in some points correspond to the elevate turbulence level observed.

Details of the streamwise discharge velocity at two $z$ positions are presented in Figure 5.16. In this Figure, the standard deviation of the velocity, i.e. root mean square velocity, is plotted using error bars. At $z = 990mm$ most of the flow goes by the outer part, near the curtain external wall, towards the interior the velocity is reduced and it remains almost constant at this position. At $z = 1350mm$, even though the velocity distribution is more uniform, velocity presents a peak near the external region. At both positions an increment of the velocity is observed near the interior side of the blade for flow orientation.

**Prototype B:** For the prototype A, both x and y-direction velocity components were measured. Results indicate that it is correct to assume flow field is one dimensional in vertical y-direction. Thus, probe TSI1210-20 is used hereafter. Measurements of the prototype B are presented in Figure 5.17. Due to the special configuration of the blade for flow orientation with small wings near both edges, longitudinal $V$-profile presents important roughness in the region where wings are mounted (see figure 5.7(a)). Therefore, characteristics of this profile produce turbulence production

165
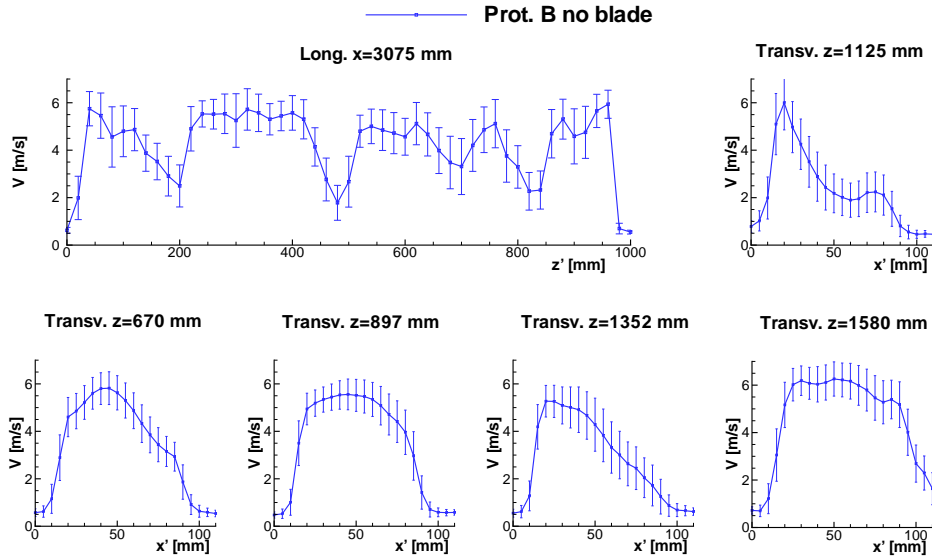
**Figure 5.17:** Prototype B with blade for flow orientation. $V$ mean velocity. Error bars $V_{rms}$ root mean square velocity. $x'$ and $z'$ according to local coordinates (measured from the external walls of the air curtain).

because of the different velocity values in an relatively small space, which is generated by shear stress between neighbor velocities.

Reviewing transversal profiles shown in Figure 5.17, it can be seen that the blade for flow orientation introduces a discontinuity in the $V$ profile. Regions in front and behind the blade are clearly separated, and most of the fluid flows toward exterior edge for $z = 670$, 1125, 1352 and 1580$mm$. Furthermore, velocity minimum near directional plate is more evident away from air curtain lateral walls ($z = 897$ and 1352$mm$). It also produces an increase of the turbulence level in this region. Furthermore, measurements acquired at $z = 1125mm$ coincide with physical obstacles such as the assembling system of the blade, therefore turbulence is specially increased near this region. Moreover, at $z = 670$ and 1580$mm$, near lateral walls, $V$ profile is very irregular (see figure 5.17). Presence of winds and edges form a stepped geometry system resulting in a flow with many scales of motion, therefore quite turbulent.

166
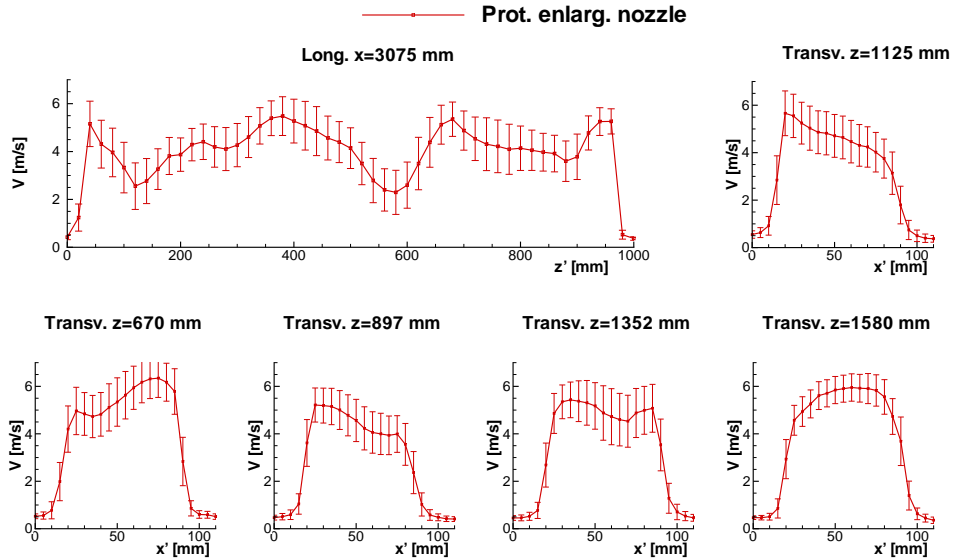
**Figure 5.18:** Prototype B without blade for flow orientation. $V$ mean velocity. Error bars $V_{rms}$ root mean square velocity. $x'$ and $z'$ according to Figure 5.13 (ordinates measured from the external borders of the air curtain).

## Discharge without blade for flow orientation: Prototype B

The third experiment is carried out in the air curtain commercial prototype B, but without blade for flow orientation. The discharge characterisation is carried out in the same form as in the previous case. First a longitudinal profile is studied, then data are measured in five transversal positions. Vertical position is preserved constant at $y = 1870mm$. Error bars are shown to indicate the fluctuating part (root mean square) of the mean velocity. Moreover, in some points where turbulence level is very high, above 30%, measurements should be taken with care.

In figure 5.18 longitudinal profile along air curtain discharge at $x = 3075mm$. Some irregularities for the $V$ profile are observed is shown. However, profile measured seems to be smoother than in the case with blade for flow orientation. In this Figure transversal profiles are also presented. A peak in mean velocity is observed towards the front (exterior, $x' \approx 25mm$) wall of the air curtain at $z = 670$, 1125 and $1352mm$. On the other hand, at $z = 897$ and $1580mm$ $V$ profile seems more a normal turbulent jet, but it is not symmetric. Fluctuating velocity is considerable and of similar magnitude in all the positions measured.

167

**Figure 5.19:** Prototype with enlarged nozzle geometry and without blade for flow orientation. $V$ mean velocity. Error bars $V_{rms}$ root mean square velocity. Local $x'$ and $z'$ coordinates according to Figure 5.13 (measured from the external borders of the air curtain).
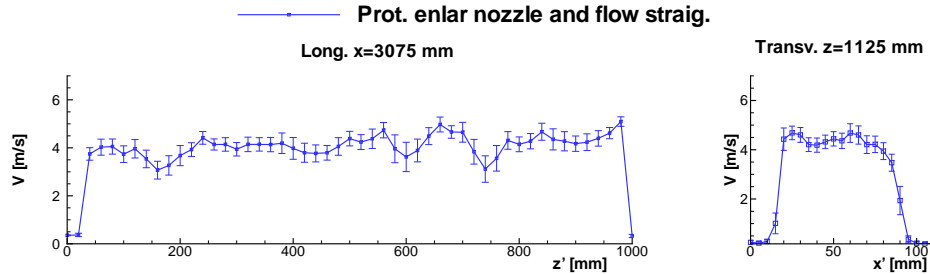
## 5.5.2 Prototype with enlarged nozzle

The second nozzle geometry is now studied. Firstly discharge is analyzed continuing with the same methodology employed above. The nozzle has been extended and the blade for flow orientation is not used. Moreover, it is applied to generate a more developed profile at the air curtain discharge.

The first study carried out is done along $z$ direction for $x = 3075mm$, $x' = 55mm$ (longitudinally). As it is expected this profile is smoother than that obtained with the prototypes A and B with blade for flow orientation. However, velocity minimums in the zones without fans are more prominent with this nozzle type (see figure 5.19). Furthermore, it causes regions with adverse pressure gradient and considerable turbulence intensity.

Streamwise $V$ velocity at different $z$ locations is also presented in Figure 5.19. Analyzing these profiles near air curtain edges ($z = 670$ and $1580mm$), it is observed that mean velocity profile is smoother and most of the flow is moved towards the interior region (see figure 5.19). Furthermore, in the another locations the peak

168

**Figure 5.20:** Prototype with new nozzle geometry and flow straightener. Longitudinal profile $x = 3075mm$. $V$ mean velocity. Error bars $V_{rms}$ root mean square velocity. Local $x'$ and $z'$ coordinates according to Figure 5.13.

observed near the front wall is less important. Thus, at $z = 897mm$ the form of the curve is changed respect to that obtained with previous prototypes, and the flow is directed towards exterior edge. Finally, at $z = 1352mm$ is observed as the velocity profile is broken and it presents two maximum points.

### 5.5.3 Prototype with enlarged nozzle and flow straightener
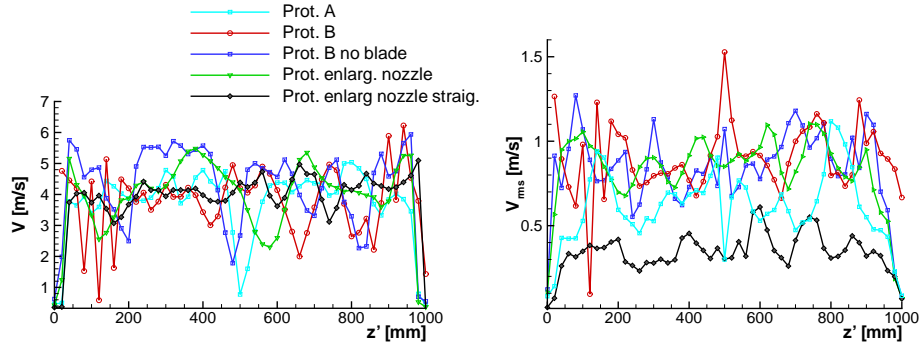
Due to enlarged nozzle has presented advantages respect to the prototypes A and B, and with the aim of improving characteristics of the discharge jet produced, which means a smoother velocity profile and even less turbulence intensities, a flow straightener is placed within the nozzle. The flow straightener has pipes with a diameter of approximately $3mm$. Therefore, it directs flow vertically and helps nozzle function. Furthermore, a resistance is imposed to homogenise discharge jet.

In figure 5.20 is shown how mean velocity presents smaller fluctuations and a smooth profile. As shown, the error bars which represent turbulence level are also reduced in the studied region. Furthermore, in the right side of figure 5.20 the importance of the role played by the flow straightener is illustrated. It is very important because less turbulence means also less mixing.

### 5.5.4 Comparative study

In this subsection longitudinal and transversal profiles measured for the nozzle configurations studied are compared.

In Figure 5.21 profiles measured at $x = 3075mm$, $x' = 55mm$ (i.e. mid point of the discharge in $x, x'$ direction) for the nozzles configurations studied are presented.

169

**Figure 5.21:** Comparison for longitudinal profiles $x = 3075mm$, $x' = 55mm$ (x-midpoint discharge jet), four configurations studied. V mean velocity. $V_{rms}$ root mean square velocity. $z'$ coordinate from Figure 5.13 (mesured from air curtain exterior lateral wall).
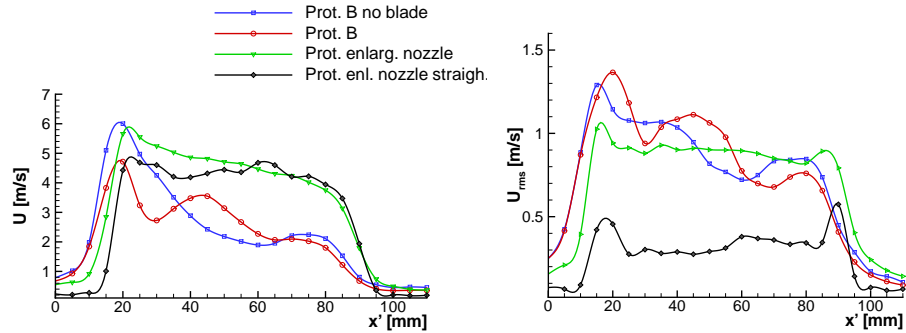
As it can be observed in the left side of Figure 5.21 resultant $V$-profile with the new prototype, and specially with the prototype with flow straightener, is smoother and presents an even profile. A velocity profile less oscillatory produce minor shear stress and eddies in $z$ direction are also reduced. Another important aspect is the reduction in the turbulence level produced by the new prototype with flow straightener (plotted at the right side of Figure 5.21). Since the flow becomes more laminar, the separation between adjacent regions at each side of the jet (which is the main objective of air curtain) shows a better behavior.

In Figure 5.22 results of mean and fluctuating streamwise velocity in the jet central plane region at $z = 1125mm$, $z' = 500mm$ and in $x$-direction are shown. The trends are similar to those presented above, mean velocity profile produced with the new nozzle with flow straightener is flatter than others. Moreover, turbulence represented by root mean square velocity is a 50% of the rest of nozzle configurations. Therefore, benefits explained for the longitudinal profile are similar in $x$-direction. The produced fluctuating velocity resembles more a plane jet, thus as with less turbulence less mixing and less infiltration. It is also expected a narrower jet as mixing process decreases.

### 5.5.5 Discharge jet experimental results

In this subsection the study is focussed on the analysis of the jet produced by the air curtain downstream discharge nozzle. Thus, a $xy$-plane is constructed by measuring fluid flow characteristics in the central region of the doorway ($z = 1125mm$, $z' =$

170

**Figure 5.22:** Comparison for transversal profiles $z = 1125mm$ (central plane $z$-direction). V mean velocity. $V_{rms}$ root mean square velocity. $x'$ ordinates mesured from air curtain exterior front wall (see Figure 5.13).
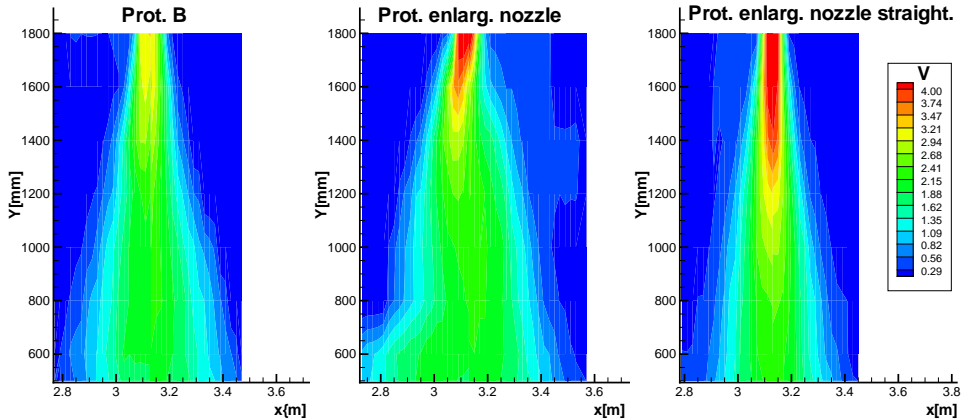
$500mm$). Prototype A and Prototype B without blade for flow orientation are not taken into account here because they have not presented improvements and their results are similar to prototype B with blade.

**Isothermal situation without crossflow**

For the first situation considered the air curtain is placed inside the climatic chamber but the temperatures at both sides of the air curtain are the same, furthermore an air crossflow is not imposed.

**Mean velocity profiles** When velocity profiles in the jet are reviewed, it is observed as the new prototype with enlarged nozzle (see central plot of Figure 5.23) produce a wider jet at the bottom region. On the other hand, the jet is narrower and core velocity is bigger in the case of prototype with enlarged nozzle and flow straightener, therefore penetration is higher. In the stagnation region the effects of the impingement wall (floor) begins to be important. Two big changes can be observed using the new prototype with enlarged nozzle and flow straightener: i) it is narrower in the base of the jet. ii) the length of the core region, thereby, penetration is larger.

**Turbulence intensity** In the inner (core) region of the jet produced by the air curtain, the prototype with enlarged nozzle produces higher turbulence levels than

171

**Figure 5.23:** Mean velocity profile. Left: commercial model Prot. B; middle: prototype enlarged nozzle; right: prototype with flow straightener. $z = 1125mm$, $z' = 500mm$ (central plane doorway).
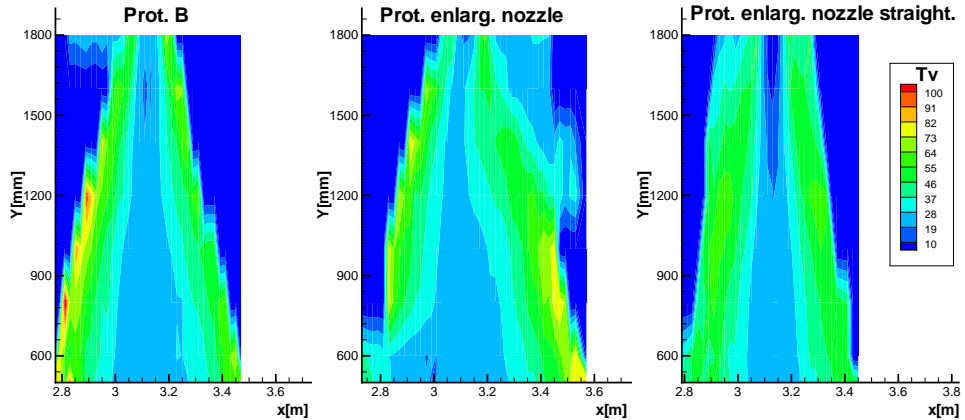
commercial prototype B. However, placing the flow straightener this trend is inverted, and the turbulence intensity is reduced (see central plot in Figure 5.24).

The external edge of the jet is the region where turbulence exhibits the highest values. However, new prototype with flow straightener generates less turbulence in that zone than the another prototypes, thus it is expected that energy gains/losses be less in the first one. Figure 5.24 also shows that higher values of turbulence intensity are located in the interior (edge) region. In general turbulence is lower using the new prototype with flow straightener. Moreover, in the prototype B turbulence intensity achieve values of as much as 100%, which is very high.

### Non-isothermal situation with crossflow

In figure 5.25 streamwise velocity and turbulence intensity are shown for the case with crossflow. These results correspond to the transversal jet produced by the air curtain with enlarged nozzle and flow straightener, with a discharge velocity of $4.5m/s$ and an imposed crossflow of $2000m^3/hr$. It has been measured at the midplane of the opening. A sampling rate of 500 samples per second and a measuring time of $40s$ are used. Therefore, a total of 20000 samples are acquired. It is worth to highlight two aspects. The first one, is the correct deflection of the jet in the crossflow direction. The second characteristic, is the high level of turbulence generated in the front boundary of the jet. This turbulence level promotes mixing, increasing also infiltra-

**Figure 5.24:** Turbulence intensity profile. Left: commercial model Prot. B; middle: prototype enlarged nozzle; right: prototype with flow straightener. $z = 1125mm$, $z' = 500mm$ (central plane doorway).

tion. However, these values remain still lower compared with ones exhibited by the commercial prototypes A and B.

## 5.6   Air curtains specific code validation

Two different sets of experimental data are used to validate the numerical code used in the air curtain simulation. Firstly, experimental data provided by a company involved in the COMHEX project [10], where the code was adapted to study air curtains, are used for comparison purposes. After that, the adapted climatic chamber used in the above presented experimental data is numerically simulated. Thus, measurements at the discharge of the prototype with enlarged nozzle and flow straightener are imposed as boundary condition and the experimental data of the jet produced by this prototype with air crossflow are used to validate the code. The mathematical models numerically implemented, which are compared in this section, have been introduced in Chapter 2 and summarized in section 5.3.
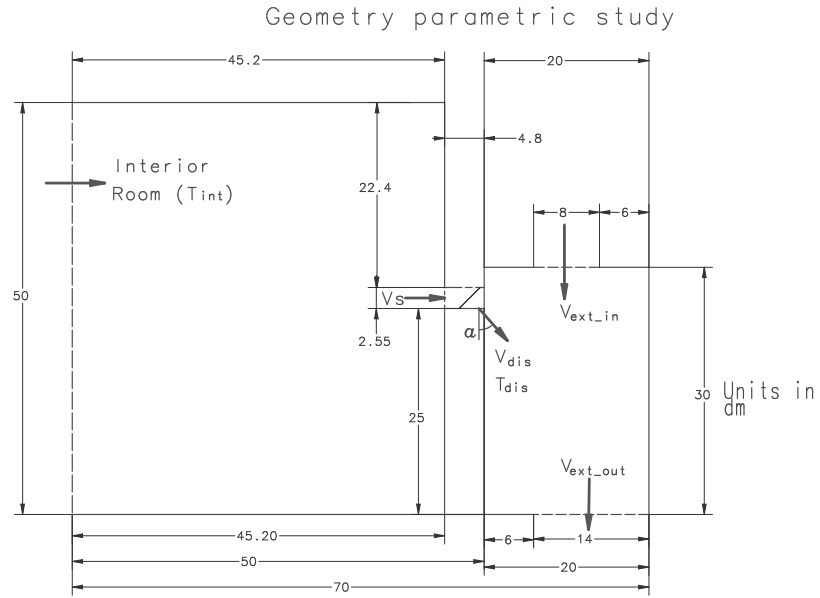
**Figure 5.25:** Air curtain prototype with enlarged nozzle and flow straightener. Jet characterisation with crossflow. Left: mean velocity; right: turbulence intensity.

### 5.6.1 Code validation using external experimental data

In the first part of this section a set of experimental data, provided by a COMHEX project partner [10], is used to validate the code adapted for air curtain simulations. The objective of these experiments is to validate the numerical code used in the simulations of three dimensional situations involving air curtains. However, experimental data only present temperature data, thus in this section comparison is restricted to temperature profiles. A schematic representation of the experimental setup geometry can be seen in Figure 5.26. The experiment represents a situation of an air curtain located at the doorway of a big building in winter season. Wall of left (interior) space is opened, therefore inflow/outflow boundary condition is applied. Air entering computational domain through this side is considered at constant temperature ($T_{int}$) and nonturbulent ($k \approx 0$), pressure is also fixed (for details see subsection 5.3.1). In the right space (exterior), a cold air inlet flow ($V_{ext-in}$) at constant temperature ($T_{ext-in}$) is imposed at the top boundary condition. Furthermore, another air outlet flow ($V_{ext-out}$) is assumed in the floor of this space. So then, a cold air flow is obligated to pass through the protected doorway. The discharge jet produced by the air curtain is characterised by means of a fixed velocity ($v_{dis}$), temperature ($T_{dis}$) and discharge angle ($\alpha$).

In Table 5.6 are summarised conditions of some tests carried out by the COMHEX partner, which are numerically reproduced, and that are used as boundary conditions in the code employed for the numerical simulation of air curtains.

**Figure 5.26:** Computational domain simulated to validate numerical code with the COMHEX partner experimental data.
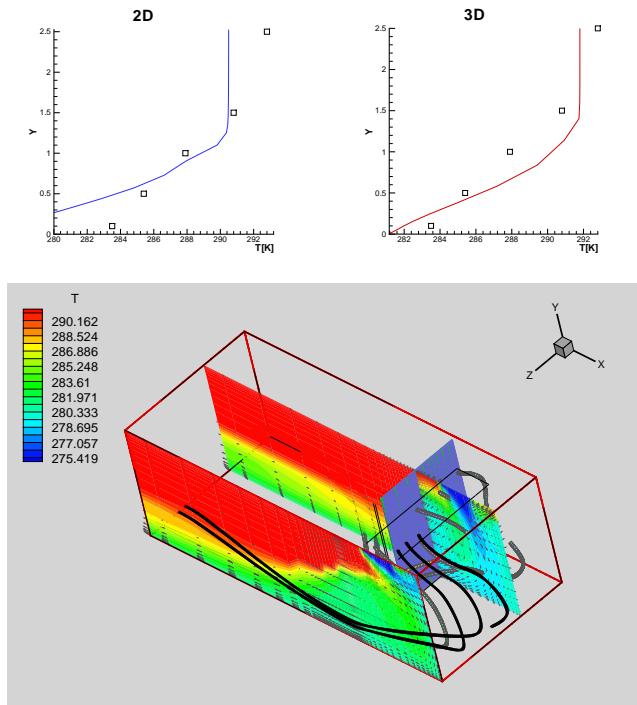
The temperature in the inner room at $3m$ from the door, and in the midplane in spanwise direction, is the variable selected for the comparison between experiments and numerical results obtained by the author. This parameter is useful because together with the comfort PED factor (percentage of people experiencing draught, see subsection 6.3.6) [2], provides an indication of the comfort level in the region. Two and three dimensional simulations are done to check the influence of the third dimension in the final results.

| | Air curtain | | | Exterior input | | Exterior output | | Interior room |
|---|---|---|---|---|---|---|---|---|
| | $\alpha$ | $v_{dis}$ | $T_{dis}$ | $T_{ext-in}$ | $V_{ext-in}$ | $T_{ext-out}$ | $V_{ext-out}$ | $T_{int}$ |
| | $(^{o})$ | (m/s) | $(^{o}C)$ | $(^{o}C)$ | $(m^3/h)$ | $(^{o}C)$ | $(m^3/h)$ | $(^{o}C)$ |
| TestA | 0 | 0.0 | 0.0 | 1.6 | 3300 | 8.7 | 635 | 17.5 |
| TestB | 15 | 7.0 | 21.0 | 2.5 | 2552 | 13.4 | 2486 | 19.5 |

**Table 5.6:** Experimental data used as boundary conditions in the numerical simulations.

175

**Test A**

In Test A no air curtain is used. Thus, this case constitutes a first approximation to air curtain simulation, and will be used for comparative purposes in later sections. In Figure 5.27 two and three dimensional simulations results are compared with COMHEX project partner experimental data for this case. In this Figure is seen as the warm room is cooled by the air coming from the refrigerated space. There are important losses of heat towards the exterior room. Three dimensional simulation performs adequately and reproduces correctly experimental data. On the other hand, results from two dimensional simulations depart from experiments in the region near the floor.
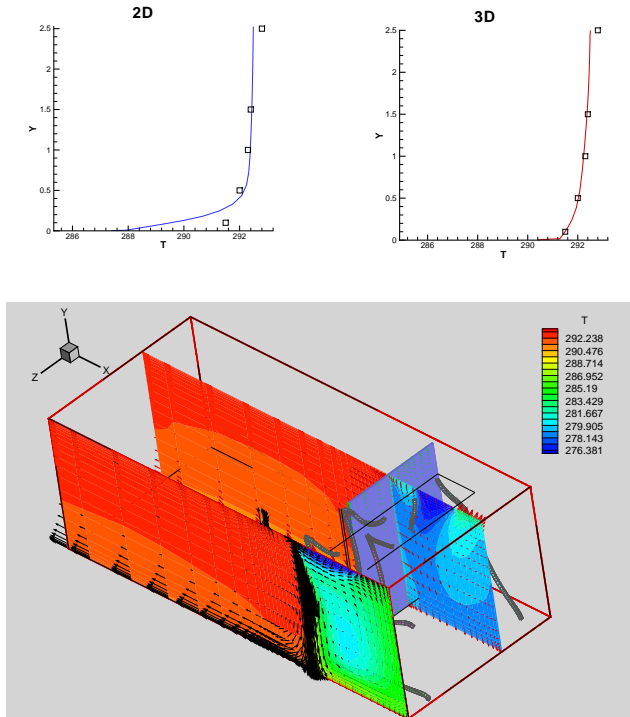


**Figure 5.27:** Code validation test A. Top: numerical vs. experimental interior temperature profiles at 3 m from door. Bottom: temperature contours and velocity vectors at two room sections.

**Test B**
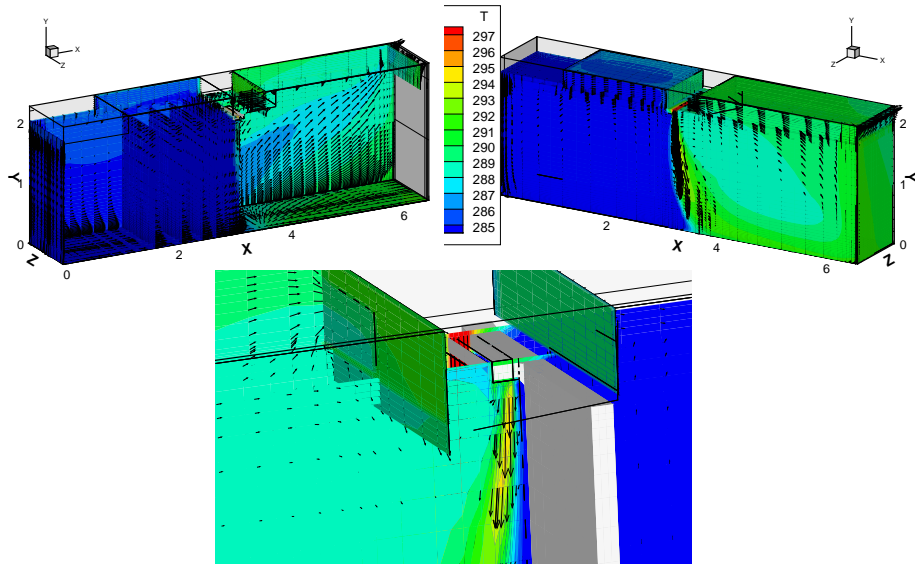
In this test an air curtain is placed just behind the door in the warm room. In Figure 5.28 are shown vectors, isotherms and the comparison with experimental data for this test. In this Figure is observed as the air-curtain prevents the entry of cold air into the inner room. It is also important to highlight the fairly good agreement between predictions and experimental data, specially for the three dimensional simulation. Air curtain contributes to maintain the warm temperature, and the energy provided by the curtain is enough to heat the air mass flow entering to the interior room. Furthermore, both the warm room and refrigerated space are maintained almost at a uniform temperature, which means air curtain is working near its ideal conditions.



**Figure 5.28:** Code validation test B. Top: numerical vs. experimental interior temperature profiles at 3 m from door. Bottom: temperature contours and velocity vectors at two room sections.

### 5.6.2   Code validation using own experimental data

As it was said before, in order to study numerically a flow it is necessary to determine inlet boundary conditions, when they are unknown, previous experiments are required. Referring to the air curtain discharge, this aspect is fulfilled in previous sections of this chapter. The results of the transversal jet produced by the air curtain with enlarged nozzle and flow straightener with imposed cross flow are selected to be simulated.
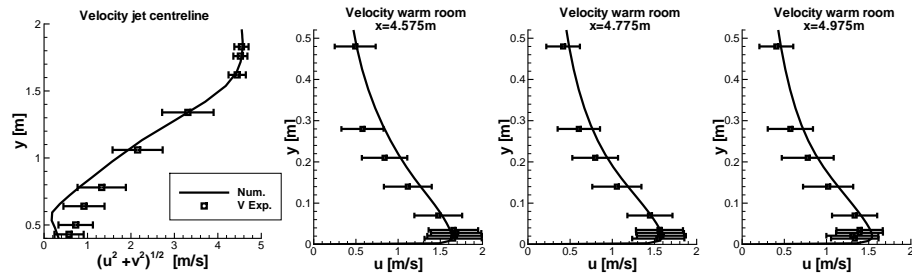


**Figure 5.29:** Code validation. Numerical results for the air curtain placed inside CTTC climatic chamber subjected to cold air cross-flow.

The climatic chamber shown in Figure 5.5 is also simulated numerically using CFD. Experimental measurements of the air curtain discharge and inlet cold air in the left room are used to feed boundary conditions in the numerical simulation. Thus, experimental data are imposed (having been previously interpolated) in the control volumes belonging to the respective inlet boundary conditions. Moreover, due to the fact that the air inside the air curtain is heated by means of electrical resistances, it is necessary to implement a subroutine in order to simulate air heating process inside air curtain. Therefore, air curtain discharge temperature depends on the air conditions at its suction and the electrical power supplied. The results are obtained with a grid with 41300 control volumes, distributed in four subdomains in order to reproduce climatic chamber experimental geometry. The grid is intensified using a tanh-like

178
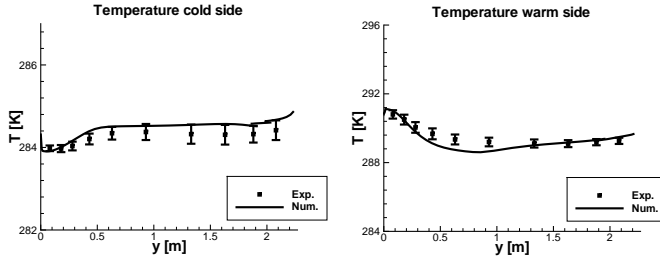
function towards the solid walls, near doorway and air curtain discharge. The model used in these numerical studies is the IL ($k\epsilon$-LEVM) model. Due to symmetry in $z$ direction, only half domain is simulated. Separating wall is $10cm$ thick and has a $\lambda = 0.03W/m \cdot K$ and a $c_p = 1210J/kg \cdot K$. The rest of the walls are simulated using an overall heat transfer coefficient ($U = 0.3W/m^2 \cdot K$) and an ambient temperature of $296K$. In Figure 5.29 numerical illustrative results of temperature contours and velocity vectors are presented.



**Figure 5.30:** Numerical and experimental mean velocity comparison for an air curtain subjected to crossflow. Jet centreline velocity decay, and streamwise velocity near the floor at $x \approx 4.575m$, $x \approx 4.775m$ and $x \approx 4.975m$ for $z \approx 1.125m$ in the warm space.

From the experiments carried out, it has been found a mean discharge velocity and turbulence intensity. Therefore, experimental measurements of the air curtain and cold air discharges are imposed as inlet boundary conditions in the numerical simulation. Furthermore, a crossflow of cold air of approximately $2000m^3/hr$ obtained from numerical experiments is imposed. Temperature of the inlet cold air is also maintained at approximately $11^oC$. Moreover, due to the fact that the air inside the air curtain is heated by means of electrical resistances, it is necessary to implement a subroutine in order to simulate this process. Then, air curtain discharge temperature depends on the air conditions at the suction of the air curtain and the electrical power supplied. In Figure 5.29 temperature contours, velocity vectors and some streamtraces are presented for the numerical results obtained using the explained conditions.

Numerical results are compared with experimental data in Figures 5.30 and 5.31. Experimental measurements are indicated with symbols, while error bars indicate the standard deviation, wich in the case of velocity means its fluctuating part or root mean square velocity. In Figure 5.30 a comparison of the air curtain discharge jet centreline velocity decay ($z \approx 1.125m$) and streamwise velocity near the floor at three different positions in $x$ direction ($x \approx 4.575m$, $x \approx 4.775m$ and $x \approx 4.975m$) in

**Figure 5.31:** Numerical and experimental temperature results comparison for an air curtain subjected to crossflow. Left: cold space at $x \approx 1.455m$, $z \approx 1.125m$; right: temperature in the warm space at $x \approx 5.35m$ and $z \approx 1.125m$.

the central plane ($z \approx 1.125m$) in the warm room is presented. In order to compare predictions and experimental data, in the case of the jet velocity centreline decay, both numerical velocity components are taken into account, due to in the experiments a one-dimensional probe is used, which only allows velocity magnitude measurement. This is not the case near the floor because velocity direction is known. As can be seen in Figure 5.30, numerical results reproduce correctly experimental data for the mean velocity in all the positions analysed. Moreover, in Figure 5.31 temperatures from experiments are presented together computational predictions in a vertical line near the centre ($x \approx 1.455m$, $z \approx 1.125m$) of cold and warm room ($x \approx 5.35m$, $z \approx 1.125m$) are presented. As shown, experimental data for temperature are numerically adequately predicted. Thus, agreement between predictions and experimental data is fairly good for velocity and temperature as well. From these results is possible to consider the mathematical model validated and thereby suitable for the study of three dimensional applications involving air curtains.

## 5.7  Conclusions

A semi-empirical model has been numerically implemented in order to have a very fast tool to calculate air curtain discharge velocity under different ambient conditions. Some shortcomings of the model have been mentioned.

A new set-up has been designed to perform experiments on air curtains. Existent climatic chamber has been adapted to achieve desired conditions. The experiment has involved the design of a special heat exchanger. Furthermore, instrumentation has been acquired and adequate post-processing tools have been created.

Air curtain prototypes have been studied experimentally. Hot wire anemometry,

specifically constant temperature anemometry has been used to determine local values of velocity. Thus, two different nozzle geometry have been tested and their discharge characterized. A modification of the air curtain discharge has been designed. This nozzle has been enlarged and finally, a variant of the second prototype has been proposed, in which a flow straightener between fans exit and air curtain discharge, has been introduced.

With this design some advantages are found, turbulence is reduced in both regions discharge and downstream jet produced. Moreover, core velocity is also increased, and the core region is maintained more distance downstream. Furthermore, velocity obtained at the air curtain discharge is more uniform and the presence of regions where fans are not blowing is minimized.

If actual nozzle configuration want to be conserved, there are some recommendations that should be considered: i) in the central region, separation between the blades for flow orientation generates turbulence. ii) improvements to the system employed for mounting the blade for flow orientation are required.

Some experiments have been numerically reproduced. Thus, a geometry of a COMHEX partner and the CTTC experimental setup are simulated using IL ($k\epsilon$-LEVM) RANS model, on cartesian grid and both two and three dimensions using multiblock technique. These results are useful to have a full detail of fluid-dynamic and thermal fields characteristics produced by the air curtain when it is placed in a doorway, and to validate the code with home-made experiments in three dimensions. Satisfactory results are obtained comparing numerical and experimental results.

# References

[1] K. Sirén. Technical Dimensioning of a Vertically Upwards Blowing Air Curtain. Part I. *Energy and Buildings*, 35:681–695, 2003.

[2] H. B. Awbi. *Ventilation of Buildings*. Chapman and Hall, 1991.

[3] M. Deru and P. Burns. Infiltration and Natural Ventilation Model for Whole-Building Energy Simulation of Residential Buildings. In *Proceedings of the ASHRAE Conference*, pages 1–10, 2003.

[4] Ashrae. *ASHRAE HANDBOOK Applications*. 1999.

[5] C.D. Pérez-Segarra, A. Oliva, M. Costa, and F. Escanes. Numerical experiments in turbulent natural and mixed convection in internal flows. *International Journal for Numerical Methods for Heat and Fluid Flow*, 5(1):13–33, 1995.

[6] S. V. Patankar. *Numerical Heat Transfer and Fluid Flow*. Hemisphere Publishing Corporation, 1980.

[7] S. Danov. *Development of experimental and numerical infrastructures for the study of compact heat exchangers and liquid overfeed refrigeration systems.* PhD thesis, Universitat Politècnica de Catalunya, 2005.

[8] H. H. Bruun. *Hot Wire Anemometry: Principles and Signal Analysis.* Oxford University Press, 1995.

[9] C. Oliet, C. D. Pérez-Segarra, S. Danov, and A. Oliva. Numerical Simulation of Dehumidifying Fin-and-Tube Heat Exchangers. Semi-Analytical Modelling and Experimental Comparison. *International Journal of Refrigeration*, 30(7):1266–1277, 2007.

[10] C.D. Pérez-Segarra, C. Oliet, S. Danov, J. Jaramillo, C. Orozco, E. Mas de les Valls, and A. Oliva. COMHEX project: Publishable Final Technical Report. Technical report, 2005.

# Chapter 6

# Air curtains. Numerical parametric studies.
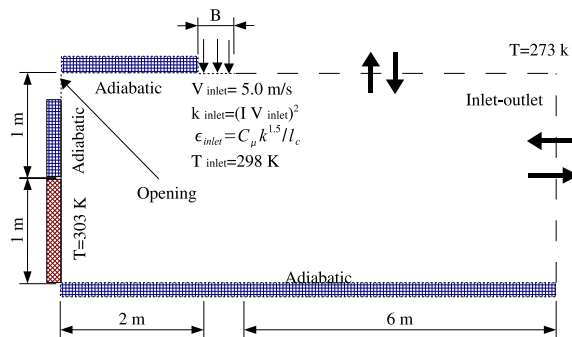
**Abstract.** The main purpose of this chapter is the development of a set of numerical studies to test air-curtains. Thus, systematic parametric studies are carried out, providing conclusions about the influence on the air-curtain behavior of its location, discharge velocity, discharge angle, and discharge temperature. Applications of air curtains in both air conditioning and refrigeration are numerically studied. Global energetic balances are specially considered together with global parameters selected in order to evaluate air curtain performance and human comfort.

## 6.1   Introduction

One of the main advantages of CFD is the possibility of performing studies of the effect of different parameters on the devices analyzed without big investments. Once, air curtains physic is understood, the code developed verified and the mathematical formulation validated, parametric studies can be carried out. Thus, in this Chapter studies are centred on the most relevant parameters influencing air curtain performance, e.g. location, discharge velocity, discharge temperature and discharge angle. Further work on the reduction of the detailed numerical results into overall energetic parameters, which are useful in air curtain or cold store rating and design codes, is also presented.

Parametric studies are divided in three different sections. In the first one, a simplified geometry is considered and two dimensional simulations are carried out as a first approximation to the study of the effect of different parameters on air curtain performance. After, a more complex geometry involving three dimensional simulations of an air curtain placed in the doorway of a building in winter season is studied. Finally, the analysis is centred in unsteady air curtain simulations in refrigeration applications.

## 6.2   Two dimensional study, air curtain device dividing two spaces
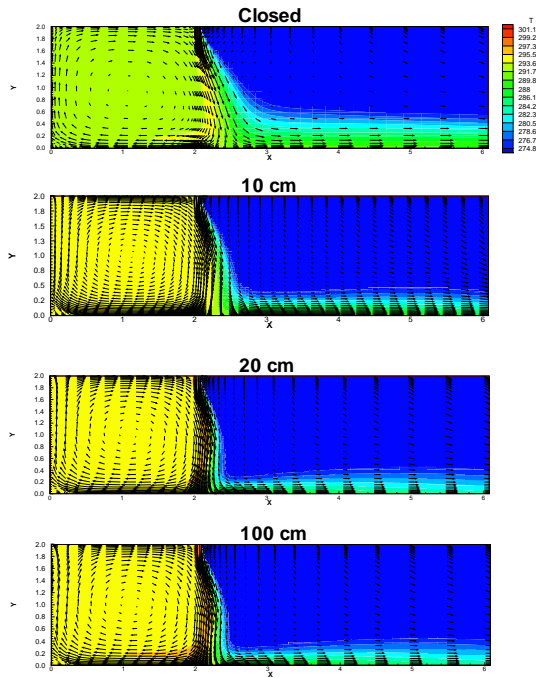


**Figure 6.1:** Configuration for the case of an air curtain dividing two spaces.

Firstly, two dimensional parametric studies of air curtains in heating applications are carried out to have an idea of the influence of different variables, e.g. discharge

velocity, conditioned space air tightness characteristics, and discharge temperature. Therefore, in this part some illustrative results obtained from two dimensional numerical simulations of complete air curtain systems are presented. In this case an air jet blows vertically from the upper zone and divides one room of $2m$ length by $2m$ height, and a bigger space that represents the open exterior space (environment) (see Figure 6.1 for details).
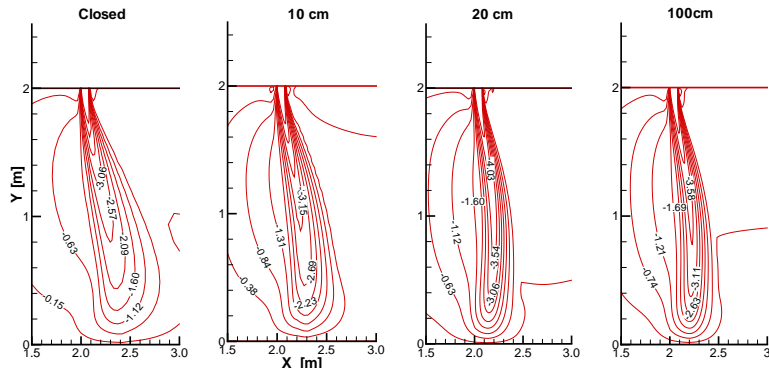


**Figure 6.2:** Influence of leakage. Velocity vectors and isotherms for air curtain device.

For all cases (if nothing different is said) the velocity imposed at the inlet is $v_{in} = 5m/s$ (Reynolds number based on nozzle width $(b_{dis})$ of 27000) and $H/b_{dis} = 25$. As is shown in Figure 6.1, the temperature at the inlet is $298K$, the floor and roof are considered adiabatic and non-slip conditions are assumed for solid walls. At the discharge, the turbulent kinetic energy $(k)$ is calculated with an intensity of $I = 0.03$, the characteristic length used to determine the dissipation rate $(\epsilon)$ is $l_c = 0.03 * b_{dis}/2$. At the exterior space (right) special boundary conditions, which permit flow inlet and outlet, are applied maintaining constant pressure equal to atmospheric pressure and

185

a constant temperature of $273K$, if the air entries the computational domain. IL ($k\epsilon$-LEVM) turbulence model is used in these simulations.

### 6.2.1 Influence of building leakage

Four cases are compared to test the influence of the building leakage: without opening, and with 10, 20, and $100cm$ openings practiced in the left wall. For all the cases a mesh with 120x90 control volumes is used. In Figure 6.2 numerical results obtained for the four cases are compared. When the wall is closed a considerable amount of heat is wasted to exterior space, whereas with any of the openings less heat is lost and the interior space is maintained warmer. The differences are clear between the case without opening and those with leakage. Furthermore, some differences remain for the cases with an opening of $10cm$ and $20cm$ in the left wall. However, similar results are obtained for $20cm$ and $100cm$ opening.



**Figure 6.3:** Influence of leakage. Velocity contours in air curtain region.

In Figure 6.3 mean velocities isolines in the air curtain region are also plotted for the four cases under consideration. As can be seen in Figure 6.3, the curtain flows almost vertically when an opening of $20cm$ or $100cm$ is done, but when the room is closed the curtain curves towards the right exterior space. In Table 6.1 are presented the impact points for each opening measured from the vertical centerline of the air curtain. The impact point of the air curtain in the floor moves depending on the size of the opening practised in the left wall. As it can be appreciated, the impact point is displaced towards the left as the opening is increased. However, in the last case the

impact point increases. This effect is produced by the air entrance through opening on the left wall.

| Opening (cm) | Impact Point (cm) | Impact point/H |
|:---:|:---:|:---:|
| Closed | 33.3 | 0.08 |
| 10 | 23.3 | 0.06 |
| 20 | 8.6 | 0.02 |
| 100 | 14.5 | 0.04 |

**Table 6.1:** Relation between impact point and protected space leakage (opening in the left wall).

### 6.2.2 Influence of discharge velocity
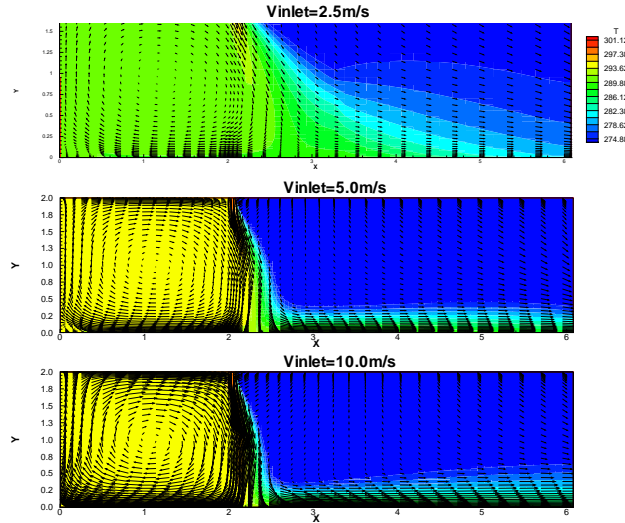
Now the geometry is fixed with an opening in the left wall of $10cm$, and the air curtain discharge velocity is changed, to evaluate its influence on air curtain performance. Thus, three values are considered $2.5m/s$, $5.0m/s$ and $10.0m/s$, which correspond to Reynolds numbers ($Re = \frac{\rho v_{in} b_{dis}}{\mu}$) of 13500, 27000 and 54000 respectively. For these studies a mesh with 128x90 control volumes is used.

In Figure 6.4 isothermal contours and velocity vectors are plotted for the three cases. As shown, with a discharge velocity of $2.5m/s$ breakthrough of the jet is presented and it is deflected towards the cold space. Therefore, the heat flux to the exterior environment is important and the temperature in the interior room decreases. Whereas, increasing the velocity to $5.0m/s$ the air curtain reaches the floor and separation between spaces is observed. However, by doubling the discharge velocity to $10.0m/s$, similar results are obtained.

In Figure 6.5 vertical velocity isolines, in the air curtain jet zone, are plotted for the three different inlet velocities studied. As it can be observed, with the velocity of $2.5m/s$ the air curtain does not reaches the floor, and the air curtain is deflected towards the exterior space. However, with discharge velocities of $5.0m/s$ and $10.0m/s$ air curtain impacts the floor, and the shape of the jet predicted is similar.

| Inlet velocity (m/s) | Impact Point (cm) | Impact point/H |
|:---:|:---:|:---:|
| 2.5 | 68.8 | 0.172 |
| 5.0 | 23.3 | 0.058 |
| 10.0 | 15.8 | 0.04 |

**Table 6.2:** Relation between impact point and inlet velocity.
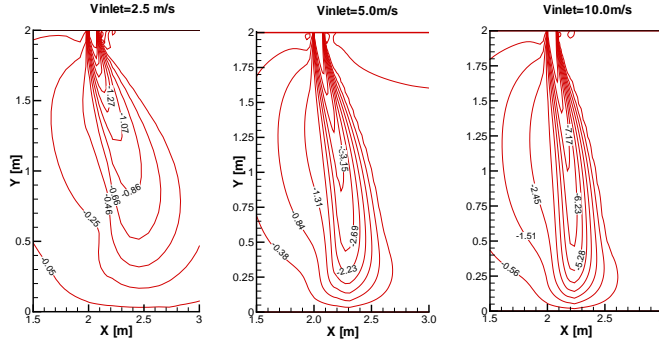
**Figure 6.4:** Influence of discharge velocity. Velocity vectors and isotherms for air curtain device for three discharge velocities.

In Table 6.2 the variation of the impact point of the air curtain, measured from the vertical centerline of the air curtain, for each one of the discharge velocities studied is shown. As it is expected, the distance of the impact point is inversely related with inlet velocity, therefore at higher velocities the point is nearer to the doorway vertical plane.
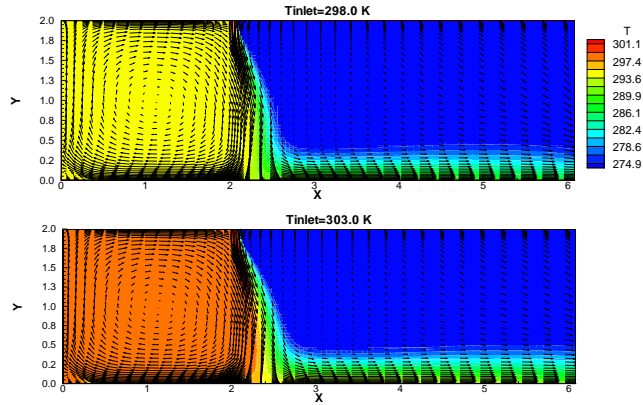
### 6.2.3  Influence of discharge temperature

A higher temperature of $303K$ is imposed at the discharge jet of the case with an opening of $10cm$ in the left wall. It is compared in Figure 6.6 with results obtained from the same geometry and conditions, but with discharge temperature of $298K$. A difference of $5K$ in the discharge temperature increases the mean temperature in the conditioned space (left side in Figure 6.6) in $4K$. Furthermore, the heat wasted to the exterior space is almost the same. The impact point for the inlet temperature is of $27.1cm$ measured from the vertical centerline of the air curtain, which is slightly larger than that with inlet temperature of $298K$. The reason for this change is the rise of the pressure generated by the stack effect when temperature difference is increased.

**Figure 6.5:** Influence of discharge velocity. Velocity isolines for three discharge velocities ($2.5m/s$, $5.0m/s$ and $10.0m/s$) in the air curtain region.
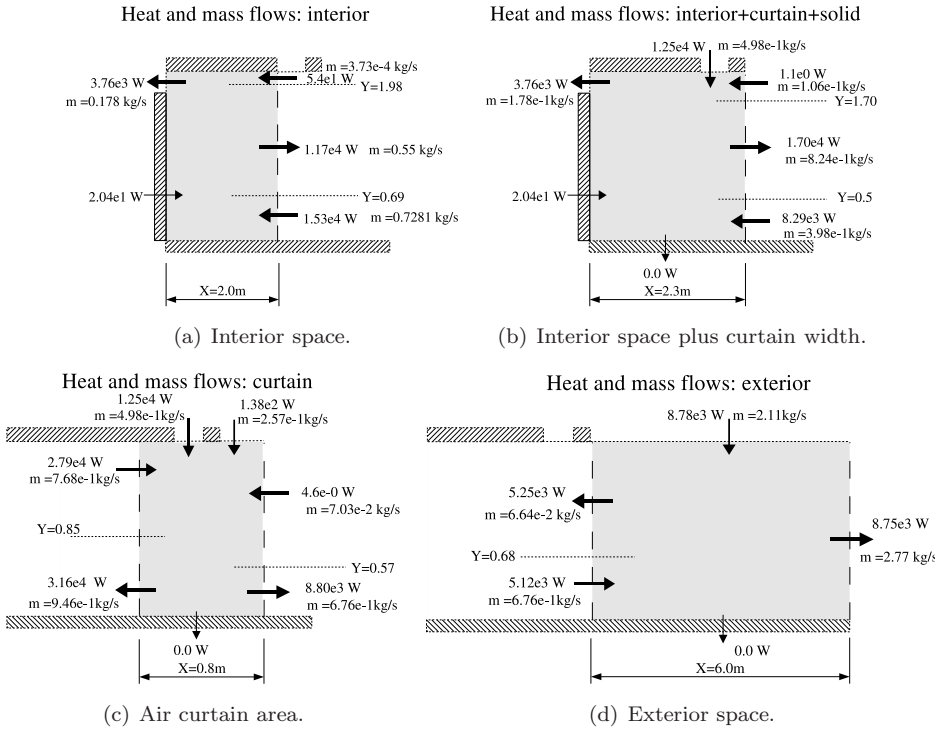


**Figure 6.6:** Influence of discharge temperature. Temperature contours and velocity vectors for two inlet temperatures.

### 6.2.4 Global energy and mass balances

The case studied with an air curtain dividing two spaces with an opening of $10cm$ in left wall, and air curtain discharge velocity of $5.0m/s$ is now analysed in terms of energy and mass balances. Different control volumes are considered. Height where the flow changes direction is also marked to separate and understand the direction of

Heat and mass flows: interior



(a) Interior space.

Heat and mass flows: interior+curtain+solid



(b) Interior space plus curtain width.

Heat and mass flows: curtain



(c) Air curtain area.

Heat and mass flows: exterior



(d) Exterior space.

**Figure 6.7:** Two dimensional energy and mass balances.

the flows.

The first balance is done over the interior room. The control volume is cut at the air curtain discharge inner corner. In Figure 6.7(a) are shown the different inlet and outlet flows of the space. In the right side transport of mass and energy is important. Moreover, it is interesting to note that in the right upper part exists a small heat and mass air entrance, maybe produced by turbulence mixing process. Entrainment of warm air into the air curtain jet, as a result of mixing process, is observed in the middle region. As product of the air curtain impingement, part of the air is re-entered to the conditioned space near the bottom wall. In the left side, a small amount of warm air leaves the room through the opening in the left wall. When the width of the air curtain is included (see Figure 6.7(b)), a flow entrance is still observed near the bottom wall at the right side of the studied volume. This agrees with the location of the impact point shown in Table 6.2. Since the impact point is located further away,

the global control volume selected to carry out energy balances does not include the whole air curtain jet.

When the area around air curtain is studied, the different contributions are clearly observed in Figure 6.7(c). As a result of recirculation generated in the warm room, a big quantity of energy returns to the air curtain through the upper part, which entries due to mixing process and sub-pressure caused by the air curtain jet. However, part of this energy is again entrained to the warm room in the bottom region after air curtain jet impingement. Reviewing right boundary, it is seen as part of the energy introduced to the domain by the air curtain is rejected to the environmental space when the jet impinges with the floor. Finally, the outside space is studied and results obtained are presented in Figure 6.7(d), where the energy losses towards the environment are shown.

## 6.3 Building doorway in winter conditions

In this section some illustrative results obtained from both two and three dimensional numerical simulations of air curtain systems in heating applications considering an air crossflow through the door are presented. Three dimensional simulations are carried out in order to evaluate the three dimensional effects on the final results. Furthermore, discharge angle is now considered within the parametric study presented. The geometry studied is similar to that used in the previous Chapter, in the section about experimental and code validation (see section 5.6). In this configuration, the air from the air curtain blows downwards from the upper zone at different angles and separates the warm room (left, opened in the left side to simulate a bigger building) from the cold space (right, which represents the exterior space,i.e. the environment). The warm room is $5m$ height, $6.2m$ depth (when three-dimensional effects are studied) and $5m$ length. The cold space is $3m$ height, $6.2m$ depth and $2m$ length. The doorway where the air curtain is mounted is $2.5m$ height and $2m$ depth (see Figure 5.26).

For all cases (if nothing different is said) the jet produced by the air curtain is characterized by imposing a constant discharge velocity, angle and temperature. At the interior space (left) a boundary condition, which permits flow inlet and outlet (see 5.3.1), is applied in the left wall. Furthermore, it is considered that the air entering the studied space is at a constant known temperature. The same turbulence model, IL ($k\epsilon$-LEVM), and grid are maintained throughout all the study (see section 2.2 for details). Taking advantage of symmetry conditions only half domain is simulated. In Table 6.3 the different situations analyzed are summarized.

The importance of this kind of studies is the low investment resources invested. This contribute to the study of several different situations of interest in short time periods demanding relatively little computational capacity. The reason why two dimensional simulations are carried out at the beginning, is to have a first vision of

| Case | $\alpha$ ($^o$) | $v_{dis}$ ($m/s$) | $T_{dis}$ ($K$) | $v_s$ ($m/s$) | $T_{ext-in}$ ($K$) | $\dot{V}_{ext-in}$ ($m^3/h$) | $\dot{V}_{ext-out}$ ($m^3/h$) | $T_{int}$ ($K$) |
|---|---|---|---|---|---|---|---|---|
| Standard | 15 | 7.0 | 308.0 | 1.73 | 273.0 | 3000 | 1000 | 293.0 |
| test1 | 15 | 7.0 | 308.0 | 1.73 | 268.0 | 3000 | 1000 | 293.0 |
| test2 | 15 | 7.0 | 308.0 | 1.73 | 278.0 | 3000 | 1000 | 293.0 |
| test3 | 15 | 7.0 | 308.0 | 1.73 | 273.0 | 4000 | 1000 | 293.0 |
| test4 | 15 | 7.0 | 308.0 | 1.73 | 273.0 | 2000 | 1000 | 293.0 |
| test5 | 0 | 7.0 | 308.0 | 1.73 | 273.0 | 3000 | 1000 | 293.0 |
| test6 | 15 | 7.0 | 313.0 | 1.73 | 273.0 | 3000 | 1000 | 293.0 |
| test7 | 15 | 5.0 | 308.0 | 1.23 | 273.0 | 3000 | 1000 | 293.0 |
| test8 | 15 | 9.0 | 308.0 | 2.22 | 273.0 | 3000 | 1000 | 293.0 |
| test9 | 30 | 7.0 | 308.0 | 1.73 | 273.0 | 3000 | 1000 | 293.0 |
| test10 | 15 | 7.0 | 303.0 | 1.73 | 273.0 | 3000 | 1000 | 293.0 |

**Table 6.3:** Boundary conditions used in the parametric study of an air curtain placed at the entrance of a building in winter conditions.

the problem to be solved. However, the most refined step to simulate an air curtain together with its adjacent areas is the use of three dimensional computational fluid dynamics.
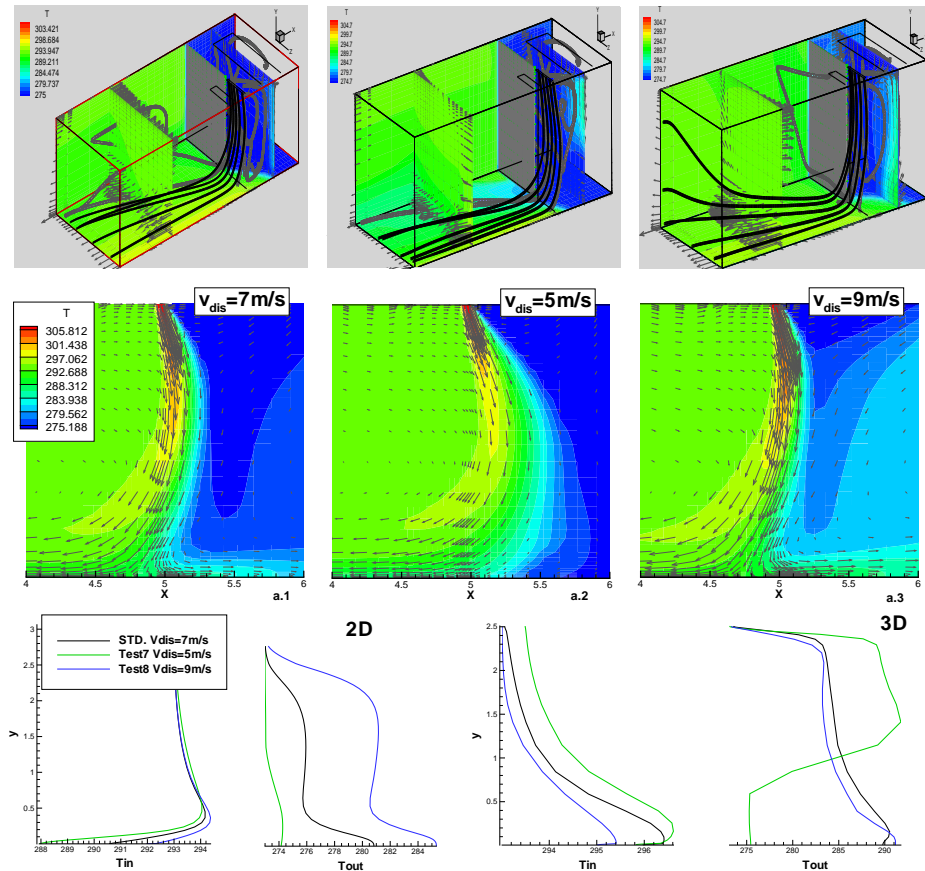
### 6.3.1    Influence of discharge velocity

Representative results obtained for different discharge velocities are herewith presented. Such parameter can be controlled by the air curtain designer and the differences among the different situations analyzed are appreciable. In the top part of Figure 6.8 an example of three dimensional simulation results is presented. Furthermore, results from two dimensional simulations in the doorway central plane are presented in the middle of the Figure. Finally, the inner room temperature profiles (3m left from the door) and exterior temperature profiles (middle plane) are presented at the bottom of this Figure.

It can be seen that for the situations analyzed, the air curtain discharge velocity has relatively little influence over the inner temperature, even though it reduces when velocity is increased as product of the mixing process. However, temperature in the right space is much more influenced, for higher velocity values it produces an increment in thermal losses to the exterior space. Referring to the exterior room, visible discrepancies between two and three dimensional results are observed in the detailed study presented at the bottom of Figure 6.8. This is expected due to three dimensional characteristics of the flow studied. Moreover, it maybe explained because

192
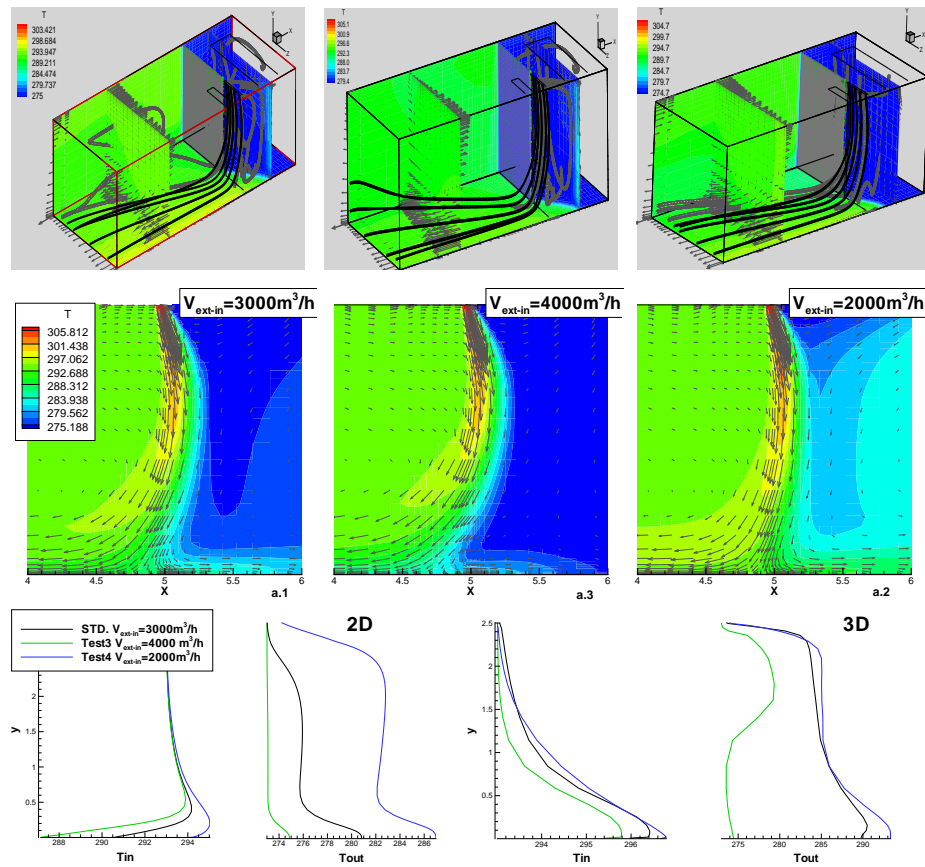
with the velocity of $5m/s$ the jet is suctioned by the vertical flow imposed in the cold space (jet too deflected), which can be seen in the central top plot of three dimensional results in the same Figure.



**Figure 6.8:** Comparative study for three jet discharge velocities. Left: standard case ($v_{dis} = 7m/s$); Centre: test 7 ($v_{dis} = 5m/s$); Right: test 8 ($v_{dis} = 9m/s$). Top: three-dimensional simulations; Mid: two-dimensional simulations, and bottom: temperature profile comparison for inner temperature ($T_{in}$) $3m$ left from door and outside temperature ($T_{out}$) $1m$ right from door.

193

### 6.3.2 Influence of air mass flow through the door

Illustrative results of different imposed air mass flows through doorway are presented in Figure 6.9.



**Figure 6.9:** Comparative study for three velocities in outside space. Left: standard case ($\dot{V}_{ext-in} = 3000m^3/h$); Centre: test 3 ($\dot{V}_{ext-in} = 4000m^3/h$); Right: test 4 ($\dot{V}_{ext-in} = 2000m^3/h$). Top: three-dimensional simulations; Mid: two-dimensional simulations, and bottom: temperature profile comparison for inner temperature ($T_{in}$) 3m left from door and outside temperature ($T_{out}$) 1m right from door.

194

Two air flow rates are imposed at the inlet (top) of exterior room, in tests3 and test4 ($\dot{V}_{ext-in} = 4000m^3/h$, $\dot{V}_{ext-in} = 2000m^3/h$), while $\dot{V}_{ext-out}$ is maintained constant. Therefore, two different air flows are obligated to pass through the protected doorway. They are also compared with *standard* case. The idea is to simulate a higher wind pressure and check its effect. At the top of Figure 6.9 three-dimensional results with representative planes are shown. In the middle two-dimensional results of air curtain region can be seen. The inner room temperature profile (3m left from the door) and exterior temperature profile (middle plane) of two-dimensional and three-dimensional numerical results are presented at the bottom of Figure 6.9.

In Figure 6.9 it can be observed as in each simulation temperature profiles change with the mass flow imposed. However, influence of mass flow is more significant in the exterior space (right), where some differences remain between two dimensional and three dimensional simulations. In the last one a big difference between a $V_{ext-in} = 2000m^3/h$ and both *standard* and $V_{ext-in} = 4000m^3/h$ cases is observed in the cold exterior room.
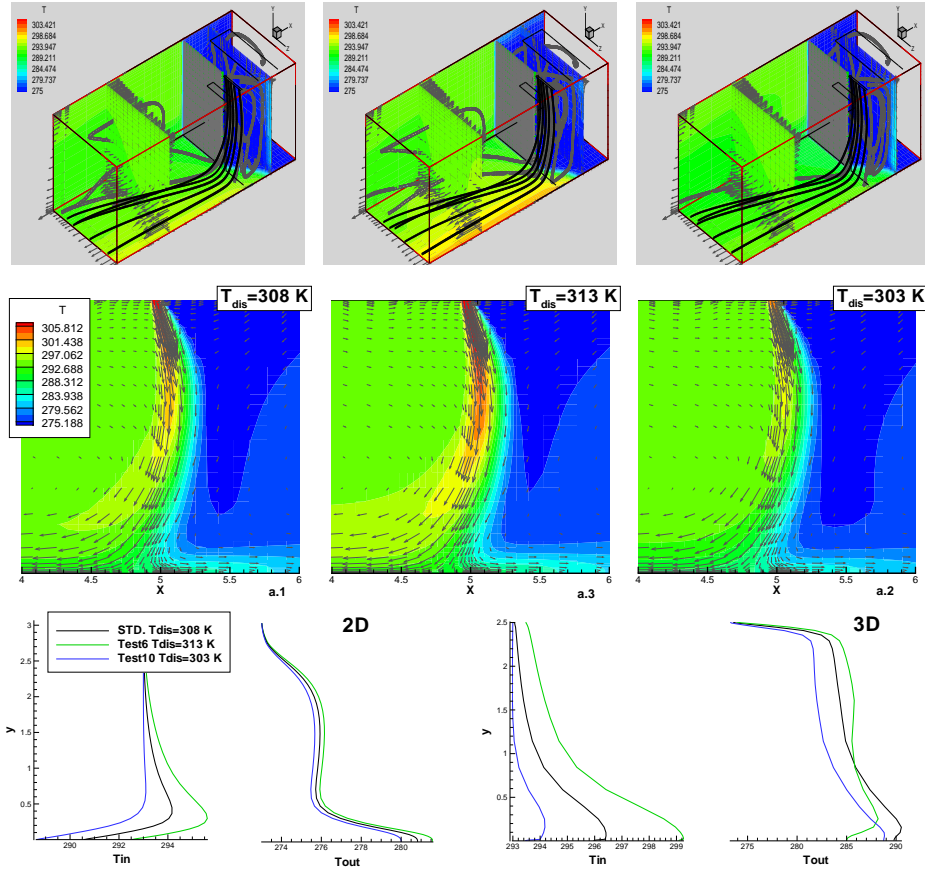
As shown in the mid plots of Figure 6.9, the bottom part of the jet is also deflected towards the interior room as the flow imposed through the door is increased. But, in the upper part the path of the jet is almost the same for the three situations studied, and it is not deflected to produce breakthrough.

### 6.3.3 Influence of discharge temperature

In Figure 6.10 are presented representative numerical results varying the air-curtain discharge temperature for a constant discharge velocity and angle (see Table 6.3). Three dimensional, two dimensional and punctual results are shown in Figure 6.10. As it can be seen, mean velocities within the domain studied are not affected by the changes in discharge temperature, which is known a priori because these cases are of the forced convection type, thus momentum results are decoupled of energy solutions.

Influence of air-curtain discharge temperature affects mainly inner temperature near the bottom region. Furthermore, with a discharge temperature bigger than $303K$ the air inside the interior room is heated considerably, which is undesirable because it can be necessary to refrigerate at the same time this space wasting energy. On the other hand, discharge temperature effects are not significant in the exterior temperature profile studied (at $1m$ right from door plane), then energy losses are comparable for the three discharge temperatures.

Even though, differences in the profiles depicted in the interior and exterior room are more marked when three dimensional simulations are reviewed, the shape of the temperature profiles analyzed is similar for two and three dimensional simulations in these cases.
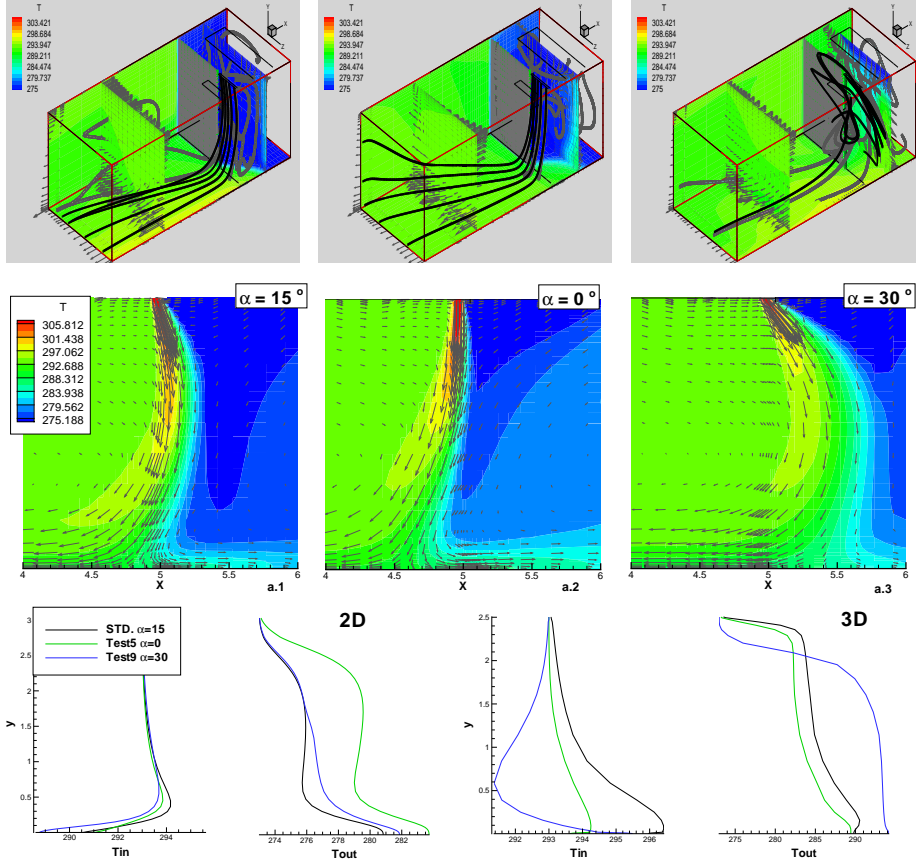
**Figure 6.10:** Comparative study for discharge temperature. Left: standard case ($T_{dis} = 308K$); Centre: test 6 ($T_{dis} = 313K$); Right: test 10 ($T_{dis} = 303K$). Top: three-dimensional simulations; Mid: two-dimensional simulations, and bottom: temperature profile comparison for inner temperature ($T_{in}$) 3m left from door and outside temperature ($T_{out}$) 1m right from door.

### 6.3.4 Influence of discharge angle

Characteristic results accomplished for different air curtain discharge angles are now analyzed. In the top of Figure 6.11 an example of three-dimensional simulation results is shown. Two dimensional results are presented in the middle of this Figure.
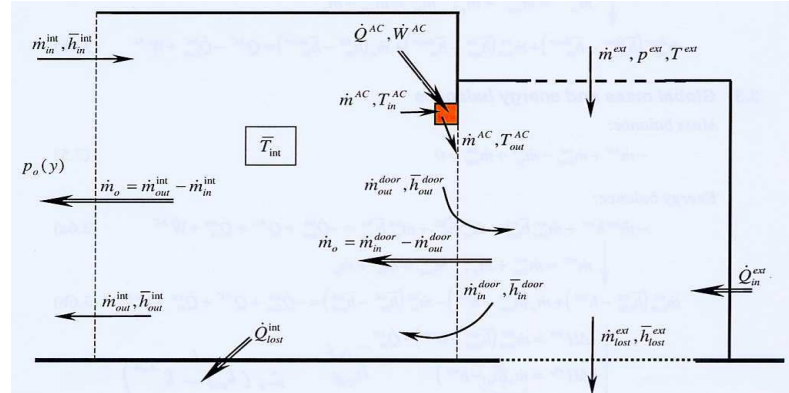
**Figure 6.11:** Comparative study for discharge angle. Left: standard case ($\alpha = 15^o$); Centre: test 5 ($\alpha = 0^o$); Right: test 9 ($\alpha = 30^o$). Top: three-dimensional simulations; Mid: two-dimensional simulations, and bottom: temperature profile comparison for inner temperature ($T_{in}$) 3m left from door and outside temperature ($T_{out}$) 1m right from door.

Moreover, the inner room temperature profiles (3m left from the door) and exterior temperature profiles (central plane) are presented at the bottom of the same Figure. When the angle is increased thermal losses to the outside cold space are also incremented. These losses are particularly important when the angle change from $15^o$ to $30^o$. Furthermore, temperature in the inner room diminishes considerably for the

197

discharge angle of $30^o$. Nevertheless, when the angle is increased from $0^o$ to $15^o$ temperature in this space becomes bigger, specially reviewing three dimensional results. Thus, in this study differences from two dimensional to three dimensional simulations are significant. This can be explained by the effects of air entrained through the ends of the jet produced by the air curtain. When the angle is increased, the air curtain is deflected towards the exterior space leaving unprotected the sides of the doorway. This effect is not taken into account in two dimensional simulations.

### 6.3.5 Global energetic study

In Figure 6.12 a simple and generic representation of a thermal system including HVAC and air curtain components can be observed. The method used in this section is different to that presented in the previous one because of the presence of cold air crossflow imposed through the air curtain and the HVAC system is also taken into account. A net mass flow is assumed from the exterior space to the warm room. This flow is discharged at certain enthalpy, $h_o$ to an external environment with a pressure, $p_o$. The air provided by the air curtain can be heated with electrical resistances or hot water, $\dot{Q}^{AC}$. Furthermore, the air is blowed by a fan using a work, $\dot{W}^{AC}$.



**Figure 6.12:** Heat, enthalpy and mass fluxes energetic study.

The internal warm temperature, $\overline{T}_{int}$ is maintained by a heater. The warm space can lose some energy to its environment, $\dot{Q}_{lost}^{int}$. Therefore, the heater must compensate the losses and perhaps, the net flow of air through the door.

The global mass (Eq. 6.1) and energy (Eq. 6.2) balances for this situation are as follows:

$$-\dot{m}^{ext} + \dot{m}_{lost}^{ext} + \dot{m}_o = 0 \tag{6.1}$$

## 6.3. Building doorway in winter conditions

$$\dot{m}_{lost}^{ext}(\overline{h}_{lost}^{ext} - h^{ext}) + \dot{m}_o(\overline{h}_{out}^{int} - h^{ext}) - \dot{m}_{in}^{int}(\overline{h}_{in}^{int} - \overline{h}_{out}^{int}) = -\dot{Q}_{lost}^{int} + \dot{Q}^{AC} + \dot{Q}_{in}^{ext} + \dot{W}^{AC}$$
$$(6.2)$$

Reordering and introducing new terms the next expression is obtained:

$$
\begin{aligned}
\Delta H^{ext} &= \dot{m}_{lost}^{ext}(\overline{h}_{lost}^{ext} - h^{ext}) - \dot{Q}_{in}^{ext} \\
\Delta H^{\dot{m}_o} &= \dot{m}_o(\overline{h}_{out}^{int} - h^{ext}) \\
\Delta \dot{Q}^H &= \dot{m}_{in}^{int}(\overline{h}_{in}^{int} - \overline{h}_{out}^{int}) - \dot{Q}_{lost}^{int}
\end{aligned}
$$

$$\Delta H^{ext} + \Delta H^{\dot{m}_o} = \Delta \dot{Q}^H + \dot{Q}^{AC} + \dot{W}^{AC} \qquad (6.3)$$
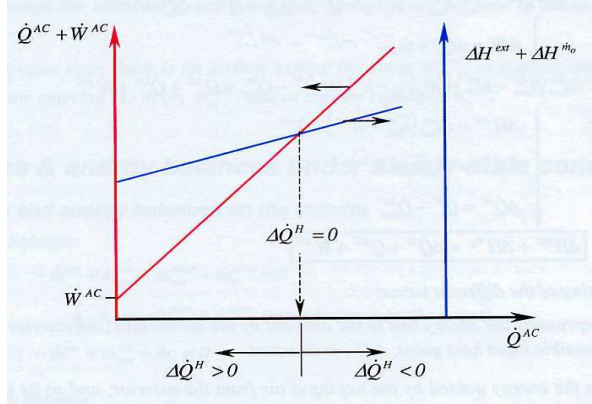
The physical meaning of the terms obtained is explained as follows:

- $\Delta H^{ext}$ : represents the energy lost to the ambient by the air curtain and possible input heat through the external walls.

- $\Delta H^{\dot{m}_o}$ : is the energy gained by the net input air from the exterior.

- $\Delta \dot{Q}^H$ : additional heating provided to face the losses in the interior (warm) room. The extra power delivered by the heater is needed to keep mean warm room temperature.

When an air curtain is heated and a heater is used, there are different possibilities to consider:

- $\Delta \dot{Q}^H = 0$ : the air curtain compensates the heat losses due to the open door.

- $\Delta \dot{Q}^H > 0$ : the heater must heat, in part, the inlet air through the open door.

- $\Delta \dot{Q}^H < 0$ : it is an undesirable situation. Too much energy is delivered by the air curtain.

By means of numerical simulations is possible to obtain each of the terms appearing in the global energy balance to obtain graphics such as that presented in Figure 6.13, in a situation with an imposed mass flow through the door. In this graphic, the optimum of the air curtain, from the energetic point of view, is found in the intersection of the two plotted lines. The energy that must be supplied to the air curtain can be read in the horizontal axe.

**Figure 6.13:** Graphical representation of energetic balance.
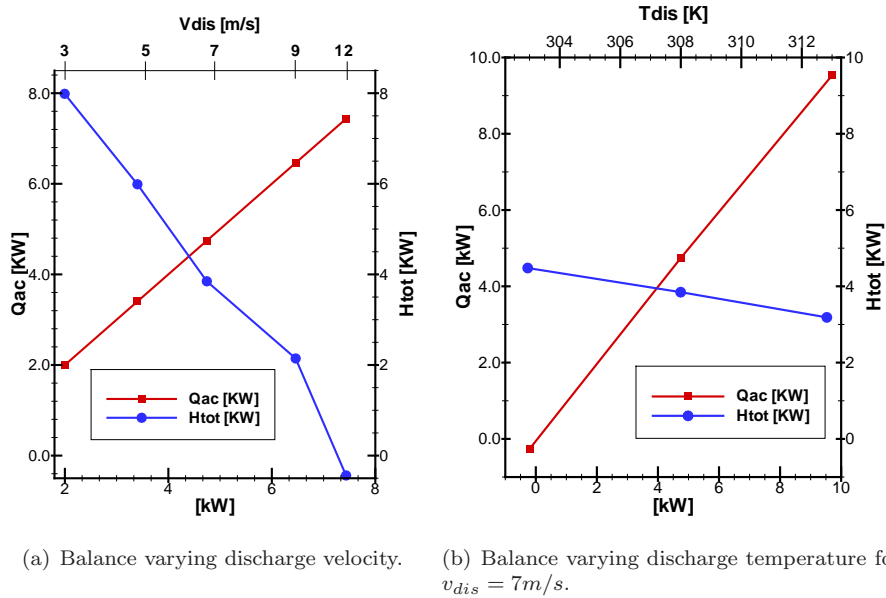
**Results global energetic study**

This energetic study is carried out on the test cases presented in Table 6.3 in order to evaluate optimum air curtain discharge jet conditions.

The discharge velocity of the air curtain has relevant effects on the jet profile, thus it is the first parameter to be considered in the energetic study. It has been observed in the parametric study how, as velocity increases, the mixing with the exterior and the heat losses are greater. When applying the above mentioned energy balance to these cases, and reviewing results presented in Figure 6.14(a), it can be concluded that a discharge velocity between 5 and $7m/s$ is the optimal. Otherwise, either the energy needed to create the jet is partly lost to the ambient, or the air curtain is not able to isolate the room from the exterior. This conclusion is made by comparison of five different discharge velocities, i.e. 3, 5, 7, 9 and $12m/s$. In all these cases the rest of parameters of the jet and the external conditions are fixed; therefore, the velocity of about $5 - 7m/s$ is only optimal under these conditions.

Now the discharge temperature is considered in the energetic analysis. As it was shown in the parametric study, the influence of the discharge temperature (among a reasonable range) is more relevant on the interior room mean temperature than the discharge velocity. Therefore, the optimum discharge temperature should also be considered in the air curtain design process. Thus, Figure 6.14(b) shows that the optimal temperature should have a value around $307K$. However, more studies should be carried out on this sense, because this point is the adequate for the discharge velocity studied, and could change for a different velocity. Therefore, these results should be considered with due regard for the range of values they have been obtained.

(a) Balance varying discharge velocity.   (b) Balance varying discharge temperature for
$v_{dis} = 7m/s$.

**Figure 6.14:** Global energetic study results. Graphic representation.

Referring to the discharge angle, it can be seen that angles greater than 15 degrees bring a situation where losses to the exterior are so important that the jet is not able to isolate the room from the exterior. The behavior of the jet respect to the discharge angle can be seen in the previous section, but to determine the optimal angle, by means of the energetic study, more cases should be studied in the range from 0 to 15 degrees.

### 6.3.6   Comfort considerations: PDE factor

In air conditioning/heating applications, the purpose of an air curtain is to isolate a room or a building from the external weather conditions for the comfort and well-being of the human occupants within these spaces. Therefore, a study of parameters like temperature, humidity or air velocity must be accomplished to determine human comfort.

The percentage of people experiencing draught (PED), is the parameter selected to evaluate the comfort of people near a doorway with an air curtain. This parameter takes into account the mean air speed ($\bar{v}$) and air temperature ($T_a$), at the height analyzed [1]. The PED is an empirical correlation product of a linear regresion analysis
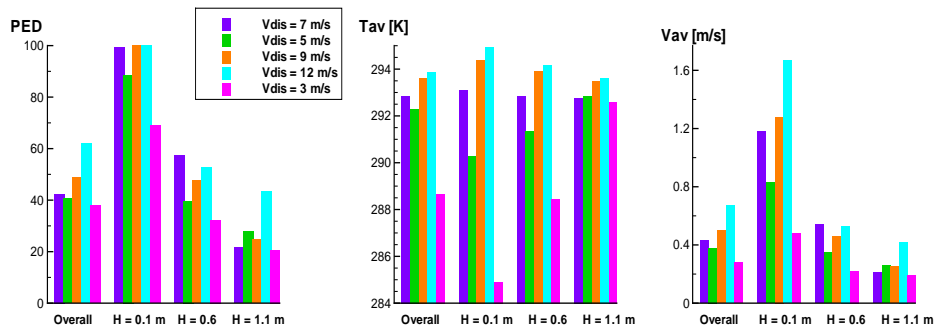
of experimental data, which can be written as follows:

$$PED = 113(\bar{v} - 0.05) - 2.15T_a + 46 \qquad (6.4)$$
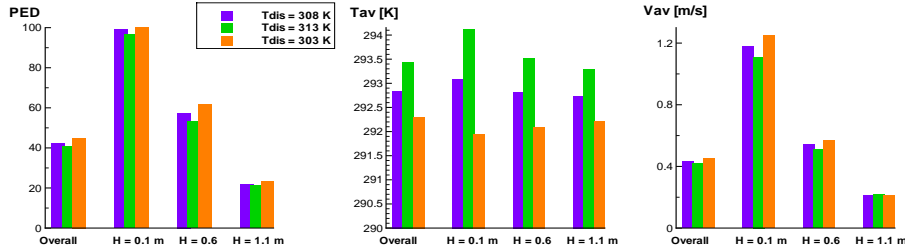
The PED is expressed as the percentage of unsatisfied people. It is evaluated at $3m$ away from the doorway where the air curtain is mounted, and until a height of $2m$. The same study is also done at specific heights like at ankle level $(0.1m)$, knee level $(0.6m)$ and neck level $(1.1m)$, to study the comfort of a person seated at $3m$ far from the air curtain in the interior room. The study is carried out comparing the different tests studied in the foregoing parametric study on a building in winter conditions.

In Figures 6.15-6.18 the PED factor, mean velocity and mean air temperature are plotted at the different height studied and for each of the parameters analyzed in the last section, i.e. discharge velocity, discharge temperature, discharge angle and mass flow passing trough the door. In these Figures is shown that the air curtain discharge velocity and air mass flow through the door are the most determinant parameters on comfort level. Moreover, for all cases the PED is too high to be acceptable due to the mean air speed at ankle height $(0.1m)$. The point is that in case of studying a fixed net flow incoming from the exterior, high velocities at ankle level always appear at $3m$ far from the doorway in the interior room. In a real situation involving air curtains is supposed that this event would be avoided.
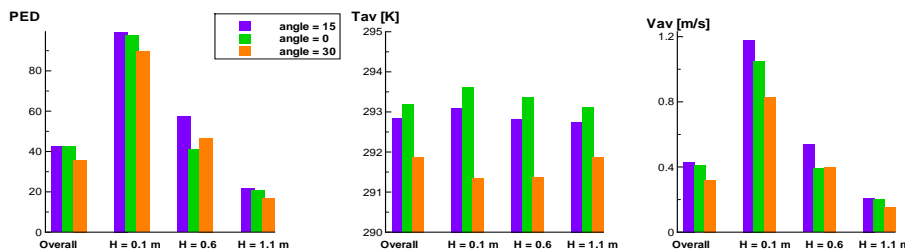


**Figure 6.15:** Comfort study varying the air curtain discharge velocity.
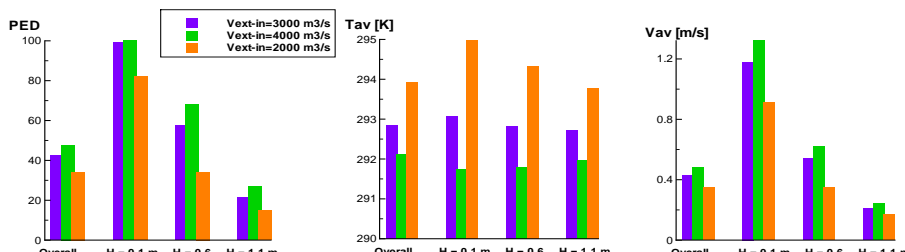
**Figure 6.16:** Comfort study varying the air curtain discharge temperature.
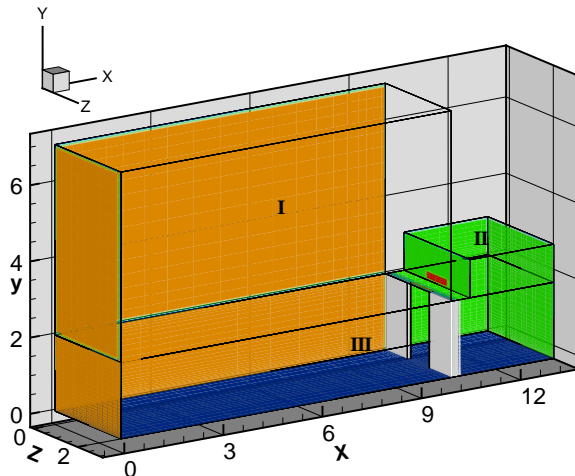


**Figure 6.17:** Comfort study varying the air curtain discharge angle.



**Figure 6.18:** Comfort study varying mass flow through door.

## 6.4   Application to refrigerated chambers

Performance of air curtains in refrigeration applications have been studied during the last years. Thus, as it was noted in the introductory Chapter, similar studies to the developed in this section, have been experimentally done by Foster et al. [2]. Moreover, Foster et al. [3] evaluated the effectiveness of a plane jet air curtain used in refrigerated rooms. They found an effectiveness between 0.2 and 0.8, depending on the air curtain discharge velocity. A study of air curtains separating two adjacent spaces was also numerically studied by Costa et al. [4], but they restricted the study to a two dimensional situation. More recently Foster et al. [5] have studied three-dimensional effects of air curtains in the entrance of refrigerated rooms, they have also compared measured air curtain efficiency at different discharge velocities against a three-dimensional CFD model.



**Figure 6.19:** Geometry for numerical studies in refrigerated chambers.

This section is devoted to the application of air curtain devices to mitigate the refrigerated chambers heat and humidity gains. Further work on the reduction of the detailed numerical results into overall energetic parameters, which are useful in air curtain or cold store rating and design codes, is also presented. Unsteady three-dimensional numerical parametric studies are carried out, simulating the process of refrigerated chamber sudden door opening, and maintaining the door opened during a certain time. In this work efficiency is evaluated, but the influence of more parameters is studied,e.g. discharge angle, discharge temperature, discharge velocity, location of

the air curtain, etc.

In Figure 6.19 the geometry used for all the numerical experiments carried out in this section is presented. It consists of two spaces separated by a wall with an opening above which air curtain is mounted. The dimensions of the left (warm) space are: $10m \times 7m \times 3m$. The dimensions of the right (cold) room are: $3m \times 3m \times 3m$. The width of the door is $1m$ and its height is $2m$. The wall is $10cm$ thick (white colour in Figure 6.19). At the beginning of the simulation the temperature is assumed to be constant in each one of the spaces for all the cases presented. Thus, in the left space a temperature of $298K$ is imposed, if nothing different is said, whereas in the right space a temperature of $273K$ is assumed. Non-slip condition is used at the walls and they are considered adiabatic with exception of separating wall which has a $\lambda = 0.03W/m \cdot K$ and a $c_p = 1210J/kg \cdot K$. For the air curtain suction a pressure outflow ($p = p_{out}$, $\frac{\partial \phi}{\partial n} = 0$, where $\phi = u, T, k, \epsilon, \omega$) boundary condition is used.

| Case | $\alpha^*$ | $V_{inlet}$ | $T_{cold}$ | $T_{warm}$ | Suction/ | Location | Model |
|------|------------|-------------|------------|------------|----------|----------|-------|
|      | $(^o)$ | $(m/s)$ | $(K)$ | $(K)$ | discharge | (side) |  |
| No curtain | 0 | 4.55 | 273.0 | 298.0 | - | - | IL |
| test 1 | 0 | 4.55 | 273.0 | 298.0 | Cold | Cold | WXT |
| test 2 | 0 | 4.55 | 273.0 | 298.0 | Warm | Warm | IL |
| test 3 | 0 | 4.55 | 273.0 | 298.0 | Cold | Cold | IL |
| test 4 | 0 | 4.55 | 273.0 | 298.0 | 50% warm | Warm | IL |
| test 5 | 0 | 4.55 | 273.0 | 298.0 | 66% warm | Warm | IL |
| test 6 | 0 | 4.55 | 273.0 | 313.0 | Warm | Warm | IL |
| test 7 | 0 | 2.50 | 273.0 | 298.0 | Warm | Warm | IL |
| test 8 | 0 | 7.50 | 273.0 | 298.0 | Warm | Warm | IL |
| test 9 | 15 | 4.55 | 273.0 | 298.0 | Warm | Warm | IL |
| test 10 | 30 | 4.55 | 273.0 | 298.0 | Warm | Warm | IL |
| test 11 | -15 | 4.55 | 273.0 | 298.0 | Warm | Warm | IL |

**Table 6.4:** Characterisation of tests studied in refrigerated chamber parametric study. $^*$angle positive towards cold side.

Furthermore, an inflow condition is imposed at the air curtain discharge, with a given constant velocity, a mean temperature equal to that of the suction and turbulence quantities set by means of a turbulence intensity of $I = 0.07$ and a $l_c = 0.3 * B/2$ (see Figure 4.1(a)). Moreover, taking advantage of the geometry proposed, only half domain is simulated due to symmetry conditions. The whole domain is divided into three subdomains to reduce CPU time. The division is marked by a horizontal black line in Figure 6.19, and the subdomains denoted as I, II and III respectively. Thus, the upper part of the warm room is solved in subdomain I, the upper part of the cold

room in II, and the bottom part of the whole domain in subdomain III.

In table 6.4 the different situations considered are shown.

### 6.4.1 Parameters selected for air curtain performance evaluation

Parameters selected in order to evaluate air curtain performance are explained in detail. These parameters give an idea about energy gains or losses of the refrigerated chamber. Using them is also easy to quantify air curtain efficiency. Therefore, they make possible from numerical experiments to select the best air curtain parameters for given outside conditions, and the set of desired conditions inside the refrigerated chamber. Thus, a post-process was implemented in the code used for the numerical simulation of air curtains in order to evaluate them.

**Energy gains of the refrigerated room**

Using CFD simulations, the temperature is known in all the domain. With this information is possible to evaluate the energy gains or losses of the air within the refrigerated chamber. This is a very important value because it represents a refrigeration load that at the end is going to increase the operation cost of the chamber. The energy variation is evaluated as follows:

$$Q = \int_{t_1}^{t_2} \dot{E} dt = \int_{t_1}^{t_2} \left( \frac{\partial}{\partial t} \int_V (\rho c_p T dV) \right) dt \qquad (6.5)$$

**Mean temperature**

Eventhough temperature is known everywhere inside domain simulated, the mean temperature inside the refrigerated room gives a global indicator of the changes in this room. For its evaluation a volumetric average is applied:

$$T_{mean} = \frac{1}{V} \int_V T dV \qquad (6.6)$$

being $V$ the volume of air inside the refrigerated chamber.

**Sealing efficiency**

The sealing efficiency of the air curtain can be also calculated from the temperature (energy) variations within the domain considered. The efficiency of the air curtain is the relation between the heat flux with or without air curtain across the doorway.

Thus, the sealing efficiency can be calculated as $Eff = 1 - \frac{Q}{Q_o}$. Where $Q_o$ is the internal energy variation without air curtain and $Q$ is the equivalent when the air curtain is working. An efficiency of one means perfect sealing, while an efficiency of zero signifies no sealing at all.

**Mass exchange**

Another interesting parameter that can be evaluated after a numerical simulation is the mass exchange between two given areas. For the situation under study the mass exchange through the opening doorway is calculated. The mass exchange is necessary specially when temperatures are all lower than zero and latent heat needs to be evaluated. A simplified model presented below has been developed to calculate mass exchange. In this model air displacement is assumed and diffusion effects are neglected. The mass exchange is calculated in terms of temperature. Considering that $M$ is the mass of air inside the refrigerated chamber, then $M = \int \rho dV$. Carrying out a energy balance in terms of enthalpy is possible to write:

$$\frac{\partial}{\partial t} \int h\rho dV + \int h\rho \overrightarrow{v} \cdot \overrightarrow{n} dS \approx 0 \tag{6.7}$$

which integrated in the whole refrigerated room

$$M \frac{\partial \bar{h}_{int}}{\partial t} + \dot{m}(h_{int} - h_{ext}) = 0 \tag{6.8}$$

where, $M = \rho V$; doing the time integration from $t = 0$ to $t = t$, and assuming that $h_{int} = h_{int}^0$ and the exterior enthalpy ($h_{ext}$) remains constant,

$$M(\bar{h}_{int} - \bar{h}_{int}^0) + \int_{t=0}^{t} \dot{m}(h_{int}^0 - h_{ext})dt = 0 \tag{6.9}$$

if now it is assumed that $m^* = \int \dot{m}dt$, expressing enthalpy variation in terms of temperature and dropping $int$ subscript, we have

$$\rho V c_p (T_{mean} - T^0) + m^* c_p (T^0 - T_{ext}) = 0 \tag{6.10}$$

reordering and working out the value of mass exchange, the following relation is obtained

$$m^* = \frac{T_{mean} - T^0}{T_{ext} - T^0} \rho V \tag{6.11}$$

where $T^0$ is the initial temperature inside refrigerated room.

**Entrainment rate and infiltration**

Infiltration ($I$) or entrainment rate ($ER$) values can be evaluated as function of global temperatures or more precisely in terms of the mass exchange across the doorway as follows:
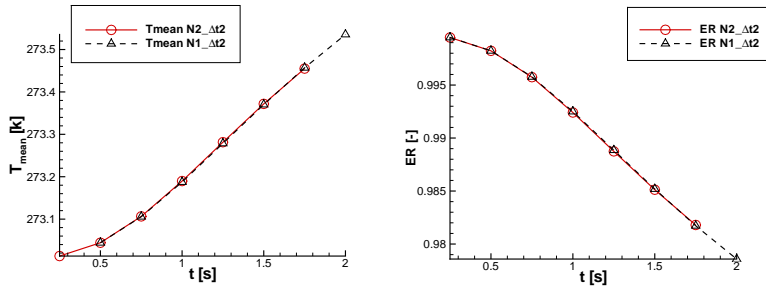
$$ER \quad = \quad 1 - \frac{m^*}{\rho V} \tag{6.12}$$

$$I \quad = \quad \frac{m^*}{\rho V} \tag{6.13}$$

An entrainment rate near to the unity is desirable. On the other hand, infiltration should be as small as possible in order to have a sealed refrigerated chamber. Infiltration is given in number of refrigerated chamber volumes exchanged.
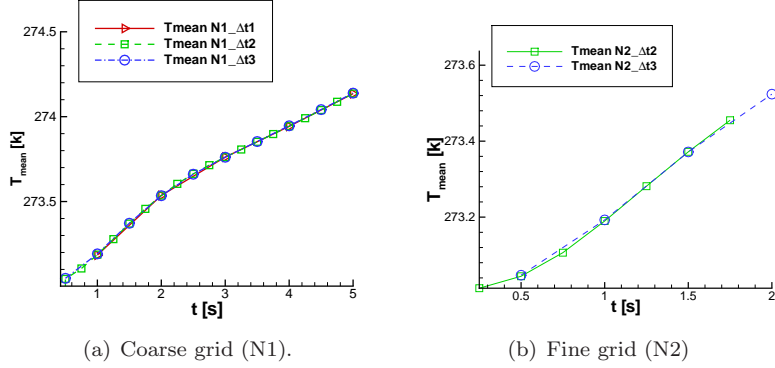
### 6.4.2 Influence of turbulence model, grid and time step

Before a set of numerical experiments is carried out, one of the most important aspects to be considered is to verify that the solution obtained is independent of the grid used and, if the problem involves a transient simulation, of the time step selected. In this work both verification procedures are considered. In a first study the original grid with approximately $N1 = 21000$ control volumes has been increased to a finer one with $N2 = 107000$ control volumes. In Figure 6.20 results obtained for the mean temperature and entrainment rate using both meshes, for the first two seconds of *test*3 case are compared. As it can be observed with both grids similar solutions are achieved, thus the coarse grid can be used in the parametric study, and the results using it can be considered grid independent.



**Figure 6.20:** Grid independence verification. Mean temperature cold room and entrainment rate. dt2 means a time step of 0.05s, N1: coarse grid and N2: fine grid.

(a) Coarse grid (N1).

(b) Fine grid (N2)
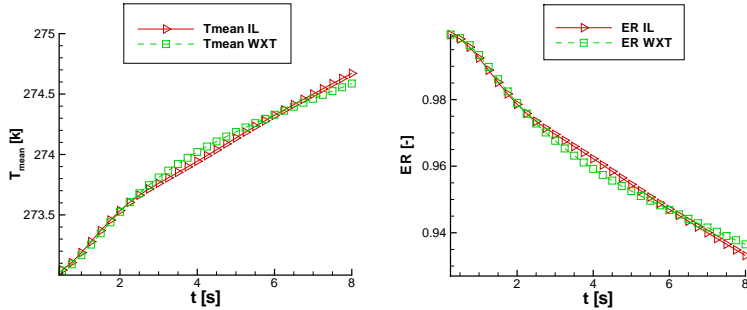
**Figure 6.21:** Time step independence verification. Mean temperature cold room.
$\Delta t1 = 0.01s$, $\Delta t2 = 0.05s$ and $\Delta t3 = 0.1s$.

The second verification procedure is done in order to check the time independence
of the obtained solutions. This is accomplished in this work using three different time
steps, with each one of the grids considered, and comparing results obtained among
them. The time steps considered are: $\Delta t1 = 0.01s$, $\Delta t2 = 0.05s$ and $\Delta t3 = 0.1s$. In
Figure 6.21(a) are presented the results of mean temperature in the refrigerated room
for the coarse grid and for the first $5s$ of simulation. Mean temperature obtained
using both $\Delta t2 = 0.05s$ and $\Delta t3 = 0.1s$ for the fine mesh is also presented in Figure
6.21(b). As shown, no influence of the time step used in the simulation is observed.
Therefore, results obtained using a time step of $\Delta t2 = 0.05s$ or $\Delta t3 = 0.1s$ can be
considered time independent and thus credible. However, for $\Delta t3$ convergence time
is extended, therefore a time step of $\Delta t2 = 0.05s$ is used throughout this section.

Even though the study of the results presented by two or more turbulence models
can not be considered as part of a verification procedure, actually it is important
to compare the different results obtained if various turbulence models are used. In
this section IL ($k\epsilon$-LEVM) [6] and WXT ($k\omega$-LEVM) [7], two-equation linear eddy
viscosity models, representative of $k - \epsilon$ and $k - \omega$ platforms, are applied to the same
case (test1 and test3 in Table 6.4), in order to check the influence of the turbulent
length scale determining variable ($\epsilon$ or $\omega$) on the final results. As it was explained
in section 2.2, both models use the low Reynolds approach to the integration of the
variables near solid walls. These models are selected for their adequate performance
in the simulation of impinging plane jets (see Chapter 4 for details).

Thus, in Figure 6.22 mean temperature and entrainment rate are plotted for both
IL ($k\epsilon - LEVM$) and WXT ($k\omega - LEVM$) models using the $N1$ grid and a $dt = 0.05s$
for the first $8s$ of simulation. Due to the differences presented by the models are not

**Figure 6.22:** Influence of the turbulence model. Mean temperature cold room and entrainment rate.

significant, any of these models can be used. However, IL ($k\epsilon - LEVM$) is selected due to WXT ($k\omega - LEVM$) has presented some convergence instabilities at the beginning of the simulation.
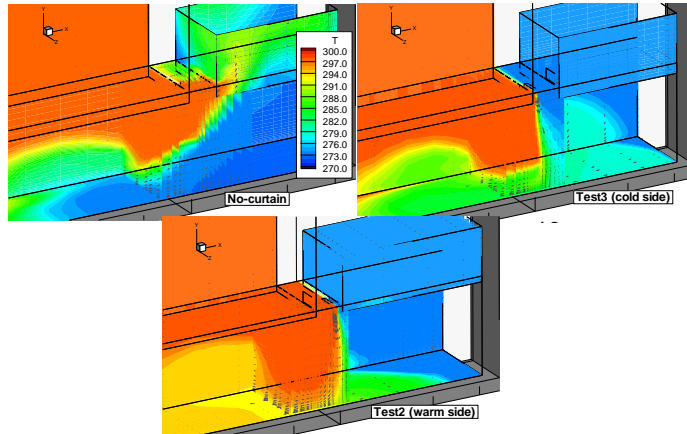
### 6.4.3 Influence of air curtain location

In the first set of studies the analysis is centred in the influence of the side where the air curtain is placed. Furthermore, for comparison purposes, first a simulation of the situation without air curtain is done (case $no - curtain$ Table 6.4), after that, the air curtain is placed in the cold side, behind the wall separating spaces (test3 Table 6.4), and finally the air curtain is located in front of the door (warm side), and the suction is of warm air (test2 Table 6.4). A temperature comparison at time $t = 7, 5s$ is presented in Figure 6.23. As it can be observed, without air curtain, warm air entries to the refrigerated space and fills almost completely its top part. However, when the air curtain is located in the cold side, it prevents warm air entering top part, but due to mixing produced warm air crosses the jet and contributes to increase temperature in the bottom part of the refrigerated space. Furthermore, when the air curtain is placed in the warm side, it brings warm air to the bottom part of the cold room, but it still remains colder than in the $test3$ configuration.
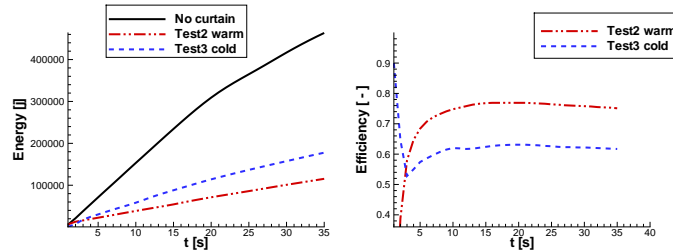
In terms of global balances, clearly air curtain reduces energy gains in the refrigerated space (see Figure 6.24). Moreover, placing the air curtain in the exterior warm space seems to be the best option for long door opening periods. But, if the door is opened for very short time intervals, it is better to place the curtain in the cold side (major efficiency). A combination of both suctions could improve results. Finally, it is important to highlight that in both cases the air curtain reaches an almost constant

value for the efficiency: for test2 it is of 0.75 and for *test*3 it is of 0.62. These results agree with those presented by Foster et al. [5].



**Figure 6.23:** Temperature comparison at $t = 7.5s$. Influence of air curtain location.



**Figure 6.24:** Energy gains of the refrigerated room and efficiency according to air curtain placement.
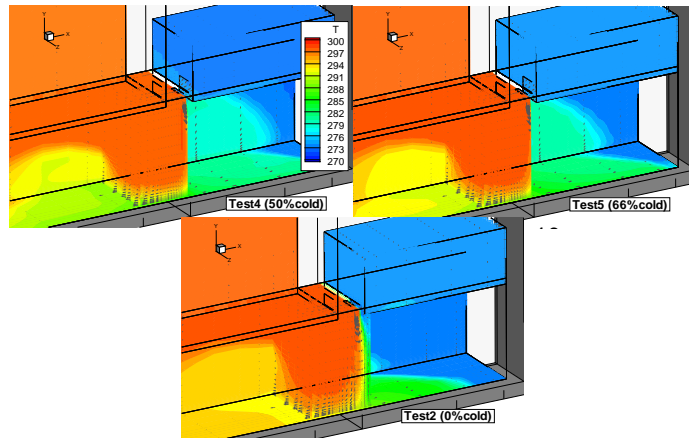
### 6.4.4   Influence of combining air suction

As it was inferred above, perhaps a combination of cold and warm air could improve the air curtain sealing efficiency. Therefore, the objective of this study is to review the effect that suction and discharge combining cold and warm air has on the global

parameters considered. In *test*2 all the air is taken from warm room, in *test*4 50% of the air is aspired from the warm (left) side, while in *test*5 66% is warm air and the rest is suctioned from the cold room. Accordingly, for *test*4 the half width of the air curtain next to refrigerated space discharges cold air, the other half discharges warm air. In *test*5 one third is of cold air and the rest warm air, i.e. air is not mixed inside the air curtain device. In both cases the air curtain is mounted in the left side of the door (warm room).
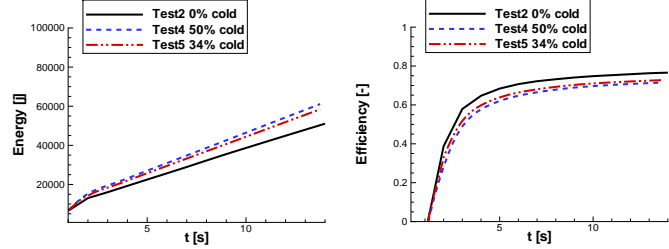
Illustrative results of the temperature contours obtained after 7.5*s* of numerical simulation are presented in Figure 6.25. In this Figure can be seen as with *test*2 temperature inside refrigerated room is still colder than with *test*4 and *test*5. Furthermore, is observed as temperature of the bottom part of the warm space diminishes proportionally with the fraction of cold air used in the air curtain.



**Figure 6.25:** Temperature comparison at $t = 7.5s$. Mixed suction effect.

It seems that a mixed air curtain suction/discharge does not increase air curtain sealing efficiency in this case. Furthermore, efficiency varies inversely with cold air used, when the quantity of cold air suctioned by the air curtain is increased, efficiency reduces (see Figure 6.26). This can be attributed to the renovation generated by the air curtain, i.e. if the air curtain takes air from the refrigerating room an air renovation is forced, cold air is extracted, mixed with warm air and then returned to the refrigerated space. Moreover, a jet with warm temperature can avoid formation of fog and ice blocks in the floor, improving in this way security.
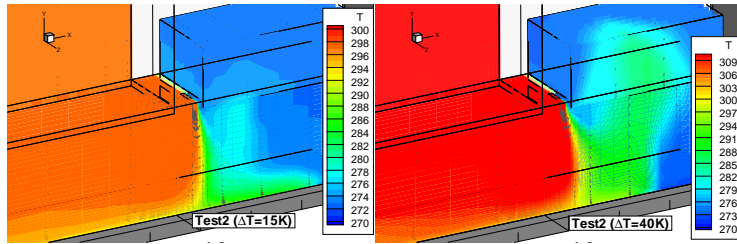
**Figure 6.26:** Energy gains of the refrigerated room and air curtain efficiency according to air curtain suction/discharge air mixing.
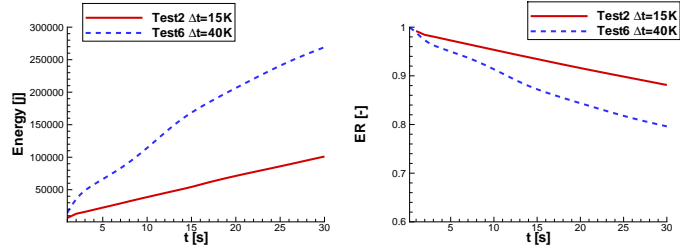
### 6.4.5 Influence of temperature difference between spaces

As it was noted before, temperature difference between spaces creates stack effect, which generates a pressure difference across the air curtain. If the temperature difference increases, so does pressure difference. Therefore, the purpose of this study is to determine how a change in the temperature difference affects air curtain performance. Then, two cases with temperature differences of 25 K (*test*2, temperature in cold and warm room are 273 K and 298 K respectively) and 40 K (*test*6, temperatures of 273 K and 313 K in cold and warm room respectively) are compared.



**Figure 6.27:** Temperature comparison at $t = 7.5s$. Temperature difference effect.

In Figure 6.27 is possible to observe that when an increase in the temperature difference occurs, an air curtain with the discharge characteristics of *test*6, is not capable of correctly counteract stack effect created. It is deflected towards the right side and the impact point is inside the cold room. In this way, a considerable amount of air is introduced to the cold space after jet impingement.

213

**Figure 6.28:** Energy gains of the refrigerated room and entrainment rate according to temperature difference between rooms.
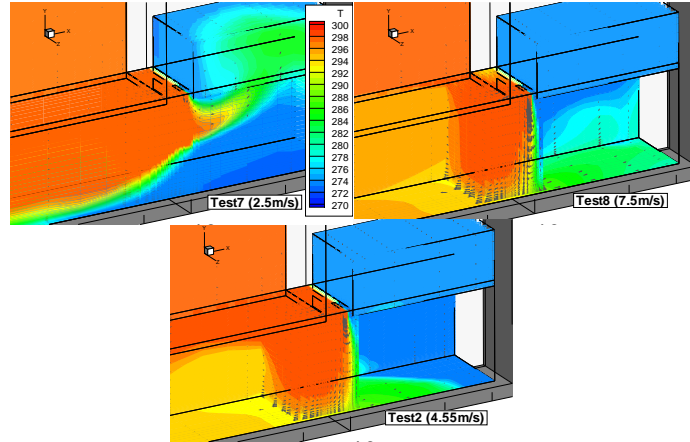
Furthermore, for $test6$ is not possible to evaluate the efficiency because the same case without air curtain has not been simulated. Therefore, efficiency is expressed in terms of entrainment rate (ER). In Figure 6.28 is observed as energy gains of the refrigerated room increases and the sealing efficiency, represented in terms of entrainmet rate, of the air curtain reduces when conditions are changed from $test2$ to $test6$. However, air curtain still gives an acceptable sealing effect, i.e. the entrainment rate does not decrease considerably. Moreover, the energy gained by the refrigerated room is somewhat less than that without air curtain when the temperature difference is $25K$ (see Figures 6.24 and 6.28).

### 6.4.6 Influence of the air curtain discharge velocity
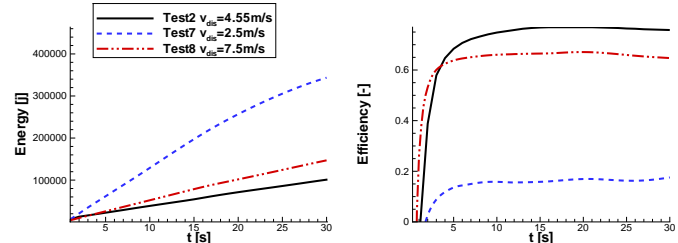
Since discharge velocity can be controlled by the air curtain manufacturer or designer, an important question that must be addressed is if the discharge velocity that is being used is correct, or what is the effect of increasing or reducing it. Thus, three different velocities of $2.5m/s$, $4.55m/s$ and $7.5m/s$, which correspond to $test7$, $test2$ and $test8$ respectively, are used in order to answer previous questions and check discharge velocity influence on temperature field and global parameters studied.

Representative results after $7.5s$ are herewith presented in Figure 6.29. In the case of $test7$, the jet produced by the air curtain is broken and deflected towards the refrigerated room as consequence of the reduction of the air curtain discharge velocity. Then, air curtain fails in the task of separating the rooms. Therefore, temperature in the upper part of the cold room is increased. Moreover, if the air curtain discharge velocity is increased to $7.5m/s$ ($test8$), air entrained with the air curtain jet is increased and therefore temperature at the bottom of the refrigerated space is augmented respect to the case studied for $4.55m/s$ ($test2$) (see Figure 6.29).

**Figure 6.29:** Temperature comparison at $t = 7.5s$. Influence of air curtain discharge velocity.
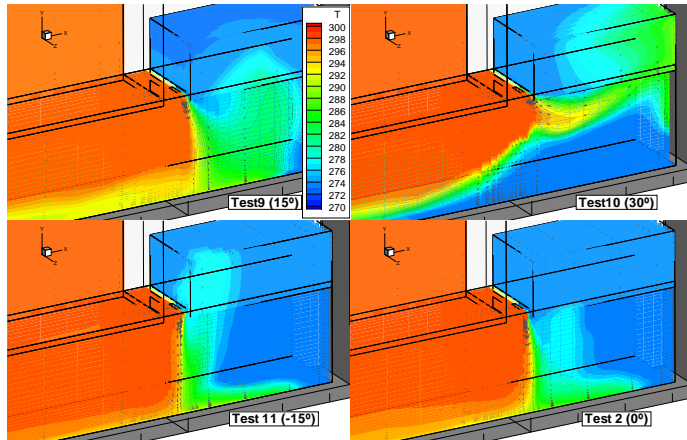


**Figure 6.30:** Energy gains of the refrigerated room and air curtain efficiency. Influence of air curtain discharge velocity.

Results of energy gains in the refrigerated space and air curtain sealing efficiency are presented in Figure 6.30. In this Figure is easy to observe the problems generated from an inadequate selection of the air curtain discharge velocity. When a too low velocity is used ($2.5m/s$, $test7$), energy gains/losses are notably increased, and a marked reduction in the sealing efficiency is also observed. Furthermore, for short time openings efficiency becomes negative, what means air curtain effect is harmful. Moreover, in Figure 6.30 it can be seen as air curtain efficiency diminishes when the discharge velocity is increased to $7.5m/s$ ($test8$), respect to that obtained with

215

a discharge velocity of $4.55m/s$. However, for the first instants the use of a higher velocity is beneficial.

### 6.4.7 Influence of the air curtain discharge angle

Another parameter that can be modified by the air curtain designer is the discharge angle. Thus, in this section four different angles ($-15^o$, $0^o$, $15^o$ and $30^o$; which correspond to $test11$, $test2$, $test9$ and $test10$ of Table 6.4 respectively) are used in order to study their influence on air curtain performance. These angles are assumed to be positive towards the cold room. In all these situations the air curtain is placed in the warm side.
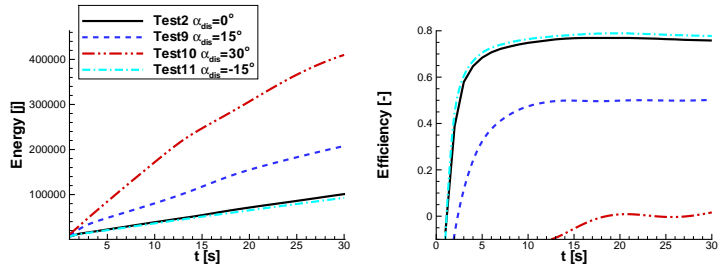


**Figure 6.31:** Temperature comparison at $t = 7.5s$. Influence of air curtain discharge angle.

In Figure 6.31 characteristic maps obtained for the different air curtain discharge angles are presented. As can be seen in this Figure, when the angle is fixed towards cold space ($test9$ and $test10$) temperature in the refrigerated room is more elevated than that of $test2$. This difference is particularly important when the angle is changed from $15^o$ to $30^o$. Taking into account the pressure distribution generated by the stack effect in an airtight building, in which the zero pressure level is placed in the middle height of the door, i.e. in the case without air curtain ($test1$), it is observed that the cold air flows by the bottom part of the doorway, from the right (cold) room towards the left (warm) room, and viceversa in the upper part. Then, if the jet is directed towards the warm side a major momentum is generated in order to

216

counteract momentum due to stack effect, therefore this is expected to improve air curtain behaviour. If the angle is set to the opposite, cold side, the pressure generated by the stack effect contributes to deflect the jet and a breakthrough is presented.



**Figure 6.32:** Energy gains of the refrigerated room and air curtain efficiency. Influence of air curtain discharge angle.

Furthermore, reviewing global results presented in Figure 6.32, it is seen that when the angle is set to $30^o$ the air curtain efficiency is always around zero, what means a null sealing effect. Moreover, energy gains with the air curtain discharge angle of $30^o$ are three times greater than those for a vertical discharge. On the other hand, when the angle is set to $-15^o$ slight improvements respect to $test2$ are observed. Thus a negative angle to some extend improves current results. Nevertheless, positive angles could be beneficial in the case of cold air suction/discharge when the air curtain is placed behind the door, i.e. in the cold room side ($test3$ in Table 6.4), where most of the cold air aspired from the refrigerated space would be returned to it.

## 6.5 Conclusions

In general two-dimensional simulation must be taken with care, and its results as a qualitative approximation. However, these simulations permit to achieve predictions in short time and with reasonable computational capacity. Throughout the first part of this chapter has been observed that is necessary to carry out three dimensional simulations to have adequate results. Furthermore, three dimensional effects are more important when flow configuration is changed,e.g. when flow rate or discharge angle are varied.

From the energetic study it can be extracted the optimum power that might be supplied to the air curtain to correctly isolate contiguous spaces, with the minimum thermal losses to the exterior, and maintaining an adequate temperature in the interior space. This optimal value depends on the imposed conditions.

Human comfort has been quantified employing PED factor. In the cases simulated a mass flow is always obligated to pass through the door, and due to the presence of the air curtain the main stream flows near the bottom wall, what creates a considerable discomfort in this region. However, as height is increased velocities are reduced, what improves comfort sensation and decreases PDE factor.

A verification procedure to ensure the grid and time independence of the numerical solutions has been applied as a previous necessary step to any parametric study. Furthermore, the effect of using a different turbulence model has been analyzed.

Cases displayed are an example of the versatility and possibilities that numerical simulation provides for the study of air curtains. Several parameters such as, air curtain location, discharge velocity, discharge angle, etc. have been studied in order to check their influence in the air curtain performance. In the case of refrigeration applications it has been found that the discharge velocity and discharge angle are the most sensitive parameters, an inadequate value for these variables can produce a undesirable effect, and contribute to increase energy gains/losses. Moreover, others parameters such as, air curtain location and the use of combined air suction/discharge, affect to some extent air curtain efficiency.

# References

[1] H. B. Awbi. *Ventilation of Buildings.* Chapman and Hall, 1991.

[2] A. M. Foster, M. J. Swain, R. Barrett, and S. J. James. Experimental Verification of Analytical and CFD Predictions of Infiltration Through Cold Stores Entrances. *International Journal of Refrigeration*, 26(8):918–925, 2003.

[3] A. M. Foster, M. J. Swain, R. Barrett, P. D'Agaro, and S. J. James. Effectiveness and optimum jet velocity for a plane jet air curtain used to restrict cold room infiltration. *International Journal of Refrigeration*, 29(5):692–699, 2006.

[4] J. J. Costa, L. A. Oliveira, and M. C. G. Silva. Energy savings by aerodynamic sealing with a downward-blowing plane air curtain-A numerical approach. *Energy and Buildings*, 38:1182–1193, 2006.

[5] A. M. Foster, M. J. Swain, R. Barrett, P. DAgaro, L. Ketteringham, and S. J. James. Three-Dimensional Effects of an Air Curtain Used to Restrict Cold Room Infiltration. *Applied Mathematical Modelling*, 31(6):1109–1123, 2007.

[6] N.Z. Ince and B.E. Launder. Computation of Buoyancy-Driven Turbulent Flows in Rectangular Enclosures. *International Journal of Heat and Fluid Flow*, 10(1):110–117, 1989.

*References*

[7] D.C. Wilcox. *Turbulence modeling for CFD.* DCW Industries, Inc. CA, 1993.

*References*

# Chapter 7

# Concluding remarks and future actions.

## Concluding remarks.

Turbulent flows are unsteady, irregular, chaotic and with many scales of motion. Therefore, an essential characteristic of flows in turbulent regime is that the velocity field varies significantly and irregularly in both position and time. Considering the complexity of these flows, it is remarkable that the Navier-Stokes equations describe them accurately and in complete detail. However, they provide a huge amount of information, which is not tractable for high-Reynolds number flows. As a result, the direct approach of solving the Navier-Stokes equations do not provide a tractable model for them. Thus, different statistical techniques, e.g. Reynolds Averaged Navier-Stokes and Large Eddy Simulations, aimed at developing tractable mathematical models that can accurately predict properties of turbulent flows have emerged. Nevertheless, their solution requires the assistance of elaborated numerical methodologies supported by computer aided systems. Due to RANS models can be appropriate to describe most of the main characteristics of the fluid motions, this technique has been selected in this thesis to analyze turbulent flows.

An air curtain is, in general, a turbulent jet of air blown across a doorway or an entrance to prevent or reduce the ingress of air at different conditions from outside the building of between two adjacent zones within a building.

The main contributions of the present thesis are: i) using RANS technique, to investigate the potential of explicit algebraic Reynolds stress models and both non-linear and linear eddy viscosity models in terms of accuracy and numerical performance in the description of turbulent internal forced convection flows. ii) to study air curtains using different approaches such as, simplified analytical models, computational fluid dynamics and experimental studies.

In Chapter 2, an introduction to the mathematical formulation used troughout this thesis has been presented. Since RANS modelling is selected the explanation has been centered on it. Moreover, the models used to relate turbulent stresses with the mean rate of strain are explained. Furthermore, a brief description of the discretization of the governing equations and computational methodology has been included. Finally, a rigorous post-processing procedure for the assessment of the quality of the numerical solutions in order to quantify errors and uncertainties used in this thesis is summarized. It is based on the generalized Richardson extrapolation for h-refinement studies and on the Grid Convergence Index.

Three basic test cases (plane channel, backward facing step, and confined imping-ing slot jet) have been studied in Chapter 3. Turbulent stresses are related with the mean rate of strain using linear and non-linear eddy viscosity models (LEVM, NLEVM) and explicit algebraic Reynolds stress models (EARSM), based on $k - \epsilon$ as well as $k - \omega$ platforms. Reviewing the plane channel, which is the simplest case studied, non-linear or explicit algebraic models show reasonably good behavior. In the case of backward facing step flow, NLEVM improve the accuracy in the predic-tions of skin friction coefficient and reattachment point, while the improvements in Stanton number, Reynolds stress tensor and mean velocity fields are limited. In the impinging jet case, it has been found that terms of higher order in the relation be-tween turbulent stresses and mean strain rates do not improve considerably results for the models studied. Whereas the use of better tuned dumping functions and/or additional terms, such as YAP correction, in the length-scale determining equation seems to play a more important role.

Further studies of the numerical performance and accuracy of models in both plane and round impinging jets have been addressed in Chapter 4. With this purpose, results from numerical simulations, using different models, have been compared among them and with experimental data available in the literature. Comparisons have been performed in terms of mean and fluctuating velocities and local Nusselt number. A verification procedure has been applied in order to ensure credibility of numerical results obtained. Reviewing the wall heat-transfer coefficient, local Nusselt number, in both plane and round impinging jet configurations, it is possible to observe the lack of generality of the models. In fact, models with good performance in the round jet case show poor results in the plane jet configuration.

The second part of this thesis has been devoted to the detailed study of air curtains. They have been analyzed numerically using different levels of description, from simple semi-empirical models to multidimensional numerical simulations, and experimentally measuring velocities and temperatures. In Chapter 5 air curtain prototypes have been studied numerically as well as experimentally. Constant temperature hot wire anemometry has been used to determine local values of velocity. Thus, experiments of two different nozzle geometry have been carried out and discharge characterized.

A variant of the third prototype has been designed introducing a flow straightener. With this design turbulence is reduced in both regions, air curtain discharge and jet downstream. Furthermore, velocity obtained at the air curtain discharge has been more uniform.

Experimental data presented in Chapter 5 are useful to have an idea of fluid-dynamic and thermal fields characteristics of the air curtain when it is placed in a doorway, and to validate the code with home-made experiments in three dimensions. Satisfactory results are obtained comparing numerical and experimental results. As a result of these comparisons, it has been learned that two-dimensional simulation must be taken with care, and its results as a qualitative approximation. Furthermore, it has been observed that is necessary to carry out three dimensional simulations to have adequate numerical predictions of air curtains.

Once, air curtains physic is understood, the code developed verified and the mathematical formulation validated, numerical experiments can be carried out. Thus, in Chapter 6 several parameters such as, air curtain location, discharge velocity, discharge angle, etc. have been studied in order to check their influence on the air curtain performance. Global indicators of the air curtain efficiency and human comfort have been applied as well. Applications to both, air conditioning and refrigeration have been numerically studied.

Cases displayed in Chapter 6 are an example of the versatility and possibilities that numerical simulation provides for the study of air curtains. It has been found that the discharge velocity, discharge angle and turbulence intensity of the jet are the most sensitive parameters. Inadequate values for these variables can produce undesirable effects and contribute to increase energy gains/losses.

## Future actions.

Due to this work has had a double purpose, future strategies to continue with this study have to be divided accordingly. Due to the shortcomings of numerical simulations using traditional RANS models (lack of generality and accuracy), unsteady three-dimensional behavior of the flow can be better solved by means of LES modelling. However, as it was commented before, due to LES solves the flow near solid walls, it still requires considerable computational resources [1]. Therefore, this limitation can be avoided if hybrid LES/RANS models are used. The main idea of these models is to modelise the wall layer with a RANS model, while the external zone is solved with LES. Furthermore, a different mathematical formulation which assures that some important properties of the Navier-Stokes equations are considered in the discretization, e.g. symmetry-preserving discretization [2], might be implemented.
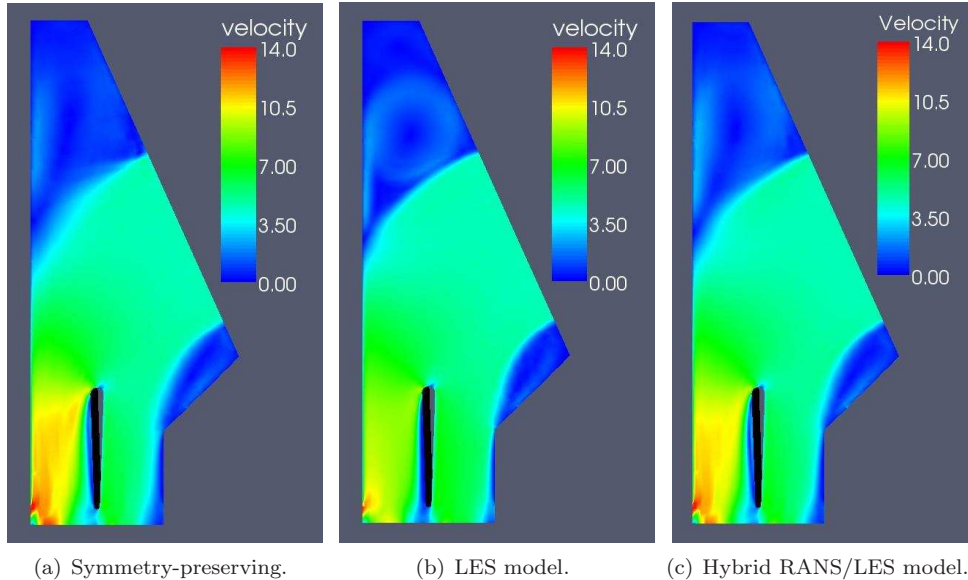
Even though, three dimensional simulations with relatively complex geometry have been numerically simulated. It is necessary to use more efficient algorithms, improve

mesh generation and develop faster solvers. Therefore, to solve the system of algebraic equations full parallel direct and iterative sparse linear solvers should be implemented. Local refinement of the grid should be allowed and Laplacian smoother post-processing tools should be applied [3]. Regarding solution of the pressure equation, a Direct Fourier Schur Decomposition using sparse Cholesky for the local variables with an iterative or direct solver for the interface system, or conjugate-gradient (CG) with a PFSAI preconditioner, might be considered [4, 5].

Despite, LES or hybrid LES/RANS models are thought to be accurate, it is important to compare results obtained for these kind of turbulence models with benchmark results as well as with experimental data, in order to establish their real advantages and shortcomings.

Turning to air curtains subject, a good air curtain should provide a jet with low turbulence level, at discharge parabolic profile skewed to the protected zone and enough momentum to counter pressure differences across the opening [6]. Consequently, the analysis of the plenum before discharge should be taken into consideration in future studies. Thus, in the near future geometry of the plenum and influence of blades for flow orientation, should be studied in detail.



(a) Symmetry-preserving.    (b) LES model.    (c) Hybrid RANS/LES model.

**Figure 7.1:** Velocity contours for air curtain with blade for flow orientation. Comparison of turbulence models.

Actually, our Group is already working in these subjects, and the author of the

present thesis has begun with some preliminary studies of the air curtain discharge plenum using a Dynamic Smagorinsky SGS LES model [7] and an hybrid RANS/LES model [8] to solve turbulence. Thus, in Figure 7.1 illustrative results of mean velocity contours obtained for a geometry including a blade for flow orientation, and using a turbulence intensity of 0.15 are shown. Similar results are observed for the RANS/LES model and the symmetry-preserving formulation without model. An increment of the velocity magnitude is seen towards the exterior wall in the discharge region at $x \approx 0$, $y \approx 0$ using these models. On the other hand, the LES model predicts a minor increase of the velocity in this zone.

These preliminary results are encouraging, but more studies are required. Different numerical works considering parameters such as: inlet and outlet boundary conditions, the size and geometry of the computational domain used, and three dimensional simulations, ought to be carried out. Moreover, a larger domain taking into account building envelope characteristics, and airflow patterns around the building where the air curtain is mounted, should be useful.

# References

[1] S.B. Pope. *Turbulent Flows*. Cambridge University Press, 2000.

[2] R. W. Verstappen and R. M. Van Der Velde. Symmetry-preserving discretization of heat transfer in a complex turbulent flow. *Journal of Fluid Mechanics*, 54(4):299–318, 2006.

[3] O. Lehmkuhl, C. D. Perez-Segarra, R. Borrell, M. Soria, and A. Oliva. TERMOFLUIDS: A new Parallel unstructured CFD code for the simulation of turbulent industrial problems on low cost PC Cluster. In *Proceedings of the Parallel CFD 2007 Conference*, pages 1–8, 2007.

[4] F.X. Trias, M. Soria, C.D. Pérez-Segarra, and A. Oliva. A Direct Schur-Fourier Decomposition for the Efficient Solution of High-Order Poisson Equations on Loosely Coupled Parallel Computers. *Numerical Linear Algebra with Applications*, 13(4):303–326, 2006.

[5] R. Borrell, O. Lehmkuhl, M. Soria, and A. Oliva. Schur complement methods for the solution of Poisson equation with unstructured meshes. In *Proceedings of the Parallel CFD 2007 Conference*, pages 1–8, 2007.

[6] H. K. Navaz, M. Amin, S. C. Rasipuram, and R. Faramarzi. Jet entrainment minimization in an air curtain of open refrigerated display case. *International Journal for Numerical Methods for Heat and Fluid Flow*, 16(4):417–430, 2006.

[7] K. Mahesh, G. Constantinescu, and P. Moin. A Numerical Method for Large-Eddy Simulation in Complex Geometries. *Journal of Computational Physics*, 197:215–240, 2004.

[8] P. R. Spalart, S. Deck, M. L. Shur, K. D. Squires, M. K. Strelets, and A. Travin. A New Version of Detached-Eddy Simulation, Resistant to Ambiguous Grid Densities. *Theoretical and Computational Fluid Dynamics*, 20(2):181–195, 2006.

# Appendix A

# Specific turbulence model constants and damping functions

In Table A.1 a summary of model closure coefficients is shown. Table A.2 shows extra terms for damping functions in low Reynolds version summarised for $k - \epsilon$ models, where $\tau = \frac{k}{\epsilon}$.

| Model | $C_\mu$ | $C_{\epsilon1}$ | $C_{\epsilon2}$ | $\sigma_k$ | $\sigma_\epsilon$ |
|---|---|---|---|---|---|
| IL [1] | 0.09 | 1.44 | 1.92 | 1.00 | 1.30 |
| GPC [2] | 0.09 | 1.44 | 1.92 | 1.00 | 1.30 |
| CLS [3] | $\min\left[0.09, \dfrac{1.2}{1 + 3.5\eta + frs}\right]$ | 1.44 | 1.92 | 1.00 | 1.30 |
| AMGS [4] | 0.081 | 1.44 | 1.83 | 1.00 | 1.5544 |

**Table A.1:** Appendix A. High Reynolds coefficients for $k - \epsilon$ models.

In tables A.1 and A.2: $x_n$ is the distance to the nearest wall, $u_\tau = \sqrt{\tau_w/\rho}$ is the friction velocity and:

$$\eta = \max[\bar{S}, \bar{W}], \quad \bar{S} = \sqrt{2\mathbf{SS}}, \quad \bar{W} = \sqrt{2\mathbf{WW}}, \quad y^+ = \frac{\rho x_n u_\tau}{\mu_t}$$

$$YAP = \max\left[0.83\rho\left(\frac{k^{3/2}}{2.5\tilde{\epsilon}x_n} - 1\right)^2 \frac{\tilde{\epsilon}^2}{k} \quad, \quad 0\right], \quad T_t = \frac{k}{\epsilon}\max[1, \sqrt{2/R_t}]$$

$$frs = 0.235(\max(0 \quad, \quad \eta - 3.333))^2 exp^{-\frac{R_t}{400}}$$

*Appendix A. Specific turbulence model constants and damping functions*

$$R_t = \frac{k^2}{\nu\epsilon}, \quad R_y = \frac{\sqrt{k}y}{\nu}, \quad \vartheta = \max[k^{1/2}, (\nu\epsilon)^{1/4}], \quad \Psi = \max\left[\frac{\partial k}{\partial x_j}\frac{\partial(k/\epsilon)}{\partial x_j}, 0\right]$$

| Model | $f_\mu$ | $D$ | $f_1$ | $f_2$ | $E$ | $Y_c$ |
|---|---|---|---|---|---|---|
| IL[1] | $\exp\left(\dfrac{-3.4}{(1.0+R_t/50)^2}\right)$ | $2\mu\left(\dfrac{\partial\sqrt{k}}{\partial x_j}\right)^2$ | $1.0$ | $1-0.3\exp(-R_t^2)$ | $2\nu\mu_t\left(\dfrac{\partial^2\bar{u}_i}{\partial x_j\partial x_k}\right)^2$ | YAP |
| GPC[2] | $\dfrac{1-\exp(-0.01R_t)}{1-exp(-\sqrt{R_t})}\times$ $\max\left[1,\sqrt{\dfrac{2}{R_t}}\right]$ | $0.0$ | $1.0$ | $1.0$ | $\dfrac{0.3\rho\vartheta\sqrt{\epsilon T_t}\Psi}{T_t}$ | $0.0$ |
| CLS[3] | $1-$ $\exp\left[-\sqrt{\dfrac{R_t}{90}}-\left(\dfrac{R_t}{400}\right)^2\right]$ | $2\mu\left(\dfrac{\partial\sqrt{k}}{\partial x_j}\right)^2$ | $1.0$ | $1-0.3\exp[-R_t^2]$ | $0.0022\dfrac{\bar{S}\mu_t k^2}{\rho\tilde{\epsilon}}$ $\left(\dfrac{\partial^2\bar{u}_i}{\partial x_j\partial x_k}\right)^2, R_t<250$ | YAP |
| AMGS[4] | $1.0$ | $0.0$ | $1.0$ | $1-\exp\left(-\dfrac{R_y}{12.5}\right)$ | $0.0$ | $0.0$ |

**Table A.2:** Appendix A. Viscous terms in low Reynolds $k-\epsilon$ models.

| Model | WX [5] | WXT [6] | WXCD [7] | WJO [8] | AJL [9] | LAR [10] | ARG [11] |
|-------|--------|---------|----------|---------|---------|----------|----------|
| $\alpha^*$ | 1.0 | $\dfrac{\frac{1.0}{40} + \frac{R_\omega}{6.0}}{1 + \frac{R_\omega}{6.0}}$ | 1.0 | $\dfrac{C_\mu}{\beta^*}$ | $\dfrac{C_\mu^* f_\mu}{\beta^*}$ | $\dfrac{1}{6.5 + \sqrt{6}cos(\phi)U^*T}$ | 1.0 |
| $\beta^*$ | 0.09 | $\dfrac{9.0\left(\frac{5.0}{18} + \left(\frac{R_\omega}{8.0}\right)^4\right)}{100\left(1 + \left(\frac{R_\omega}{8.0}\right)^4\right)}$ | $\beta_o^* f_{\beta^*}$ | $\dfrac{9.0\left(\frac{5.0}{18} + \left(\frac{R_\omega}{10.0}\right)^4\right)}{100\left(1 + \left(\frac{R_\omega}{10.0}\right)^4\right)}$ | $\dfrac{9.0\left(\frac{\beta}{0.27} + \left(\frac{R_\omega}{9.0}\right)^4\right)}{100\left(1 + \left(\frac{R_\omega}{9.0}\right)^4\right)}$ | 0.09 | 1.0 |
| $\alpha$ | $\dfrac{5.0}{9.0}$ | $\dfrac{5.0\left(\frac{1.0}{10} + \frac{R_\omega}{2.7}\right)}{9.0\left(1.0 + \frac{R_\omega}{2.7}\right)\alpha^*}$ | $\dfrac{13.0}{25.0}$ | $\dfrac{5.0\left(\frac{1.0}{10} + \frac{R_\omega}{2.7}\right)}{9.0\left(1.0 + \frac{R_\omega}{2.7}\right)\alpha^*}$ | $0.45\alpha^*$ | $\dfrac{5.0}{9.0}$ | 0.5467 |
| $\beta$ | $\dfrac{3.0}{40}$ | $\dfrac{3.0}{40}$ | $\beta_o f_\beta$ | $\dfrac{3.0}{40}$ | 0.0747 | $\dfrac{3.0}{40}$ | 0.83 |
| $\sigma_k$ | 2.0 | 2.0 | 2.0 | 2.0 | $\dfrac{1.2}{f_t}$ | 2.0 | 1.4 |
| $\sigma_\omega$ | 2.0 | 2.0 | 2.0 | 2.0 | $\dfrac{1.5}{f_t}$ | 2.0 | 2.0 |
| $E_w$ | 0 | 0 | 0 | 0 | $E_w$ | 0 | 0 |

**Table A.3:** Appendix A. Model parameters for $k - \omega$ models.

Table A.3 shows the different parameters for $k - \omega$ models. Where $(R_\omega = \dfrac{\rho k}{\omega \mu})$ and in the WXCD model:

$$\beta_o = \frac{9}{125}, \quad f_\beta = \frac{1 + 70\chi_w}{1 + 80\chi_w}, \quad \chi_w \equiv \left| \frac{\bar{W}_{ij}\bar{W}_{jk}\bar{S}_{ki}}{(\beta_o^*\omega)^3} \right|$$

$$\beta_o^* = \frac{9}{100}, \quad f_{\beta^*} = \left\{ \begin{array}{ll} 1, & \chi_k \leq 0 \\ \dfrac{1 + 680\chi_k^2}{1 + 400\chi_k^2}, & \chi_k > 0 \end{array} \right\}, \quad \chi_k \equiv \frac{1}{\omega^3}\frac{\partial k}{\partial x_j}\frac{\partial \omega}{\partial x_j}$$

At the solid walls non-slip boundary condition is used $\vec{v}_{wall} = 0$. At that point, turbulent kinetic energy disappears, $k_{wall} = 0$, and the value imposed for $\epsilon$ or $\omega$ depends on the model applied:
$k - \epsilon$ models,

$$\epsilon_{wall} = 2\nu \left( \frac{\partial \sqrt{k}}{\partial x_n} \right)^2 \quad \text{or} \quad \tilde{\epsilon}_{wall} = 0$$

$k - \omega$ models,

$$\omega_{wall} = \frac{6\nu}{\beta x_n^2}$$

Tables A.4 and A.5 show the coefficients used for NLEVM and EARSM in the relation used to evaluate the Reynolds stress tensor. For $C_\mu$ and $f_\mu$ functions see Tables A.1 and A.2 respectively.

In Tables A.4 and A.5 both models AMGS and ARG use:

$$\eta^2 = \alpha_2(S_{ij}S_{ij})(\tau^2) \qquad \xi^2 = \alpha_3(W_{ij}W_{ij})(\tau^2)$$

$$\alpha_1 = (4/3 - C_2)(g/2) \quad \alpha_2 = (2 - C_3)^2(g^2/4) \quad \alpha_3 = (2 - C_4)^2(g^2/4)$$

$$\alpha_4 = \left( \frac{2 - C_4}{2} \right) g \quad \alpha_5 = (2 - C_3)g \quad g = \frac{1}{0.5C_1 + C_5 - 1}$$

while AMGS model uses:

$$C_1 = 6.8, C_2 = 0.36, C_3 = 1.25, C_4 = 0.40, C_5 = 1.88 \quad \text{and} \quad \tau = \frac{k}{\epsilon}$$

.

ARG model uses:

$$C_1 = 3.0, C_2 = 0.8, C_3 = 1.75, C_4 = 1.31, C_5 = 2.0 \quad \text{and} \quad \tau = \frac{1}{\omega}$$

.

*Appendix A. Specific turbulence model constants and damping functions*

| Model | AMGS [4] | CLS [12] | LAR [10] |
|---|---|---|---|
| $C_\mu^*$ | $\dfrac{\alpha_1(3(1+\eta^2)+0.2(\eta^6+\xi^6))}{3+\eta^2+6\eta^2\xi^2+6\xi^2+\eta^6+\xi^6}$ | $C_\mu$ | $C_\mu$ |
| $f_\mu^*$ | 1.0 | $f_\mu$ | 1.0 |
| $\beta_1$ | $\alpha_5 C_\mu^*$ | $-0.4 C_\mu^* f_\mu^*$ | 0.0 |
| $\beta_2$ | $\alpha_4 C_\mu^*$ | $0.4 C_\mu^* f_\mu^*$ | $2\dfrac{\sqrt{1-(3C_\mu S^* T)^2}}{1.0+6S^*\Omega^* T^2}$ |
| $\beta_3$ | 0.0 | $-1.04 C_\mu^* f_\mu^*$ | 0.0 |
| $\gamma_1$ | 0.0 | $40(C_\mu^*)^3 f_\mu^*$ | 0.0 |
| $\gamma_2$ | 0.0 | $40(C_\mu^*)^3 f_\mu^*$ | 0.0 |
| $\gamma_3$ | 0.0 | 0.0 | 0.0 |
| $\gamma_4$ | 0.0 | $-80(C_\mu^*)^3 f_\mu^*$ | 0.0 |

**Table A.4:** Appendix A. Coefficients for non-linear stress-strain relationship.

In the case of LAR model:

$$U^* = \sqrt{S_{ij}S_{ij}+W_{ij}W_{ij}}, \qquad \Omega^* = \sqrt{W_{ij}W_{ij}}, \qquad S^* = \sqrt{S_{ij}S_{ij}}$$

$$W^* = \frac{S_{ij}S_{jk}S_{ki}}{(S^*)^3}, \qquad T = \tau = \frac{1}{\beta^*\omega}, \qquad \phi = 0.333 a cos\sqrt{6}W^*$$

In the WJO model, the following relations arise:

$$B_1 = -\frac{6}{5}\frac{N}{N^2-2II_w}, \qquad B_4 = -\frac{6}{5}\frac{1}{N^2-2II_w}$$

| Model | ARG [11] | WJO [8] | AJL [9] |
|---|---|---|---|
| $C_\mu^*$ | $\dfrac{\alpha_1(3(1+\eta^2))}{3+\eta^2+6\eta^2\xi^2+6\xi^2}$ | $-0.5B_1 f_\mu$ | $C_B C_\mu^* f_\mu$ , $C_\mu^* = 0.12$ |
| $f_\mu^*$ | 1.0 | 1.0 | 1.0 |
| $\beta_1$ | $\alpha_5 C_\mu^*$ | $\dfrac{(1-f_\mu^2)(3B_2-4)}{\max(II_S, II_S^{eq})}$ | $4C_D C_B (C_\mu^* f_\mu)^2 (1 - f_w(A)|_{A=26})$ |
| $\beta_2$ | $\alpha_4 C_\mu^*$ | $-\dfrac{B_2(f_\mu^2 B_4 - (1-f_\mu^2))}{2\max(II_S, II_S^{eq})}$ | $4C_D C_B (C_\mu^* f_\mu)^2 (1 - f_w(A)|_{A=26})$ |
| $\beta_3$ | 0.0 | 0.0 | 0.0 |
| $\gamma_1$ | 0.0 | 0.0 | 0.0 |
| $\gamma_2$ | 0.0 | 0.0 | 0.0 |
| $\gamma_3$ | 0.0 | 0.0 | |
| $\gamma_4$ | 0.0 | 0.0 | 0.0 |

**Table A.5:** Appendix A. Coefficients for non-linear stress-strain relationship.

where,

$$II_S = [\mathbf{S}^2], \qquad II_W = [\mathbf{W}^2], \qquad II_S^{eq} = 5.735, \qquad B_2 = 1.8$$

$$f_\mu = 1 - \exp\left(-\frac{2.4\sqrt{Re_y} + 0.003Re_y^2}{26.0}\right), \quad \tau = \max\left(\frac{1.0}{\beta^*\omega}, 6.0\sqrt{\frac{\mu}{\rho\beta^* k\omega}}\right)$$

$$N = \begin{cases} \dfrac{c_1'}{3} + (P_1 + \sqrt{P_2})^{1/3} + sign(P_1 - \sqrt{P_2})\left|P_1 - \sqrt{P_2}\right|^{1/3}, & P_2 \geq 0 \\[3mm] \dfrac{c_1'}{3} + 2(P_1^2 - P_2)^{1/6}\cos\left[\dfrac{1}{3}\arccos\left(\dfrac{P_1}{\sqrt{P_1^2 - P_2}}\right)\right] & , \quad P_2 < 0 \end{cases}$$

being,

$$P_1 = \left( \frac{1}{27} c_1'^2 + \frac{9}{20} II_S - \frac{2}{3} II_w \right) c_1', \quad P_2 = P_1^2 - \left( \frac{1}{9} c_1'^2 + \frac{9}{10} II_S + \frac{2}{3} II_W \right)^3$$

$$c_1' = \frac{9}{4}(c_1 - 1), \quad c_1 = 1.8$$

In the AJL model, the basic constitutive relation ($\tau_{ij}' \equiv$ eq. 2.73) is additioned with the two next fragments intended to account, respectively, for high normal straining and strong near-wall anisotropy [9],

$$\frac{\overline{u_i' u_j'}}{k} = \tau_{ij}' + \tau_{ij}^{(s)} + \tau_{ij}^{(w)} \tag{A.1}$$

where,

$$\tau_{ij}^{(s)} = (1 - f_w(A)|_{A=26}) \left[ -2 f_{s1} C_B C_\mu^* f_\mu \mathbf{S} + 4 f_{s2} C_D C_B (C_\mu^* f_\mu)^2 \left( \mathbf{S}^2 - \frac{1}{3} [\mathbf{S}^2] \right) \right]$$

$$\tau_{ij}^{(w)} = f_w(A)|_{A=26} \left\{ - \alpha_w \left( d_i d_j - \frac{\delta_{ij}}{3} d_k d_k \right) + 2(1 - f_{r1}^2) \right.$$

$$\times \left[ - \frac{\beta_w C_w}{1 + C_w \sqrt{s_2^* w_2^*}} (s_{ik}^* w_{kj}^* - w_{ik}^* s_{kj}^*) \right.$$

$$\left. + \frac{\gamma_w C_w}{1 + C_w s_2^*} \left( s_{ik}^* s_{kj}^* - \frac{\delta_{ij}}{3} s_2^* \right) \right] \right\}$$

In the above,

$$f_{s1} = f_{r1} f_{r2} C_{s1} (C_D C_\mu^* f_\mu)^2 \tau^2 (\mathbf{W}^2 - \mathbf{S}^2),$$

$$f_{s2} = -f_{r1} f_{r2} \left[ 1 + C_{s2} C_D C_\mu^* f_\mu \tau (\sqrt{\mathbf{W}^2 - \mathbf{S}^2}) \right],$$

$$f_{r1} = \frac{w^2 - s^2}{w^2 + s^2}, \quad f_{r2} = \frac{s^2}{w^2 + s^2}, \quad s^2 = S_{mn} S_{mn}, \quad w^2 = W_{mn} W_{mn},$$

$$f_w(A) = \exp \left[ - \left( \frac{y_n^*}{A} \right)^2 \right], \quad y_n^* = \frac{y_n (\nu \beta^* \omega k)^{1/4}}{\nu},$$

$$C_D = 0.8, \quad C_{s1} = 15.0, \quad C_{s2} = 7.0,$$

also,

$$s_{ij}^* = \tau_D S_{ij}, \qquad w_{ij}^* = \tau_D W_{ij},$$
$$s_2^* = s_{ij}^* s_{ij}^*, \qquad w_2^* = w_{ij}^* w_{ij}^*,$$

$$\tau_D = (1 - f_w(A)|_{A=15})\frac{1}{\beta^* \omega} + f_w(A)|_{A=15}\sqrt{\frac{\nu}{\beta^* \omega k}},$$

$$\alpha_w = 1, \qquad \beta_w = 0.25, \qquad \gamma_w = 1.5, \qquad C_w = 0.5,$$

and

$$d_i = \frac{N_i}{\sqrt{N_k N_k}}, \qquad N_i = \frac{\partial y_n}{\partial x_i} \tag{A.2}$$

represent the orientation of the wall to which the distance $y_n$ relates.

Eventhough this model uses $k - \omega$ platform, a number of features derives from the $\epsilon$-equation. Thus,

$$\mu_t = \rho C_\mu^* f_\mu \frac{k^2}{\epsilon} = C_\mu^* f_\mu \frac{k^2}{\beta^* \omega k} = \left(\frac{C_\mu^* f_\mu}{\beta^*}\right)\frac{k}{\omega} = \alpha^*\frac{k}{\omega},$$

where

$$f_\mu = \left\{1 + \frac{35}{R_t^{3/4}}\exp\left[-\left(\frac{R_t}{30}\right)^{3/4}\right]\right\}(1 - f_w(A)|_{A=26})$$

$$f_t = 1 + 5.0 f_w(A)|_{A=5},$$

$$E_\omega = (1 - f_w(A)|_{A=600})C_{\omega 1}C_\mu^* f_\mu \tau \frac{\partial k}{\partial x_j}\frac{\partial \omega}{\partial x_j}, \qquad C_{\omega 1} = 1.5,$$

$$C_B = \frac{1}{1 + (C_D C_\mu^* f_\mu)^2\left(\frac{22}{3}\mathbf{W}^2 + \frac{2}{3}(\mathbf{W}^2 - \mathbf{S}^2)f_B\right)},$$

$$f_B = 1 + 100 C_D C_\mu^* f_\mu \tau(\sqrt{\mathbf{W}^2 - \mathbf{S}^2})$$

235

# References

[1] N.Z. Ince and B.E. Launder. Computation of Buoyancy-Driven Turbulent Flows in Rectangular Enclosures. *International Journal of Heat and Fluid Flow*, 10(1):110–117, 1989.

[2] U. Goldberg, O. Peroomian, and S. Chakravarthy. A Wall-Distance-Free k-$\epsilon$ Model with Enhanced Near-Wall Treatment. *Journal of Fluids Engineering*, 120(3):457–462, 1998.

[3] T. J. Craft, H. Iacovides, and J. H. Yoon. Progress in the Use of Non-linear Two-Equation Models in the Computation of Convective Heat-Transfer in Impinging and Separated Flows. *Flow, Turbulence and Combustion*, 63(1):59–81, 1999.

[4] R. Abid, J.H. Morrison, T.B. Gatski, and C.G. Speziale. Prediction of Aerodynamic FLows with a New Explicit Algebraic Stress Model. *AIAA Journal*, 34(12):2632–2635, 1996.

[5] D. C. Wilcox. Reassessment of the Scale-Determining Equation for Advanced Turbulence Models. *AIAA Journal*, 26:1299–1310, 1988.

[6] D. C. Wilcox. Simulation of Transition with a Two-Equation Turbulence Model. *AIAA Journal*, 32:247–255, 1994.

[7] D.C. Wilcox. *Turbulence modeling for CFD*. DCW Industries, Inc. CA, 1998.

[8] S. Wallin and A. V. Johansson. An Explicit Algebraic Reynolds Stress Model for Incompressible and Compressible Turbulent Flows. *Journal of Fluid Mechanics*, 403:89–132, 2000.

[9] K. Abe, Y. J. Jang, and M. A. Leschziner. An Investigation of Wall-Anisotropy Expressions and Length-Scale Equations for Non-Linear Eddy-Viscosity Models. *International Journal of Heat and Fluid Flow*, 24(2):181–198, 2003.

[10] J. Larsson. Two-Equation Turbulence Models for Turbine Blade Heat Transfer Simulations. In *Proceedings 13th ISABE Conference*, pages 1214–1222, 1997.

[11] R. Abid, C. Rumsey, and T.B. Gatski. Prediction of Nonequilibrium Turbulent FLows with Explicit Algebraic Stress Models. *AIAA Journal*, 33(11):2026–2031, 1995.

[12] T.J. Craft, B.E. Launder, and K. Suga. Development and Application of Cubic Eddy-Viscosity Model of Turbulence. *International Journal of Heat and Fluid Flow*, 17(1):108–115, 1996.

# Appendix B

# Publications in the context of this thesis

**Journal papers:**

- J. E. Jaramillo, C.D. Pérez-Segarra, A. Oliva, and K. Claramunt. Analysis of Different RANS Models Applied to Turbulent Forced Convection. *International Journal of Heat and Mass Transfer*,50(19-20):3749–3766, 2007.

- J. E. Jaramillo, C.D. Pérez-Segarra, I. Rodriguez and A. Oliva. Numerical Study of Plane and Round Impinging Jets Using RANS Models. *Numerical Heat Transfer: Part B*, 54(3):1–25, 2008.

**International conference papers:**

- J. E. Jaramillo, K. Claramunt, C. D. Pérez-Segarra, R.Cònsul, and J. Cadafalch. Numerical study of different RANS models applied to turbulent forced convection. In *Proceedings of the IV International Symposium on Turbulence, Heat and Mass Transfer*, pages 671–680, 2003.

- J. E. Jaramillo, K. Claramunt, J. Cadafalch, and C. D. Pérez-Segarra. Comparative Study of Different RANS Models on Impinging Plane Jets. In *Proceedings of the Fourth European Congress on Computational Methods in Applied Sciences and Engineering (ECCOMAS)*, pages 258–258, 2004.

- J. Jaramillo, E. Mas de les Valls, C. Oliet, and J. Cadafalch. Numerical simulation of the behavior of thermosyphon systems. In *Proceedings of the 5th ISES Europe Solar Conference (EUROSUN 2004)*, 2004.

- J. E. Jaramillo, C. D. Pérez Segarra, and A. Oliva. Simulation of Flow and Heat Transfer in Impinging Jets Using RANS models. In *Proceedings of the V International Symposium on Turbulence, Heat and Mass Transfer*, pages 445–448, 2006.

- J. E. Jaramillo, C. D. Pérez Segarra, and A. Oliva. Suitability of Different RANS Models in the Description of Turbulent Plane and Round Impinging Jets. In *Proceedings of the Fifth European Congress on Computational Methods in Applied Sciences and Engineering (ECCOMAS)*, pages , 2008.

- J. Jaramillo, A. Oliva., C. D. Pérez Segarra, and C. Oliet. Application of Air Curtains in Refrigerated Chambers. In *Refrigeration and Air Conditioning Conference*, 2008.

- J. E. Jaramillo, C. D. Pérez Segarra, and A. Oliva. A Detailed Study of the Plenum and Discharge Jet Produced by Air Curtains. In *Proceedings of the Sixth International Conference on Enegineering Computational Technology*, 2008.

**National conference papers:**

- F. X. Trias, M. Soria, J. E. Jaramillo, A. Oliva, and C.D. Pérez-Segarra. Uso de ordenadores paralelos de bajo coste para Simulaciones avanzadas en dinámica de fluidos y transferencia de calor. In *Anales de Ingeniería Mecánica (Revista de la Asociación Española de Ingeniería Mecánica, Año 14)*, 2002.

- K. Claramunt, J. E. Jaramillo, X. Albets, and D. Piedrafita. Simulación numérica de flujos turbulentos en base a modelos de de dos ecuaciones de transporte turbulento. In *Anales de Ingeniería Mecánica (Revista de la Asociación Española de Ingeniería Mecánica, Año 14)*, 2002.